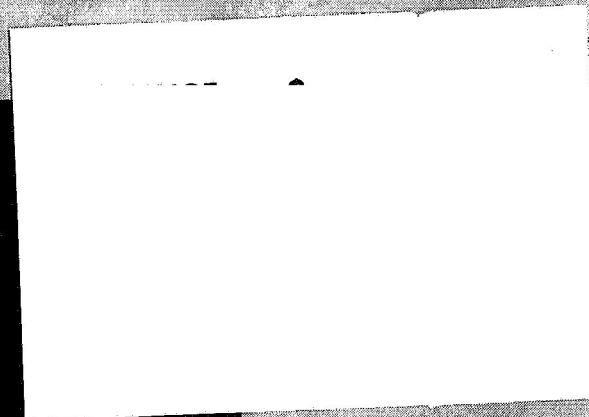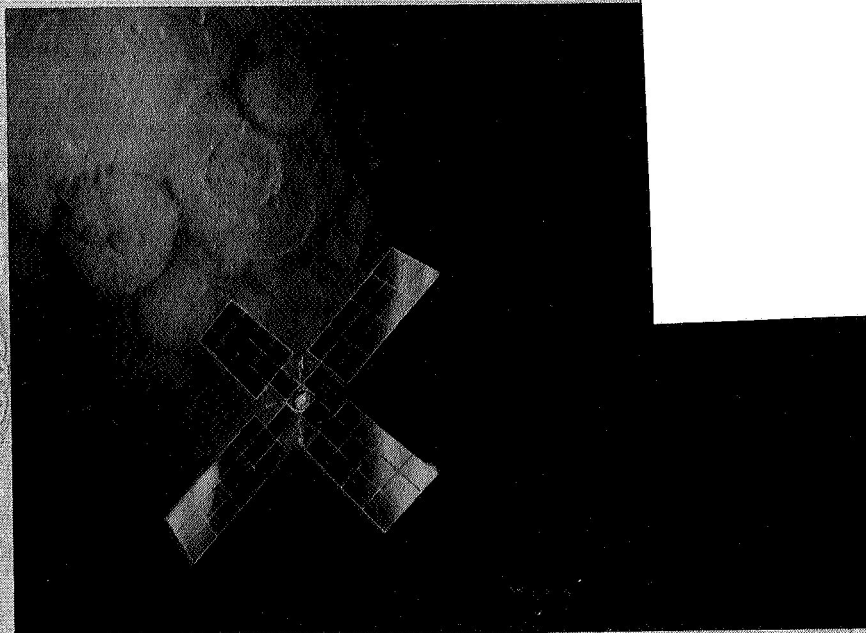# LARGE AREA
SOLAR ARRAY

D2-113355-6 (Part I)

3RD QUARTERLY REPORT — PHASE II

Prepared for
Jet Propulsion Laboratory
Under Contract
JPL 951934

THE *BOEING* COMPANY - SPACE DIVISION

D2-113355-6 (Part I)

3RD QUARTERLY REPORT— PHASE II

Prepared for
Jet Propulsion Laboratory
Under Contract
JPL 951934

LARGE AREA SOLAR ARRAY

June 1968

Prepared by

THE BOEING COMPANY
Aerospace Group
Space Division
Seattle, Washington

PART I

Prepared by ___R. C. Weikel___   ___6-13-68___
                          R. C. Weikel   Date

___John J. Morey for F.W. McAfee___   ___6-12-68___
                          F.W. McAfee   Date

___J.L. Apperson___   ___6-12-68___
                          J.L. Apperson   Date

___D.A. Norsen___   ___6-12-68___
                          D.A. Norsen   Date

Approved by ___W.I. Ratcheson___   ___6-13-68___
                          W.I. Ratcheson   Date

NOTICE

D2-113355-6

ABSTRACT

Part I of this report on the LASA Phase II third quarterly development contract covers the engineering, technology, and manufacturing accomplishments during the reporting period from March 1, 1968, through May 31, 1968. It summarizes the mechanisms test activity, fabrication progress and problems with the Main Subpanel 1, and the progress made in GSE development.

CONTENTS

ILLUSTRATIONS

TABLES

1.0 INTRODUCTION AND SUMMARY

This Large-Area Solar Array Phase II third quarterly development report is a contractual requirement under JPL Contract 951934. It is divided into two parts under one cover and has one document number. Part I describes the LASA Phase II third quarterly activity, and Part II summarizes the technical analyses of large-area solar arrays that have resulted since the beginning of Phase I in September 1966. The time period covered by Part I of this report is from February 29 through May 31, 1968.

The document format has been designed to ease the readers task of extracting data to the degree (or level of detail) he needs for effective evaluation. This document can be read at three distinct levels of detail.

1) Part I describes briefly the document's content and reports the status of the program.

2) For more technical detail, the proposition statements (typed in script) within the sections can be read.

3) If more detail is desired, it is available throughout the document in the individual sections.

Part I of this report has been limited to only the significant achievements of the third quarter so that a more detailed technical description of the program to date could be presented (Part II). Therefore, Part I consists of only two sections:

1) Section 1.0, "Introduction and Summary";

2) Section 2.0, "Summary of Phase II Third-Quarter Activities."

1.1 PHASE II OBJECTIVES

Phase II objectives are being met as planned, except for schedule revisions resulting from damaged panels in final assembly.

The Phase II objectives are: (1) mechanisms development, (2) partial fabrication and structural verification, and (3) partial development of the deployment and verification equipment. Mechanisms development tests were completed on schedule; however, all test objectives were not met and some retesting will be required. Fabrication of Main Subpanel 1 (major test article, MTA-1) is 95% complete. However, damage to some intercostal bonds must be repaired before the test article can be used to support a revised test schedule. Phase II development of the deployment and verification equipment was completed during this quarter, 3 months ahead of schedule; permission has been granted to extend some of this effort during Phase II. This effort was originally planned as Phase III work.

1

1.2 FOURTH-QUARTER PLANNING

Work planned for the fourth quarter will complete the development phase.

During the next quarter, MTA-1 will be reworked and final assembly completed, it will be checked out, and delivered for testing. Vibration testing will be conducted and test reports completed. Mechanisms retesting will be accomplished and reports written. Additional tests (CCN activity) for power degradation and vibration will be run on the 16-square-foot panel, fabricated during Phase I. The additional work planned for the deployment and verification equipment will be completed, and final documentation and reporting will be completed and submitted to JPL during the fourth quarter.

2.0 SUMMARY OF PHASE II THIRD-QUARTER ACTIVITIES

This section summarizes the activities of the LASA organization in
performing the tasks required by the Phase II contract during the 3-month
period beginning March 1 and ending May 31, 1968. The purpose is to give
a concise summary of the status of the work accomplished. The functional
areas of engineering, manufacturing, and testing are reported by task,
with items of particular interest emphasized. Preliminary test results
are also reported.

2.1 MECHANISMS COMPONENT DESIGN, FABRICATION, AND TEST---TASK 2

*Testing will be completed by July 1, 1968, including retest of tiedown
release mechanisms.*

The test articles were selected from the solar-panel tiedown, release,
and deployment systems. Figures 2-1 and 2-2 show the location of the
components tested. Figure 2-1 shows the main components tested in the
SCM-1 and SCM-2 tests. Each of the four solar panels, making up the
solar array, are made of five units, numbered 1 through 5, from the space-
craft outboard. Unit 1 has only one main subpanel and no auxiliaries.
Units 2 through 5 have one main subpanel and two auxiliary subpanels.
There are 13 subpanels for each solar-panel assembly. The main hinge
assembly and latching mechanism, the auxiliary hinge, damper and latching
mechanism, and the quadrant assembly illustrated show the location for
one of each assembly. The tiedown and release-system components tested
are shown in Figure 2-2. The cable tiedown at Station 10.5 is typical
of the tiedown at four of the six stations with circumferential ties.
The tiedown system at Station 170, the top of the panel assembly, and
at Station 124, the top of Subpanel 5, also ties the four solar-panel
assemblies to each other. These ties and the train for releasing all
circumferential ties will be tested in Phase III. The tiedown system
at the center spar consists of a clamp assembly used at five of the six
stations. The tiedown release at Station 124 is a cable cutter, and
releases the solar-panel stack simultaneously with the actuation of the
deployment system. The components selected and scheduled for test pro-
vide data that will be useful in Phase III testing.

During this quarter, all of the scheduled tests for the mechanism compo-
nents were completed. A summary of test results is given in Table 2-1.
Details of the problems and results are detailed in subsequent paragraphs.
The deployment tests on the simulated main subpanel (SCM-1) were satis-
factorily completed in an air and vacuum environment. The deployment
motor performs at -63°F, with more than expected consistency in cable
rate. The deployment tests on the auxiliary subpanels (SCM-2) were com-
pleted in the air and vacuum environment. The damper operated at a tem-
perature of -110°F, which was better than expected. Deployment rate was
low but acceptable. The release tests on the cable tiedown system at
Station 10.5 were performed satisfactorily; however, the effect of a

3

MAIN
HINGE
ASSEMBLY

QUADRANT
ASSEMBLY

SOLAR ARRAY

AUXILIARY
HINGE ASSEMBLY
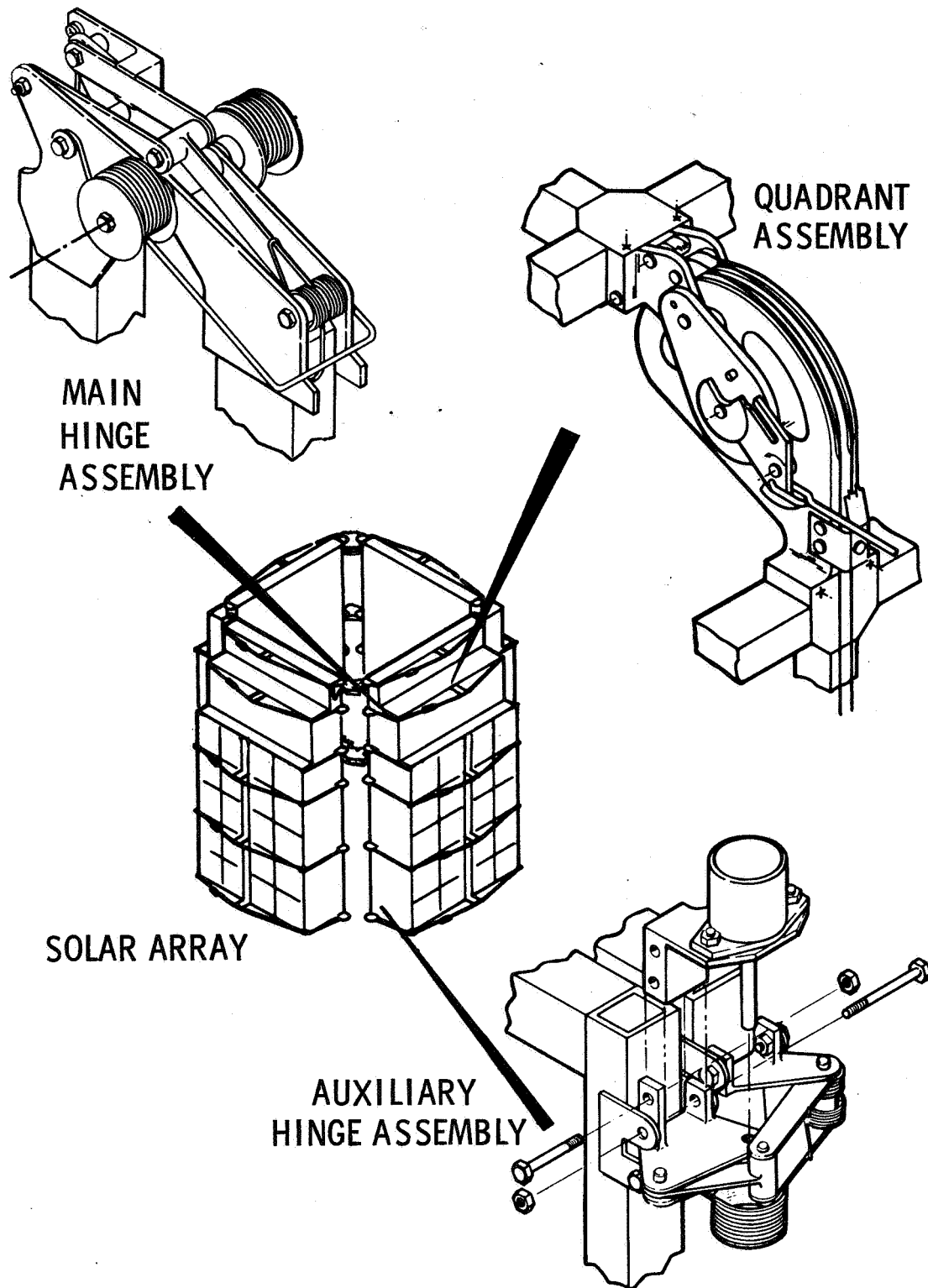
Figure 2-1:   DEPLOYMENT MECHANISMS TESTS

CENTER-TIEDOWN
RELEASE (TYPICAL)

CENTRAL TIEDOWN
STA 124

SOLAR ARRAY

TYPICAL
TIEDOWN
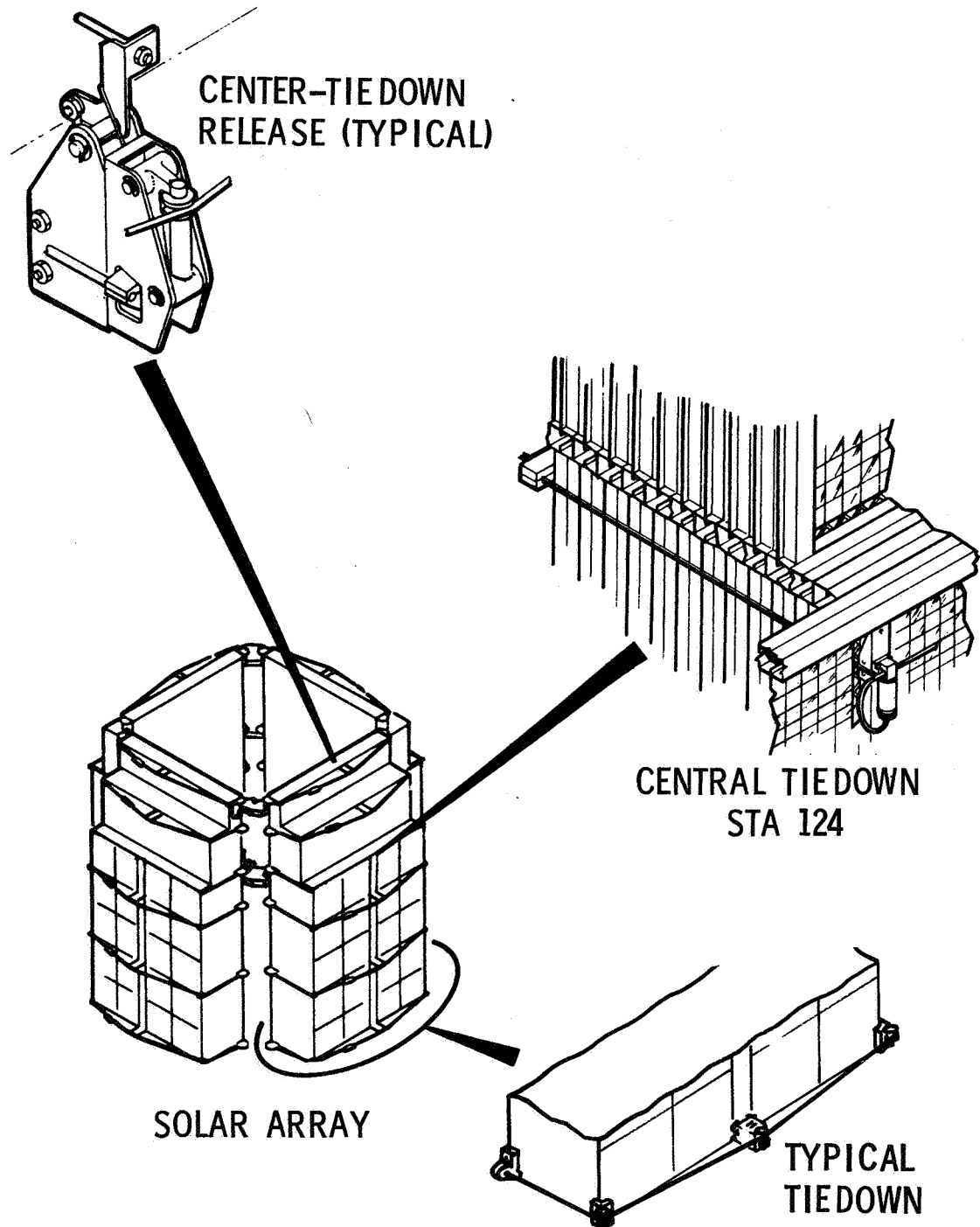
Figure 2-2: TIEDOWN AND RELEASE SYSTEM

Table 2-1: MECHANISMS COMPONENT TEST SUMMARY

Test	Results	Recommendations
SCM-1 ambient deployment tests (main subpanels)	Deployment satisfactorily performed in 10 minutes; motor operated at uniform rate within 570 to 600 sec	Ambient test data on main subpanel deployment accepted as satisfactory
SCM-2 ambient deployment tests (auxiliary subpanels)	Auxiliary subpanels deployed at 70°F in 79 to 100 sec; dampers maintained 12.5 in-lb radian/sec damping coefficient at 70°F	Special attention must be given alignment of hinge lines in fab
SCM-1 & -2 vacuum deployment tests (main and auxiliary subpanels)	Auxiliary subpanels deployed at -100°F and 1 x 10⁻⁸ torr; main subpanel deployed in 10 min., 34 sec; motor temp was -63°F	Provide thermal coating on damper to control rate of activation
SCM-30-2 tiedown and cable release test	Test confirmed that release method and stored energy were adequate to jettison tiedown cables; electrical anomaly prevents assessment of delay function	Test must be repeated to ensure delay timing, with adequate instruments to confirm delay action
SCM-30-3 center-spar-cable tiedown & release test	Cable deflection with time becomes assymptotic at about 70% of rigger load; clamp, as designed, is adequate to hold 4 of 5 stations when polyurethane inserts used and jaws are polyurethane coated	Test must be rerun using tapered clamping surface, coated, uncoated, smooth, and threaded to develop full capability of clamping method; look at dual-cable release for Sta 10.5

differential in release timing was not determined. Retest will be run in June 1968 to obtain this information when new squibs are available. The test on the center-tie release system produced usable data on the Nomex cable, but further development of the clamp assembly and rigging loads will be continued during June.

Problems identified in the design, fabrication, and testing of the mechanism components were minor, and were solved before testing was started in most cases. The following problems and their solutions are considered the most significant.

Hinge Alignment---The simulated main- and auxiliary-panel hinges were both sensitive to hinge alignment. The austere tooling used was inadequate in alignment of hinges, and both tests required rework of the hinge brackets to obtain satisfactory alignment before testing. Better alignment methods and additional instructions will be required for future parts.

Overcenter Latching Interference---The overcenter latch links interfered with the large bracket attach bolt heads. Three solutions were available for this problem. Countersink the bolt head, change the link, or use more links on the outside of the bracket. Moving the links on the outside of the bracket was selected as the best method, and the latches were changed before testing. Another interference in the latching occurred when excess material was left on the link to allow for adjustment. The excess material was removed after the part was located. The original design provided for the dead center of the linkage to fall about 22 degrees from the subpanel, and was intended to ensure positive latching. The location of the dead center, 22 degrees from parallel to the subpanel, allows an overtravel of the subpanel and results in a top dead-center condition when tension remains in the cable. These problems will be corrected on future parts by drawing changes and by improving the fabrication method used to locate hinge and link-pin locations.

Overcenter Latching Springs---The springs used to hold the main subpanel latching links on or beyond dead center were not strong enough to overcome the friction forces and deployment torque. This gave the appearance in testing of the links not latching because the links did not move beyond dead center. Future latching mechanisms will be equipped with stronger springs to provide more apparent motion in latching.

Deployment-Cable Spring Rate---The solar-panel deployment cables, during manufacturing and mechanism-testing operations (Task 4), became bent at spots where they passed over small-diameter pulleys. These bent areas provided a low, variable spring rate at the beginning of testing. A plan to replace the two deployment cables on the array with a flat tape is being investigated. The tape would be spliced to the cables at a point behind Subpanel 1 to retain operational redundancy. This plan may also reduce the weight of the system.

Cost reduction in fabricating mechanism components was a result of the experience gained during fabrication and testing of the mechanism test article. The following changes are the most significant.

7

Deployment Quadrant-Assembly Revision---The design of the quadrant
attachment to the subpanel will be revised to allow the titanium parts
to be predrilled, and the quadrant drilled to match assembly installation.
This will eliminate the necessity of drilling titanium on installation
and also make it easier to locate the quadrant.

Replace Bolts and Nuts with Pins and Retaining Rings---Changing bolts
and nuts to pins and retaining rings will increase clearance in many
places, reduce the weight, and facilitate assembly of the mechanisms.

The status of mechanism testing on the mechanism component tests is
shown in Figure 2-3. All of the originally scheduled tests were com-
pleted with the following results.

Main-Subpanel Deployment in Air (SCM-1)---Tests were completed on
March 26, 1968. All mechanisms operated satisfactorily. The hinge
friction was low, both free and deflected. Hinge misalignment produces
the major friction forces. The overcenter latch spring appeared
inadequate.

Auxiliary-Subpanel Deployment in Air (SCM-2)---These tests were completed
on March 25, 1968, with the following results:

1) Auxiliary hinge latches could not be opened after latching by
   applying manual force to the panels;

2) Friction forces for the deflected panel simulating deflection due
   to 100°F thermal gradient between surfaces will fall within the
   allowed deployment forces;

3) The undeflected condition friction force was a maximum of 1.1
   inch-pounds.

*Vacuum Test of Main- and Auxiliary-Subpanel Deployment (SCM-1 and
SCM-2)*---The results of the vacuum tests were considered exceptional.
The motor deploying the main panels operated at -63°F and a cable rate
above 2 inches/minute. Both dampers operated at temperatures of -100°F
or lower. Figure 2-4 provides a history of the environment during test.
There was no evidence of cold welding. Pressures of 6 x 10^{-10} torr were
obtained before test, and all testing was performed at pressures below
1 x 10^{-8} torr. The auxiliary subpanels deployed at temperatures below
-100°F. The rate of deployment of the auxiliary subpanels was initially
45 degrees in 9 minutes for Panel 2A and 20 minutes for Panel 2B. The
final deployment rate before the heaters were turned on was approximately
3 degrees in 20 minutes for Panel 2A and 15 degrees in 20 minutes for
Panel 2B. The last 35 degrees of deployment after the heaters were
turned on the panels took 18 to 23 minutes. All test objectives were
met satisfactorily.

Tiedown Release Test (SCM-30-2)---The results of this test proved
satisfactory for simultaneous release. An objective of the test was
to determine the effect of nonsimultaneous release. This effect was
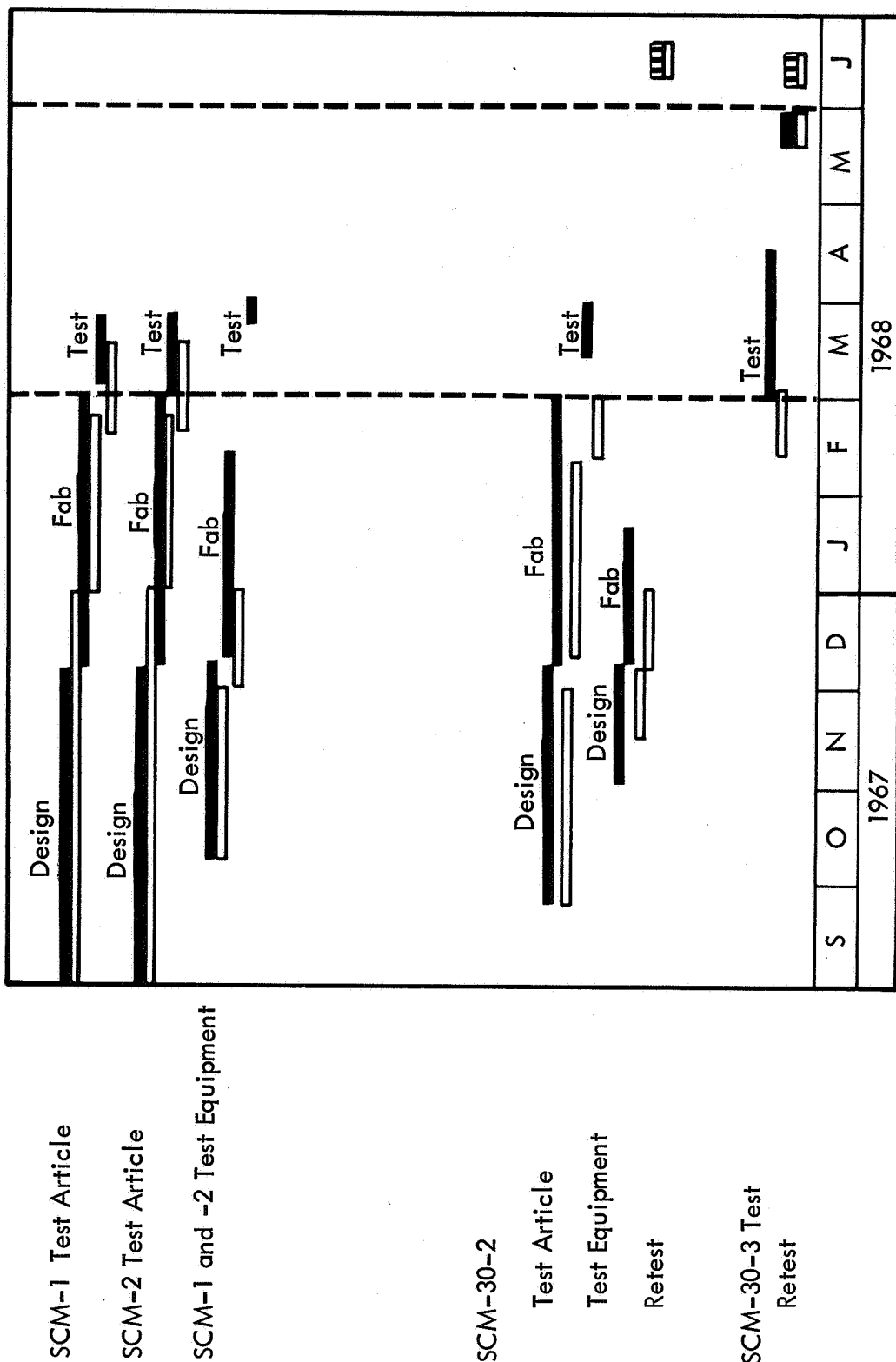
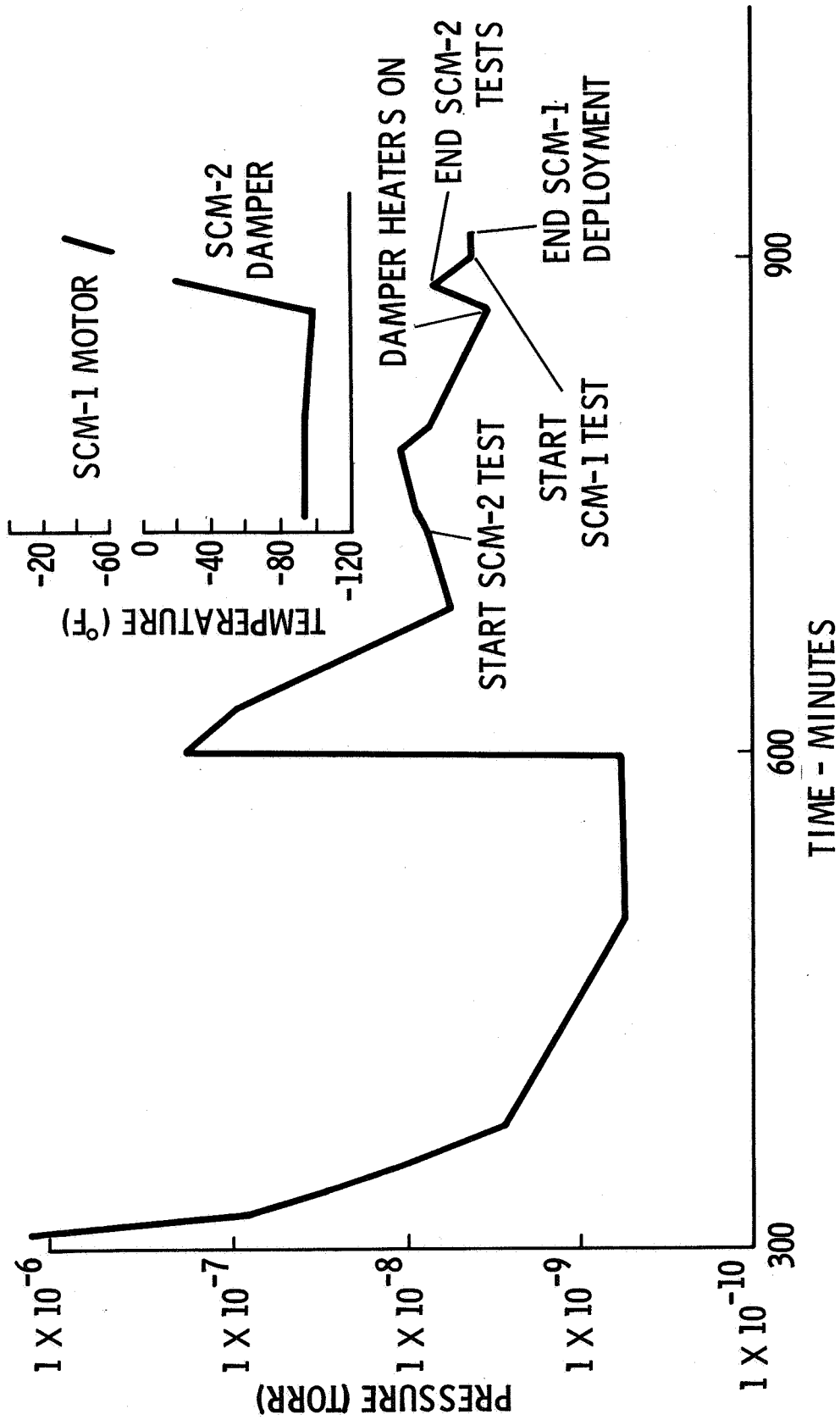Figure 2-3:   TASK 2 TESTING STATUS

Figure 2-4: MAIN- AND AUXILIARY-SUBPANEL VACUUM TEST RESULTS

not obtained when the squib, which was set for a 0.1-second firing delay, released almost simultaneously with the first squib. Retest is scheduled for June 25, 1968, when new squibs are available.

Center-Tie Release Test (SCM-30-3)---The tests conducted on the Nomex cable and center-tie clamp assembly were conducted in March 1968. The tensile characteristic of the Nomex cable was determined, and the adjusting-screw torque versus load-carrying capability was determined for different cable configurations. Best clamping performance was obtained using polyurethane-coated clamp jaws and a polyurethane rod inserted within the hollow cable near the clamp jaws. The load relaxation was determined for the selected cable clamp arrangement. The results showed the cable strength to be marginal for the 1,090-pound required load at Station 10.5; however, it is satisfactory for all other tiedown locations. Development of the clamp assembly and determination of the rigging loads are planned for completion in June 1968. A wedge-clamp design is being fabricated for these later tests.

2.2 FABRICATION AND TEST OF MTA-1 AND TEST FIXTURES---TASK 3

The MTA-1 fabrication and assembly status was improved to within 8 days of the original manufacturing schedule when damaged intercostal bonds caused a delay in part completion.

Major Test Article 1 (MTA-1) is Subpanel 1. A photo of the test article in final bond is shown in Figure 2-5. This is a beryllium subpanel structure, about 8 by 13 feet long. It is made of a dark-side frame assembly consisting of the cross brace; edge members; outboard spar; center spar and intercostals; and sunside assembly consisting of the outboard spars, center spar, upper- and lower-edge members, and the lateral spar. These two frames are bonded together with a fiberglass substrate upon which the solar cells are mounted.

As of June 1, 1968, the Subpanel 1 structure assembly is complete, except for damaged intercostal bonds. Repair procedures are being developed. The Task 7 manufacturing effort, which includes cell installation and bus-bar installation, will be completed; and the MTA-1 will be ready for delivery to the test area for instrumentation 10 days after repairs to the structure are completed. The repair time will be established as soon as removal of damaged items is complete. The delay, up to final structural bond, has been caused primarily by delays in the detail fabrication of beryllium parts and by increased setup time for frame bonding. Several days were lost when the etch, clean, and prime-process-validation coupons failed at approximately 50% of specified bond-shear values. Recleaning and priming of the parts affected was required. Many of the bonding problems are the result of movement of parts during the bonding cycle. Either pneumatic or spring pressure must be used to apply uniform bond pressure. Therefore, rigid fixing of pressure applicators is impossible; yet it is necessary to devise locators that apply no side loads during the bond cycle. The time required to rework and improve the tooling for

Figure 2-5: SUBPANEL 1 (MTA-1)

the dark-side frame doubled the anticipated bonding setup time. The
failure of the intercostal bonds during cure is being investigated, and
a plan for repair will be developed and implemented in the next quarter.

Patches were also required for three beryllium cap strips or shear webs
damaged slightly during the setup. One titanium gusset failed to clear
the tool and was bent by pressure. This resulted in partial bonding and
required hand-filing and application of a doubler. Shear-tie parts and
compression pads required hand-filing to clear the center-spar tiedown
cables. This discrepancy was the result of misinterpretation of a drawing
change.

Although these problems caused considerable delay, the bonding operations,
up to final structural bond, are considered successful because of the size
of the assembly and its complexity. Substantial improvement in Phase III
tooling will be made from Phase II experience. However, the bonding
operation will continue to require careful and competent technicians to
produce the necessary bond quality.

The six solar-cell submodules (7 by 58 strings) are assembled, ready for
installation, and the dummy-cell submodules (7 by 29 strings) are mounted
on tape backing, ready for installation. The copper and aluminum bus
bars are fabricated, and will be bonded after the solar cells are in-
stalled. The installation of diodes and interconnection of live modules
are planned for accomplishment concurrently with panel-instrumentation
test. The MTA-1 test equipment has been fabricated and is ready for
installation. The panel assembly and the test equipment will be ready
for instrumentation in July 1968.

The test plan was submitted to JPL by Memo 2-1101-94-2-482, dated
April 30, 1968.

2.3 DEPLOYMENT EQUIPMENT AND MTA-3 INSTALLATION AND TEST---TASK 4

Installation and test of the Phase II deployment equipment was accomplished
during this quarter. Analysis and reporting of test results are the only
uncompleted activities remaining in Task 4.

2.3.1 DEPLOYMENT-EQUIPMENT INSTALLATION AND CHECKOUT

*Installation of the deployment equipment is well ahead of schedule, pro-
viding sufficient time to correct minor equipment problems that might
otherwise have delayed the program.*

Installation of the deployment equipment was completed ahead of schedule.
During subsequent calibration and test activities, some delays were expe-
rienced due to minor equipment problems. Examples of the problems encoun-
tered are discussed below.

Suspension Lines---The overhead lines that support MTA-3 continued to creep under the weight of the subpanels. Changing the line from nylon to a music-wire and coil-spring configuration corrected this condition.

Track Fairing---Maintaining fairing between adjacent track sections remained a problem throughout this test period. After initial fairing was achieved, it was necessary to check and smooth the track joints with beeswax before each test run.

Mechanism Interferences---During deployment and latching of the MTA-3 subpanels, several mechanism interference problems were discovered. The interference of the 2-3 latch link with the 4-5 hinge plates shown in Figure 2-6 is an example. Interferences were corrected by shop work-arounds to prevent testing delays; drawings will be updated to eliminate interference problem areas during Phase III.

Diagonal Strut---The diagonal strut failed to lock at the end of the first deployment swing because of incorrect parts (see Figure 2-6). As this condition did not affect the time-history data, no action was taken. Strut parts will be revised for Phase III.

Deployment Cable---The deployment cable developed kinks where it was routed over rollers (see Figure 2-6). The kinks affected the cable spring rate and changed the shape of the time-history curves. Alternate cable designs are being investigated.

Hinge-Pin Alignment---Poor hinge-pin alignment caused excessive friction and required realignment of the pins by optical means in the test area. Tighter drawing tolerances and improved assembly tooling will improve alignment in Phase III.

2.3.2 TEST OPERATIONS

The mechanisms and aerodynamic tests successfully provided all experimental data required for evaluating the MTA-3 deployment analysis.

The mechanisms and aerodynamic tests were conducted to obtain operational data on mechanisms for design applications, to provide data for verifying the MTA-3 deployment analysis, and to determine aerodynamic effects on test results. During the tests, subpanel-hinge angle, deployment-cable tension, motor-windup rate, motor current, and the output of the strain gages on the diagonal strut, all of which were recorded. In addition to visicorder and "grocery" tape printouts, the data was recorded on magnetic tape for future computer reduction and analysis.

14
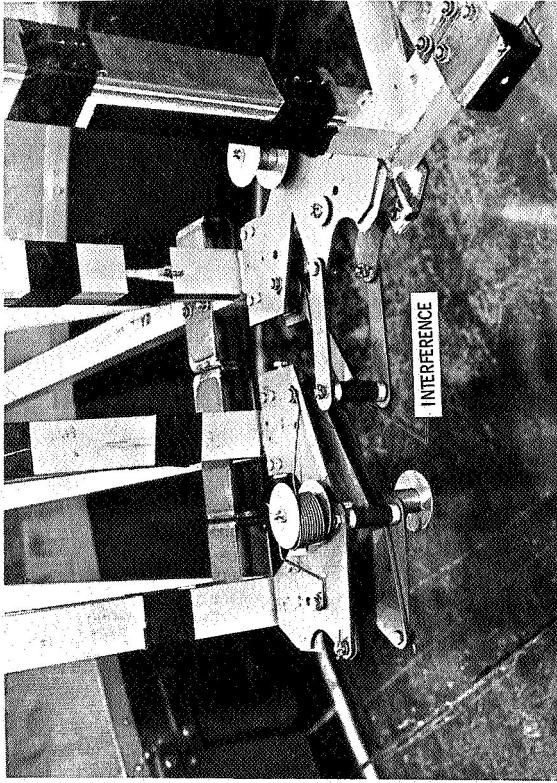
HINGE-LATCH INTERFERENCE
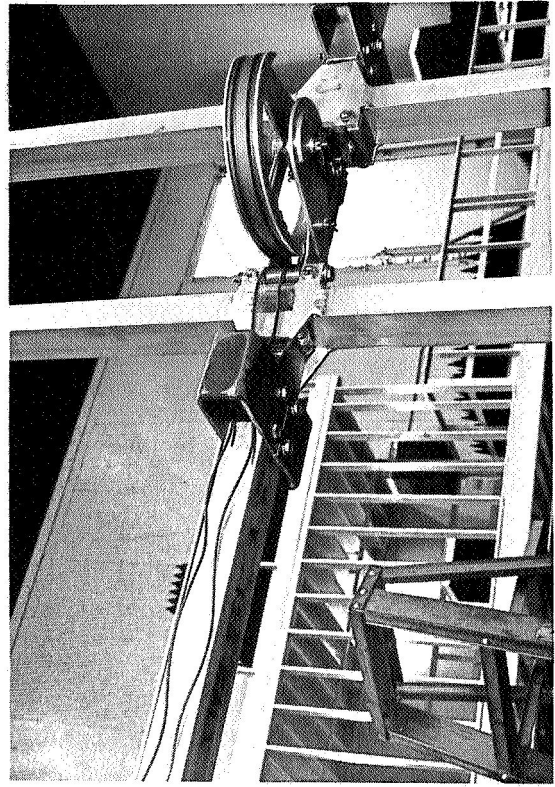
DEPLOYMENT CABLE

FAIRING OF AIRBEARING TRACK

DIAGONAL STRUT

Figure 2-6:   PROBLEMS ENCOUNTERED IN DEPLOYMENT EQUIPMENT CHECKOUT

2.3.3 TEST RESULTS

Preliminary test data analysis indicates satisfactory operation of the test article and equipment.

The Phase II deployment tests demonstrated that MTA-3 can be successfully deployed under its own power, well within the capacity of the deployment motor. Deployment-cable tension never exceeded 8.5 pounds. The frictions encountered in the deployment system and hinges tended to smooth out the time-history curves more than anticipated. The deployment-cable spring r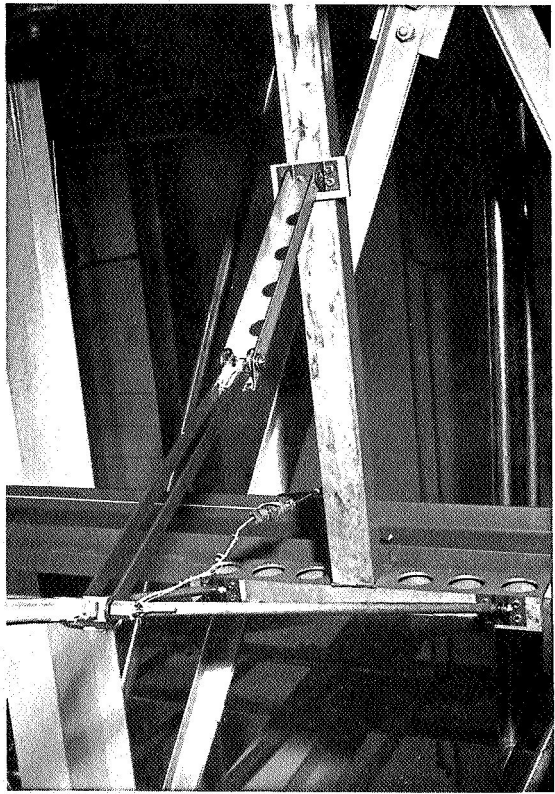ate changed from soft to relatively stiff during individual subpanel swings, as the deployment motor stretched out the cable kinks. Although the deployment was not adversely affected, the variable spring rate complicates test-data analysis.

Performance of the test equipment was excellent. Hangup of the airbearing feet due to track-section misfairing was the only problem of consequence. However, hangups were prevented by checking the track fairing before each test run.

Aerodynamic tests were conducted with plastic membranes attached to the frames of MTA-3, as shown in Figure 2-7, to simulate the effect of the MTA-4 substrate and cells. The time-history curves obtained during these tests showed appreciable damping because of aerodynamic effects.

2.4 DESIGN AND FABRICATION OF GROUND SUPPORT EQUIPMENT---TASK 5

Final design of Phase II equipment and preliminary design of Phase III equipment has been completed. A development test (SCG-4) of elements of the deployment demonstration system was successfully completed during the quarter. Final design and fabrication of additional deployment-demonstration equipment components was initiated in accordance with TDM 951934-4. This effort, to be completed by July 1, 1968, was originally planned for early in Phase III, is being financed with Task 5 underrun funds.

2.4.1 SCG-4 TEST

Phase II tests have shown that the overhead track, carriage, and winch system will provide suitable deployment demonstration.

SCG-4 was used to evaluate the operation of the demonstration equipment. The test setup (see Figure 2-8) consisted of a prototype track section, carriage, and spreader bar. Power was provided by a hand winch. The track was suspended from an overhead framework, located between the sides of the deployment-fixture base tower. A plywood panel was used to simulate an MTA-3 subpanel unit.

Figure 2-7: MTA-3 DEPLOYED WITH MEMBRANE INSTALLED

LIGHTWEIGHT AUXILIARY SUBPANEL

CATWALK &
LADDER

TRACK &
CARRIAGE

SPREADER
BAR

CATWALK

DEPLOYMENT
FIXTURE
STRUCTURE

AUXILIARY
SUBPANEL

MTA-3 MAIN
SUBPANEL #4

AUXILIARY SUBPANEL
DEPLOYMENT DEMONSTRATION
TEST SETUP

Auxiliary Subpanel
Deployment Demonstration
Test Setup
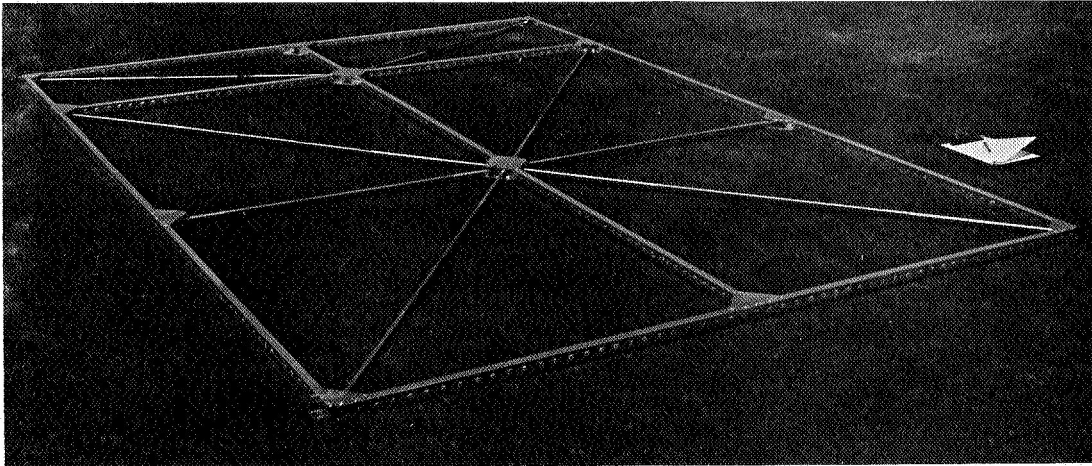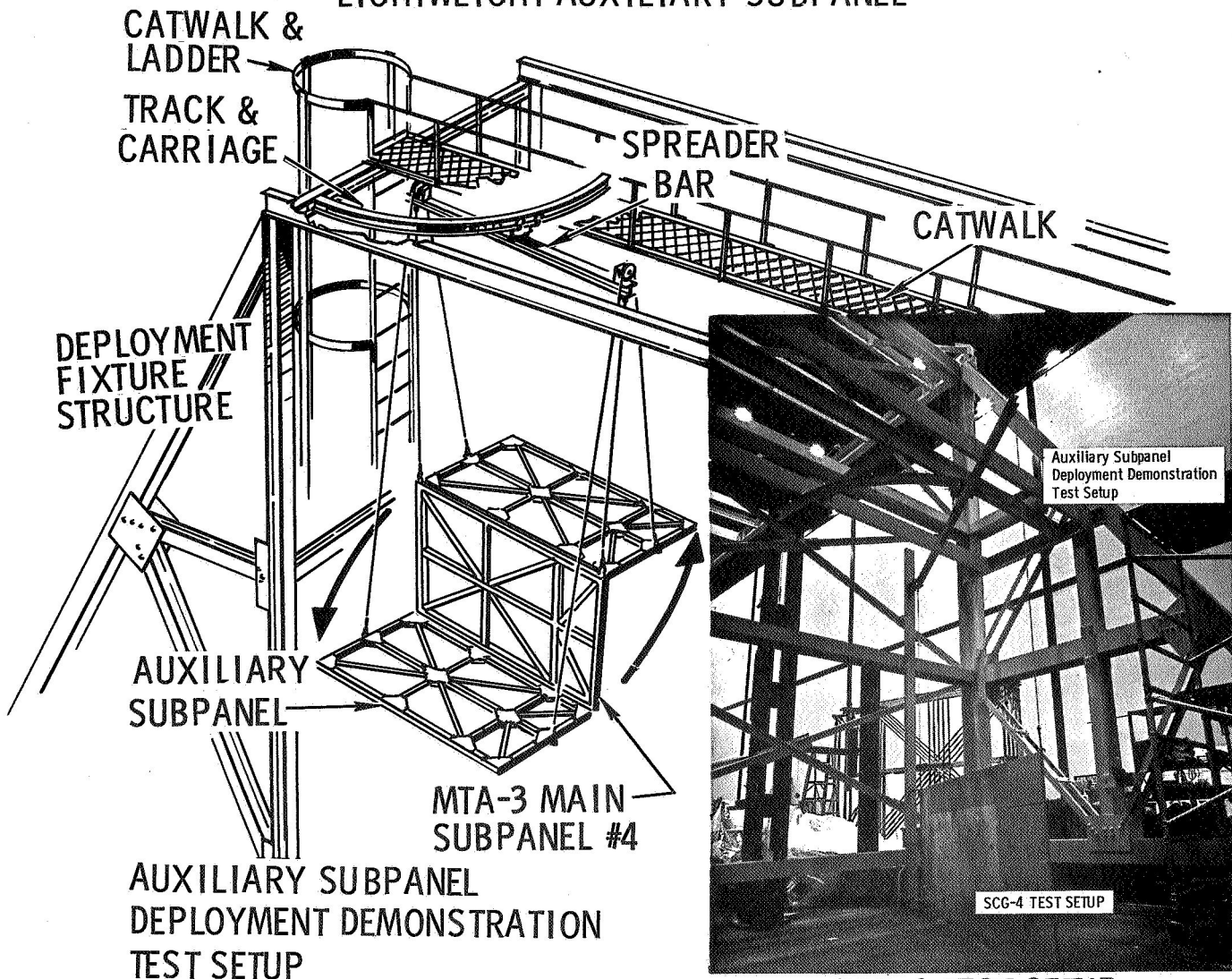
SCG-4 TEST SETUP

SCG-4 TEST SETUP

Figure 2-8:   DEPLOYMENT DEMONSTRATION EQUIPMENT
FABRICATION AND TESTING

Some friction in the carriage assembly was noted. The major source of friction, causing the subpanel to deploy at an uneven rate, was paint on the track surfaces. These surfaces will be left bare on the track fabricated in Phase III.

Operation of the carriage-tow and release systems was satisfactory. The effects of track deflection on the system were insignificant.

2.4.2 DEPLOYMENT-DEMONSTRATION EQUIPMENT DESIGN

Advanced testing of the auxiliary-subpanel deployment concept will provide early confidence in the MTA-3 deployment demonstration system.

TDM 951934-4 authorized the final design and fabrication of the deployment-demonstration equipment catwalk and ladder, lightweight auxiliary subpanel and auxiliary-subpanel suspension system. These components will be assembled in preparation for testing auxiliary-subpanel deployment (to be performed in Phase III), as shown in Figure 2-8. MTA-3 Subpanel Unit 4 will be supported during test by the same overhead monorail track, carriage, and spreader-bar system as used in the SCG-4 test. The auxiliary subpanels will be connected by cables that drape over pulleys on the spreader bars. A light counterweight added to the down-swinging subpanel will provide the deployment force. Helper springs, located at the auxiliary hinges, will augment the counterweight force and sustain subpanel motion through dead-center points.

The test will consist of repetitive deployments of the auxiliary subpanels to verify helper-spring operation, to determine the correct counterweight size, and to observe the general behavior of the deployment system.

2.5 STATUS OF WORK---TASKS 7 AND 8

Work was started on MTA-1 (Task 7) to delete live cells, and SCS-43 vibration test setups were initiated before CCN approval to prevent a program slide.

Drawing revisions and new drawing releases deleting all but six live solar-cell modules and substituting simulated cells and busses have been completed. The six solar-cell modules and the simulated solar cells of microsheet glass are ready for final assembly on MTA-1. The simulated cells were ordered before release of the CCN to maintain the manufacturing schedule. The solar-cell modules are located in areas where the highest vibration amplitude is predicted. The electrical busses are nonoperative, but stiffness and mass are the same as electrically operative busses. The SCS-43 vibration test plan and procedures have been released and approved by JPL.

The SCS-43 test article was received from JPL and inspected visually. One broken, simulated cell was replaced. Strain gages and accelerometers were installed on the substrate and structure.

The first power-degradation test, A, was made on SCS-43 with the X-200 solar simulator. Some degradation is shown by the following values taken from the V-I curves.

Power-Degradation Test 3 (9-21-67)   Power-Degradation Test A (5-10-68)

I_{sc} = 1.69 amperes I_{sc} = 1.62 amperes

V_{oc} = 31 volts V_{oc} = 30.8 volts

The test fixture with simple supports for Panel Vibration Test 2 was designed, and drawings were released for fabrication.

A Ling 249 Vibrator (30,000 pounds-force) was installed in the 50,000-cubic-foot vacuum chamber. The Phase I test fixture (rigid-clamp-type) was installed on the vibrator, and a checkout was made in air and 1/20th atmosphere. Sine sweeps (15 to 150 Hz) were made for each condition to the maximum test level of 4.3 g's peak. Vibration 1 (ambient and 1/20th atmosphere) tests were run on the setup illustrated in Figure 2-9.

The work to be accomplished during the next quarter will include completion of Vibration Test 2, both ambient and in 1/20th atmosphere, and Power-Degradation Test B. Test reports for Tests 1 and 2 will be released.

2.6 QUALITY ASSURANCE STATUS AND REPORTING

Quality assurance support of Task 3 processing peaked at approximately midquarter. At this time, some 700 manufacturing plans had been reviewed and approved. Quality Control certification laboratories completed 5 more adhesive and primer analyses, bringing the total to 16. Production at the beryllium-surface conditioning supplier at this this time was also at its highest. The Boeing Quality Control representative activity participated in receival of beryllium parts at the supplier's facility; participated in processing; and checked, cleaned, and primed parts before returning the shipment to Boeing. Continual telephone communication between the Boeing supplier representatives and Boeing Quality Assurance was maintained and provided expedited direction, as required. SCS-43 was received and inspected at Boeing, upon return from JPL. No additional discrepancies (compared to Phase I delivered part conditions) were apparent. This test article was then released to test personnel.

Analysis of nonconformance data indicates that experience has been gained and fed back into program operations.

Table 2-2 reveals that fewer MTA-1 parts were rejected during this quarter than during the previous quarter. This is attributed to experience gained by manufacturing and inspection personnel. The tabulation also indicates
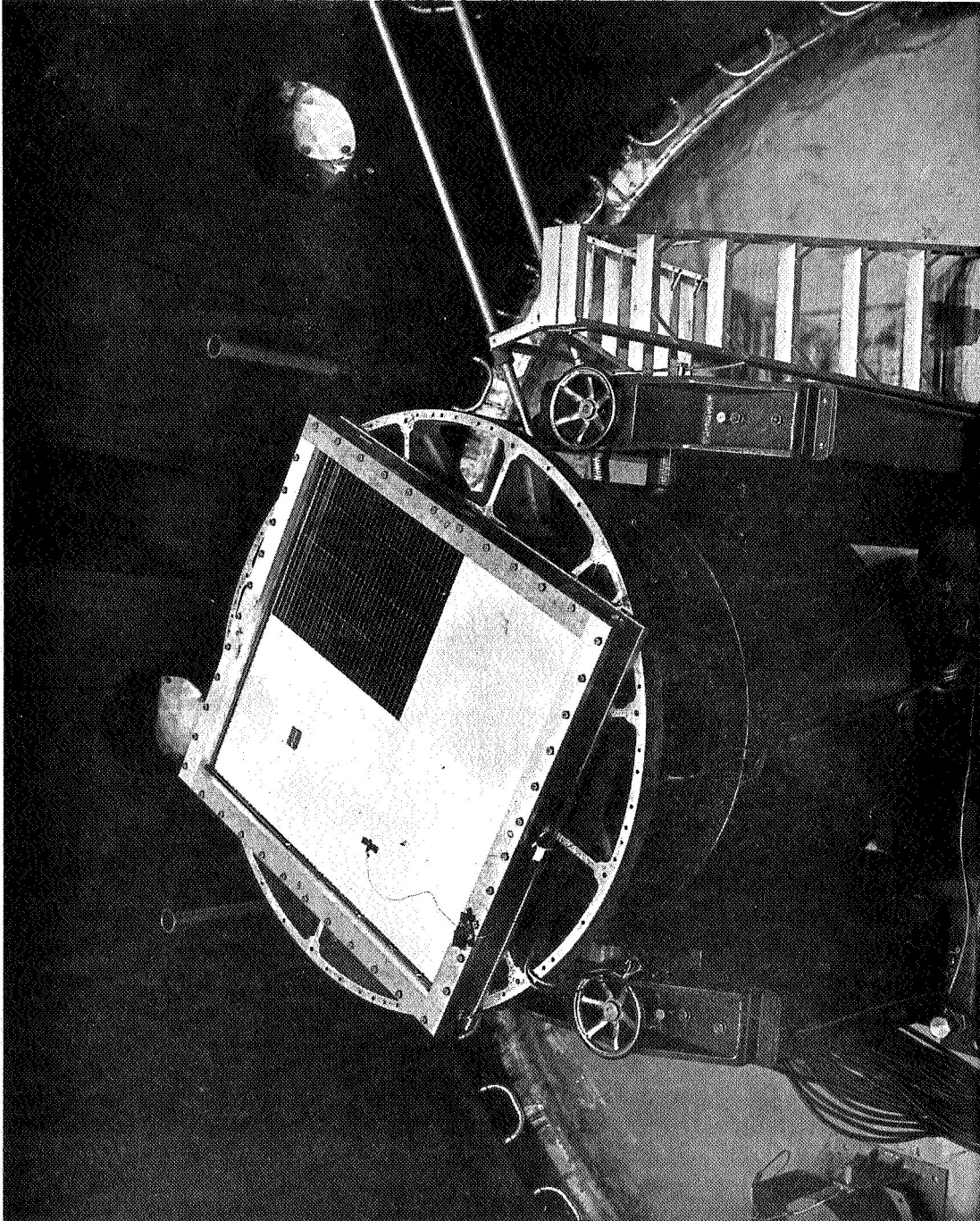
20

Figure 2-9: VIBRATION TEST SETUP—SUBPANEL MODEL SCS-43

Table 2-2: TABULATION OF BERYLLIUM NONCONFORMANCES (APRIL 1968)

Process Causing Rejection	Total Parts Rejected (% of Part Operations)*		Engineering Dispositions (% of Rejections)			Comments
	Nov. 1967 to Feb. 1968	Feb. 1968 to Apr. 1968	use-as-is	rework and use	Scrap	
Forming and Trimming	39 (9.1)*		46	46	8	February to April 1968 shows: 1) Fewer rejections ("learning curve" within Manufacturing and Quality Control); 2) Fewer use-as-is (clearer engineering requirements). **Dimension errors and cracks from forming and trimming
		21 (4.5)*	34	54	14**	
Chem-Milling	41 (9.7)*		88	12	0	***Represents 2 parts, 1 - excess material removed during chem-mill. 1 - part not straight even after rework.
		39 (8.3)*	82	13	5***	
Total Part Operations (Forming, Chem-Milling, and Trimming)	426	469				426 + 469 = 895 Operations (Nov. 67 to April 68) = beryllium forming = chem-mill + cut to length + trimming (on any one or several parts).
Bonding	No bonding	7	85	0	15 (1 part)	

that fewer engineering dispositions on discrepant parts were encountered that were acceptable without rework. Consequently, from the feedback of information from the shop discrepancy reports, design drawing and process changes were instigated. The effect of this action resulted in the more acceptable "spread" of engineering dispositions during this reporting period. At least 85% of engineering drawing changes were intended to clarify fabrication and inspection requirements.

On several occasions, normal penetrant inspection of beryllium parts was followed with eddy-current inspections when a flaw was indicated. Eddy-current inspection provided exact flaw dimension and location data, which was evaluated and used by engineering to direct the disposition of re-jected parts.

2.7 MATERIEL SUBCONTRACT STATUS

*All planned Materiel procurement activities for Phase II were completed during this quarter.*

The last shipment of beryllium processed at Chemical Energy Company (CEC) was received on April 26, 1968. A total of 900 parts were processed by CEC at a cost of $41,261. An increase of 208 parts over the original estimate of 692 was due to additional backup material being processed, and to such miscellaneous detail parts as shims, clips, and angles not included in the original estimate.

CEC encountered a problem in maintaining the production flow because of the erratic and large number of individual shipments for processing. Sufficient material was not available to maintain continuous processing, which required starting and stopping several times, thereby increasing operating costs. This problem had no affect on the price negotiated with CEC.

Many parts with defects were reworked several times by CEC at no addi-tional cost to Boeing. One center splice plate was broken by CEC, and another part developed a crack during processing. The cost of replacing the beryllium was borne by Boeing. The additional processing and over-time required to meet the schedule were absorbed by CEC.

The cooperation of CEC in meeting Boeing requirements has been outstand-ing. A few of the operations, such as chem-milling, inspection, and testing, are shown in Figure 2-10.

Receipt of the qualification and production units completed the motor and cable assembly procurement. The qualification test report was received on May 20, 1968; the reliability data was received on June 3, 1968. Approval of Purchase Order Change 2 is being withheld by JPL pending receipt of an executed copy of the instrument of waiver for the new technology clause. A copy of this waiver has been requested from United Shoe; when received, it will be mailed to JPL so that the change order can be released.
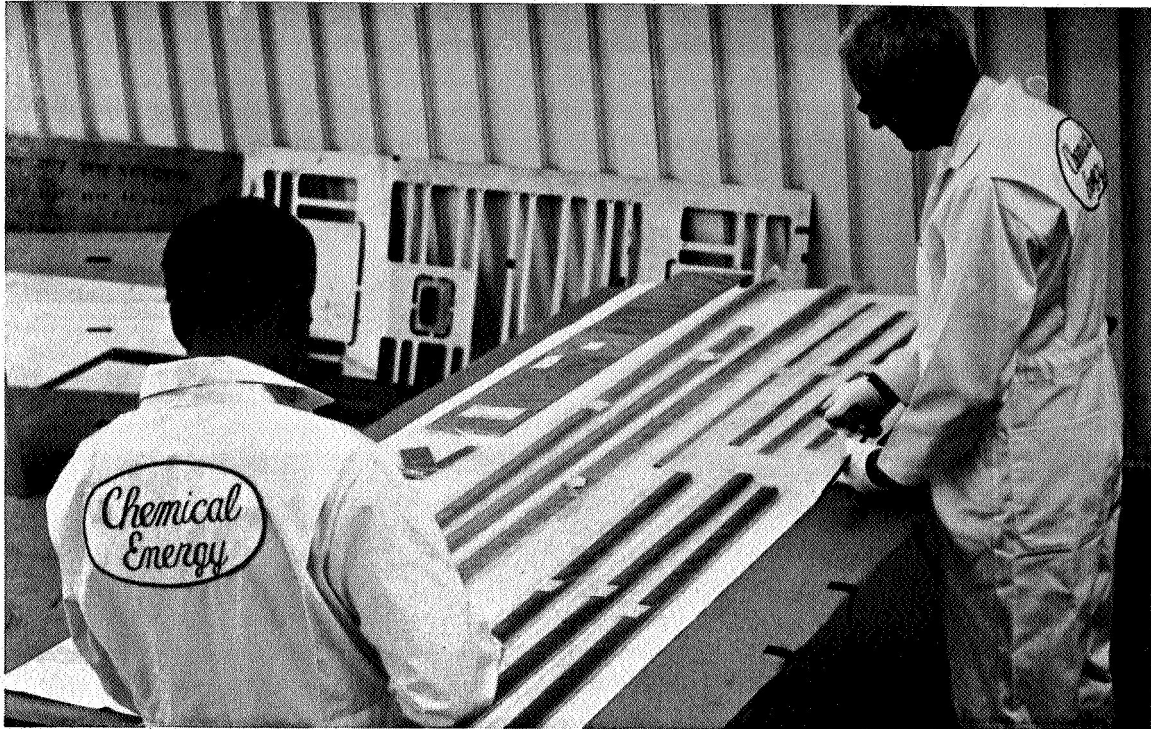
FINAL INSPECTION OF CLEANED AND PRIMED BERYLLIUM

CHEM-MILLING AND
CLEANING FACILITY

PREPARING CLEANED AND
PRIMED COUPONS FOR TESTING

Figure 2-10: BERYLLIUM FABRICATION OPERATIONS

Additional titanium shear-teeth processing was completed by Roselle Tool and Die Company in a 5-day turnaround time. Roselle Tool and Die Company processed the total quantity of shear fittings for a total program savings of $6,900.

Materiel completed preliminary industry surveys to obtain information on beryllium-forming and chem-milling capabilities. Preliminary estimates were received from Solar, North American, and Republic Aviation on forming. These estimates are being evaluated for Phase III backup planning. Additional sources for chem-milling, cleaning, and priming beryllium are being investigated to reduce proposed beryllium-processing costs in Phase III by obtaining competitive bidding.

The deployment structure was the only major item purchased in Tasks 4 and 5, and was completed on January 31, 1968. Miscellaneous parts, equipment, standards, and raw material were the only items purchased during this quarter, and delivery of these items supported program schedules.

Materiel activity in the fourth quarter will be devoted to obtaining firm cost proposals on beryllium processing; reviewing Phase III schedules and materials to support program-planning activities; and reviewing the earned-value concept for application to the Materiel organization activities.

D2-113355-6 (Part II)

3RD QUARTERLY REPORT— PHASE II

Prepared for
Jet Propulsion Laboratory
Under Contract
JPL 951934

LARGE AREA SOLAR ARRAY

June 1968

Prepared by

THE BOEING COMPANY
Aerospace Group
Space Division
Seattle, Washington

PART II

Prepared by _R. C. Weikel_   6-13-68
          R. C. Weikel   Date

John A Morey for F.W. McAfee   6-12-68
          F. W. McAfee   Date

J. L. Apperson   6-12-68
          J. L. Apperson   Date

D. A. Norsen   6-12-68
          D. A. Norsen   Date

Approved by _W. I. Ratcheson_   6-13-68
          W. I. Ratcheson   Date

FOREWORD

A review of the technical analysis required to develop the configuration, fabrication, and testing of the Large Area Solar Array is presented in this section. The factors affecting these items include:

- Effects of launching;

- Requirements of deployment;

- Behavior of the deployed array;

- Requirements of ground deployment and testing;

- Effect of fabrication problems on structural configuration and electrical components.

The objective of the three-phase program is to develop the technology for the design and fabrication of a solar array having a specific performance of 20 watts per pound. It is the purpose of Part II to show that the technical analyses performed in Phases I and II support this objective.

The analyses reflect the following:

- The dynamic response to and the internal loads derived from the boost environment;

- The dynamics of solar array deployment on the ground and in space;

- The prediction of temperature distribution and the establishment of appropriate thermal control;

- Selection of materials;

- Prestressing of the array;

- Computing and verifying the weight distribution;

- Analysis of the electrical performance;

- Problems of quality assurance;

- Analysis of reliability and product assurance.

CONTENTS

CONTENTS (Cont.)

CONTENTS (Cont.)

FIGURES

FIGURES (Cont.)

FIGURES (Cont.)

TABLES

1.0 DESIGN CRITERIA AND REQUIREMENTS

1.1 JPL SPECIFICATION GMP-50505-FNC-B

JPL Specification GMP-50505-FNC-B established the primary constraints on the LASA design.

It is assumed that the shroud is ejected 4 minutes after engine ignition and that Centaur burnout occurs 20 minutes after engine ignition. During the 16-minute period from shroud ejection to Centaur burnout, the maximum dynamic loads are assumed to occur simultaneously with the most adverse thermal condition of the first 20 minutes.

Figure 1-1 defines the direct Earth escape trajectory portion of the mission and shows that the array deploys approximately 3 hours after launch.

Environments that significantly affect the LASA primary structure during the stowed phase are:

1) Lateral sinusoidal vibration input applied at the aft hinge-line interface with the spacecraft at levels shown below:

Input (g's)	Frequency (Hz)
2.0	$2 \leq f \leq 20$
1.5	$20 \leq f \leq 200$

The sine sweep is at 2 octaves per minute.

2) Steady-state accelerations are 13 g's longitudinal combined with 2 g's lateral;

3) The critical thermal condition is solar heating due to exposure of the array after the shroud is ejected. It is assumed that the temperature of the solar array environment at shroud ejection is 77°F (25°C);

4) The static preload environment is substrate tension and stack tiedown loads to be determined by analysis;

5) The design limit load factor is 1.0 with a fitting factor of 1.15, whereas the ultimate load factor is 1.25 applied to the limit design load;

6) The stowed arrays will withstand the flight acoustic environments during the launch phase (Figure 1-2).
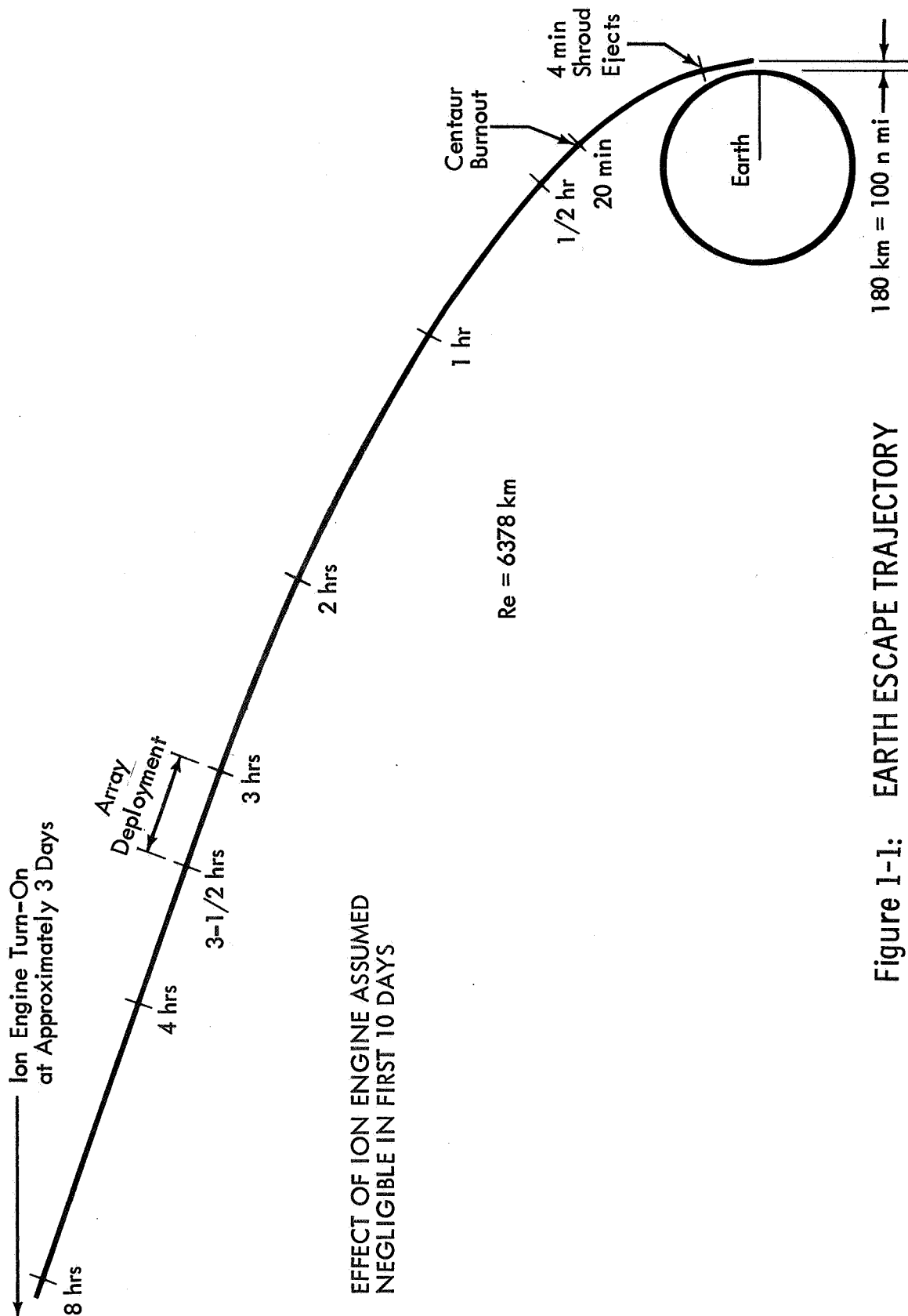
Figure 1-1: EARTH ESCAPE TRAJECTORY
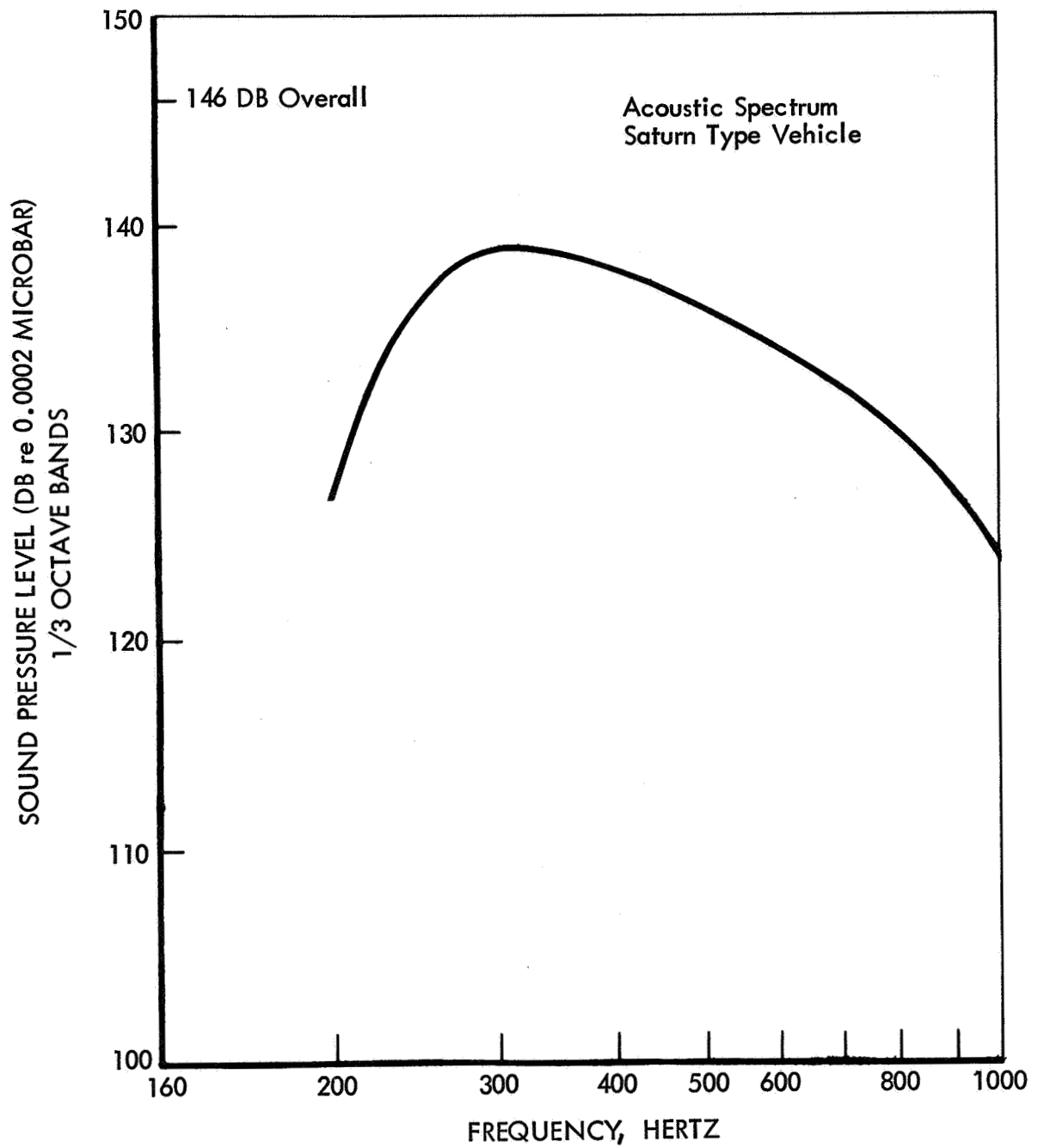
Figure 1-2: ACOUSTIC ENVIRONMENT SATURN VEHICLE

Criteria affecting the primary structure of LASA in the deployed configuration are:

1) The solar array will be capable of full deployment without interference between the array elements and between the array and the spacecraft;

2) No structural or electrical degradation will occur due to or during the following conditions:

   a) The thermal gradients that will develop between the Sun and dark sides of the array due to solar illumination at 140 mw/cm^2 intensity,

   b) Transient thermal shock from -100 to +75°C at rates not less than 30°C per minute,

   c) A steady-state acceleration of 3 x 10^{-5} directed at 45 degrees to the plane of the array. This loading simulates that imposed by the cruise engines,

   d) Repeated discrete applications to the entire array of a square wave pulse with duration not less than 13 seconds or more than 5 minutes and maximum amplitude of 2 x 10^{-5} radians/sec^2 pitch angle accelerations;

3) The first-mode resonant frequency of the entire deployed array will be greater than 0.04 cps to prevent deleterious coupling with the spacecraft autopilot system.

1.2 ASSUMED DESIGN CONSTRAINTS

It was necessary to establish or assume additional design constraints as the design and analyses evolved.

1) An initial tension of 12 pounds per inch (effective) is required in the substrate to keep the natural frequency of the substrate, vibrating as a membrane, above 45 Hz. Also this tension is required to make the substrate panels more effective in shear (especially stiffer) and to keep the panels flat.

2) A preload tension is required in the tiedown cables sufficient to prevent separating of the panels, unlocking of latches, and slackening of cables and to keep compression on all bearing surfaces.

3) It is assumed that the spacecraft is relatively rigid in the plane of Subpanel 1 at the interface of the main center hinge and the spacecraft.

4) Design requirements for the ground-testing and transportation fixtures are required for the protection of the array during test and transportation and to comply with certain safety, building, and facility regulations.

5) To establish appropriate hinge loads, auxiliary dampers control the closing velocities of the deploying sequences.

6) It is necessary to assume a controlled or known thermal environment in the spacecraft prior to shroud ejection.

7) No acoustic test duration was designated in Specification GMP-50505-FNC-B; therefore, 2 minutes was selected as a reasonable time at maximum level.

8) An assumption of structural load transmissibility of $Q = 15$ was made for design.

2.0 EFFECT OF BOOST ENVIRONMENT ON DESIGN

This section discusses the analysis of the effect of the boost environment on the stowed solar array. The following sections describe the analysis of the structural loads and deformations produced by the boost environment, analysis of the temperature distribution and resulting thermal-control requirements, and the analysis and design of the boost-tiedown and shear-tie systems.

2.1 DYNAMIC AND INTERNAL LOADS FOR STOWED CONFIGURATIONS

2.1.1 MATHEMATICS OF STRUCTURAL ANALYSES

The displacement method formulated in matrix algebra is the preferred method of structural analyses.

The direct stiffness method described in Reference 3, Section 11.0 was used to write the basic load-deflection equation:

$$\begin{Bmatrix} F \\ R \end{Bmatrix} = \begin{bmatrix} K_{11} & K_{12} \\ K_{21} & K_{22} \end{bmatrix} \begin{Bmatrix} u \\ c \end{Bmatrix} + \begin{bmatrix} A_1 \\ A_2 \end{bmatrix} \begin{Bmatrix} \Delta T \end{Bmatrix}$$

where:

$\quad$ F = Loads applied to the node points (given);

$\quad$ R = Reactions at the boundaries (unknown);

$\quad$ u = Displacements of node points (unknown);

$\quad$ c = Displacements of boundaries (given);

$\quad$ T = Temperatures at the node points (given);

$\quad$ K_{ij} = Stiffness coefficients;

$\quad$ A_{ij} = Thermal-restraint coefficients.

Solution of these equations gives:

$$\begin{Bmatrix} u \end{Bmatrix} = \begin{bmatrix} K_{11} \end{bmatrix}^{-1} \begin{Bmatrix} F \end{Bmatrix} - \begin{bmatrix} K_{11} \end{bmatrix}^{-1} \begin{bmatrix} K_{12} \end{bmatrix} \begin{Bmatrix} c \end{Bmatrix} - \begin{bmatrix} K_{11} \end{bmatrix}^{-1} \begin{bmatrix} A_1 \end{bmatrix} \begin{Bmatrix} \Delta T \end{Bmatrix}$$

$$\begin{Bmatrix} R \end{Bmatrix} = \begin{bmatrix} K_{21} \end{bmatrix} \begin{bmatrix} K_{11} \end{bmatrix}^{-1} \begin{Bmatrix} F \end{Bmatrix} + \begin{bmatrix} K_{22} - K_{21} K_{11}^{-1} K_{12} \end{bmatrix} \begin{Bmatrix} c \end{Bmatrix} + \begin{bmatrix} A_2 - K_{21} K_{11}^{-1} A_1 \end{bmatrix} \begin{Bmatrix} \Delta T \end{Bmatrix}$$

The stresses are determined from the equation:

$$\{\sigma\} = [S]\ \{u\}.$$

The technique of determining the appropriate stress average is described in Reference 3 of Section 11.0. The stiffness coefficients of the structural elements are mutually independent; therefore, the stiffness matrix K_{ij} in the above equations can be derived by addition. Because of this, K can quickly be computed by a merging process. Also, the equations can be adjusted to changes in design without determination of unknowns.

COSMOS, the comprehensive digital computer program, developed by Boeing, was used extensively to solve the load deflection equations. This program enforces joint equilibrium, compatibility of deformations, and satisfaction of the boundary conditions.

The dynamic response was analyzed by the calculation of a number of natural frequencies and mode shapes of each of several components and the formulation of modal analysis using Hurty's method described in Reference 2.

The following matrix equation is solved to yield eigen-values (frequencies) and eigen-vectors (modal displacements):

$$\lambda\{q\} = [K]^{-1}[M]\{q\} \text{ yields } \{\phi\} \text{ and } \{\omega\}$$

The matrix equation of motion for sinusoidal excitation is then solved:

$$\{\ddot{q}\} + [2\gamma\omega]\ \{\dot{q}\} + [\omega^2]\ \{q\} = \frac{[M]\{\phi\}\ N\ \sin\ \bar{\omega}t}{[\phi][M]\{\phi\}}$$

where

  ϕ = modal displacement;

  ω = natural frequency;

  K = stiffness coefficient;

  q = generalized coordinate;

  M = mass;

  γ = damping coefficient;

  $\bar{\omega}$ = excitation frequency;

  N = acceleration input in./sec^2;

  t = time;

$$\{\delta_i\} = [\phi]\{q\} = \text{deflections};$$

$$\{\ddot{\delta}_i\} = -[\phi][\omega^2]\{q\} = \text{accelerations};$$

$$\{\text{loads}\} = [M]\{\ddot{\delta}\} = \text{loads}.$$

The model used for structural analyses consists of an aggregate of a finite number of discrete structural elements and a finite number of lumped masses, all joined to a finite number of nodes. The applied load model is a finite number of concentrated loads applied to the joints.

Several comprehensive dynamic and internal loads analyses have been made of the LASA stowed configuration. The first idealization considered each stowed solar panel assembly as being made up of five separate structures (Figure 2-1). Each panel type was restricted to a single type of motion; that is, the in-plane panels moved in an in-plane direction, and the out-of-plane panels moved in an out-of-plane direction (see Figure 2-2a).

A second panel assembly idealization was developed that allowed both in-plane and out-of-plane motion simultaneously (see Figure 2-2c).

Only the displacement method and the availability of appropriate digital programs permitted the structural analyses associated with the developments described above to be completed in the time covered.

2.1.2 SUMMARY OF LOADS ANALYSIS

The dynamic conditions create the critical loads and deformations in the stowed panel.

In the first analysis, all four panel assemblies of a LASA were considered to be coupled together in vibration. However, each type of panel assembly was restricted to a single type of motion; that is, the in-plane panels moved in an in-plane direction and the out-of-plane panels moved in an out-of-plane direction (see Figure 2-2a). The second panel assembly idealization that was developed allowed both in-plane and out-of-plane motion simultaneously. The resulting critical natural modes were nearly identical to those obtained by the first analysis, and it is concluded that, in this case, the predominance of a "single-type motion" makes it an acceptable assumption for final analysis.

The substrate was analyzed as a 24-inch square component bounded by beryllium outer spar members and yielded a substrate natural frequency of 48 Hz. When this analysis was refined to consider the effects of intercostals and additional substrate sections, the substrate natural frequency dropped to approximately 36 Hz. Note that this frequency is for the substrate-intercostal structure located between the centerline spar and an outer spar, between the lateral spars located at Stations 10.5 and 123.7, and typical of Subpanels 2 through 5. The small
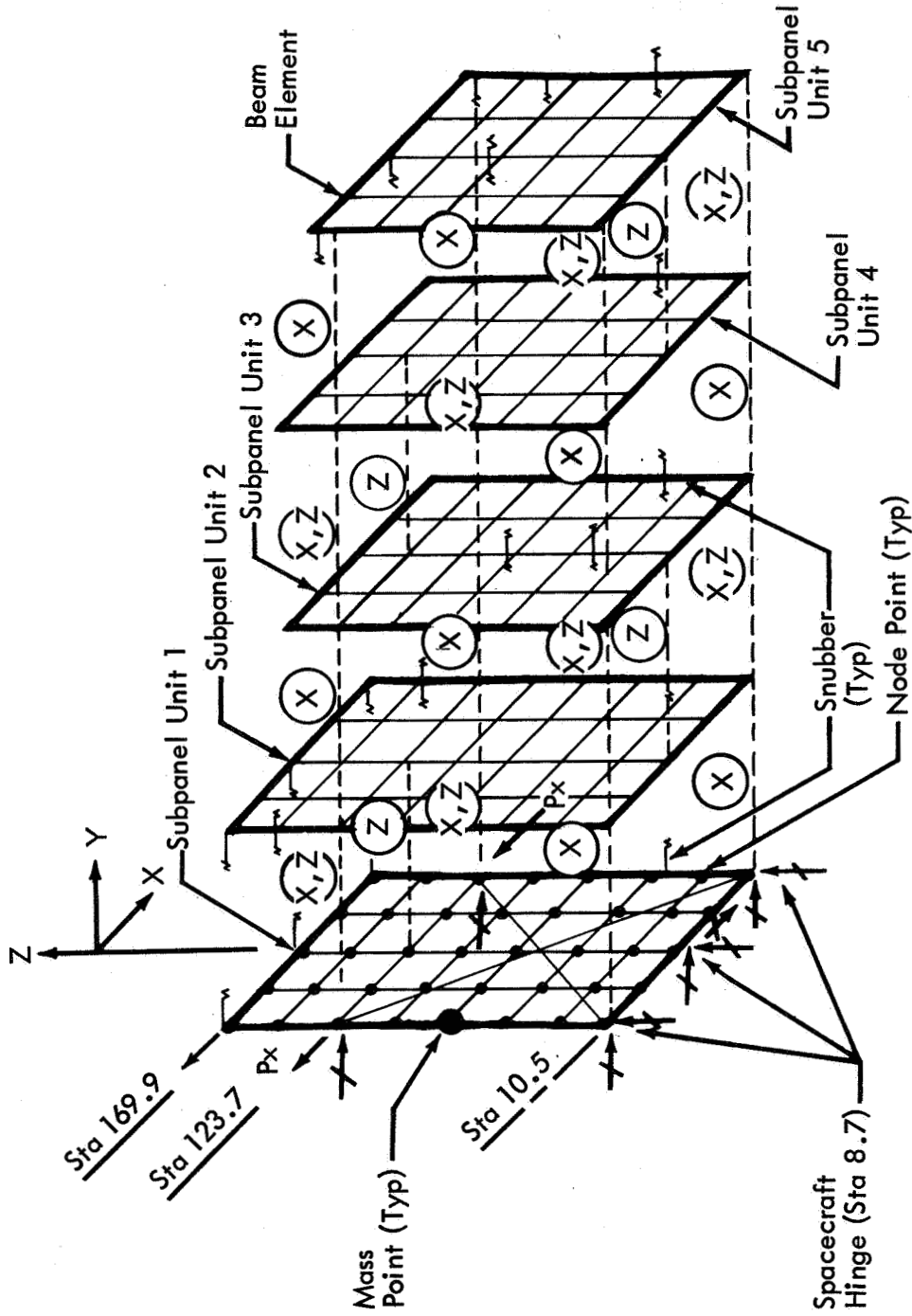
Figure 2-1:   STRUCTURAL IDEALIZATION

1st Quarter COMPARISON OF PANEL MOTIONS 2nd Quarter
(a)

COMPARISON OF SUBSTRATE IDEALIZATION
(b)

COMPARISON OF OUTER SPAR IDEALIZATION
(c)

COMPARISON OF SPAR CROSS SECTIONS
(d)
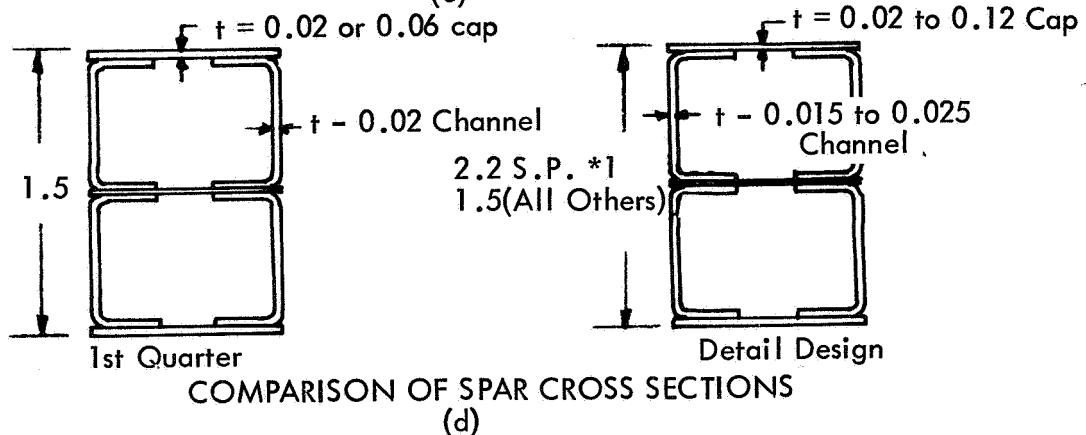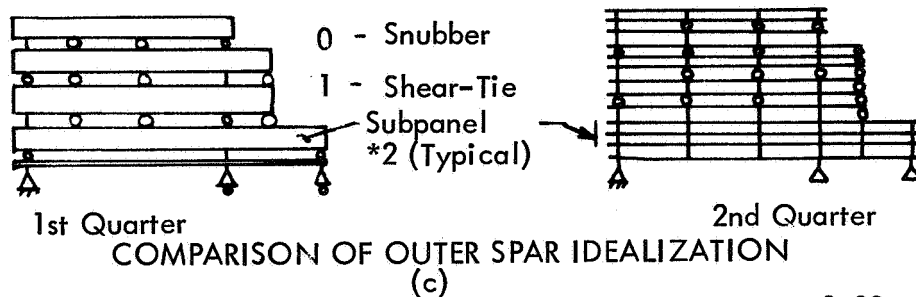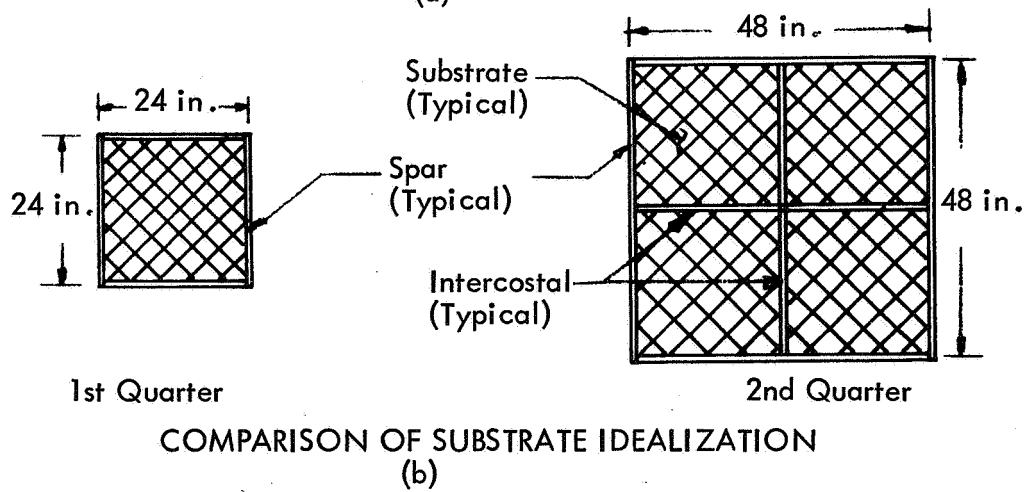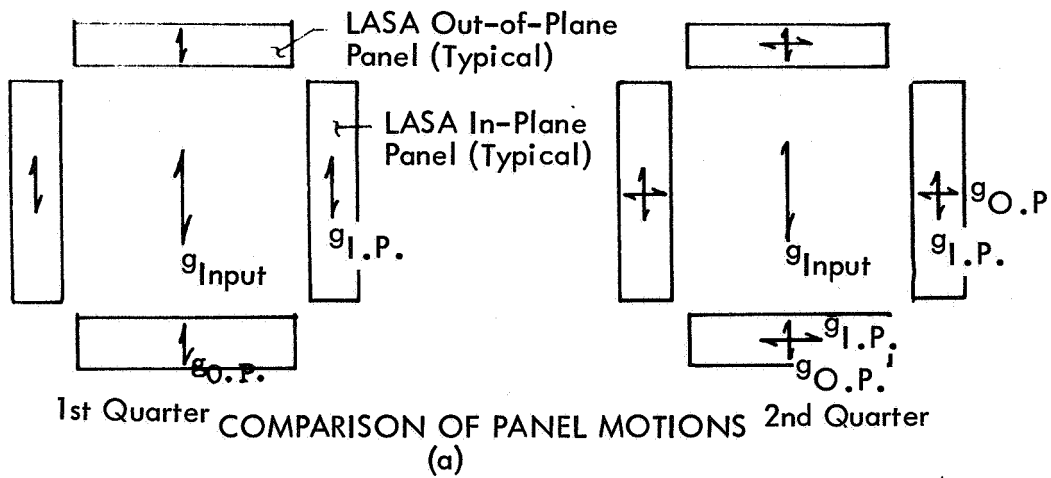
Figure 2-2:   SUBSTRATE BOUNDARY CONDITIONS

component test SCS-43 was typical of the substrate structure in Sub-
panel 2 above Station 123.7 (48 inches square). The predicted frequency
for SCS-43 was 41.9 Hz for pinned ends to 45.0 Hz for fixed ends, as
compared with measurements of 39 Hz of 0.20 g input to 35 Hz at 3.00 g
input.

Figure 2-2 illustrates the different substrate boundary conditions.
Originally the frequency separation between the substrate and the array
resonance was sufficient so that the substrate was considered rigid;
however, when the substrate frequency was determined to be 36 Hz, more
substrate-to-panel coupling occurred. It was found that this shift in
substrate resonance: (1) did not change the total external load; and
(2) increased the maximum total deflection at the substrate (relative
to data from 0.56 to 1.16 inch due to 1.5-g lateral sinusoidal vibration
input). This deflection does not represent an interference problem, as
the structure and substrate are in phase; and the LASA fundamental
frequency was lowered to 21.5 Hz. On the basis of these results, it was
necessary to include the substrate interaction with the primary structure
for a final analysis.

The shear ties located along the spar caps of each subpanel are impor-
tant in determination of the total out-of-plane bending stiffness and
out-of-plane bending internal load paths of a panel assembly. During
the first quarter, the panel assembly was idealized as five planar
frames representing the five subpanel units. The out-of-plane bending
stiffnesses of the spars were calculated on the basis that out-of-plane
shear would be transferred from one spar to another through all shear
ties; however, for simplicity only the original baseline shear ties were
represented in the model, thus affecting the detailed internal load
paths. During the second quarter, the out-of-plane bending character-
istics of the outer spars and the principal lateral spars located at
Station 123.7 were examined in detail. In each case all 13 spars were
idealized and all shear ties represented in their actual locations.
Figure 2-2c shows schematically the idealization differences for an
outer spar. The different shear tie idealizations used during the first
and second quarters lead to significant differences in the internal
loads.

In the third quarter of Phase I, the final dynamic analysis of the array
was undertaken. The elements of the configuration that appear to be
most critical to the structural performance and, hence, most important
in structural idealization, were the shear ties and tiedown system. The
previous analytical model utilized an in-plane planel and an out-of-
plane panel, which were coupled together using Hurty's component mode
technique. The dynamic performance of the tiedown system is obscured
by the use of the component mode technique. Visibility of such perform-
ance can best be expressed in a single model. Because of the significance
of the tiedown system, it was decided to idealize the structure by a
model that could be generated in one COSMOS run, saving both calendar
time and computer time.

To represent the structure for purposes of dynamic analysis in a single COSMOS run, the stiffness matrix must be reduced to about 100 x 100. Because the array weight is quite uniformly distributed over the array, the nodes retained in the stiffness matrix must be similarly distributed. It was concluded from previous analyses that the response of the substrate on the out-of-plane panel cannot be ignored and must be considered in the model. The decision was made to idealize half of the array by modeling one in-plane panel by three equivalent subpanels and two out-of-plane panels (half panels), each by a single equivalent frame, including the out-of-lane substrate.

Out-of-Plane Panel---The main elements of the out-of-plane panel requiring caution in idealization are the shear tie effects. The tiedown system and shear ties cause all spars to behave as deep beams in the out-of-plane direction. The shear ties at the ends of the spars also provide some end fixity that must be idealized. A two-dimensional representation of the lateral spar, including shear ties, was analyzed by the MIT STRESS computer program to evaluate the effect of the shear ties. These results indicate that each spar of this 13-spar stack carried about the same bending moment, whereas only the outer spars (Panels 1 and 5A) had significant axial load. Using this information, the spar stack was idealized by a beam in which the moment of inertia was the sum of the moments of inertia of each panel, the shear area was the sum of the shear areas of each panel spar, and the cross-sectional area was the area of Panel 1. A second element was composed of a member that carried axial load only; its cross-section area was that of the Panel 5A spar. This member was supported by stiff beams attached to the first beam at the shear-tie locations that simulate the end fixity conditions. This idealization is shown in Figure 2-3.

This results from this idealization compared very well with the MIT STRESS program results. Each spar was simulated likewise. In addition to providing a good idealization of the spars, the simulation properly located the tiedown system attachments.
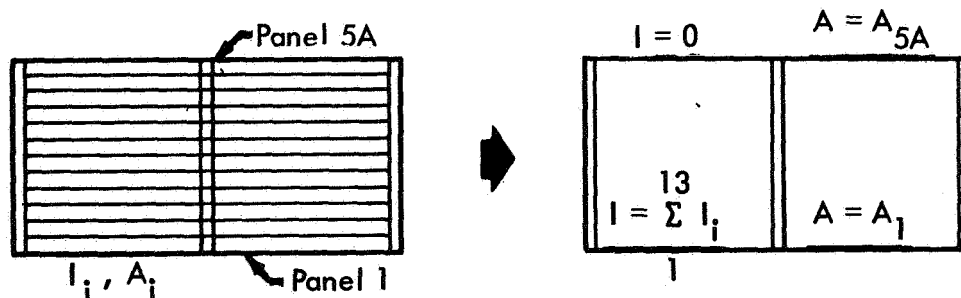
Figure 2-3: PANEL IDEALIZED STRUCTURE

The intercostal properties were idealized as the sum of the properties of the individual intercostals. The substrates in each 24- by 24-inch section were assumed to act together; that is, all 13 substrates in each section were represented by a mass supported by two beams in a cruciform pattern connected to the array spars and intercostals. The stiffness of these beams was adjusted to yield the natural frequency of the substrate determined from a membrane analysis. It must be recognized that representing the structure and substrate this way assumes that all of the structure remains in phase and that adjacent spars and substrate do not move in relation to each other. This is a reasonable assumption because the tiedown system constrains the spars to move together, and the total loads in the structure and peak deflections would be reduced if the substrate and intercostals were out of phase. This assumption results in peak deflections and loads.

In-Plane Panel---Three subpanels were used to idealize the in-plane panel of the stowed array. The principal reason for using three panels was to include the effects of the assembly center-of-gravity offset from Panel 1. The first subpanel was composed of Subpanel Units 1 and 2, the second of Units 3 and 4, and the third, Unit 5. The section properties of the idealized structure were taken as the sum of the properties of the individual panel elements. The diagonal substrate was idealized as an equivalent beryllium sheet. Shear ties were placed at Stations 10.5 and 123.7. The principal structural element of the in-plane panel is the diagonal brace, which contributes most of the stiffness and is the primary load path.

The tiedown system is easily idealized by elements capable of taking axial loads only. The idealized panels accommodated the geometry of the tiedown system. Figure 2-4 is a schematic of the idealized array.

After the dynamic analysis of the stowed array, an analysis was performed to ensure that unsymmetric loading and excitation in directions other than those normal to the panels would not impose additional design conditions and constraints. A simplified model of the total array was developed, neglecting the out-of-plane panel, and the results indicated that this method of idealizing the spars is satisfactory for in-plane as well as out-of-plane panel motion. For this reason, this appears to be the most attractive method of building the dummy panels for MTA-4.

Figures 2-5 and 2-6 show the pertinent results of the dynamic analysis for a 1.5-g lateral sinusoidal vibration input and an assumed transmissibility (Q) of 15. The peak structural deflection of 0.62 inch occurs at the center spar between Stations 55.5 and 100.2. The maximum relative deflection between the substrate and its adjoining structure is 0.5 inch. Because the array structure extends 0.75 inch beyond the substrate, no interference effects will be caused by substrate vibration. Table 2-1 compares the static envelope with the dynamic deflections at various points in the array. Although there are no overall interference problems with the spacecraft envelope, it is indicated analytically that there are a few local interferences at diagonal strut and tiedown fittings. It was stated in Boeing Document D2-113355-2 that, because the spacecraft is not fully defined at this time, it is assumed that local interferences will be eliminated when spacecraft details are known.
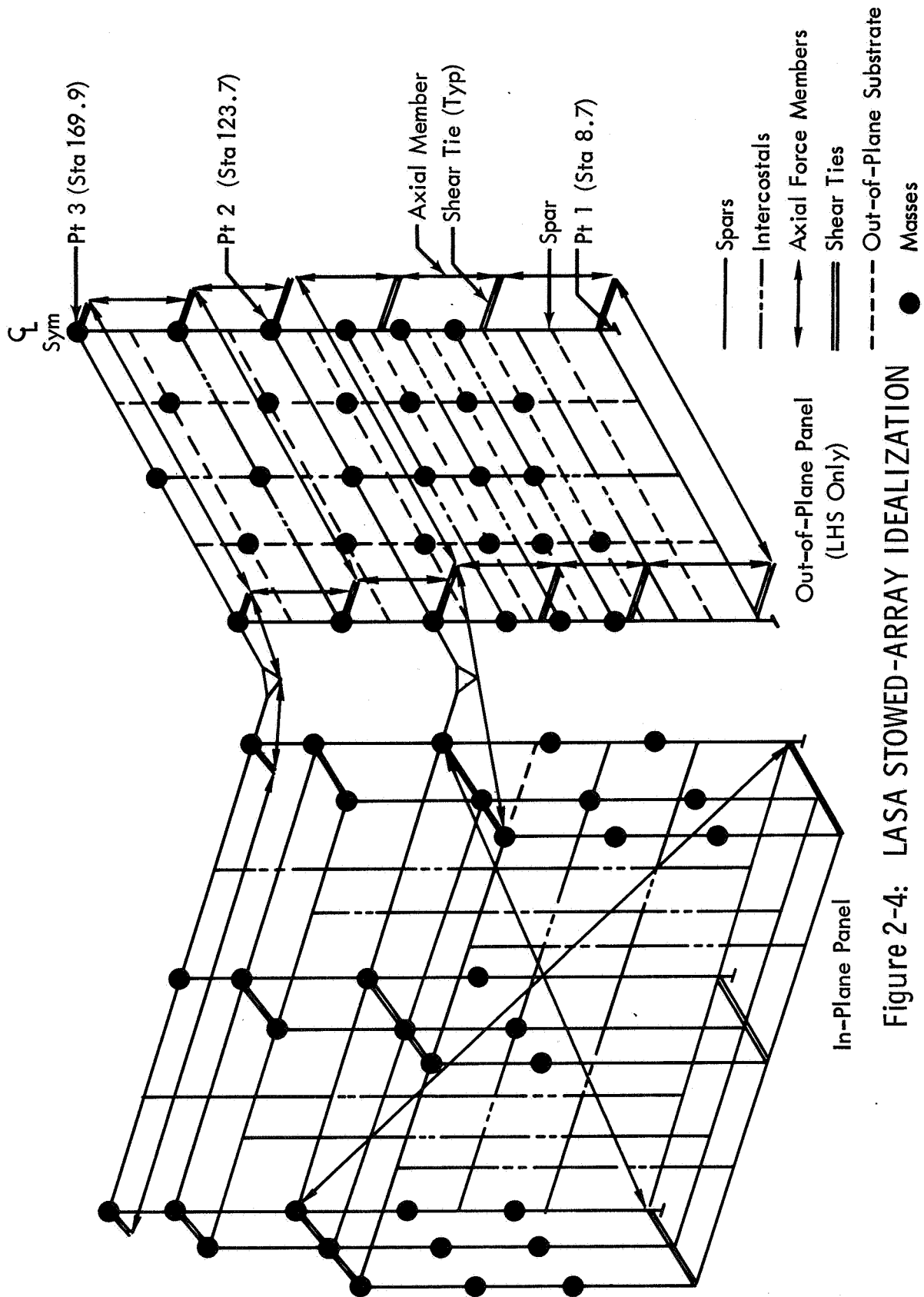
Figure 2-4: LASA STOWED-ARRAY IDEALIZATION

- INPUT–1.5g SINE SWEEP Q=15

- NATURAL FREQUENCY: 22H$_z$

- PEAK STRUCTURAL: 0.62 IN. DEFLECTION

- PEAK SUBSTRATE: 1.06 IN. DEFLECTION

- LATERAL SHEAR: 21,200–LB~ SPACECRAFT HINGE

- BENDING MOMENT: 1.9x10^6 IN. – LB~ SPACECRAFT HINGE
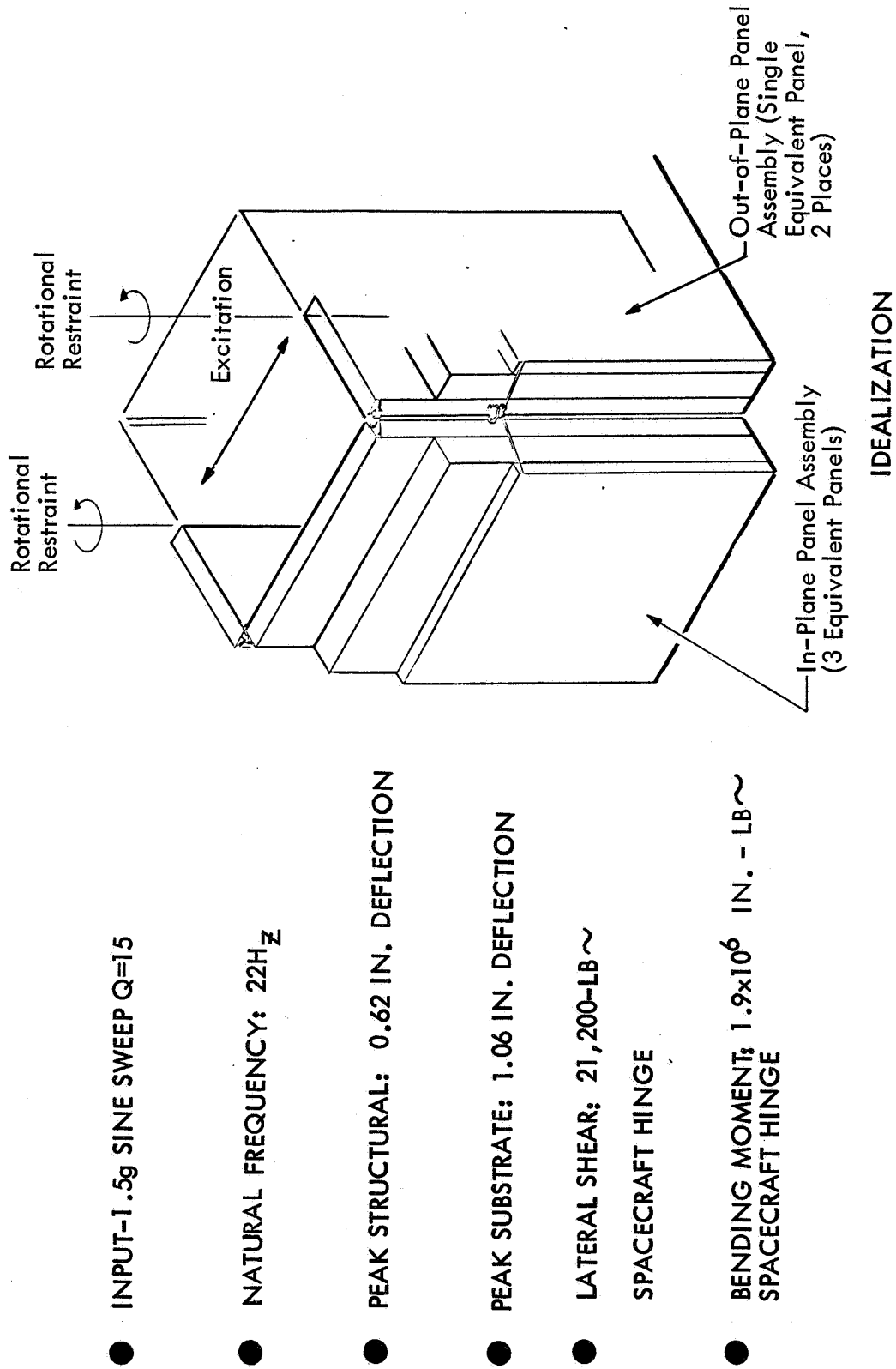
Figure 2-5:   DYNAMIC ANALYSIS OF STOWED ARRAY

1st MODE
22.0 CPS

2nd MODE
23.0 CPS

3rd MODE
30.0 CPS

4th MODE
31.0 CPS

5th MODE
31.4 CPS

6th MODE
31.5 CPS
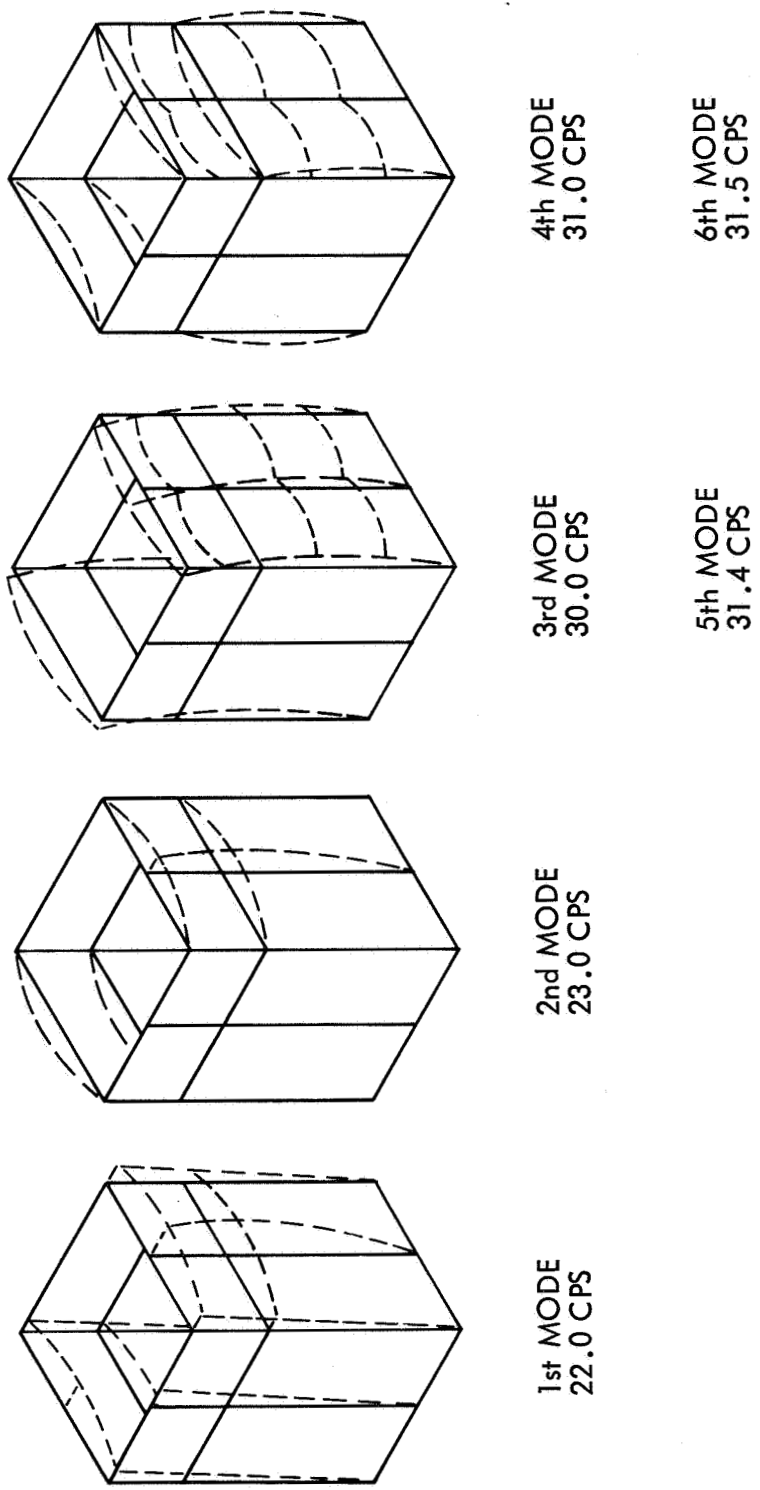
Figure 2-6:   PANEL DYNAMIC ANALYSIS MODES

Table 2-1: LASA TO SPACECRAFT NET CLEARANCES

Location of Clearance	Clearance	LASA Static Clearance (inches)*	Dynamic Deflection (inches)**	Net Clearance or Interference (inches)
Stations 10 to 40				
● Tiedown fitting at station 10.5 to spacecraft	Local	0.1	0.06	0.04
● Diagonal strut fitting at station 27.3 to spacecraft	Local	0.40	0.30	0.10
● Diagonal strut to spacecraft	General	0.84	0.55	0.29
● LASA frame to spacecraft	General	1.85	0.55	1.30
Stations 40 to 87				
● Diagonal strut to spacecraft	General	0.84	0.62	0.22
● LASA frame to spacecraft	General	1.85	0.62	1.23
Stations 87 to 125				
● Tiedown fitting at station 100.2 to spacecraft	Local	0.1	0.17	(0.07)
● Diagonal strut fitting at station 119.20 to spacecraft	Local	0.40	0.62	(0.22)
● Diagonal strut to spacecraft	General	0.84	0.62	0.22
● LASA frame to spacecraft	General	1.85	0.62	1.23
● Tiedown fitting at station 123.7 to spacecraft	Local	0.10	0.16	(0.06)
Stations 125 to 151				
● LASA frame to spacecraft	General	1.85	0.60	1.25
● Tiedown fitting at station 147.5 to spacecraft	Local	0.10	0.15	(0.05)
● Overcenter lock at station 150.2 to spacecraft	Local	1.33	0.15	1.18
Stations 151 to 171				
● Tiedown fitting at station 169.9 to spacecraft	Local	0.10	0.15	(0.05)
● LASA frame to spacecraft	General	1.85	0.35	1.50

*Includes stack tolerance buildup
**Based on lateral sine vibration input of 1.5 g's

The results of the latest dynamic analysis indicate improved structural
performance. There has been a slight increase of the first natural fre-
quency (from 21.5 to 22.0 Hz); there has been a reduction of the magnitude
of the overall deflection pattern; and there has been a significant re-
duction of the total external loads acting on the LASA. Out-of-plane
panel loads have reduced by 18%, and in-plane panel loads have reduced
by 49%. The net effect of these changes has been to decrease the total
shear and moment acting on the spacecraft hinge from 31,500 pounds and
26.0×10^5 inch-pounds to 21,200 pounds and 19.0×10^5 inch-pounds,
respectively.

The internal loads analyses were updated to account for all of the LASA
configuration changes mentioned earlier in this section. It was decided
not to incorporate the most recent dynamic loads into the internal loads
analyses because these loads---as described above---have decreased sub-
stantially from earlier levels. Because the loads are too dependent on
coupling of the in-plane to out-of-plane panel assemblies, it was felt
that a conservative approach would be to use the earlier more critical
set of dynamic loads.

The Large Area Solar Array in the stowed condition was analyzed to deter-
mine the significance of antisymmetric bending modes on the array design.
This was accomplished with the use of a simplified model of the total
array that incorporated the principal structural elements of the array:
namely, the outer spars, center spars, lateral spars, diagonal brace,
in-plane substrate, and boost tiedown system. Each panel assembly was
modeled by a single panel. Refinements such as out-of-plane substrate
effects and inclusion of all intercostals were not included, but their
effects are secondary and do not affect the validity of the results.

Three conditions were examined in the analysis:

Case 1---Symmetric condition that corresponds with the current design
        analysis;

Case 2---Symmetric array structure with the mass of one panel assembly
        increased 10%;

Case 3---Symmetric array structure with the masses of two adjacent panels
        increased 10%.

The natural modes, frequencies, external loads, and internal loads for
each case were determined. Case 3 is critical in response for excitation
of 45 degrees to the panel plane. Condition 2 is critical for excitation
perpendicular to the panel plane, with one panel loaded higher than the
rest. The array torsional modes and "diamond" modes have frequencies of
42.5 and 37.5 Hz, respectively, and antisymmetric loadings do not cause
them to respond significantly.

The responses and the external and internal loads for the three conditions
have been compared and are presented in Table 2-2. These values do not
correspond precisely to the design values because of the necessary model

Table 2-2: SUMMARY OF DYNAMIC LOADS

	Critical Frequency (Hz)	Maximum Structural Deflection (inches)	Total Shear at S/C Hinge (pounds)	Total B.M. at S/C Hinge (inch-pounds)	Load in Outer Spar (inch-pounds)	Load in Center Spar (inch-pounds)	Load in Lateral Spar (inch-pounds)	Cable Load at Sta 123.7 (pounds)	Cable Load at Sta 169.9 (pounds)	Mode Description
Case 1	24.7	0.534	17,200	1.845×10^6	15,023	57,125	38,400	1140	270	Fundamental bending
Case 2	23.8	0.510	15,600	1.675×10^6	13,800	51,066	34,320	1050	208	Fundamental bending
Case 3	23.7	0.33	17,500	1.875×10^6	12,160	35,456	23,336	1195	263	Fundamental bending (excited at -5°)
Case 2	42.0	0.003	70	1160						Torsional mode

simplifications, but they serve as a comparison to select the critical
case. The external loads and deflections of the torsional mode are pre-
sented for Case 2 to indicate the insignificance of that mode to design.
The diamond mode is even less significant. Therefore, the antisymmetri-
cal loads were less significant to the configuration and sizing of the
structure than were the symmetrical loads.

The results of the analyses of the stowed configuration as it evolved
from the original baseline of September 1966 to September 1967 are sum-
marized in Table 2-3. It is obvious from these tables that the dynamic
loads are the more critical and that the modifications to the baseline
are justified.

2.2 VIBRATION ANALYSIS

2.2.1 DETERMINATION OF SUBPANEL VIBRATION CHARACTERISTICS

*Analysis of the vibration characteristics of the MTA-1 will be verified
by the following test program.*

The basic test objectives are:

1) Determine the electrical degradation caused by large-amplitude
   substrate motion;

2) Compare measured with calculated frequencies in air and in vacuum;

3) Evaluate damping characteristics in air and in vacuum.

An analysis of the resonant frequencies and mode shapes has been com-
pleted. From this analysis the locations and sizes of the vibrators
were determined, as shown in Figure 2-7. The analysis was influenced
by the necessity to try to duplicate the boost vibration and environ-
ment at the substrate supporting the cells.

The normal modes of the pinned-free MTA-1 panel have been determined to
predict the response levels and to select optimum shaker locations. The
modes were calculated for the following conditions:

1) Panel alone in vacuum;

2) Panel with 3.5-pound shaker mass at top of center spar (Station
   169.9) in vacuum;

3) Panel in air with 3.5-pound shaker mass at top of center spar
   (Station 169.9);

4) Panel in air with 3.5-pound shaker mass at center of lateral spar
   (Station 123.7);

5) Two 25-pound shakers at Station 169.9 on outer spar in vacuum.

Table 2-3: ANALYSIS OF STOWED CONFIGURATION DYNAMIC-LOAD CONDITIONS

Parameter Configuration Dates	Static Configuration		Dynamic Configuration			
	9-66	12-66	9-66	12-66	3-67	9-67
Critical external load condition	13-g long. + 2-g lat	13-g long. + 2-g lat	2-g lateral (Q = 15)		1.5-g lateral (Q = 15)	
Total horizontal shear at spacecraft hinge line station (lbs)	3,500	3,800	31,400	31,600	31,300	21,200
Total moment at spacecraft hinge line station (in.-lb)	2.5×10^5	2.7×10^5	33×10^5	28.5×10^5	26.0×10^5	19.0×10^5
Equivalent lateral steady-state acceleration (g's)	2	2	18	16.5	16.5	10.1
Peak lateral acceleration (g's)	2	2	53	31.5	31.5	31.5
Fundamental frequency (Hz)	---	---	4.6	22.0	21.5	22.0
Peak lateral structural deflection (in.)	1.0	0.06	24.5	0.56	0.64	0.62
Peak lateral substrate deflection (relative to data)	---	---	---	0.56	1.16	1.06

Chamber A
Floor Area

MTA-1

Panel Support Tie

25-lb Force
Vibrator (2 Places)
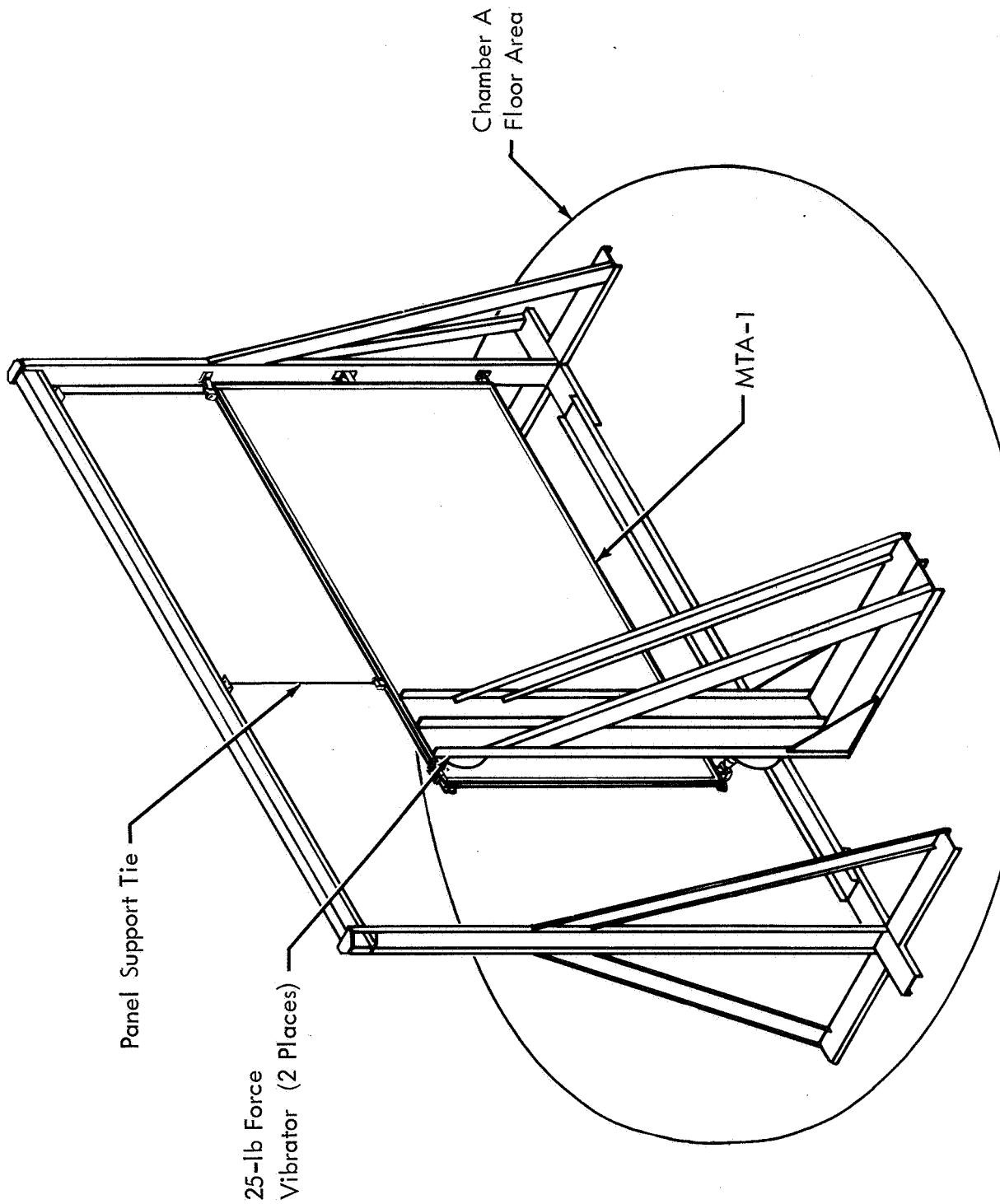
Figure 2-7:   MTA-1 VIBRATION TEST FIXTURE

Subsequent to analysis of the first four conditions, it was determined that the shakers available for the test were two 25-pound shakers with 10-ounce voice coils. The fifth condition was analyzed to reflect this. This condition is now the nominal one.

The mass of air applied to the panel for the ambient atmospheric test was taken as the mass in the volume shown in Figure 2-8.
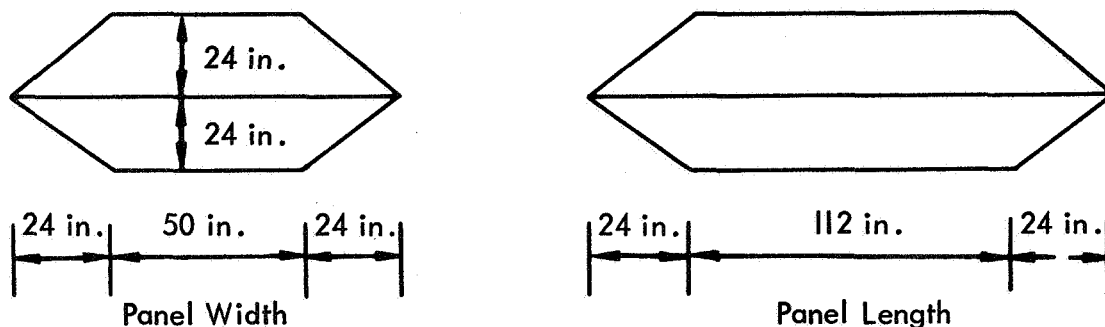
Figure 2-8: ASSUMED VOLUMES OF AIR MASS

The mass of air in a 2-foot-diameter sphere was applied to each substrate mass, and the remainder was distributed over the panel structure. A summary of the analysis of the nominal case (Condition 5 above) is given in Table 2-4. The first five mode shapes and frequencies are shown in Figures 2-9 through 2-13.

Table 2-4: SUMMARY OF ANALYSIS OF MTA-1 VIBRATION CHARACTERISTICS

Mode	Frequency (Hz)	Generalized Mass	50-1b Input Substrate Response	50-1b Input Structure Response
1	6.50	0.00330	--	--
2	15.4	0.00230	33.4	32.9
3	24.3	0.00187	--	--
4	31.6	0.000736	37.6	6.15
5	32.6	0.000471	42.6	3.42

Condition 5: Vacuum, two 25-1b shakers at Station 169.9 outer spars; Shaker Mass = 1.25-1b total.

A 2-pound force from each shaker (out of phase) will result in a 1-inch tip deflection in the first torsional mode (W = 6.5 Hz).

Station

169.9

147.2

123.7

100.2

77.8

55.5

33.1

10.5
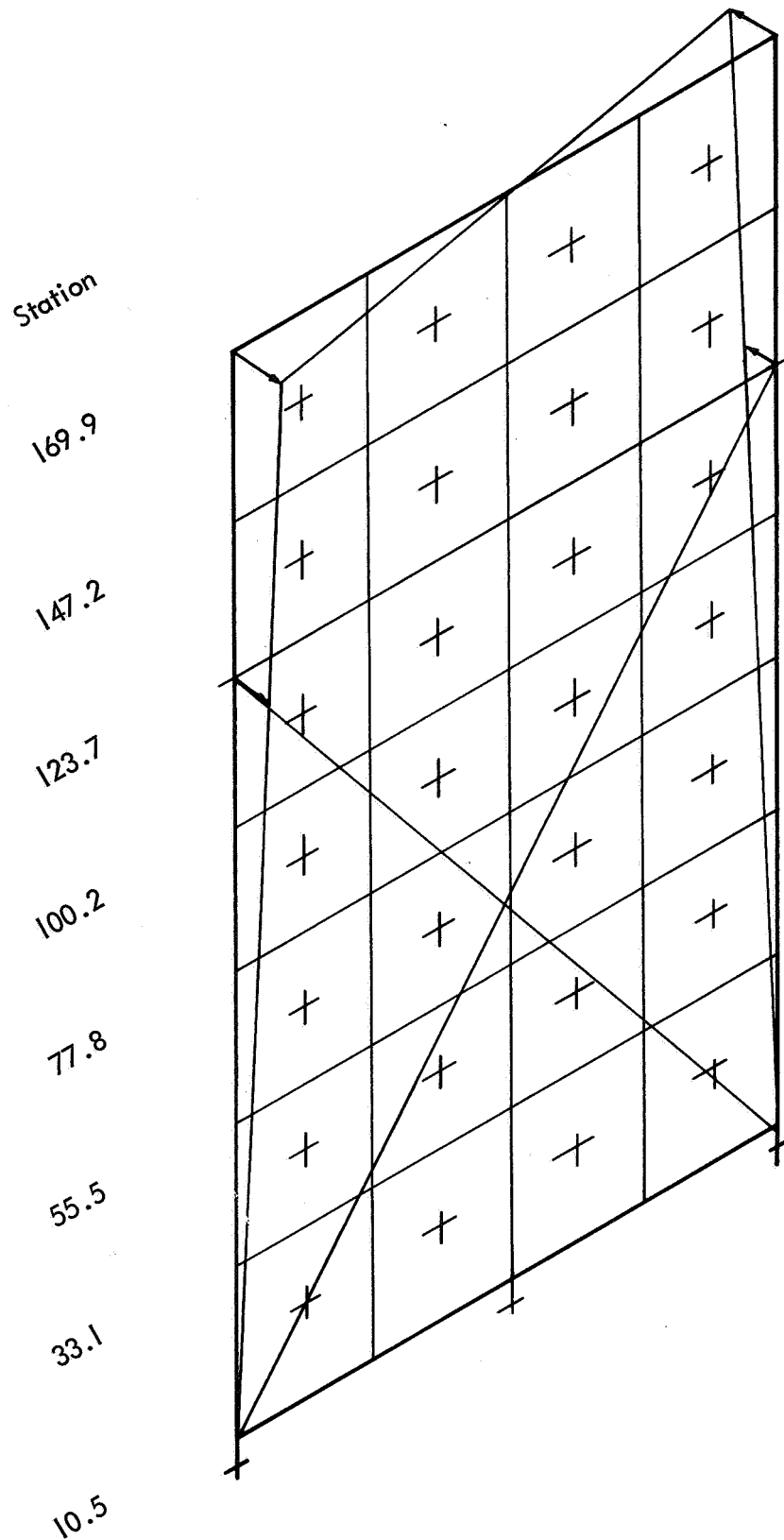
Figure 2-9: MTA-1 PINNED FREE MODES, f_1 = 6.5
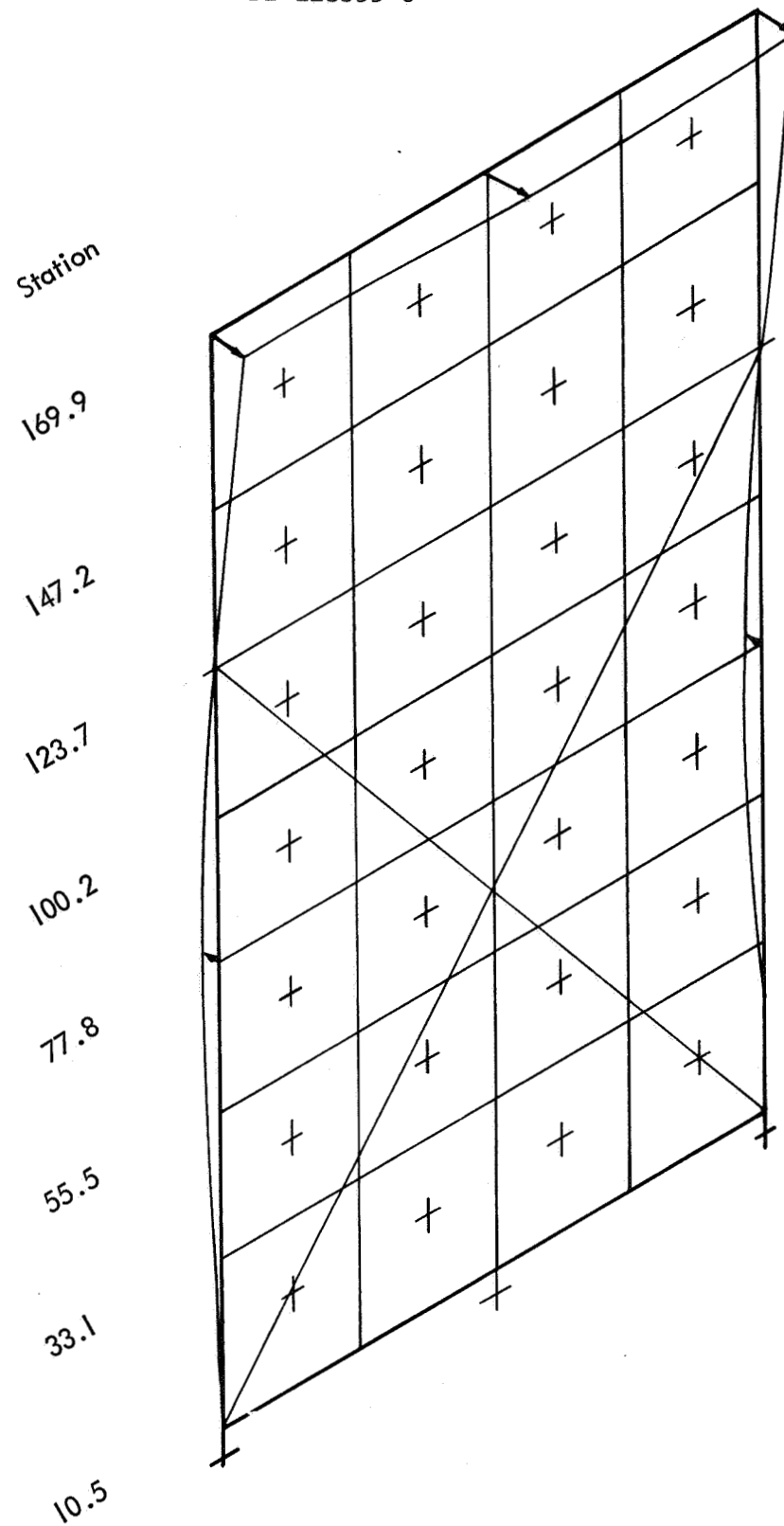
Figure 2-10: MTA-1 PINNED FREE MODES, f_2 = 15.4
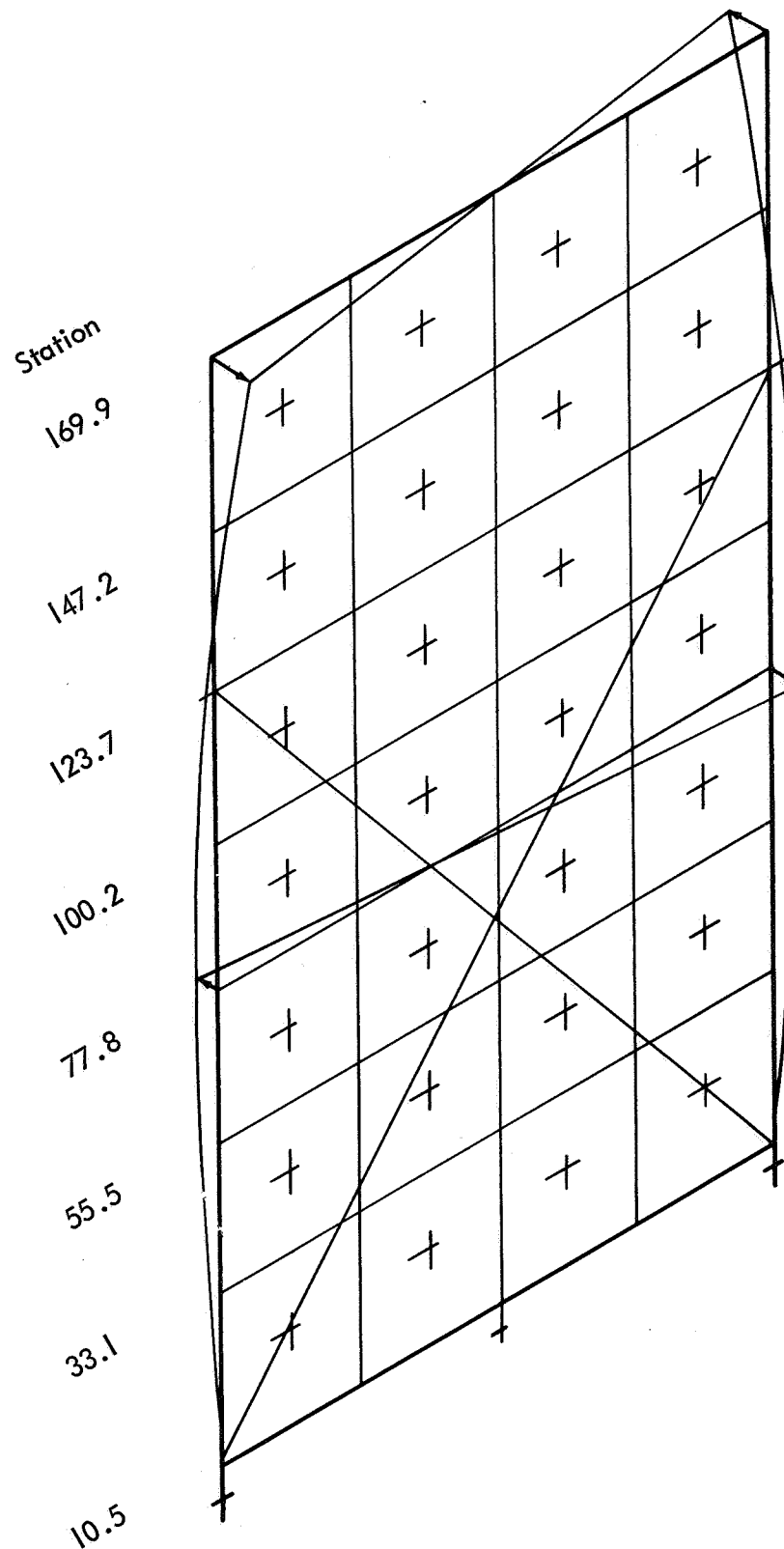
Figure 2-11: MTA-1 PINNED FREE MODES, f3 = 24.3
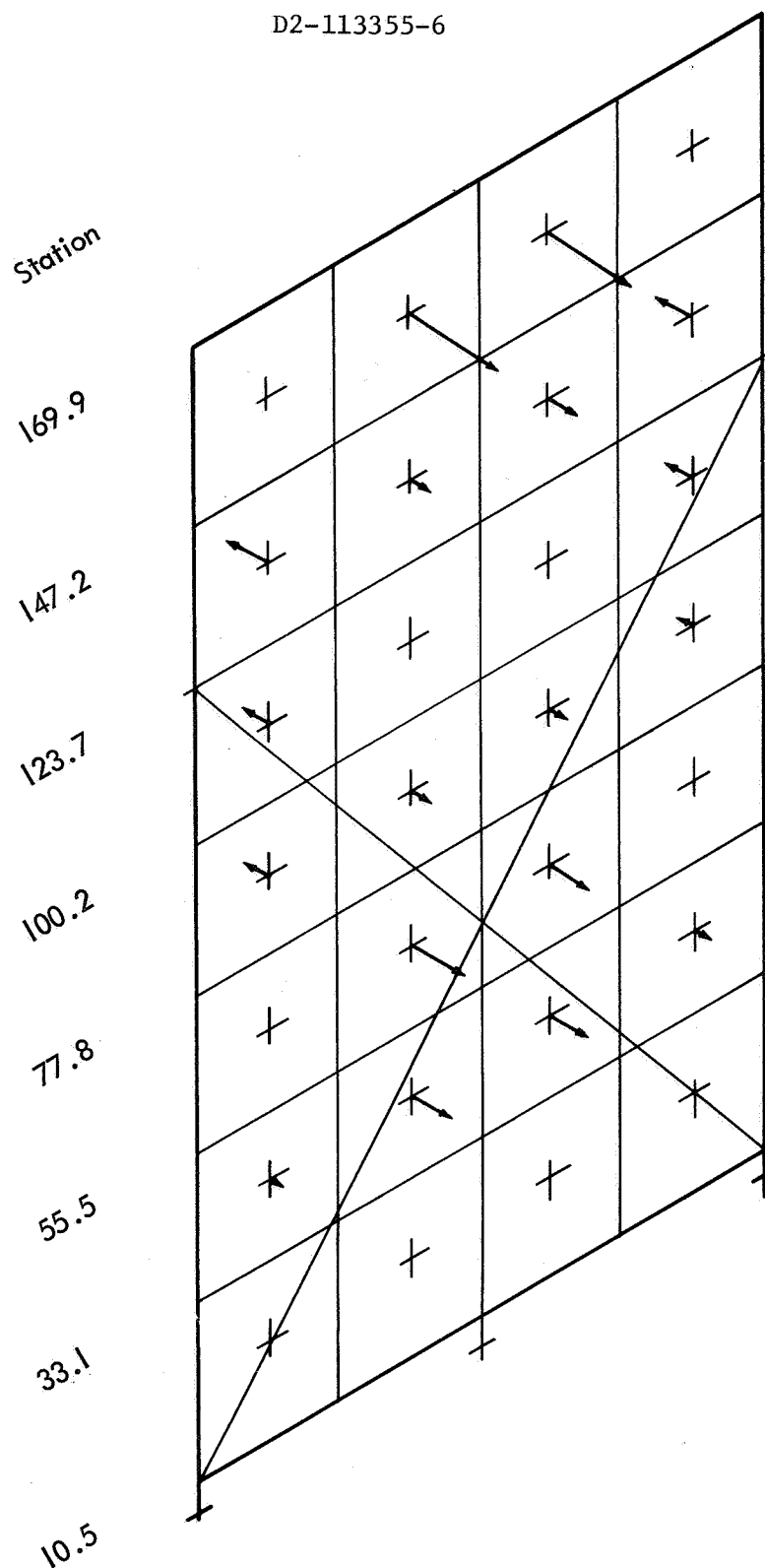
Figure 2-12: MTA-1 PINNED FREE MODES, $f_4 = 31.6$
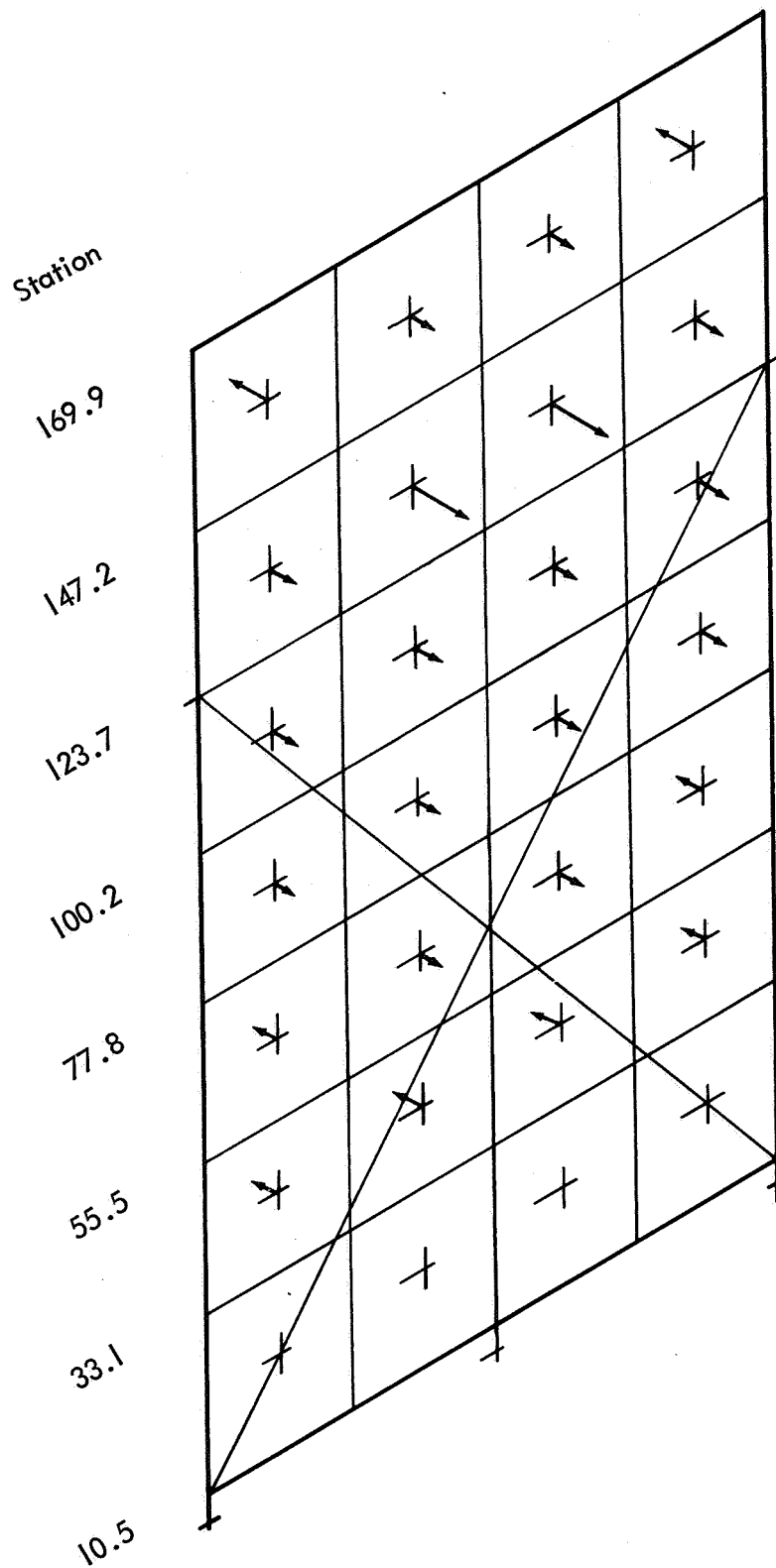
Figure 2-13: MTA-1 PINNED FREE MODES, f_5 = 32.6

During the MTA-1 vibration tests, the displacements and accelerations will be monitored by accelerometers located on the panel as shown in Figure 2-14. Strain gages located as shown in Figure 2-15 will be used to monitor the stress levels.

2.2.2 VIBRATION OF SCS-43

Testing of subpanel model SCS-43 previewed local substrate and intercostal vibration characteristics.

The SCS-43 test panel was tested in Phase I (Figure 2-16) to determine the response and damping of the panel subjected to vibration excitation. The results of these tests indicated the advisability of additional testing. The purpose of these tests is to determine the effect of air on the resonant frequencies and damping, and to obtain test data for another panel support condition.

The tests started with an initial low-level diagnostic sweep to determine the general characteristics of the panel. This was followed by sweeps at increasing levels of excitation, with dwells at one low and one high frequency, followed by a decay record for each dwell. All test data were recorded on tape. In addition, quick-look visicorder records were made of certain accelerometers and strain gages for use in selecting the input excitation for the subsequent sweep.

The Phase I test was analyzed by an array of six beams representing the substrate stiffness for each of the four sections. The panel weight was distributed as concentrated weights at the nine stations in each sector that defined the intersection of the beams. The beam stiffness was selected to match the substrate fundamental frequency calculated by energy methods. Solutions for all four edges pinned and for all four edges clamped were obtained.

Analysis of the stowed array showed an undesirable increase in effective weight and a consequent reduction in the first resonant frequency when the substrate primitive frequency was not sufficiently higher than the array frequency. The substrate tension value was selected to ensure an adequate frequency separation, and the Phase I vibration test devised to verify that the selected tension was adequate. However, comparison of measured and calculated frequencies could only be made by assuming an effective air mass, so the verification was not complete. In addition, the damping was large, and the relative amounts of air and structural damping were not separable.

Analysis for the second series of tests used the same model as Phase I, except that the edge constraints were changed to two edges pinned and two edges free. Solutions have been obtained for three conditions: (1) in vacuum, (2) with a hemisphere of air moving with each of the four sectors, and (3) with a hemisphere of air moving with the entire panel. Figure 2-17 shows the mode shape for the first resonance in vacuum. Only small differences for the resonant frequencies of the first four modes

Figure 2-14: MTA-1 ACCELEROMETER LOCATIONS FOR VIBRATION TEST
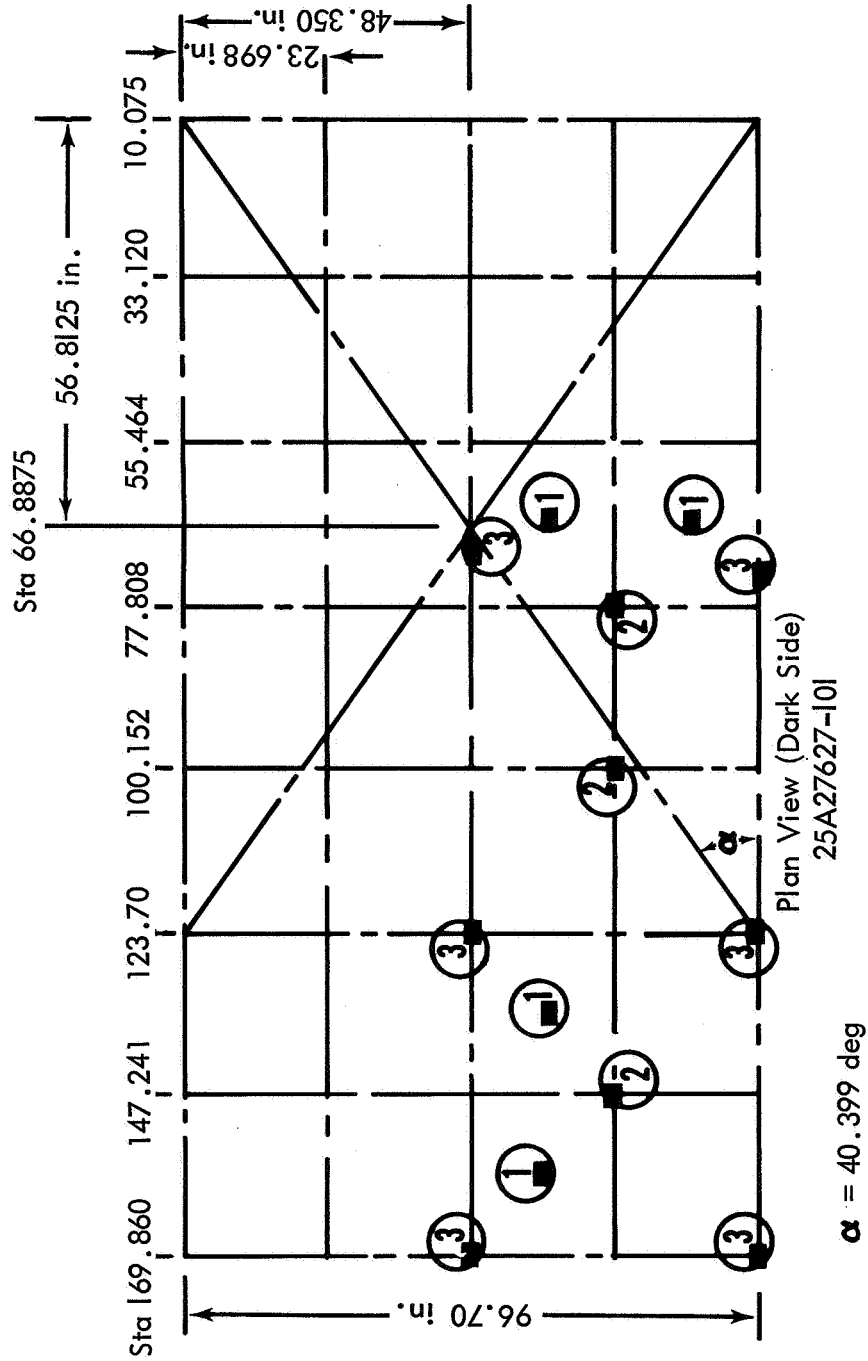
① Locate on dark side of substrate

② Locate on dark side of intercostal gusset

③ Locate on dark-side spar cap

α = 40.399 deg

Plan View (Dark Side)
25A27627-101

Figure 2-15: MTA-1 STRAIN GAGE LOCATIONS FOR VIBRATION TEST
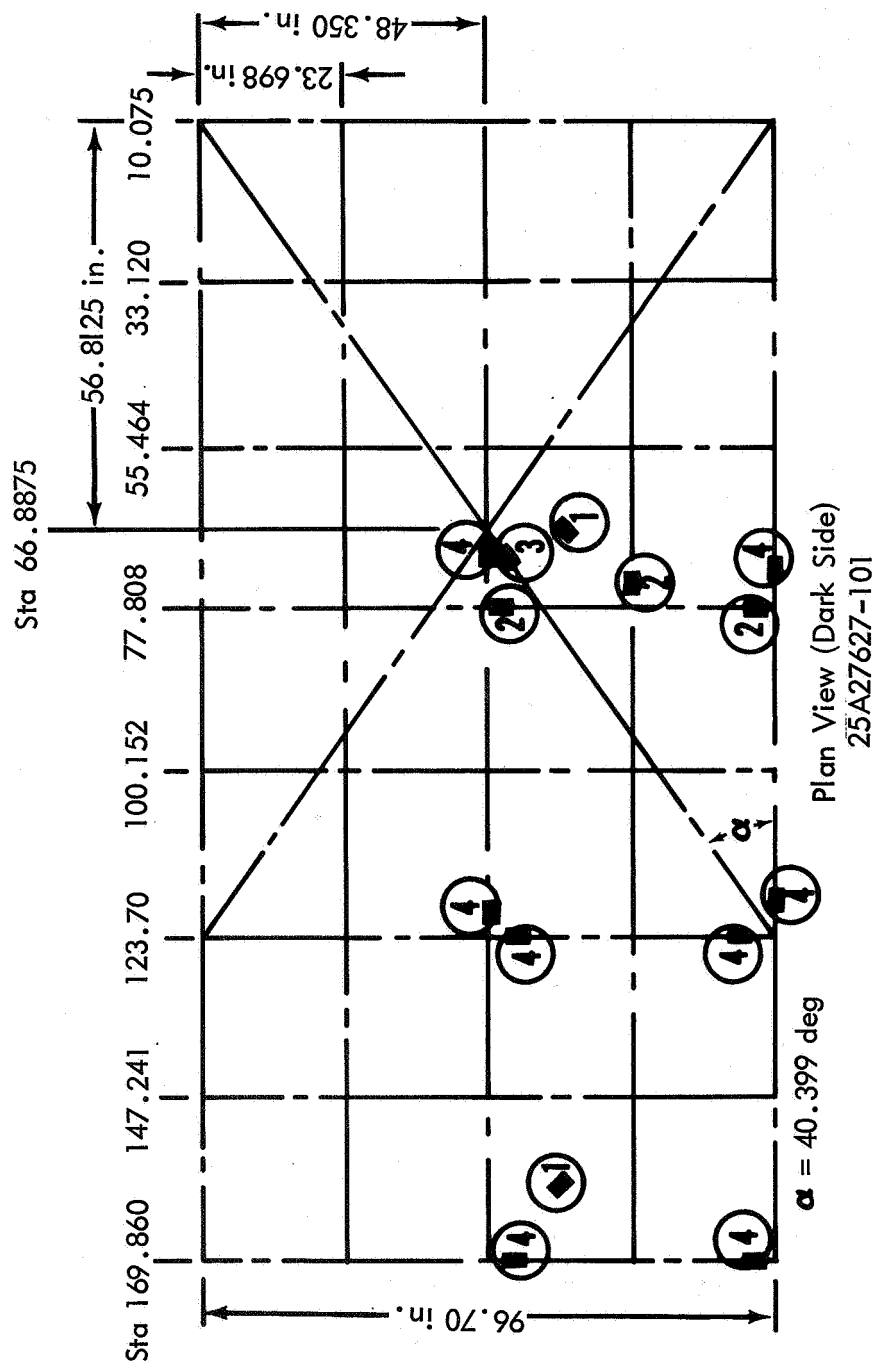
① Locate on dark side of substrate

② Locate on dark-side intercostal cap only

③ Locate on dark-side diagonal brace cap only

④ Locate on dark-side and Sun-side spar cap

Do not locate any gage on a gusset or splice plate
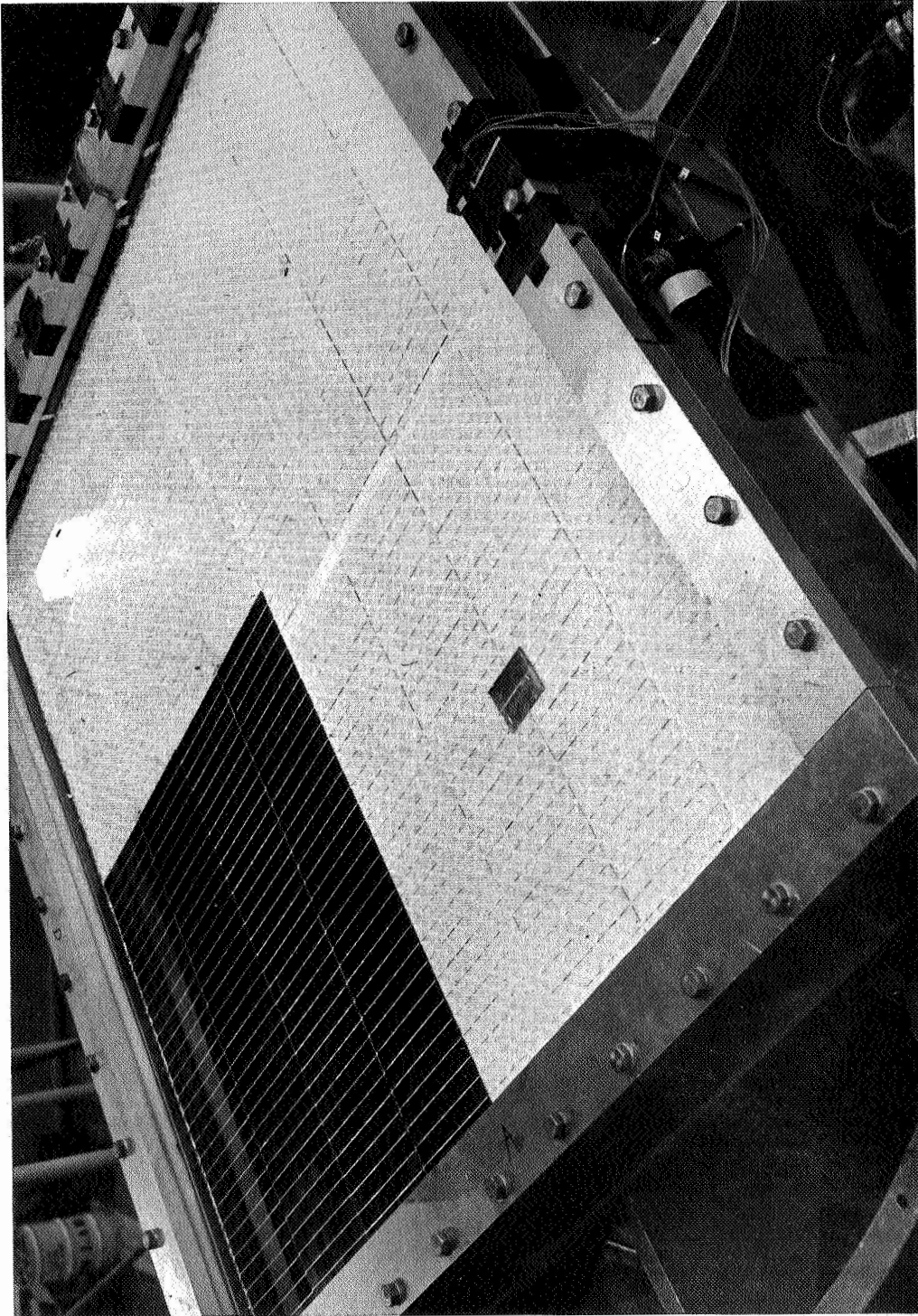
Figure 2-16:   SCS-43 VIBRATION TEST SETUP
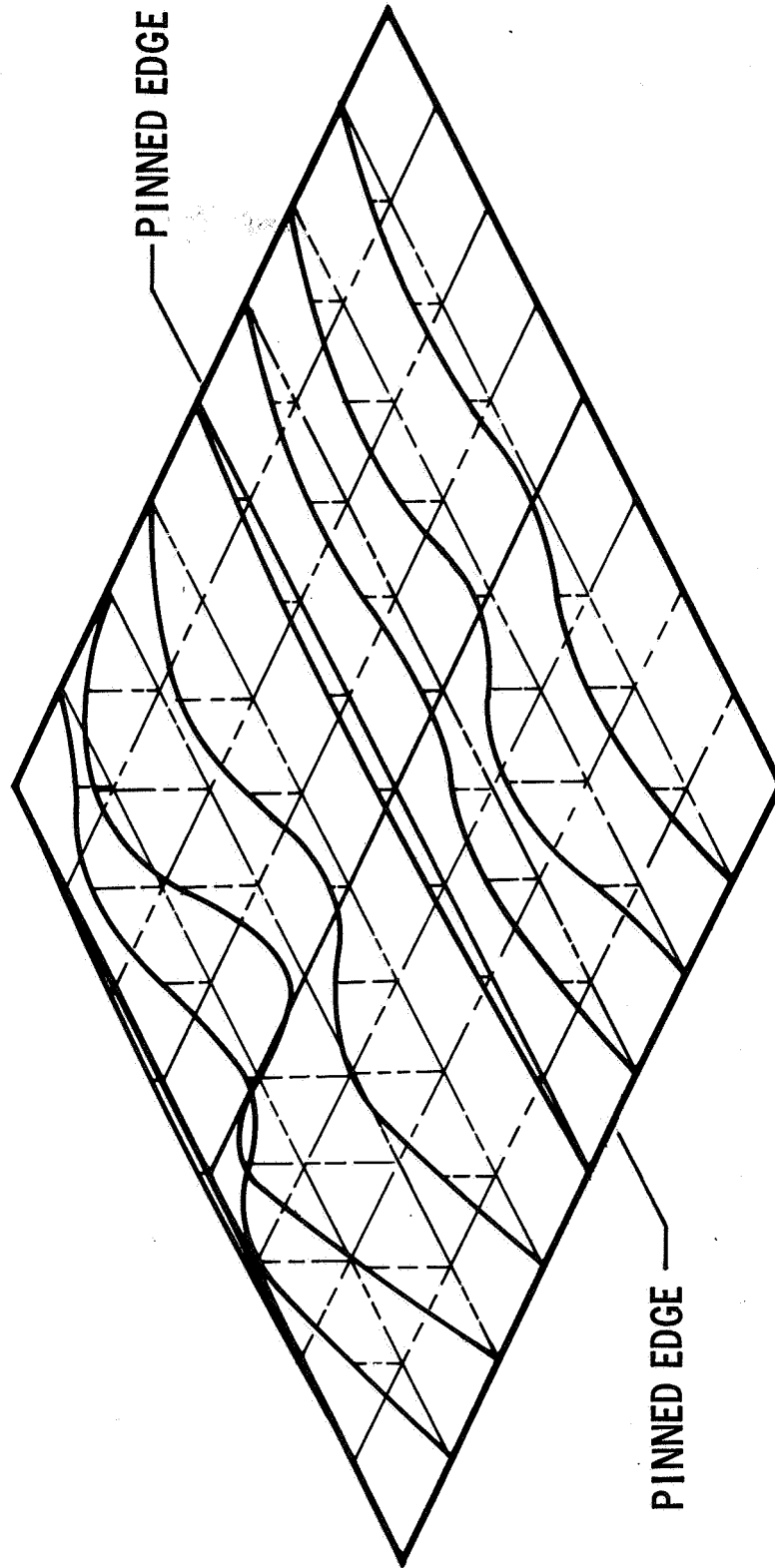
Figure 2-17: SCS-43 VIBRATION TEST—
Pinned-Pinned Vacuum Configuration First Mode-Frequency 44 Hz.

were obtained, and the motion of the edge beams in bending was also
small. This was expected: the frequency of an edge beam is well above
the substrate frequency. A band of frequencies between 85 and 100 Hz
appears to be similar to those measured in the Phase I test. In vacuum
the fundamental frequency was between 43.2 and 44.5 Hz, in good agree-
ment with the calculated frequency of 44.2 Hz. Damping evaluation has
not been made, but the response in vacuum was roughly 20 times that
in air.

2.3 PRESTRESS CONDITIONS

2.3.1 SUBSTRATE PRE-TENSION LOAD ANALYSIS

*An average pre-tension load of 12 pounds per inch in the substrate field
is a reasonable and acceptable requirement for LASA design.*

It is reasonable to assume that some tension is necessary in the substrate
to keep it flat during the fabrication of the panel and to keep it from
going slack during boost. Some tension is also required to keep the
natural frequency of the substrate above those of other elements of the
structural system. However, too much tension will produce deleterious
effects.

It is believed that a sufficiently accurate estimate of the pre-tension
effects is obtained from the analysis of a single 24-inch square panel
of substrate, bonded by four typical spar members.

1) Consider the effects of the flexible edge frame on the distribution
    of the tension loading in the panel. The basic equation for the
    deflection of the edges may be written as:

$$\frac{d^4y}{dx^4} + \lambda^2 \frac{d^2y}{dx^2} + \beta^4 y = \beta^4 h$$

where: x = Coordinate axis of edge beam;

   y = Deflection axis of edge beam;

   h = Prestretch in substrate for a uniform load of N_{max};

$$\lambda^2 = \frac{N_{ave} L}{2E_B I_B} \; ;$$

$$\beta^4 = \frac{2E_s t_s}{L E_B I_B} \; ;$$

where: L = Length axis of edge beam;

N = Load in substrate in pounds/inch;

E_S = Young's modulus for substrate;

t_S = Thickness for substrate;

E_B = Young's modulus for beam;

I_B = Moment of inertia for beam;

It can be shown that λ is small enough to be ignored and the above analysis reduces to:

$$\frac{d^4 y}{dx^4} + \beta^4 y = \beta^4 h$$

Given typical values as follows:

$$E_S = 8.5(10)^6; \quad t_S = 0.003 \text{ inch},$$

$$L = 24 \text{ inches},$$

$$E_B = 44(10)^6; \quad I_B = 0.023 \text{ inch}^4,$$

the axial load on the edge beams is 120 pounds.

The solution of the above equation gives the following ratio of the maximum tension load (at the middle of side) to the maximum load:

$$\frac{N_{min}}{N_{max}} = 0.266$$

In other words, it can be expected that for the LASA design the panels at the edge will possibly have a minimum substrate tension of approximately 25% to 30% of the maximum value.

2) Next, consider the effects of the substrate tension on the frequency of the substrate. It is expedient to assume tension distributions in the substrate as follows:

For the orthogonal tapes

$$T_x = \frac{N_o}{2} \left\{ (1 - k) \cos \frac{2\pi y}{L} + (1 + k) \right\}$$

$$T_y = \frac{N_o}{2} \left\{ (1 - k) \cos \frac{2\pi x}{L} + (1 + k) \right\}$$

$$T_{xy} = 0$$

For the diagonal tapes

$$T_x = T_y = \frac{N_o}{2} \left\{ (1 - k) \cos \frac{2\pi x}{L} \cos \frac{2\pi y}{L} + (1 + k) \right\}$$

$$T_{xy} = \frac{N_o}{2} \left\{ (1 - k) \sin \frac{2\pi x}{L} \sin \frac{2\pi y}{L} \right\}$$

where: $N_o = N_{max}$

$$k = \frac{N_{min}}{N_o}$$

$$N_{ave} = N = \left(\frac{1 + k}{2} \right) N_o$$

For a modal deflection of:

$$W = W_o \sin \frac{\pi x}{L} \sin \frac{\pi y}{L} \cos \omega t$$

the following natural frequencies may be derived:

$$\omega_{orthogonal} = \frac{\pi}{L} \sqrt{\frac{N_o}{m} \left(\frac{1 + 3k}{2} \right)} \quad \text{(radians/second)}$$

$$\omega_{diagonal} = \frac{\pi}{L} \sqrt{\frac{N_o}{m} \left(\frac{5 + 3k}{4} \right)}$$

$$\omega_{I \to \infty} = \frac{\pi}{L} \sqrt{\frac{2N_o}{m}}$$

Typical values of frequencies for N_o = 10 pounds per square inch and an "m" based on a weight of 0.182 pounds per foot are:

$$\omega_I = \infty = 51.5 \text{ Hz};$$

$$\omega_{diagonal} = 44.0 \text{ Hz};$$

$$\omega_{orthogonal} = 34.5 \text{ Hz};$$

These frequencies are sufficiently high and they show that the diagonal tapes are superior to the orthogonal tapes.

3)   Lastly, consider the possibility of instability of the frame caused by tension in the substrate. Let the idealization be as shown in Figure 2-18, and the deflection pattern be assumed as follows, and equate the internal work to the external work.

   N = Membrane load pounds per inch (assume N is uniform)

   M = Twisting moment

Assumed Rate of Twist:

$$\theta = \frac{v_o}{14ab} \quad (rad/in)$$

Assumed Displacement:

$$v = v_o \frac{xz}{14ab} = \theta xz$$

The internal work versus the external work gives the following:

$$\sum_{\text{Horizontal Bars}} \sigma_x \epsilon_x A_x a \quad + \quad \sum_{\text{Vertical Bars}} \sigma_z \epsilon_z A_z b \quad + \quad \iint_{\text{Horizontal Tape}} \sigma_x \epsilon_x t \; dxdz$$

$$+ \quad \iint_{\text{Vertical Tape}} \sigma_z \epsilon_z t \; dxdz \quad + \quad \frac{1}{2} GJ_{eff} \theta^2 L = \frac{1}{2} M\theta L$$

from which the torsional stiffness becomes:

$$\frac{M}{\theta} = GJ_{eff} - \frac{2}{3} Na \left(a^2 + \frac{b^2}{7} \right)$$

which in turn gives:

$$N_{cr} = \frac{3GJ_{eff}}{2a \left(a^2 + \frac{b^2}{7} \right)}$$

with GJ_{eff} being for N = C.

It can be shown that for LASA it is sufficiently accurate to use:

$$GJ_{eff} = \frac{1}{4A} \sum GJ_{vert} + \frac{1}{7b} \sum GJ_{int}$$
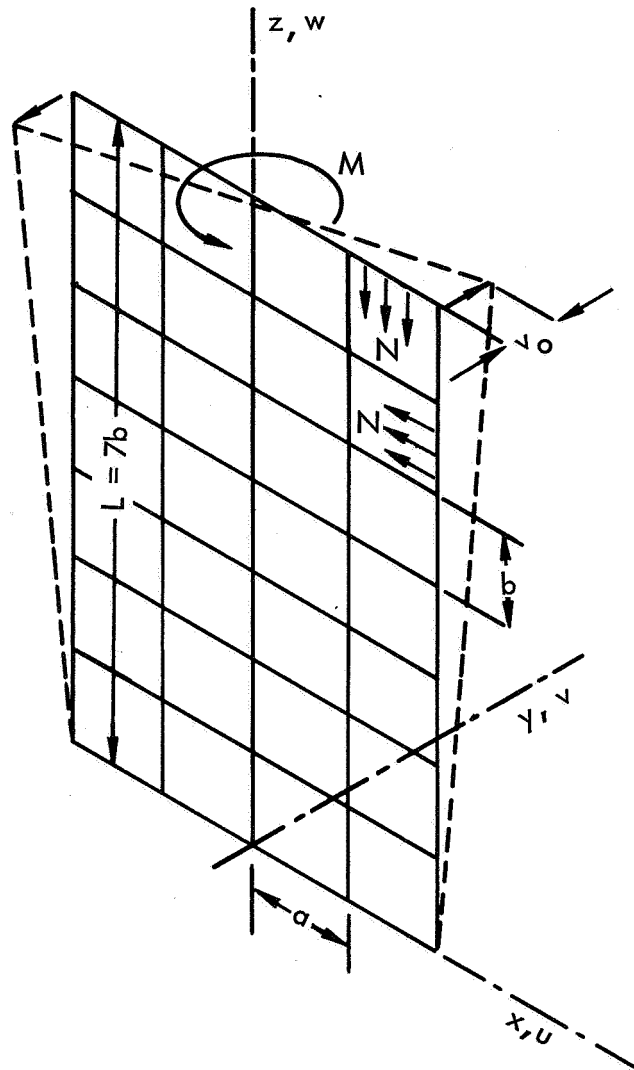
Assumed Normal Strains

$$\varepsilon_z = \frac{1}{z}\left(\sqrt{z^2 + v^2} - z\right) \approx \frac{1}{2}\left(\frac{v}{z}\right)^2 = \frac{1}{2}\theta^2 x^2 \underline{\qquad}$$

$$\varepsilon_x = \frac{1}{x}\left(\sqrt{x^2 + v^2} - x\right) \approx \frac{1}{2}\left(\frac{v}{x}\right)^2 = \frac{1}{2}\theta^2 z^2 \underline{\qquad}$$

Figure 2-18: FRAME IDEALIZATION

Heat Pad

Aluminum Load Bar

Air Piston
For Load

Pressure Film

Substrate

Alignment
Pins

Aluminum Load Bar

Beryllium Frame
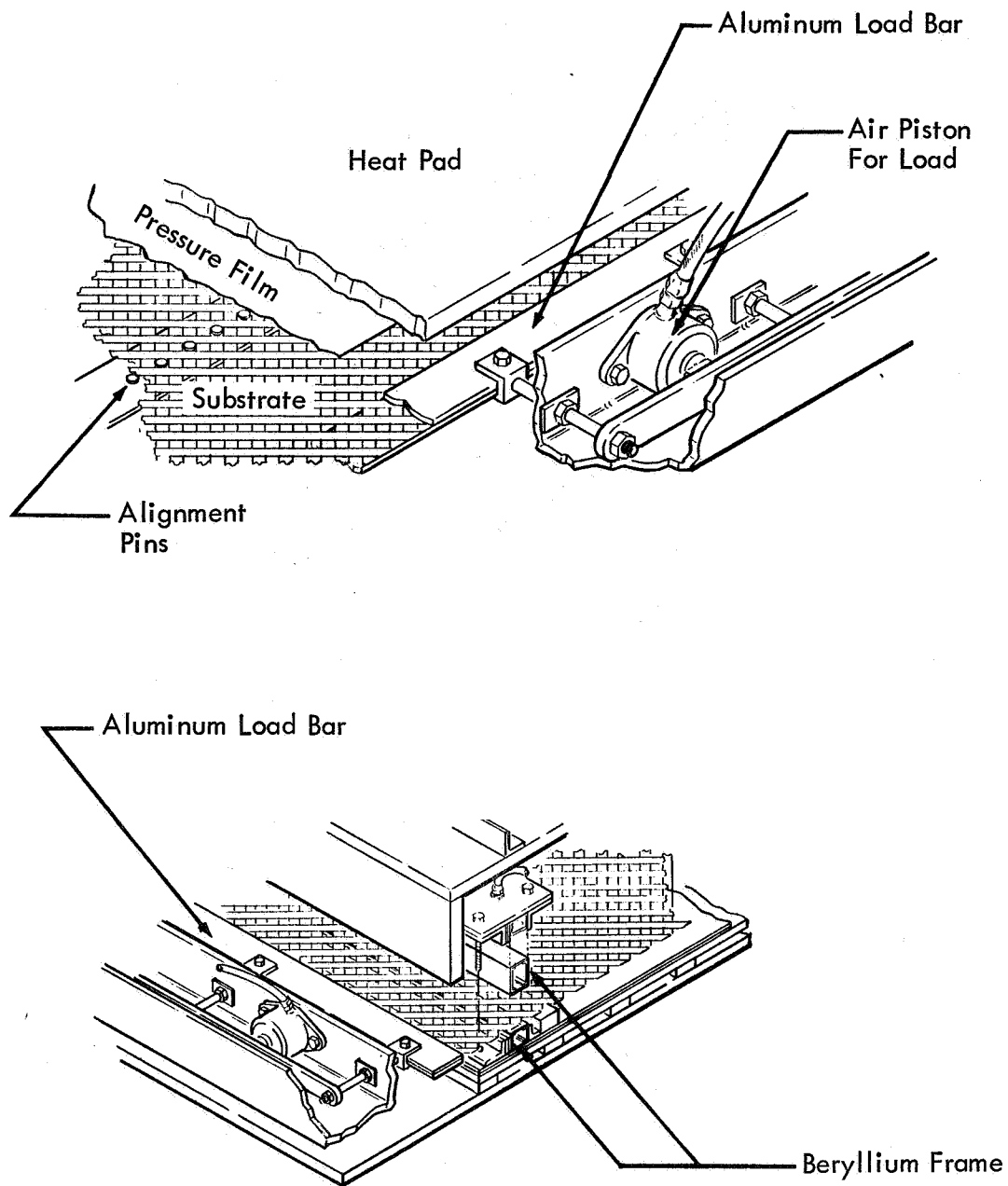
Figure 2-19: SUBSTRATE ASSEMBLY AND PRETENSIONING

For GJ_{eff} = 0.1805

N_{cr} = 340 pounds per inch

which indicates that the array frame is sufficiently stable for N = 12 pounds per inch.

In conclusion, a tension load of 12 pounds per inch will satisfy the nominal requirement, while at the same time the frame is sufficiently stiff to permit a higher value if future tests indicate it necessary.

2.3.2 FABRICATION FOR INITIAL TENSION IN SUBSTRATE

A special thermal-loading program is required to provide a flat substrate having a given initial tension.

The curing of adhesives used in the assembly of the substrate and frame requires exposure to various temperature cycles that would result in incompatible expansions. The loads and the thermal expansion in the substrate can be controlled separately if the longitudinal expansion of the edge loading bars can be independently maintained. The ideal thermal-load program will maintain an isotropic state of stress and strain in the substrate.

The procedure for installing the tape is described below. The substrate must be stretched and bonded at the node points and to the aluminum loading bars (Figure 2-19). The "green" tape is stretched at a low load across the aluminum load bars spaced by alignment pins, the grid is flattened with a vacuum bag slightly tensioned to straighten the fibers, and the nodes are bonded at 350°F.

After the grid is bonded at the nodes as well as to the aluminum load bars, the next process is, nominally, as follows:

Step 1---Apply membrane load of 12 pounds per inch to aluminum load bars and heat these bars (strip heating) to 225°F. Apply no heat or pressure to beryllium or substrate. The aluminum load bars elongate the same as the substrate during this operation. The substrate should be fabricated undersize to have proper alignment at room temperature and the design pre-tension.

Step 2---Heat substrate and beryllium frame to 250°F and simultaneously increase membrane load to 17.2 pounds per inch and, by strip heating, increase temperature of aluminum bar to approximately 320°F. During this step, the nominal relative position of the fiberglass substrate and beryllium does not change. The aluminum bar elongates at the same rate as the substrate.

Step 3---Apply pressure and bond.

Step 4---Cool down beryllium frame and substrate.

Step 5---Cool aluminum and unloaded tape.

Figure 2-20 shows the temperature-load versus time.

The procedure described above is an ideal program for isotropic pre-
tensioning. However, there are some practical difficulties in executing
the steps. In particular, the strip heating of the aluminum bars is
difficult to control. If the temperature of the aluminum bars were less
than 250°F, a gap would exist in the bars in the corners (Figure 2-20),
which in turn would result in lower loadings in the longer tapes and
higher loadings in the shorter tapes. A practical method of controlling
the temperature in the aluminum bars is to observe for this gap and adjust
temperature until gap disappears. Preliminary analyses have indicated
that such a situation may be tolerable. The present opinion is that some
local reduction (or increase) in the membrane load will not be serious
so long as the average loading of 17.2 pounds per inch is maintained at
maximum temperature.

Basic processing and tooling requirements are listed below:

1) A stretch frame (see Figure 2-21) capable of carrying substrate
   tension loads of up to 20 pounds per inch is used to restrain fixed
   links on two sides and air cylinders on two sides attached to ser-
   rated aluminum tension bars. Tape locator pins on these bars are
   set to a shrink scale which allows for the growth of the tapes when
   tensioned for bonding into the subpanel. Electric strip heaters are
   attached to the tension bars to lengthen them to suit the various
   conditions of substrate temperatures and tension. The critical
   node spacing of the substrate tapes and the relationship of these
   locations to the beryllium frame are controlled by the length of
   the tension bars and their position relative to the platen or jig
   base. The links along one side and one end, between the tension
   bars and the frame, are adjustable, and a fixed relationship is
   maintained on the same side and end between the frame and the jig
   base.

2) A steel jig base is required that has a good finish with no holes or
   crevices, is vacuum tight, can be heated to 350° by electric blanket
   under the base, and is at least 4 inches larger in overall dimensions
   than the beryllium subpanel frame. Temperature must be controllable
   to ±10°F over the entire jig base. The surface must be covered with
   FEP film, held flat.

3) After tapes are located, gripped, and the 3/4-pound tension applied,
   they are restraightened. The two tape layers are separated slightly
   with a pneumatic tube around the edges and allowed to realign and
   then come back together on the platen. The vacuum bag is applied
   and sealed through the tapes to the periphery of the platen (see
   Figure 2-22).

$$\Delta T = \frac{\text{Tape Stress}}{\alpha E}$$

ISOTROPIC CONDITIONS
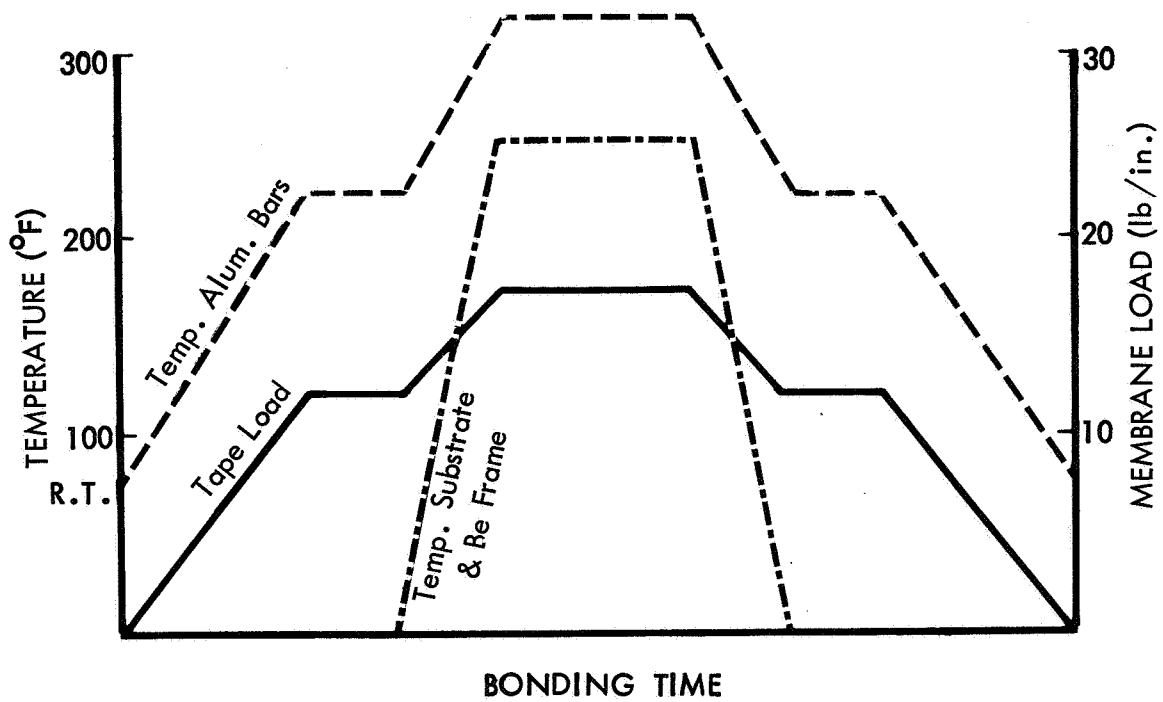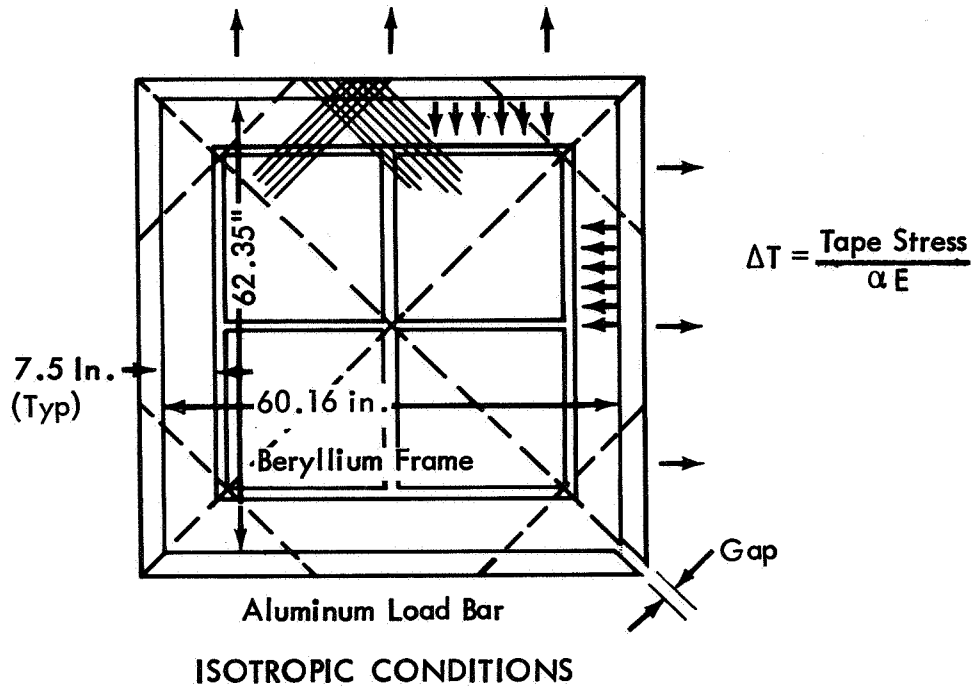
Figure 2-20: IDEAL PROGRAM TO GIVE ISOTROPY
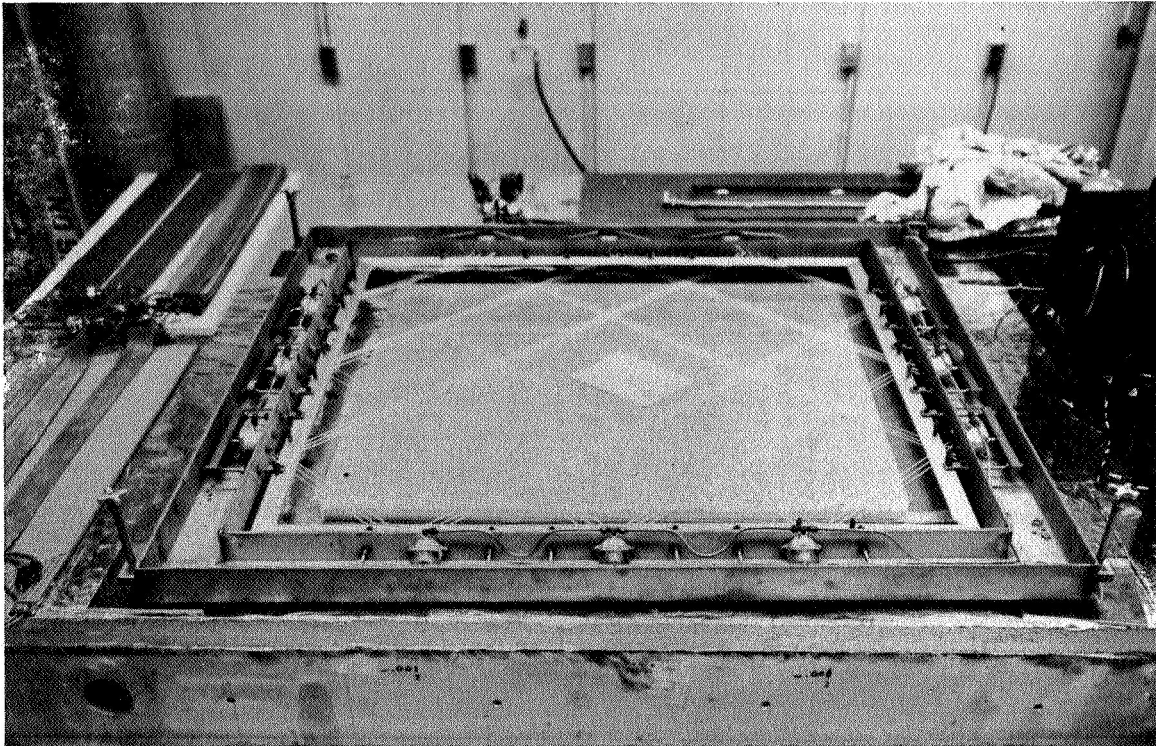
Figure 2-21:   SUBSTRATE LAYUP IN STRETCHING TOOL
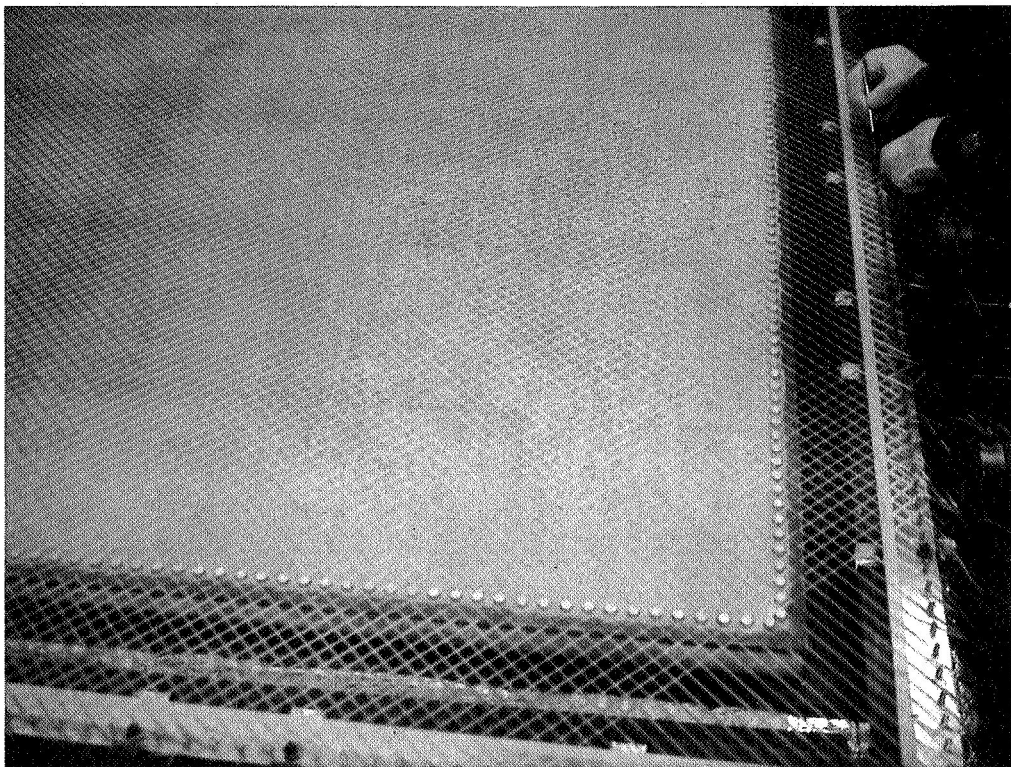
Figure 2-22:   SUBSTRATE ASSEMBLY READY FOR BONDING

4) Heat is applied to the platen, and additional heat applied to the tension bars to match the tape expansion, as platen temperature increases to 350°, following the chart shown in Figure 2-23 and cure cycle completed.

Before removing the substrate, it is stretched to 12 pounds per inch by applying heat and pressure to the tension bars as shown in Figure 2-24, and the node locations are checked against the drawing. The tension bars along the fixed sides are adjusted to bring the node points into exact position to suit the frame locators and the tiedown cable locations on the jig base.

5) The substrate and tension bars are then picked up on a strongback, maintaining only slight tension, and stored in an upright position on the wall adjoining the fixture.

2.4 TEMPERATURE DISTRIBUTION AND THERMAL CONTROL

2.4.1 MATHEMATICAL APPROACH TO THERMAL ANALYSIS

Use of finite difference equations is preferred in formulating the thermal analysis.

A numerical method of solving the partial differential equations of heat flow has been used throughout the LASA thermal analysis. The physical problem is broken into a finite-difference network of elements represented by nodes located at their centroids, such as Nodes i and j in Figure 2-25. Corresponding to each time interval, a set of heat balance equations in the finite-difference form may be conveniently written, one for each node. The general equation for Node i can be written as:

For transient heat transfer:

$$\sum_j K_{ij}\left(T_j - T_i\right)^m + \sum_j \sigma A_i F_{ij}\left(T_j^4 - T_i^4\right)^m + S_i = \frac{(C_p V)_i}{\Delta t}\left(T_i^{m+1} - T_i^m\right)$$

For steady-state heat transfer:

$$\sum_j K_{ij}\left(T_j - T_i\right)^m + \sum_j \sigma A_i F_{ij}\left(T_j^4 - T_i^4\right)^m + Si = 0$$

where subscript j refers to any other node of the nodal network having heat transfer with Node i by conduction and/or radiation, and superscripts (m+1) and m refer to time step numbers---(m+1) is one time step later than m,

K_{ij} = Conductance between Nodes i and j;

T_i, T_j = Temperature at Node i, Node j;

SUBSTRATE/DRAWBAR TEMPERATURES

DRAWBAR TEMPERATURE °F
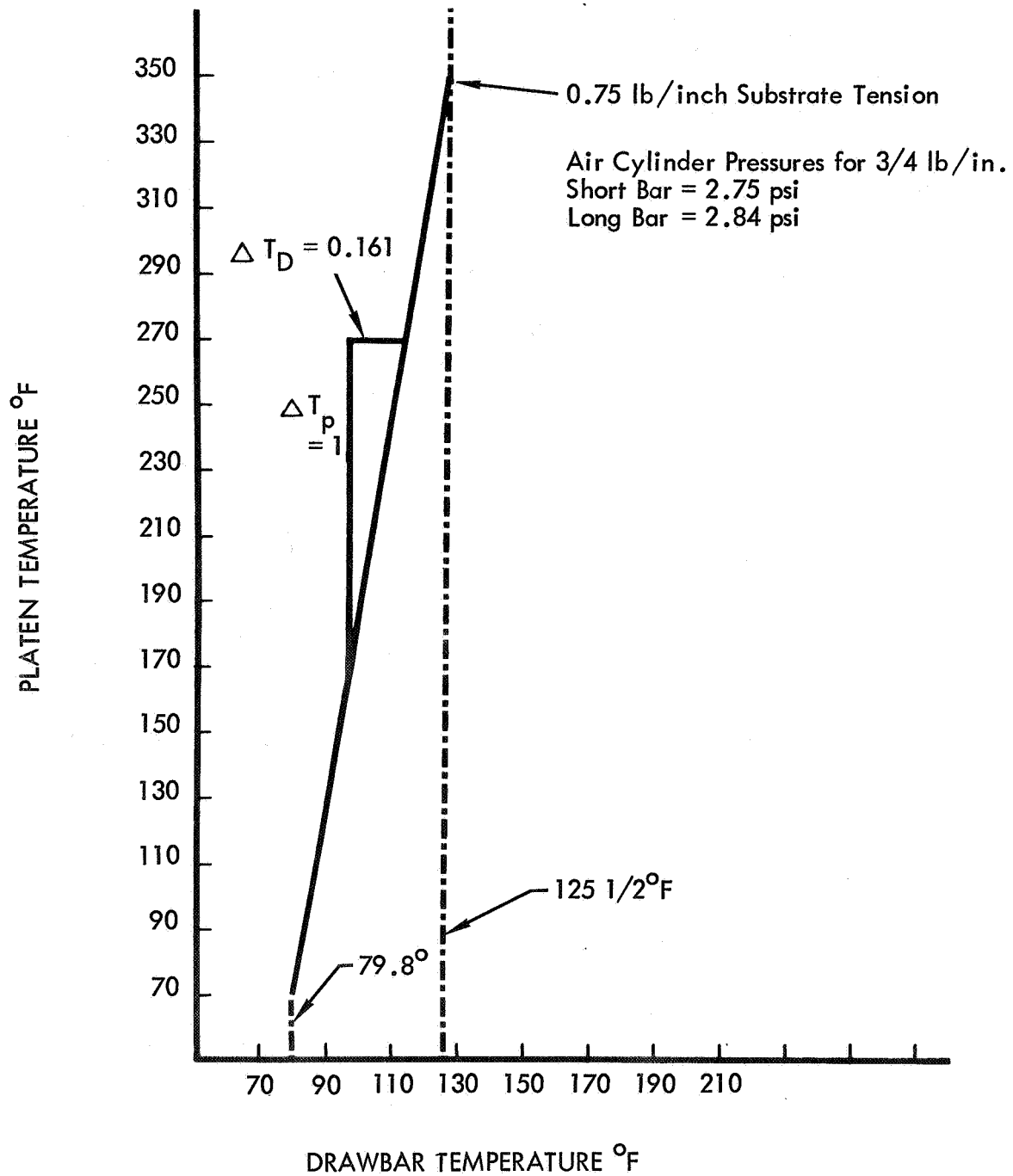
BONDING OF SUBSTRATE (TAPES TO TAPES)

Figure 2-23: SUBSTRATE BONDING CHART
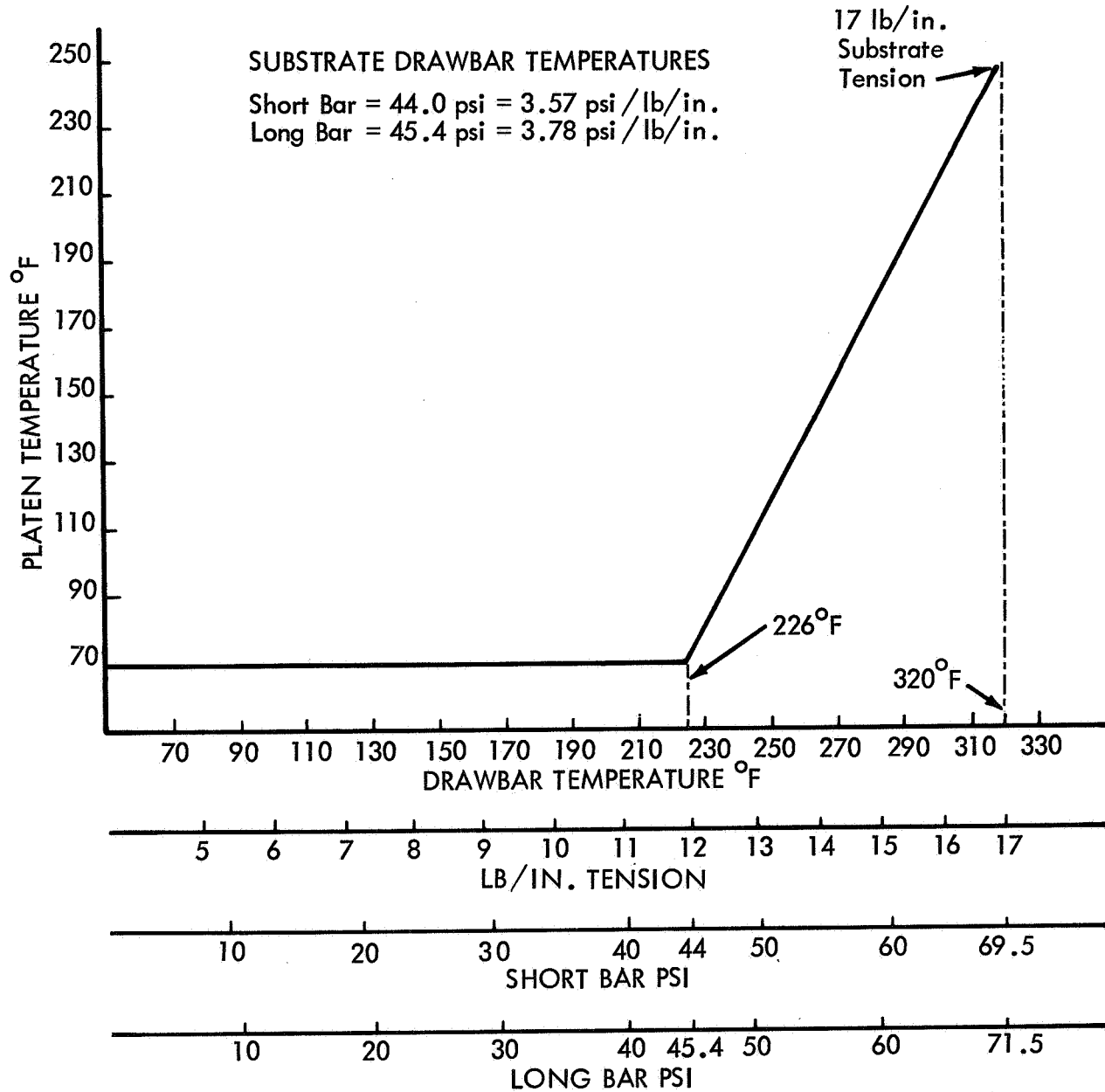
Figure 2-24: SUBSTRATE TENSIONING CHART
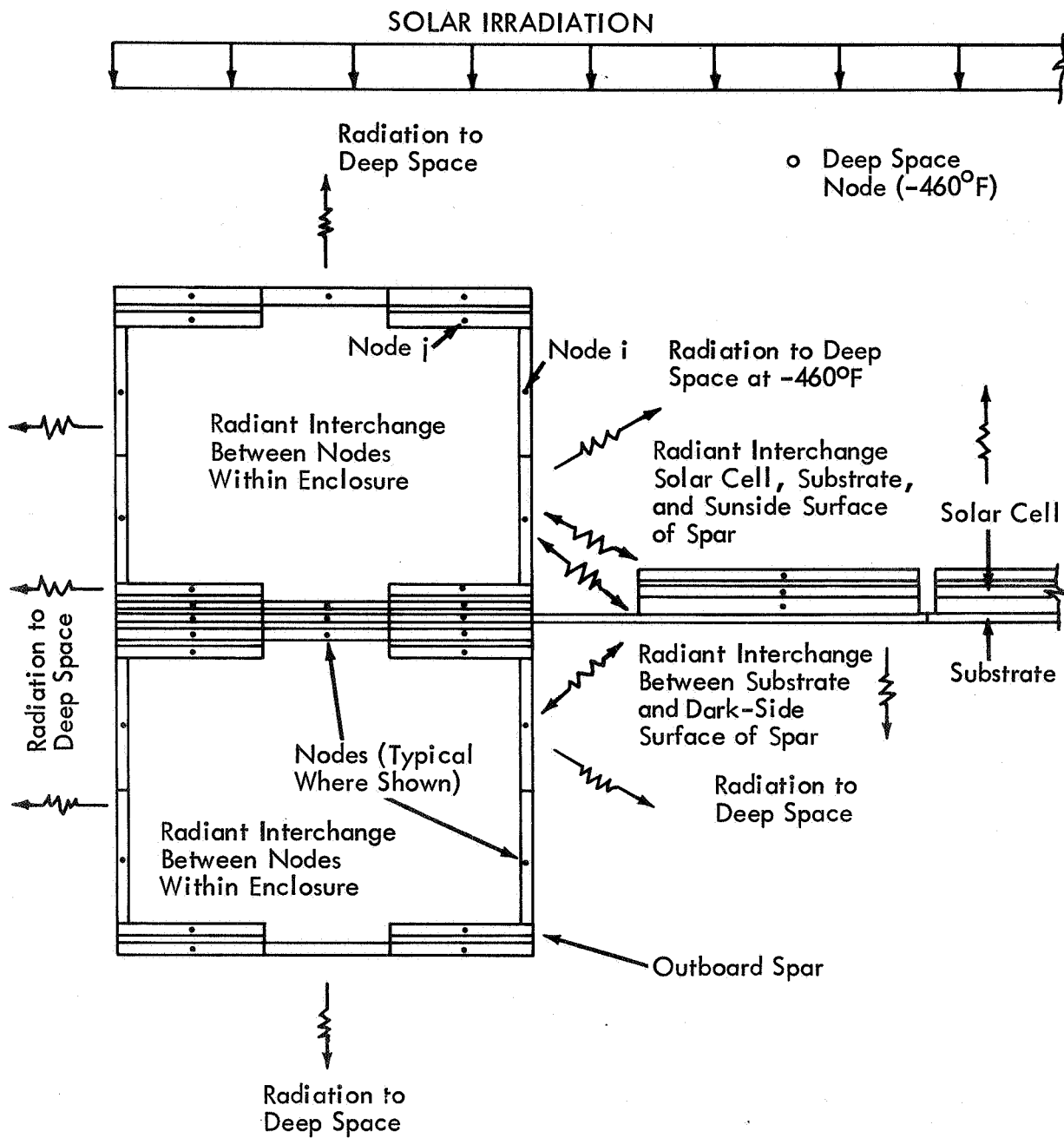
Figure 2-25: TWO-DIMENSIONAL THERMAL ANALYSIS MODEL —
Nodal Network, LASA Outboard Spar Deployed
Configuration

σ = Stefan-Boltzmann constant;

A_i = Surface area of Node i;

F_{ij} = Radiative interchange factor, including reflection;

S_i = Heat sources at i, including solar heat absorbed at i, direct and/or reflected; heat generated by an electric bus; power drawn from the solar cells;

C_p = Specific heat;

ρ = Density;

V = Volume.

The set of heat balance equations to each successive time interval can be solved by an iterative process using a high-speed digital computer, if the inputs of thermal properties, radiation view factors, heat sources, and initial temperatures are prescribed.

The solutions of the above equations are readily obtained with the Boeing thermal analyzer program (Reference 8, Section 11.3) for which the 1108 Digital Computer is used. This computer has been used extensively in thermal analysis work on many Boeing projects (such as X-20 and Lunar Orbiter), and the program has been used for the LASA thermal analysis because of its availability and efficient operation. With this program, it was possible to include the inputs of thermal properties as functions of temperature and to easily obtain problem solutions, both steady state and transient.

A sufficient accuracy may be obtained by proper idealization of the problem setup. The proper idealization includes the proper fineness of time-and-space meshing of the problem nodal network and the appropriate boundary conditions. In the LASA thermal analysis these factors were weighed from past experience. Solutions of the LASA problems are considered sufficiently accurate so long as the inputs of assumed thermal properties are correct or sufficiently close to the actual material thermal properties.

Figure 2-25 is presented as an example of a two-dimensional nodal network for the LASA deployed outboard spar thermal analysis. The spar and the adjacent solar cells are subdivided into many elements represented by nodes at their centroids, as indicated. The modes of heat transfer considered in the steady-state heat flow analysis include:

1) Solar flux to the sun-facing nodes, S_i. Calculated inputs are values of $Si = \alpha_s A_i S$, where α_s = solar absorptance and S = solar flux.

2) Radiation from all surface nodes to space, $\sigma A_i F_i$-space T_i^4. Calculated inputs are values of $\sigma A_i F_i$-space. F_i-space is the view factor of node i with respect to deep space.

3) Radiant interchange between nodes seeing each other, $\sigma A_i F_{ij}(T_j{}^4 - T_i{}^4)$. Calculated inputs are values of $\sigma A_i F_{ij}$.

4) Conductions between adjacent nodes, $K_{ij}(T_j - T_i)$. Calculated inputs are values of $X_{ij} = kA_{ij}/\ell_{ij}$, where k = conductivity, A_{ij} = cross-sectional area across which heat flows between node i and node j, and ℓ_{ij} = length of conduction path between nodes i and j.

The 1108 digital computer solution for this sample steady-state problem entailed little machine time. The printouts included resulting temperatures of all nodes coded for solution.

2.4.2 CONTROL OF ARRAY STRUCTURAL TEMPERATURES

The array structural temperatures were adequately controlled through the use of a passive system and the proper control system.

Thermal analysis of the original baseline configuration revealed extreme temperatures of the stowed array: 335°F (maximum) and -230°F (minimum) at the end of a 3-hour stowed period and 280°F (maximum) and -98°F (minimum) at the end of the 20 minutes following shroud ejection. The configuration considered laminar X-500 coating only on the dark side of each panel. These temperatures were compared against the limits of 167°F (75°C) maximum and -148°F (-100°C) minimum as specified in JPL Specification GNP-50505-FNC-B for the deployed configuration. The extreme high temperatures were not considered acceptable because they exceeded the thermal capability of common adhesives (such as BMS 5-29) to be used in the array design.

The use of a passive system and the proper control coating on the solar array to reduce the extreme high temperatures has been investigated. The study showed large temperature reduction of the stowed array was possible through the combined use of a 3-mil B-1060 white paint and aluminized mylar solar shades. The white paint was to be applied over all exposed areas of the stowed array except in Subpanels 4B and 2B, where the front surfaces of solar cells were exposed and should not be coated. These uncoated areas were to be protected with roll-up solar shades. (The roll-up concept assumes that each shade can be rolled up after the stowed period and immediately following the deployment of the subpanel where the shade is installed.) From the above thermal control system, the stowed-array extreme temperatures were predicted to be: 116°F (maximum) and -255°F (minimum) at the end of a 3-hour stowed period, 92°F (maximum) and -98°F (minimum) at the end of 20 minutes following shroud ejection. The predicted temperatures were based on the following assumed thermal properties.

	3-mil B-1060	0.5-mil Aluminized Mylar	
		Aluminized Side	Nonaluminized Side
Solar Absorptance	0.235	0.12	0.17
Emittance	0.85	0.03	0.63

Tests on B-1060 revealed difficulty in applying thin coatings because of the low resin content of the paint. It was concluded that B-1060 should not be used for the array; instead, a similar compound, B-1060A, 3 mils thick, with increased resin content could be satisfactorily used. The B-1060A has a higher ratio of solar absorptance to emittance: 0.29:0.89 for a 3-mil thickness. Its use will, therefore, result in a higher maximum temperature, approximately 150°F at the end of a 3-hour stowed period, and 115°F after shroud ejection. Figure 2-26 presents the thermal characteristics of B-1060A and the thermal coverage plan.

Tests on RTV-40 indicate its feasibility as a thermal control coating on the dark-side surfaces of the deployed array, excluding those surfaces that become exposed in the stowed condition. A 2-mil thickness of RTV-40 will be used to replace the Laminar X-500 originally proposed for the baseline configuration. Besides its compatibility with the adhesives used in the array, RTV-40 has an emittance value of 0.875 (comparable to that of Laminar X-500) and a solar absorptance value of 0.375 (compared with 0.95 for Laminar X-500). The use of RTV-40, with the added advantage of a lower solar absorptance to emittance ratio, will ensure that the Sun-facing array subpanel surfaces in the deploying condition will stay cooler and within the limiting temperature of 167°F (75°C).

In summary, the array maximum structural temperatures were considered to be adequately controlled through the combined use of B-1060A, RTV-40, and the roll-up solar shades of aluminized mylar described above. The allowable maximum temperature of 167°F (75°C) would not be exceeded for the array either in the stowed or deploying condition. The maximum temperature of the deployed array was predicted to be far below 167°F. Two temperature conditions worthy of attention are:

1) Thermal shock rates of solar cells in the deployed array are predicted to be much greater than 54°F (30°C) per minute. The rate of temperature rise from initial temperature of -148°F is 140°F for the first minute, and the rate averages 53°F per minute for the first 5 minutes from -148°F to 115°F.

2) Solar cells in the deployed array are predicted to experience temperatures lower than -148°F (-100°C) if the array is shadowed by a planet for longer than 6.5 minutes.
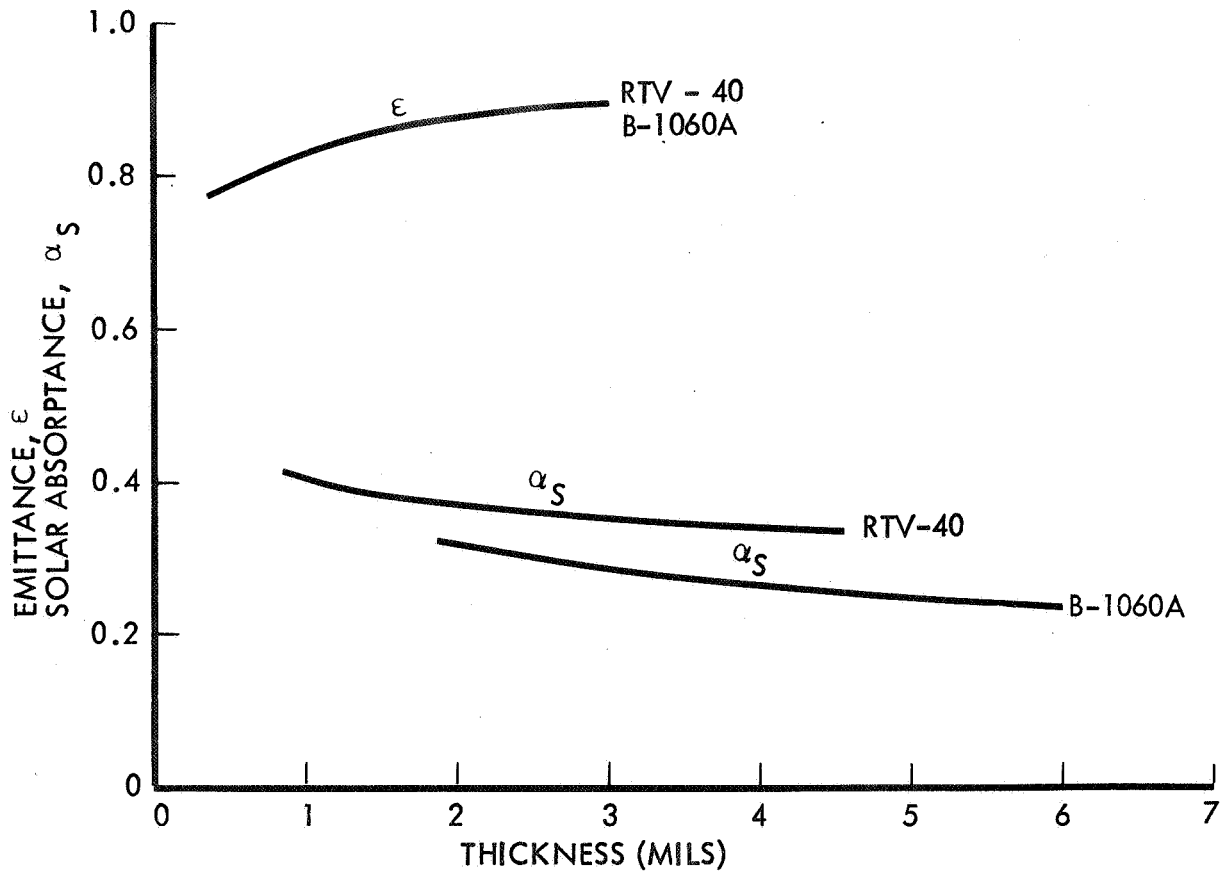
THERMAL CHARACTERISTICS OF TRV-40 & B-1060A
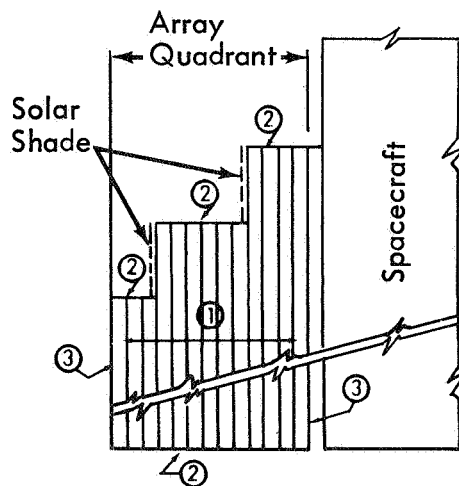
AREAS FOR B-1060A COATING:

① Exposed Areas of Outboard Spars

② Exposed Areas of Edge Members

③ Subpanel Dark Side Surfaces
(Subpanels 1 & 5A Only)
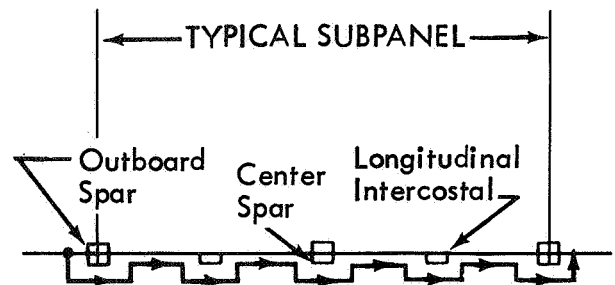
AREAS FOR RTV-40 COATING:

Entire Dark Side Surfaces of All
Subpanels Except Subpanels 1 & 5A

THERMAL COATING COVERAGE PLAN

Figure 2-26: B-1060A THERMAL CHARACTERISTICS AND THERMAL
COATING COVERAGE PLAN

2.4.3   TEMPERATURES IN SCS-43

Temperatures measured in SCS-43 provided useful comparison with those predicted.

The temperatures measured in SCS-43 thermal vacuum test were much higher than predicted temperatures for the LASA deployed configuration. For steady-state simulated solar heating of the test panel, outboard spar temperatures 120° to 170°F, intercostal temperatures 115° to 160°F, and solar cell temperatures 145° to 170°F were measured at various locations of the test panel. These values are high compared with previously predicted design values of approximately 80°, 100°, and 120°F for the outboard spar, intercostal, and solar cell. The test results were expected to be on the high side, primarily because of a shroud fixture that served as a shield for the IR lamps and prevented them from seeing the test panel portion that was subjected to simulated solar heating. During the test, the shroud became heated by the IR lamps, maintained radiant heat interchange with the panel, and reduced the radiation view factor between the panel and the cold test chamber wall. If the shroud had been actively cooled to maintain a temperature as low and constant as that of the chamber wall (-320°F), the test would have undoubtedly resulted in much lower overall temperatures.

The test results indicated small local thermal gradients in the test panel structure. Maximum thermal gradients for the one-Sun simulated heating resulted in approximately 30°F in the outboard spar and 10°F in one intercostal. These were compared with the calculated values of 10 to 20°F.

The test results provided a good correlation with predicted temperature response rates or thermal shock rates of the solar cells in the case of exposure to solar heating after emergence from the shadow. Figure 2-27 presents time-temperature plots of the solar cells based on test values, as shown in solid lines, for two representative locations in the test panel. Predicted values from the first quarterly report, replotted here for comparison, are shown as dotted lines. The slopes of the test and predicted curves indicated good agreement for the initial 2 minutes of solar heating and disclosed thermal shock rates as high as 140°F for the first minute. (Beyond this time, comparison is less meaningful: the effect of the heated shroud fixture on the test panel temperatures would be appreciable, as mentioned previously.)

Good agreement was also noted between test and predicted temperature response rates in an intercostal member when the panel at initially low temperatures was subjected to sudden one-Sun simulated solar heating. The temperature rise (Figure 2-28) was on the order of 50°F for the first minute of heating.

Figure 2-28: INTERCOSTAL-TEMPERATURE RESPONSE

Figure 2-27: SOLAR-CELL TEMPERATURE RESPONSE

2.5 STRESS-DEFORMATION ANALYSIS

2.5.1 STRUCTURAL ANALYSIS OF SUBPANEL 1

Several iterations of stress analysis of Subpanel 1 were required to account for design developments and revisions in loads.

The changes in the tiedown and shear tie system made it possible to reduce the loads at the tiedown fitting interface with Subpanel 1 and to reduce the lateral spar moment. Also, as a result of shifting the locations of two intermediate tiedowns and shear ties to align with existing intercostal stations, the internal load distribution for the outer and center spars changed. In spite of these changes, Subpanel 1 is still required to transmit all of the in-plane loads to the spacecraft hinges and to react a large portion of the out-of-plane panel inertia loads at Station 123.7 through the forward tiedown fittings.

The center hinge internal loads were defined in detail to allow for better design and test definition. Figure 2-29 shows a summary of the center hinge fitting loads. The loads shown are joint-ultimate loads based on a limit load of 1.5-g lateral sinusoidal vibration input and two safety factors: (1) ultimate factor, 1.25; and (2) fitting factor, 1.15. The 20,000-pound thrust load represents 45% of the total shear load transmitted to the spacecraft. Thus the center hinges for the two in-plane panel assemblies carry 90% of the total shear load, and the remaining 10% is carried by the hinges on the out-of-plane panel assemblies. The outer spacecraft hinges are not considered to carry any of the lateral thrust loads, because they will have positive clearance in that direction with respect to the spacecraft. For the center hinge load analysis, it has been assumed that the spacecraft is translationally rigid (at Points a and b in Figure 2-29; this rigidity results in 30% of the moment produced by the eccentricity of the lower edge member neutral axis to the bolt axis being carried into Subpanel 1, and the remainder being carried into the spacecraft.

Figure 2-30 shows another sampling of the internal loads at a critical joint in Subpanel 1. The forward tiedown fitting at Station 123.7 is an important structural joint because it ties together the diagonal brace, outer spar, lateral spar, and tiedown fitting. The significance of this joint is that it serves as a focal point of three reactions: (1) it transmits loads from the out-of-plane panel assembly through the tiedown corner fitting (4,600 pounds); (2) it transfers the shears from the outboard panels into MTA-1 (3,700 pounds); and (3) it reacts the tiedown normal loads to the panel (4,100 pounds and 4,400 pounds). The joint loads shown in Figure 2-30 are joint-ultimate loads and include the effects both of vibration and of tiedown preloads.
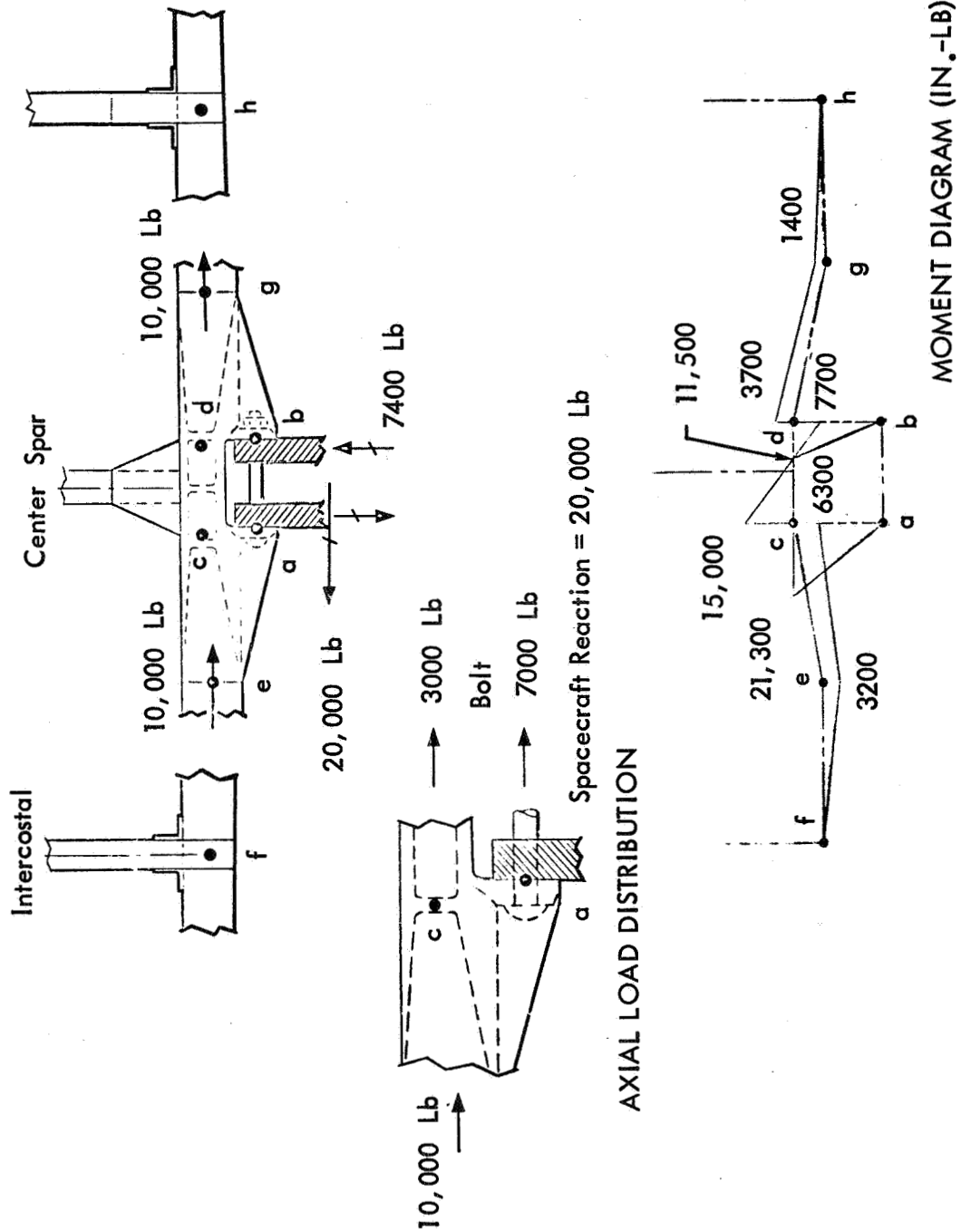
Figure 2-29: CENTER-HINGE FITTING LOADS
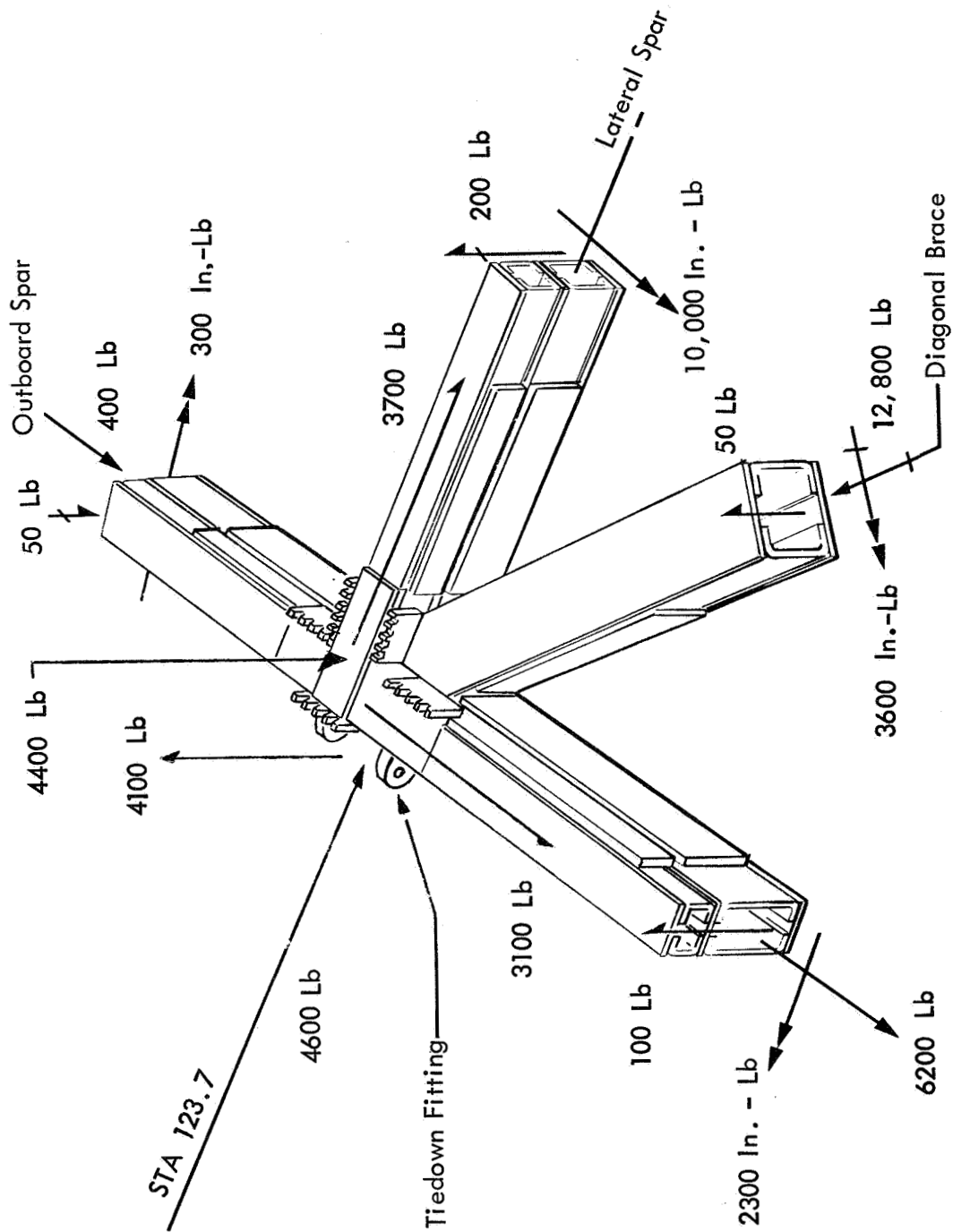
Figure 2-30: FORWARD TIEDOWN FITTING LOADS

A summary of typical stress analysis results for Subpanel 1 is presented in Table 2-5. Subpanel 1 stress analysis was performed with the latest internal loads, which represent the final set of internal loads for Phase I. The effects of vibration, substrate preload, tiedown system preloads, and temperature were accounted for in the stress analysis. With the exception of the intercostals and the center spar, the critical vibration direction for all members and joints in Subpanel 1 is vibration-parallel to the plane of the panel containing the members (the in-plane panel). For the center spar and intercostals the critical vibration is normal to the plane of the panel (that is, out-of-plane). Three general types of areas were analyzed: the basic beryllium members, the titanium fittings, and the splices or joint areas that connect the members to the fittings.

The beryllium members, such as the outboard spar or a later spar, were sized with an ultimate factor of safety of 1.25. Four modes of failures were considered: (1) tension failure in the beryllium; (2) compressive yield or crippling of the cross section; (3) several member instability (including beam-column effects where applicable); and (4) adhesive bond failures due to excessive shear stresses.

Table 2-5: MTA-1 STRESS ANALYSIS SUMMARY---BERYLLIUM

Member	Critical Condition*	Margin of Safety
Outboard spar	In-plane panel vibration; channel crippling due to combined axial and bending loads	+0.00
Lateral spar (Station 123.7)	In-plane panel vibration; spar cap tension due to lateral spar bending	+0.04
Lower edge member (Station 10.5)	In-plane panel vibration; Sun side spar cap crippling due to combined axial and bending loads	+0.06
Diagonal brace	In-plane panel vibration; channel crippling due to combined axial and bending loads	+0.00

*Using ultimate safety factor of 1.25, applied to limit loads obtained from 1.5-g sine vibration input.

Once the beryllium channels and spar caps had been sized, the fitting areas were designed and analyzed to provide a 1.15 factor of strength over the basic member capability. Because the caps and channels often are terminated at a fitting, it is necessary to provide both top and side splice plates (usually beryllium) heavier than the member gages. Sufficient bond lengths are provided at the splices to develop the full strength of the splice plate material. In general, the titanium fittings are not highly stressed and are of minimum practical gages, with the exception of increased land thicknesses at weld locations and at areas of high stress intensity. The use of titanium for fittings was dictated by two principal structural requirements: (1) the need for preventing high local stresses, commonly found in fitting areas, from occurring in beryllium; (2) the necessity for choosing a material with a coefficient of thermal expansion as close to the beryllium coefficient of thermal expansion as possible, to minimize resulting thermal stresses in the adhesive.

Figure 2-31 shows the essential points associated with stresses due to differential thermal expansion that will occur in an adhesive joint involving two dissimilar metals. The shear stresses that exist in the adhesive are a function of the shear modulus and thickness of the adhesive, the thickness and elastic modulus of the two plate materials, the coefficient of thermal expansion for each material, the incremental change in temperature, and finally, to a smaller degree, the length of the bond. The curves shown in Figure 2-31 compare the adhesive shear stress distribution that would occur during boost and at the end of a 3-hour postboost thermal soak period if aluminum or titanium were bonded to beryllium. The high shear stresses induced by an aluminum-to-beryllium bonded joint are not acceptable in view of current adhesive allowables.

2.5.2   STRUCTURAL ANALYSIS OF SUBPANELS 2 THROUGH 5

An integrated analysis of Subpanels 2 through 5 was needed to reflect changes in the loads analysis and improvements in design.

The changes in the tiedown system, the relocation of two lines of intermediate shear ties, and the addition of a number of shear ties required that the internal loads and stress analyses applicable for Subpanels Units 2 through 5 be updated. Table 2-6 shows a typical internal load distribution that exists in Subpanel Units 2 through 5 for a 1.5-g lateral sinusoidal vibration input. Subpanel Units 2 through 5 carry relatively small axial loads and their predominant design load is a bending moment. However, the Subpanel Unit 2 outer spars, located in the in-plane panel, share a portion of the axial load from Subpanel 1 as a result of the interaction of the shear ties; Subpanel 5A lateral spars carry a significant axial load as a result of interfacing with the tiedown system.

$$G_{ADH} = 200,000 \text{ psi}$$

Be/Al 3-Hour Soak $\Delta T = 300^\circ F$

Be/Al Boost $\Delta T = 70^\circ F$

Be/Ti 3-Hour Soak $\Delta T = 300^\circ F$

Be/Ti Boost $\Delta T = 70^\circ F$

$\tau(x)$ (1000 psi)

X DISTANCE (In.)
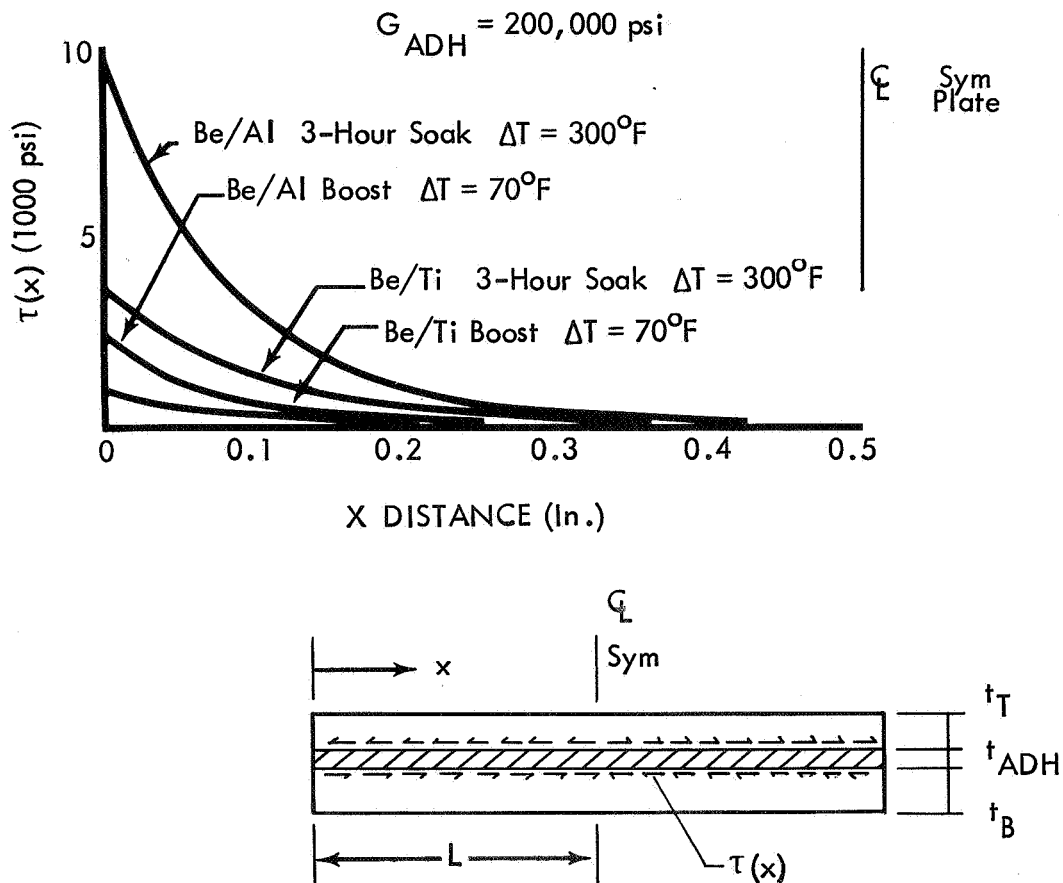
$$\tau(X) = \tau_{MAX} \left[COSH(KX) - \frac{COSH(KL)}{SINH(KL)} SINH(KX) \right]$$

$$\tau_{MAX} = \frac{\sqrt{\dfrac{G_{ADH}}{t_{ADH}}} \, \Delta\alpha\Delta T}{\sqrt{\dfrac{1}{t_T E_T} + \dfrac{1}{t_B E_B}}} \qquad \frac{SINH(KL)}{COSH(KL)}$$

Where

$$K = \text{Joint Constant} = \sqrt{\frac{G_{ADH}}{t_{ADH}} \left(\frac{1}{t_T E_T} + \frac{1}{t_B E_B} \right)}$$

G_{AHD} = Shear Modulus of Adhesive

ΔT = Temperature Increment

$\Delta\alpha$ = Difference Between Top Plate and Bottom
     Plate Thermal Expansion Coefficient

E = Modulus of Elasticity of Top or Bottom Plate

Figure 2-31: STRESSES DUE TO DIFFERENTIAL THERMAL EXPANSION

TABLE 2-6. OUTER SPAR DISTRIBUTION OF MAXIMUM LOADS
RESULTING FROM N = 1.5-g VIBRATION INPUT

| | In-Plane Panel | | Out-of-Plane Panel | |
Subpanel	Axial Load (pounds)	Out-of-Plane Moment (inch-pounds)	Axial Load (pounds)	Out-of-Plane Moment (inch-pounds)
2B	1950	2150	220	1230
2M	950	410	84	1100
2A	350	142	73	950
3B	120	344	50	860
3M	34	388	26	810
3A	10	400	12	795
4B	4	400	8	790
4M	22	390	8	780
4A	44	380	36	760
5B	61	354	70	705
5M	105	280	180	605
5A	240	160	500	330

The stress analyses for Subpanel Units 2 through 5 were performed with
the latest internal loads representing the finalized set of internal
loads for Phase I. Table 2-7 summarizes the results of the stress
analyses performed on these panels. A computer program was formulated
that can solve for the minimum weight section properties in terms of cap
and channel gages required to produce positive margins of safety.

The use of fittings other than shear ties were kept to a minimum in
Subpanels 2 through 5. This was possible in view of the reduced inter-
nal loads environment found in these subpanels as compared to the high
internal loads found in Subpanel 1. In several key areas, such as Sub-
panel 2B and 5A, with relatively large localized loads, titanium fittings
were specified. In most cases, the shear ties served to transmit not
only shear loads from subpanel to subpanel but also the normal loads
between subpanels and the concentrated reactions between intersecting
members, where possible (i.e., in lighter loaded areas), beryllium
gussets and clips were used to transfer loads at member joints, particu-
larly at intercostals.

Table 2-7: STRESS SUMMARY FOR SUBPANELS 2 THROUGH 5 MEMBERS

Subpanel No.	Outboard Spar			Center Spar			Bottom Edge (Sta 10.5)			Lateral Spar (Sta 123.7)			Upper Edge (Sta 169.9)		
	t_{cap}	Margin of Safety	Critical Condition	t_{cap}	Margin of Safety	Critical Condition	t_{cap}	Margin of Safety	Critical Condition	t_{cap}	Margin of Safety	Critical Condition	t_{cap}	Margin of Safety	Critical Condition
2B	0.080 0.045 0.025	0.008 0.003 0.062	Sta 10.5-55.5 I1 Sta 55.5-123.7 I1 Sta 123.7-169.9	0.025	0.05	OP2	0.035	0.003	I1	0.085	0.009	I2	0.02	0.04	OP1
2M	0.02	0.09	I1	0.025	0.20	OP2	0.03	0.014	I1	0.055	0.04	I2	0.02	0.12	OP1
2A	0.02	0.28	OP1	0.02	0.15	OP2	0.03	0.070	I1	0.04	0.06	I2	0.02	0.17	OP3
3B	0.02	0.37	OP1	0.02	0.04	OP2	0.025	0.030	I1	0.03	0.05	OP1			
3M	0.02	0.42	OP1	0.02	0.11	OP2	0.02	0.013	I1	0.03	0.05	OP1			
3A	0.02	0.45	OP1	0.02	0.14	OP2	0.02	0.09	I1	0.03	0.05	OP1			
-B	0.02	0.46	OP1	0.02	0.21	OP2	0.02	0.18	I1	0.03	0.05	OP1			
4M	0.02	0.47	OP1	0.02	0.23	OP2	0.02	0.32	I1	0.03	0.05	OP1			
4A	0.02	0.48	OP1	0.02	0.25	OP2	0.02	0.47	I1	0.03	0.04	OP1			
5B	0.02	0.37	OP1	0.02	0.33	OP2	0.02	0.66	I1	0.03	0.02	OP1			
5M	0.02	0.43	OP1	0.02	0.45	OP2	0.02	0.87	I1	0.04	0.06	OP1			
5A	0.02	0.62	OP1	0.02	0.87	OP2	0.02	0.76	I1	0.055	0.05	OP1			

NOTES: 1. The above summary represents the strength requirements of the basic members.
        2. All values are based on an ultimate factor of safety of 1.25. Limit load is
            1.5-g sine vibration. 0.02-inch channel gage used with indicated cap gages (t_{cap}).

NOTATION:

I ---In-plane panel vibration
OP---Out-of-plane panel vibration

1 ---Cap tensile stress
2 ---Cap compression yield or crippling stress
3 ---Channel crippling

2.5.3 CHANGES IN DESIGN OF MTA-4 CENTER SPARS

Only the center-spar gages for Subpanels 2 through 5 needed to be resized; all other members of the LASA design are conservatively designed.

A reanalysis of the internal loads using the final (second) iteration of the dynamic loads showed that certain design loads used for sizing were unconservative. To understand this, consider the idealizations used for the analyses of the dynamic and internal loads, shown in Figures 2-32 and 2-33. Each of these idealizations was designed for the analysis to be made in one computer run.

Dynamic responses and external loads were obtained by using the idealization model shown in Figure 2-32. The spar-shear-tie system of the out-of-plane panel was represented as a single spar, six rigid shear ties, and an axial member (note that each individual panel is not represented in explicit detail; rather, the sum of its effects along with that of other panels is used to construct an equivalent but simpler element).

The idealization shown in Figure 2-32 was used to calculate the center-spar internal loads resulting from out-of-plane vibration responses. Note that only the mobility of the points at Stations 10.1, 123.7, and 169.9 are common to both idealizations. Station 10.1 was considered to be a simple pinned support, whereas Stations 123.7 and 169.9 were considered as simple spring supports with no coupling between springs.

It was discovered that the deflections at the spring boundaries of Figure 2-32 did not agree with those predicted by the second dynamic analysis based on Figure 2-33. The springs at Stations 123.7 and 169.9 are coupled, not independent as was originally assumed.

A reanalysis of the internal loads was made on the basis of the stiffness characteristics of Stations 123.7 and 169.9, taken from the second dynamic analysis. The results of this analysis indicate that the internal loads for the center-spar design were found to be unconservative below Station 110. All other structural elements of the LASA design are conservatively sized.

Figure 2-34 compares the deflected shape of the center spar for the original loads analysis, as well as the latest dynamic and internal loads analyses.

The center-spar gages shown in Table 2-8 have been resized. The change resulted in a weight increase of only 12 pounds.
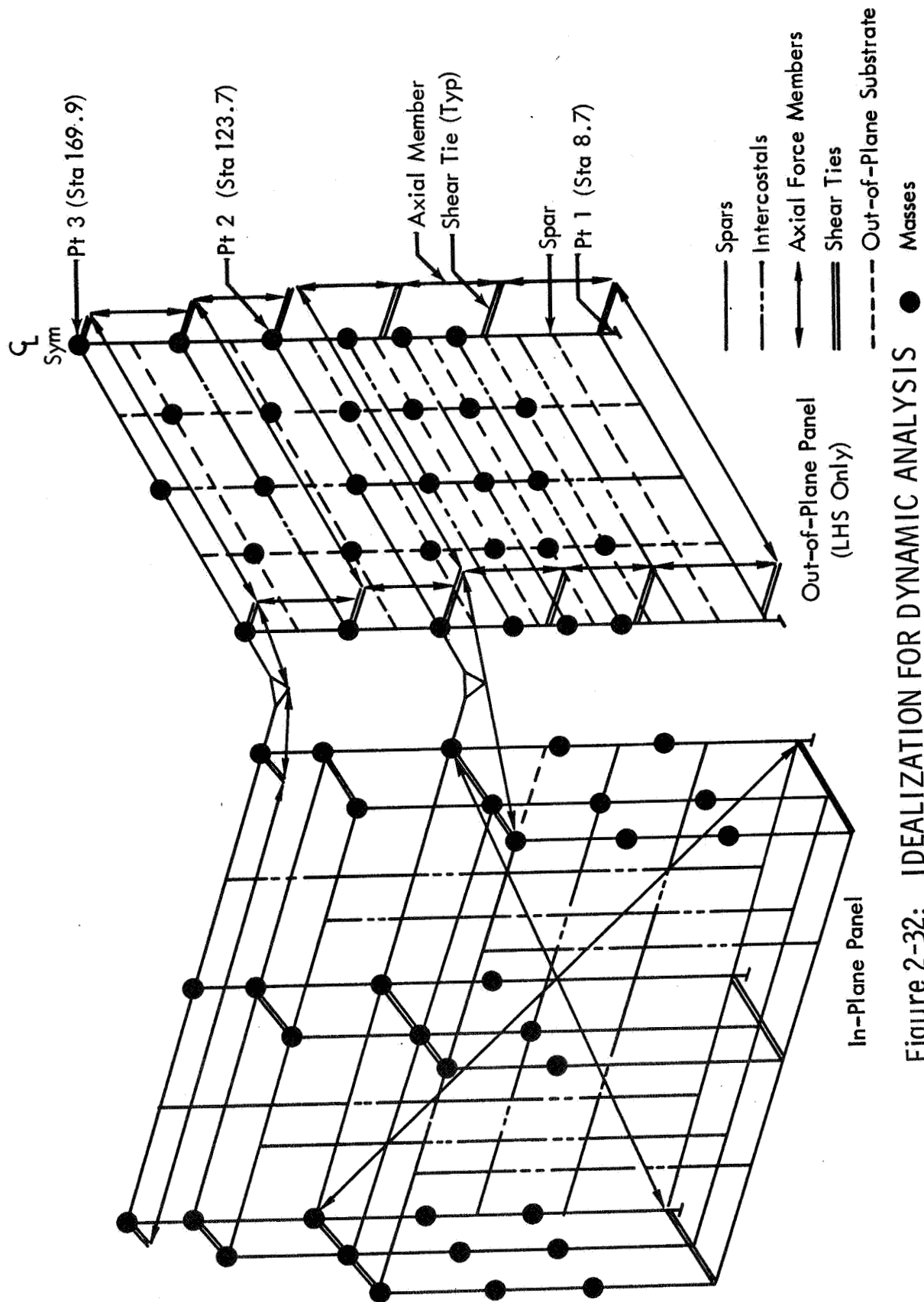
Figure 2-32: IDEALIZATION FOR DYNAMIC ANALYSIS
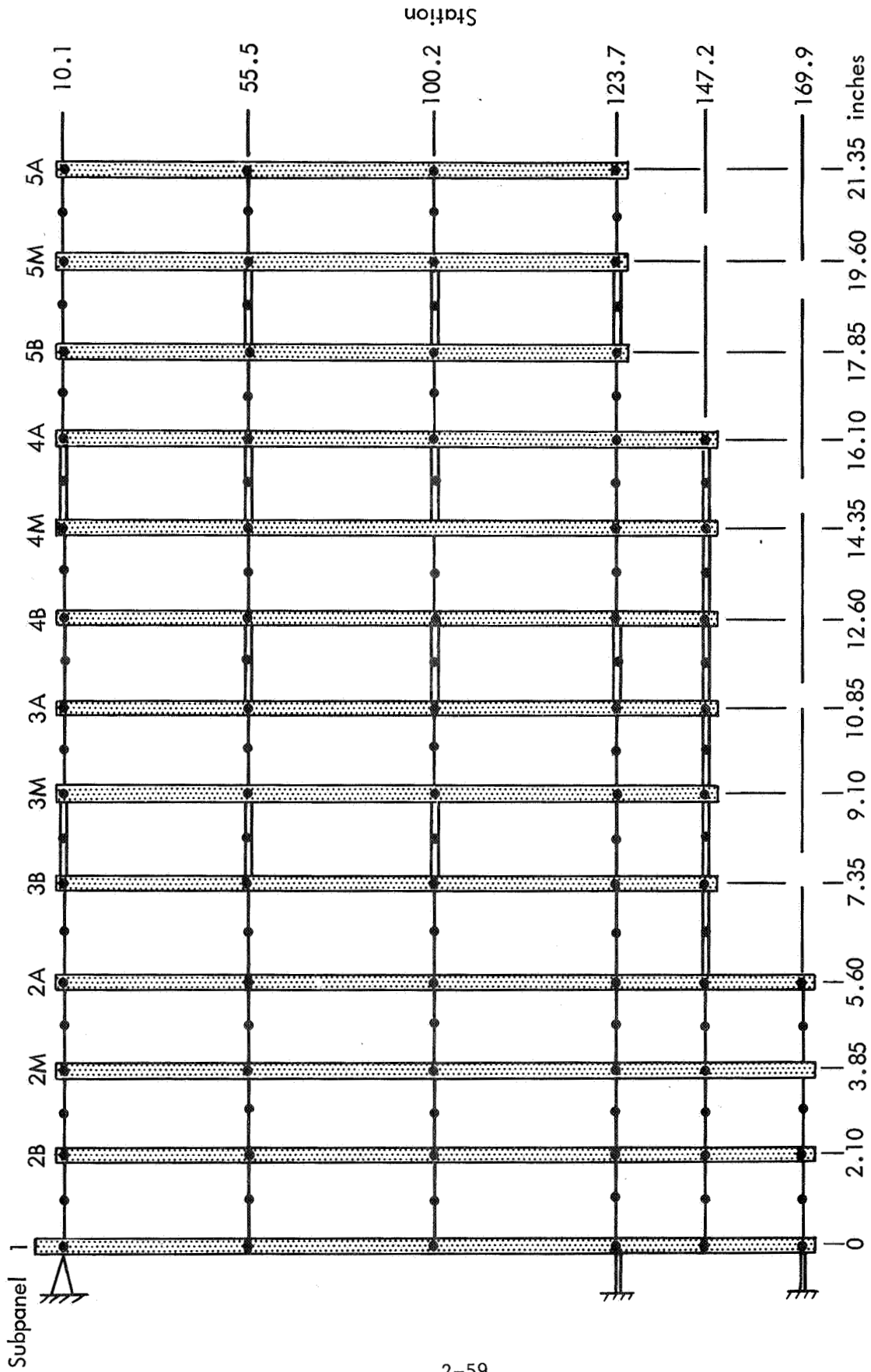
Figure 2-33: IDEALIZATION FOR INTERNAL LOADS ANALYSIS
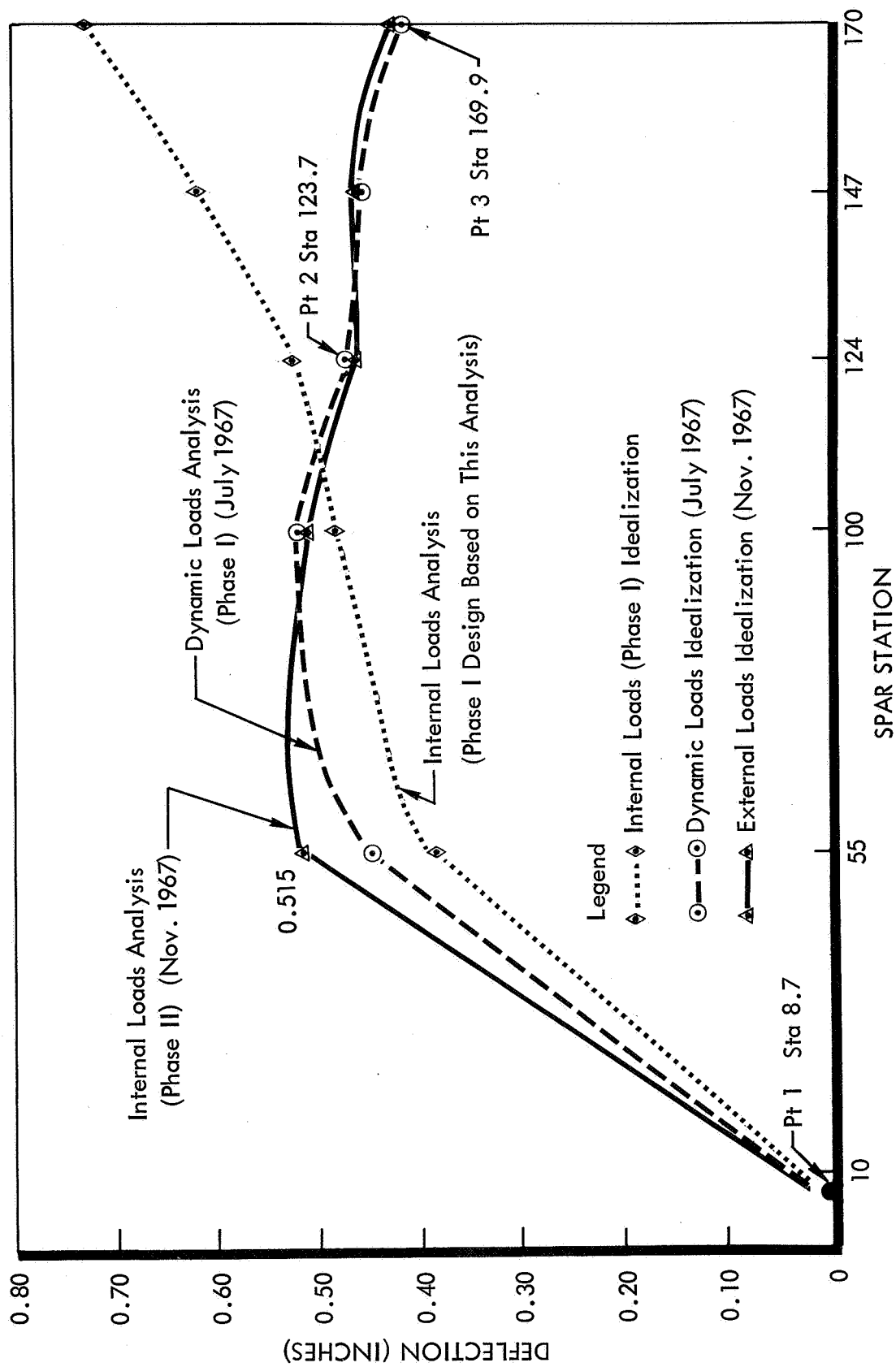
Figure 2-34:   COMPARISON OF CENTER-SPAR DEFLECTIONS

Table 2-8: MTA-4 CENTER-SPAR CHANGES

Subpanel No.	Phase I Design t Cap (in.)	h Chan (in.)	11/67 Design Load Requirements t Cap (in.)	h Chan (in.)	Weight Change per Panel Assembly (lb)
2B	0.025	0.694	0.050	0.662	0.546
2M	0.025	→	0.035	0.694	0.218
2A	0.020		0.035	→	0.326
3B – 4A	→		0.035		1.689
5B			0.030		0.155
5M			0.025		0.078

$$\sum = 3.012 \text{ lb/ Panel Assembly}$$

2.5.4 THE BOOST TIEDOWN SYSTEM

The boost tiedown system requires a tie at six locations to stiffen the panel assembly.

The boost tiedown system (see Figure 2-35) provides a circumferential method of binding the four solar panels of the array into a semirigid structure that will withstand the rigors of the launch environment. Subpanel 1, designed to support 12 subpanels, is supported by the spacecraft with three hinges. The subpanels are tied to Subpanel 1 by a system of shear tie connections held in place by pre-tensioned cables at six selected stations. Each solar panel is under a compression force at 12, 15, or 18 points, depending upon its size. The six circumferential cables working in conjunction with shear members between panels tie all panel assemblies into a single structural unit.

Pre-tensioned center tie cables maintain the shear teeth in engagement along the center spar. There are four, five, or six of these ties, depending upon the panel size. Figure 2-36 shows the center tie fittings at Station 123.7.

The primary load paths between the four solar panels of the array are at Staions 123.7 and 169.9. The fittings at the corners between adjacent panels can carry both in-plane and out-of-plane loads. The other four tiedown stations carry out-of-plane loads.

The boost tiedown system requires machined titanium fittings at primary tiedown Stations 123.7 and 169.86 and at intermediate tiedown Stations 10.5, 55.46, 100.15, and 147.24 on Subpanel 1 to react the cable preloads into the subpanel structure. The intermediate tiedown fittings are located within the outboard spar assemblies on the dark side only. Each fitting has an integrally machined shear bulkhead to efficiently react the tiedown cable preloads. Electron-beam (E-B) welding is used to attach the titanium closeout caps to the machined fittings.

Station 123.7 tiedown fitting is a primary tiedown on Subpanel 1. Integral machined lugs extend from the dark-side titanium fitting to provide the load path for tiedown loads into the outboard spar, lateral spar, and diagonal brace. A sun-side shear tie fitting has been incorporated at Station 123.7 to provide structural capability to react compression loads through the shear ties from the tiedown preload and to react dynamic shear loads between Subpanels 1 and 2.

2.5.5 STRUCTURAL ANALYSIS OF BOOST TIEDOWN SYSTEM

The boost tiedown system was modified in the third quarter to reduce internal loads and spar weight.

The boost tiedown system serves three functions: (1) a suitable way to preload the subpanels so that separation does not occur during boost,
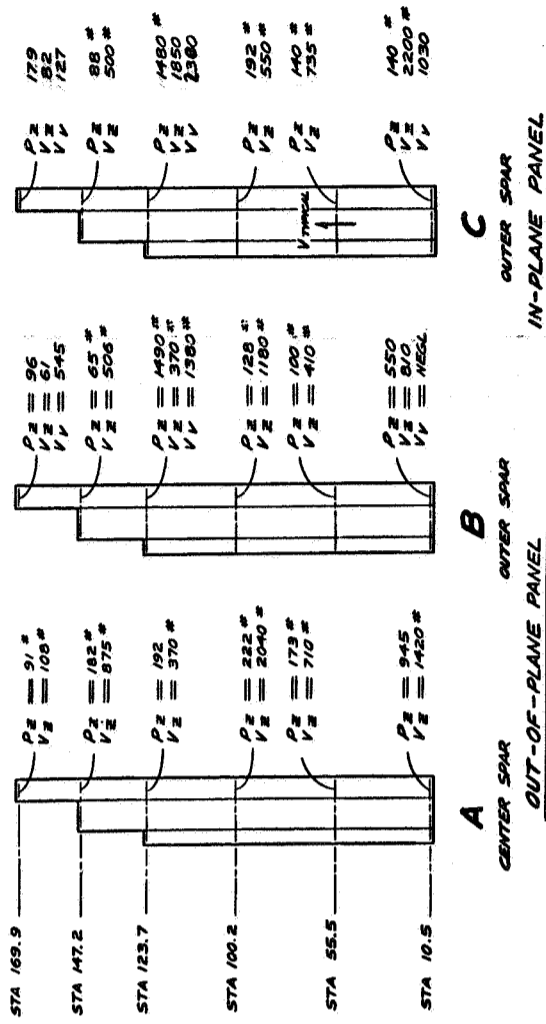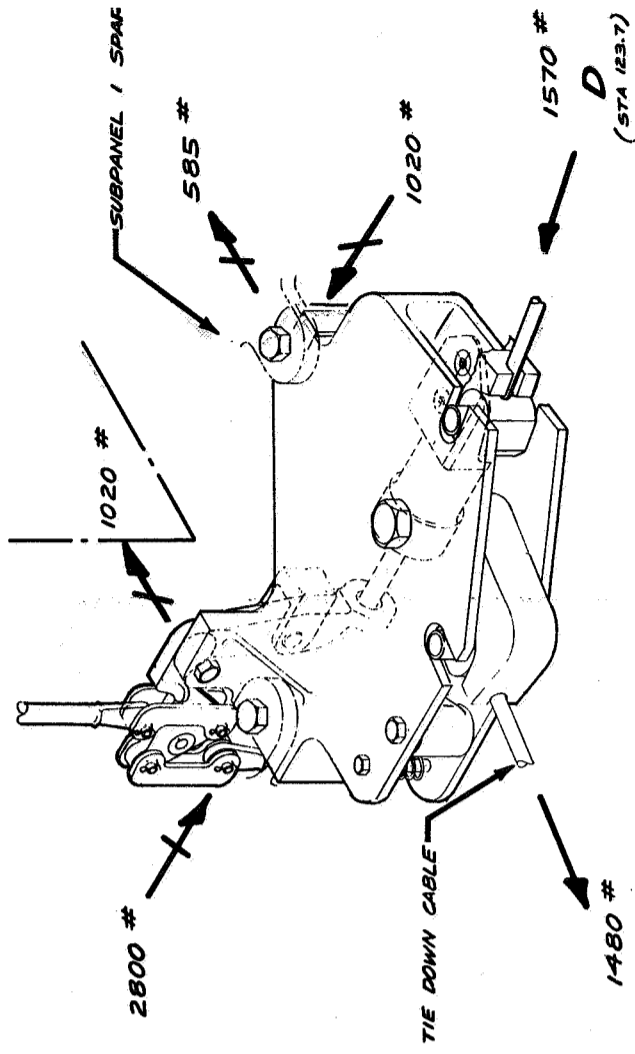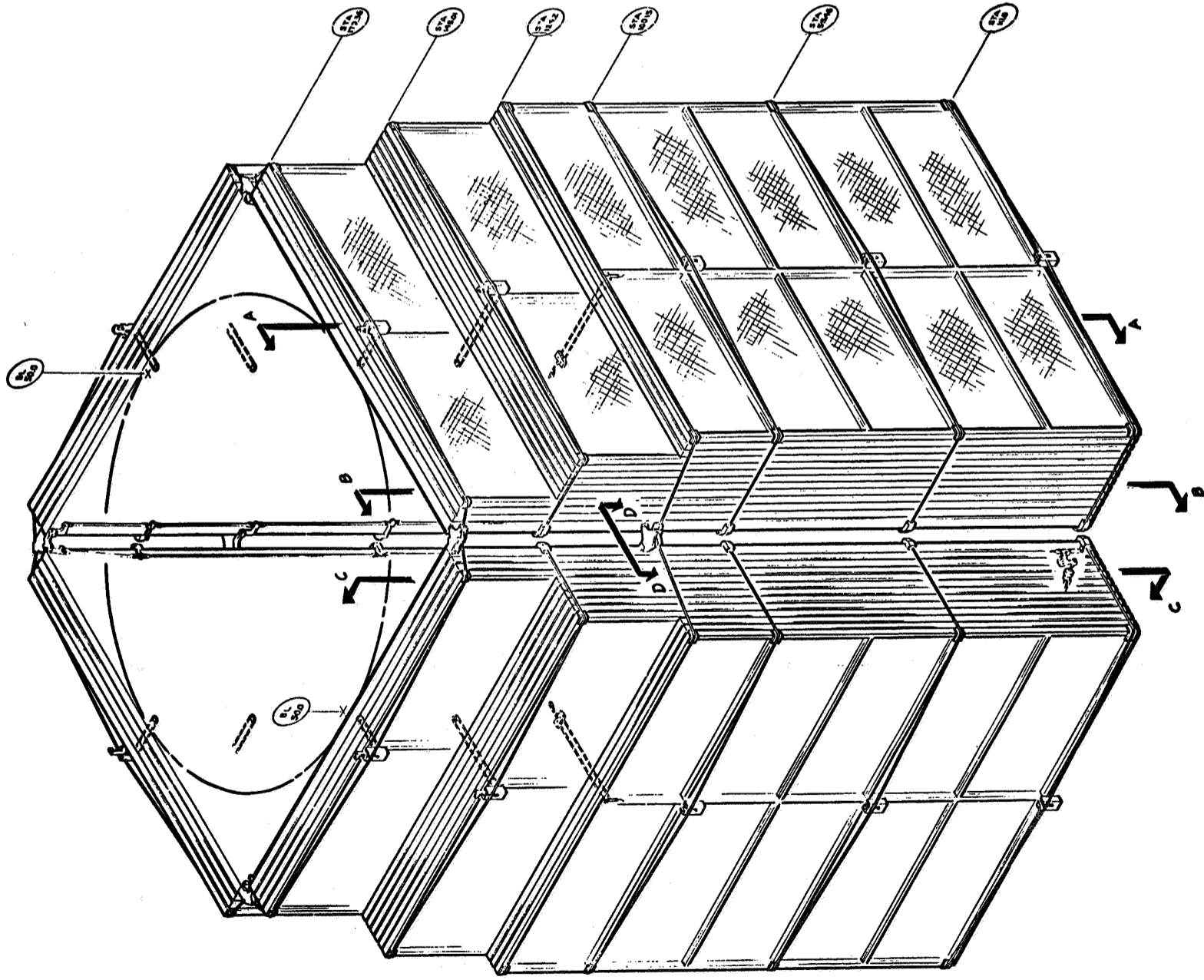
Figure 2-35: BOOST TIEDOWN SYSTEM

2-63
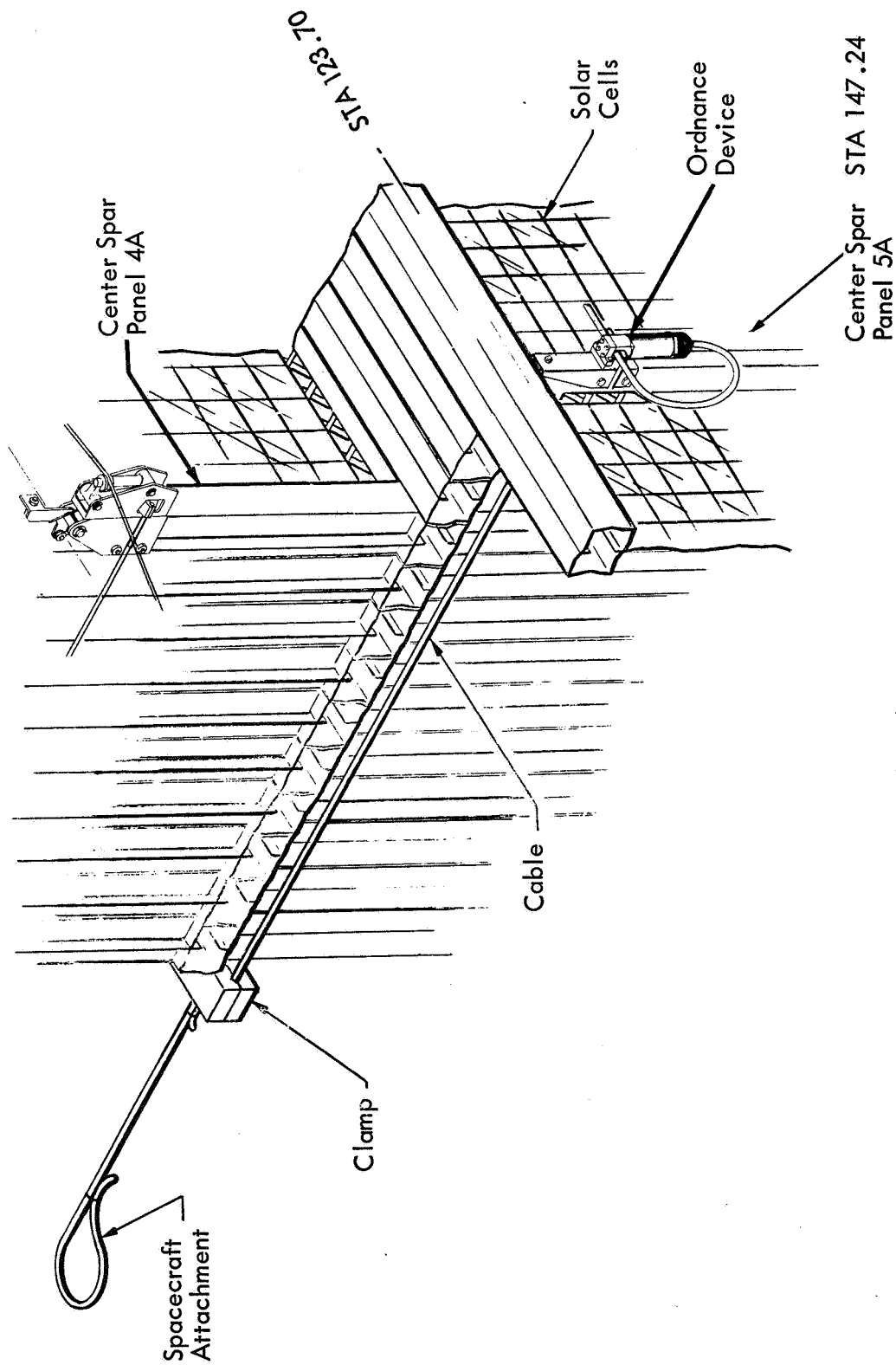
Figure 2-36: CENTER SPAR TIEDOWN
STA 123.70 & STA 147.24

(2) efficient of transmission of internal loads, and (3) a reliable release system required for panel deployment.

The structural efficiency of the primary tiedown system is shown by the reduction of lateral spar internal loads and weight. Figure 2-37 compares the internal moment and lateral spar weight for two types of tiedown systems lateral spar corner details. The basic difference between the two systems lies in the type and manner of fixity provided to each fitting. In the baseline type of corner detail (Type 1), a single pin was provided at the intersection of the neutral axis for the two adjacent Subpanel 1 members, and a full fixity was provided at Section A-A, representing the interface between the fitting and Subpanel 1. This structural arrangement resulted in excessive moments at Section A-A and within the subpanel lateral spars, as a result of the large distance between the pin and Section A-A. By locating two pins much closer to the interface Section A-A (as shown for Type 2), it was possible to reduce significantly the moments at the fitting-to-spur interface and throughout the lateral spar system. The net weight savings due to this reduction in internal loads is 10 pounds per array.

Figure 2-35 shows internal load characteristics of the new tiedown system. In particular, the loads are for a 1.5-g lateral sinusoidal vibration input. P_z-loads are the maximum normal loads that act between subpanels. The V_z loads are the maximum shear loads that act at the shear ties along the axis of the outer and center spars; the V_1 loads are the maximum shear loads that act at the shear ties, which are oriented along the axis of the lateral spars. A typical distribution of the tiedown cable loads and pin reactions is shown at Section D-D for the new corner fitting at Station 123.7. One of the cable loads is shown acting in compression; however, because these loads are representative of only the alternating vibration-load component, they will be prevented from going into compression by a sufficient preload.

The preload requirements for the modified tiedown system have been established, and are identified in Figure 2-38. The requirements are established by ensuring that no cable goes into compression during vibration; that all shear ties have a positive clamp-up load during vibration; and that excessive deformation does not cause the release system to function accidentally during boost vibration. Once these requirements have been established, a safety factor of 1.25 is applied to the preload value that will just meet the requirements stated above. This new value is then defined as the limit-load condition for the preload component.
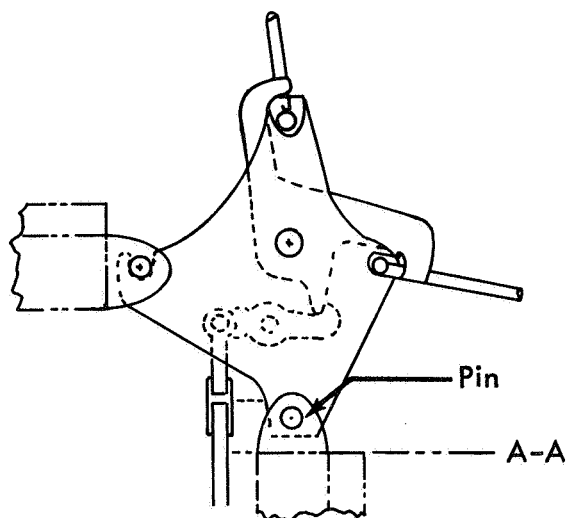
EXISTING TIEDOWN SYSTEM
LATERAL SPAR CORNER DETAIL

TYPE 2
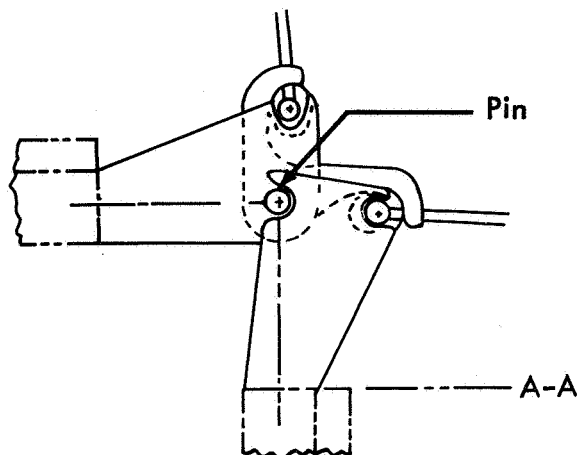
BASELINE-TYPE TIEDOWN STYSTEM
LATERAL SPAR CORNER DETAIL

TYPE 1

Parameter \ Type Of Tiedown	Baseline-Type Tiedown Type ①	Existing Type Of Tiedown Type ②	Ratio Of ①/②
Maximum Moment At Fitting To Subpanel 1 Interface (A-A) In-Lbs	16000	4000	4.0
Maximum Lateral Spar Moments (Total For Subpanel Unit) In-Lbs			
Subpanel 1	11800	5900	2.0
Subpanel 2	13100	10500	1.3
Subpanel 3	7350	6500	1.1
Subpanel 4	7200	6500	1.1
Subpanel 5	6800	8300	0.8
LATERAL SPAR WEIGHT DIFFERENCE PER ARRAY DUE TO HIGHER LOADS IN TYPE ① TIEDOWN IS 10 LBS.			

Figure 2-37:   COMPARISON OF TIEDOWN SYSTEM
STRUCTURAL EFFICIENCY

P (Center Spar)

P (Outer Spar)
(Typical)
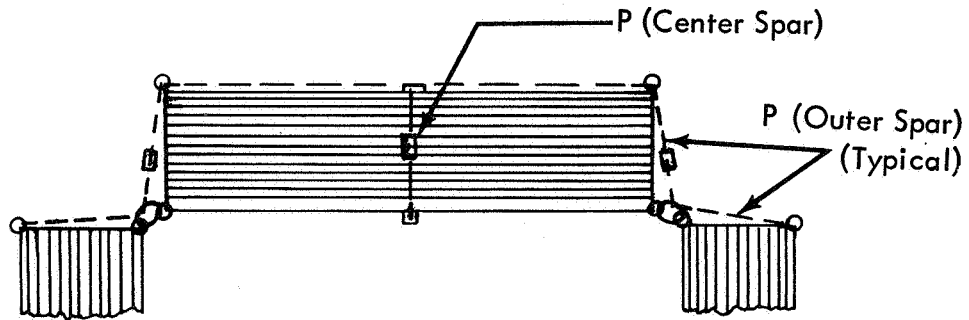
| Tiedown Station | Outer Spar Cable Preload | | Center Spar Cable Preload |
	Type Of Tiedown	P (Outer Spar) (lb)	P (Center Spar) (lb)
10.5	Intermediate	755	1090
55.5	Intermediate	240	280
100.2	Intermediate	288	455
123.7	Main	2240	272
147.2	Intermediate	154	216
169.9	Main	288	115

Figure 2-38:   TIEDOWN PRELOAD REQUIREMENTS

2.5.6 SHEAR TIE DESIGN

The shear teeth and compression pads are required to provide satisfactory load paths between subpanels.

The boost tiedown system preloads the stowed subpanels to make them act as a structural unit during boost. The primary shear transfer members are the titanium shear tie fittings (including shear teeth and compression pads) between each of the 13 stowed subpanels. This arrangement provides shear continuity from outboard Subpanel 5A to inboard Subpanel 1. Figure 2-39 shows the locations of the shear ties and the number of shear teeth at each location. The Z shear teeth and X-Z shear teeth indicate the load direction capability at each location.

An X-Z shear tie joint assembly is shown in Figure 2-40. The titanium compression pad-angle serves also as a shear clip to transmit shear from the lateral spar to the outboard spar.

Figure 2-41 shows a typical shear tie assembly cross section. The shear teeth fittings are machined with a multiple-tooth cutter that provides minimum additive tolerances in the teeth. The shear teeth and compression pads are machined from 6A1-4V titanium plate and bonded with AF-126 epoxy adhesive. The shear tie assembly provides a direct load path through the stack and minimizes compression loading of the beryllium spar cross section.

Alignment of the shear teeth during the bonding assembly sequence is a critical manufacturing operation. Frame subassembly jigs and a controlled manufacturing sequence align the shear tie assemblies during the bonding operation. The shear teeth are independent fittings that can be adjusted and shimmed on three axes to match the adjoining subpanel during the bonding operation.

2.5.7 STRUCTURAL ANALYSIS OF SHEAR TIES

Shear ties were designed to minimize local loads on beryllium spars.

The shear ties transmit shear loads and normal loads through the panel stack and provide the shear continuity necessary to stiffen the panels. To satisfy the first requirment, shear ties are located both along the longitudinal outer and ceter spars and along the lateral spars and edge members, and are thus capable of resisting multidirectional loads. Figure 2-42 shows a typical cross section for a shear tie mated to a beryllium spar section and indicates how the beryllium spar is bypassed while carrying a normal load through the section. The normal loads will be carried through the titanium feet, thus relieving the beryllium channels from sustaining high localized bending and crushing stresses. The location of shear ties throughout the panel assembly was dictated by the need for sufficient stiffness to meet envelope requirements without undue increases in structural weight.

⊖ = Z-Shear Teeth

⊕ = X-Z Shear Teeth

STA 169.86

STA 147.24

STA 123.70

STA 100.15

MTA-2

MTA-1

STA 55.46

STA 10.50

Unit #5   Unit #4   Unit #3   Unit #2   No. 1

PANEL ASSEMBLY — MTA-4

Z

X ← → X

4 — 2 — 4
3 — 2 — 3
5 — 4 — 5
3 — 2 — 3
3 — 2 — 3
4* — 2 — 4

Z

*Nos. indicate qty of individual teeth ftgs at each location. ▷2
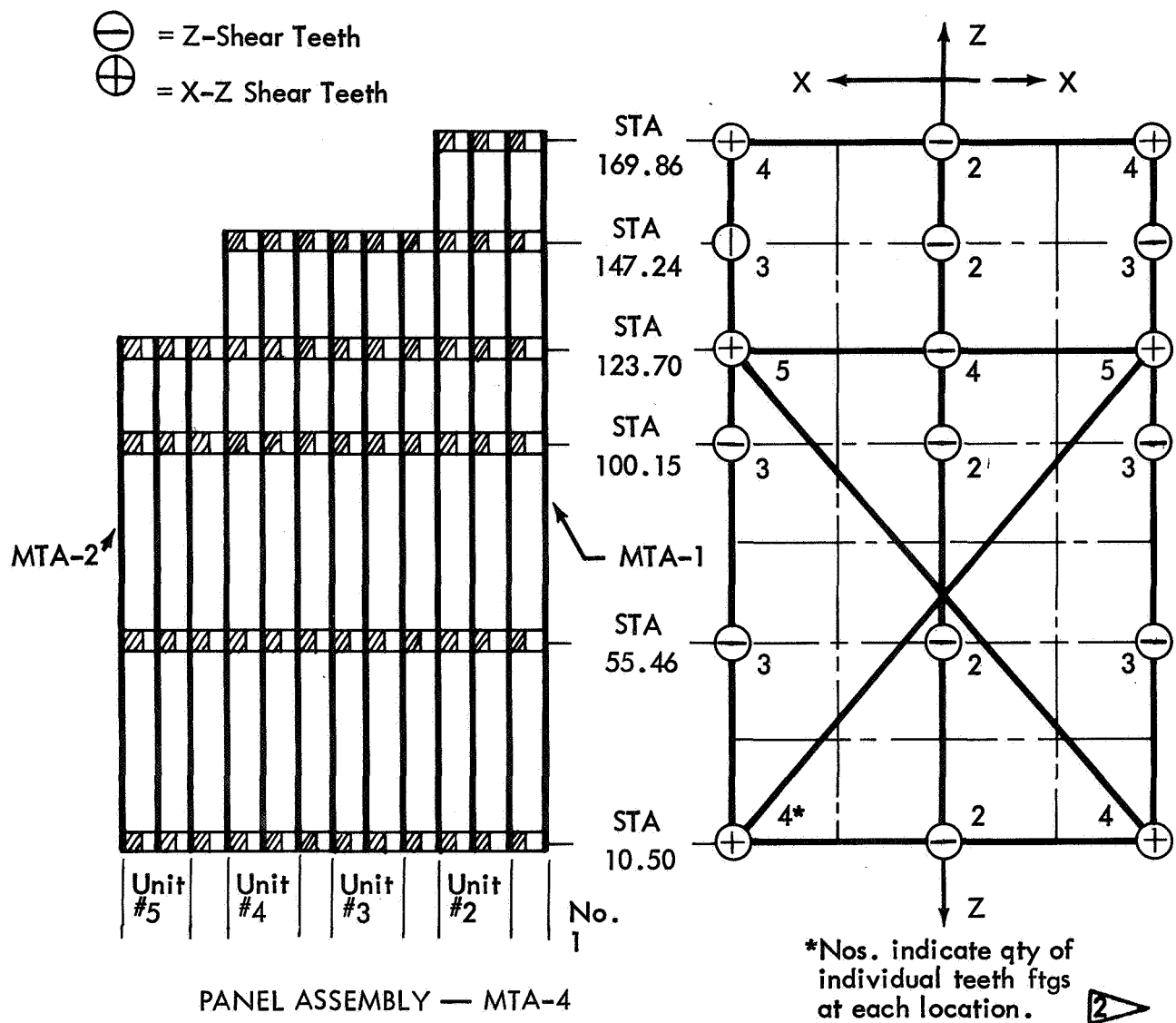
Panel No.	No. of Locations ▷1		No. of Shear Teeth	
	⊖	⊕	⊖	⊕
MTA-1	12	6	32	26
Subpanels No. 2 thru No. 5	126	54	646	500
Total	138	60	678	526

▷1 Each location includes the Sun side & dark side.

▷2 The quantity indicates number of teeth per side of each subpanel that has mating subpanel teeth.

Figure 2-39: SHEAR-TIE LOCATIONS
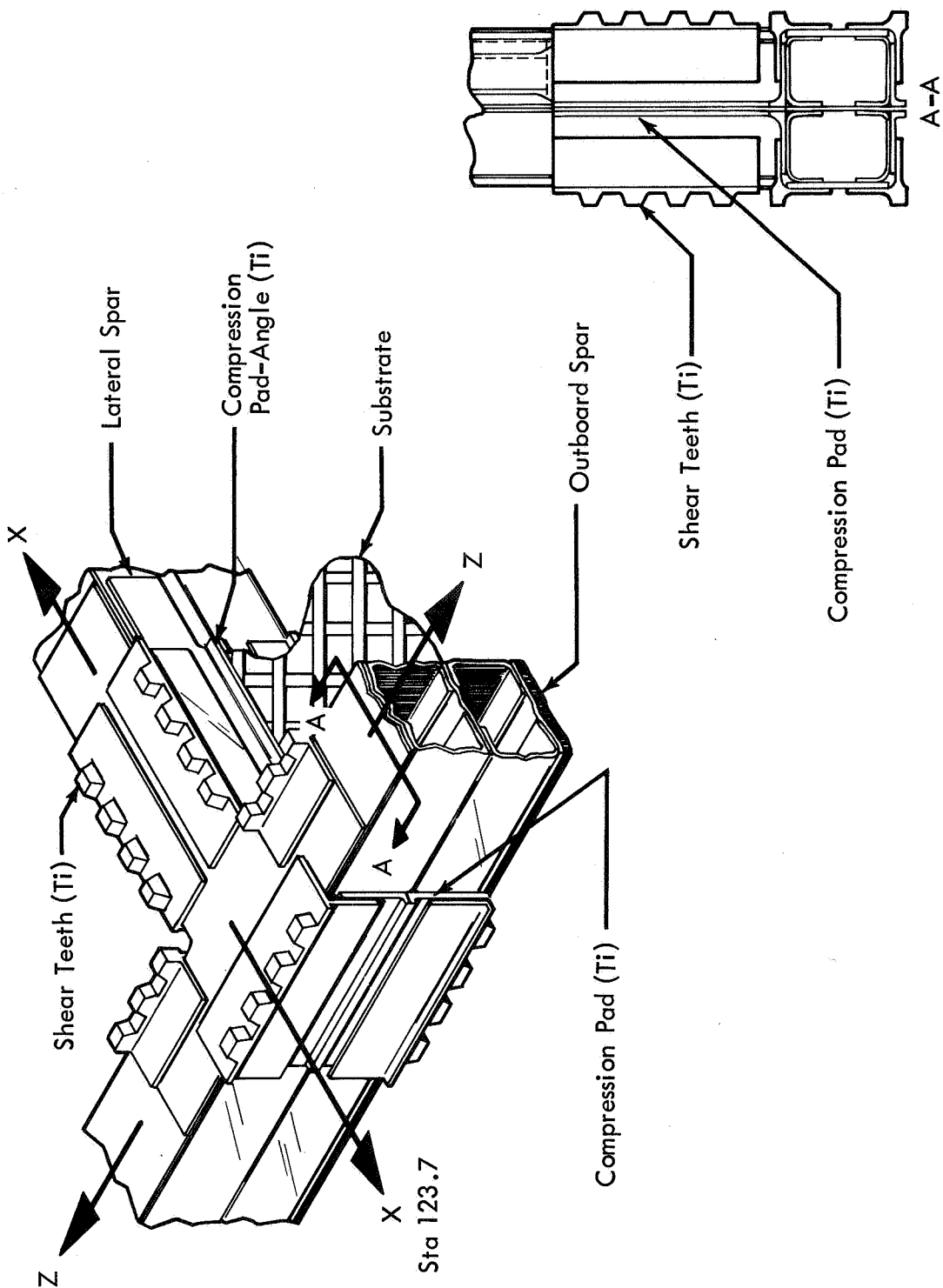
Figure 2-40: SHEAR-TIE FITTINGS AND JOINTS
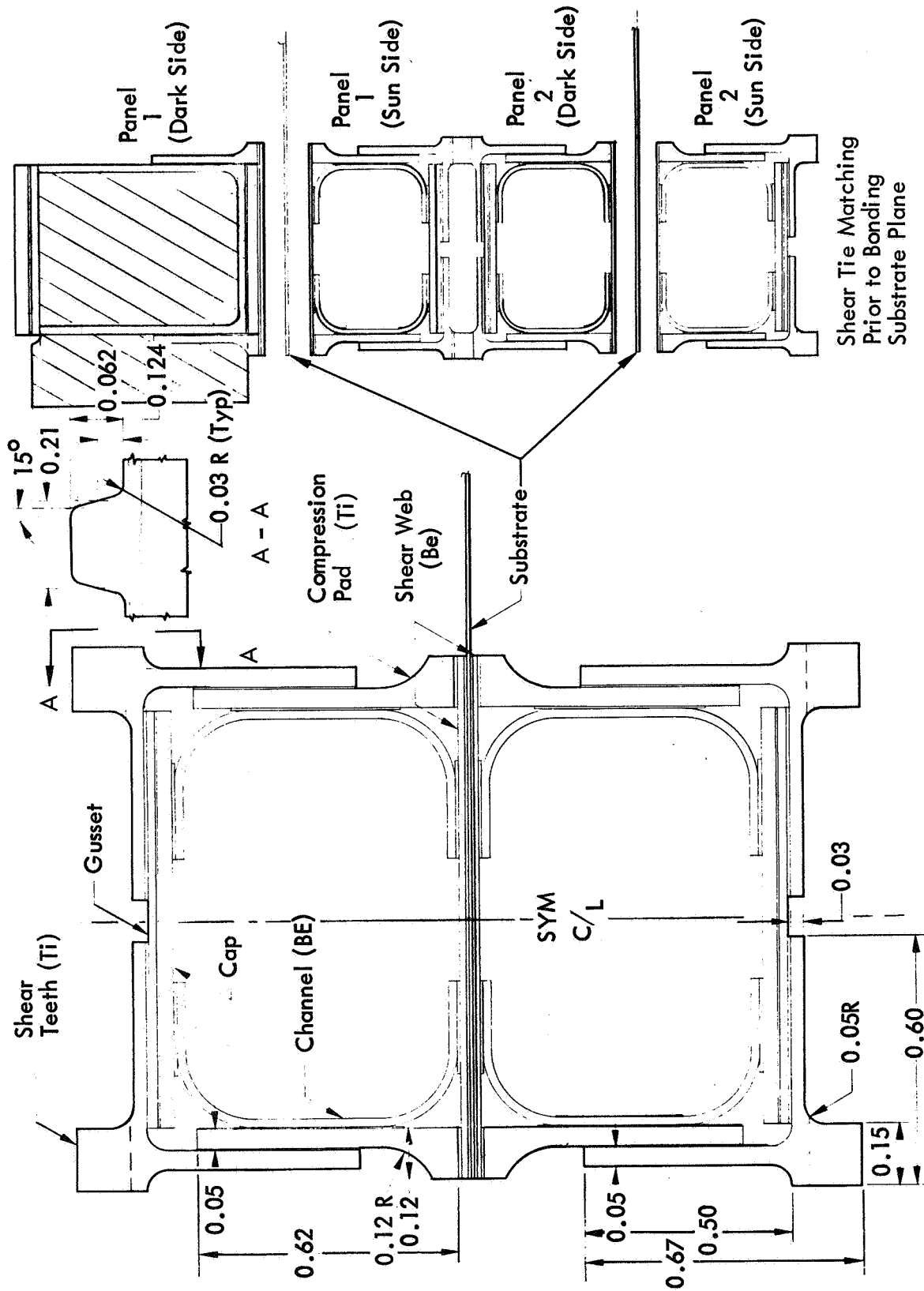
Figure 2-41:   SHEAR-TIE CROSS SECTION
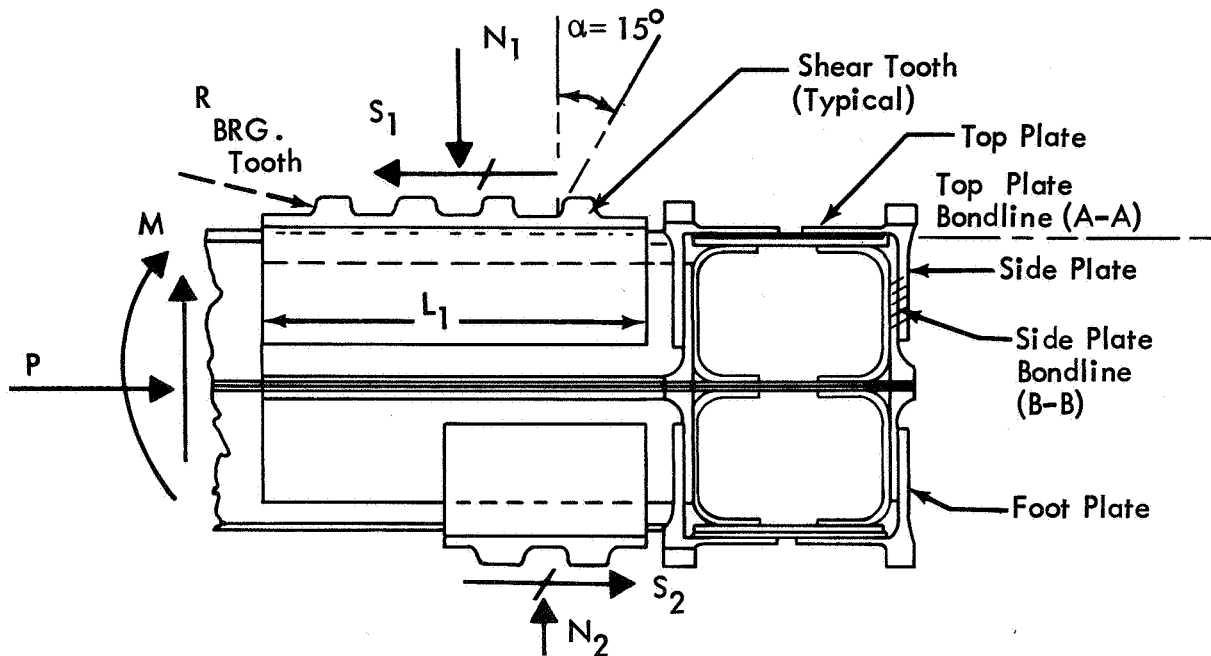
ITEM	MATERIAL	DESCRIPTION	ULTIMATE LOAD CAPABILITY (Lb/Sq In.)
Shear Teeth	6Al-4V Ti (Annealed)	Tooth Bearing Stress Governs Bearing Load Per Tooth $R_{BRG.\ Tooth} = F(N,S,m,\alpha,f)$	$R_{BRG.\ Tooth} = 1380$
Top Plate Bonding (Bondline A-A)	Adhesive BMS 5-51	L_1 Determined by Bond Strength Requirement Between Top Plate and Gusset	$S_{ULT} = 1950$
Side Plate and Foot Plate	6Al-4V-Ti (Annealed)	Combined Axial and Bending Stress Limited by Fey = 126,000 psi	$N_{ULT} = 2700$
Side Plate Bonding (Bondline B-B)	Adhesive BMS 5-51	Bond Length Requirement	$N_{ULT} = 2700$

NOMENCLATURE

N   Clamp Load
S   Shear Load
m   Number of Teeth per Tie
α Ramp Angle
f   Friction Factor

Figure 2-42: STRESS SUMMARY FOR TYPICAL SHEAR-TIE FITTING

2.5.8   THERMAL DISTORTION

The thermal distortion of the array in the deployed configuration is insignificant.

Figure 2-43 shows a center spar temperature distribution. The temperatures of Elements 2 and 19 essentially determined the curvature of the array. The curvature of the center spar is:

$$\frac{I}{R} = \frac{\alpha \Delta T}{D}$$

Where: α = Coefficient of thermal expansion;

ΔT = Temperature differential of the extreme fibers;

D = Depth of spar;

L = Length

For ΔT being constant length and assuming the beam is cantilevered, the tip deflection and slope are, respectively:

$$\delta \, \text{Tip} = \frac{L^2 \alpha \Delta T}{2RD}$$

$$\theta \, \text{Tip} = \frac{L \alpha \Delta T}{2RD}$$

For the dimensions and temperatures shown in Figure 2-43:

δ Tip = 4.45 inches or approximately 1% of span;

θ Tip = 0.60 degrees.

Such deformations are inconsequential.
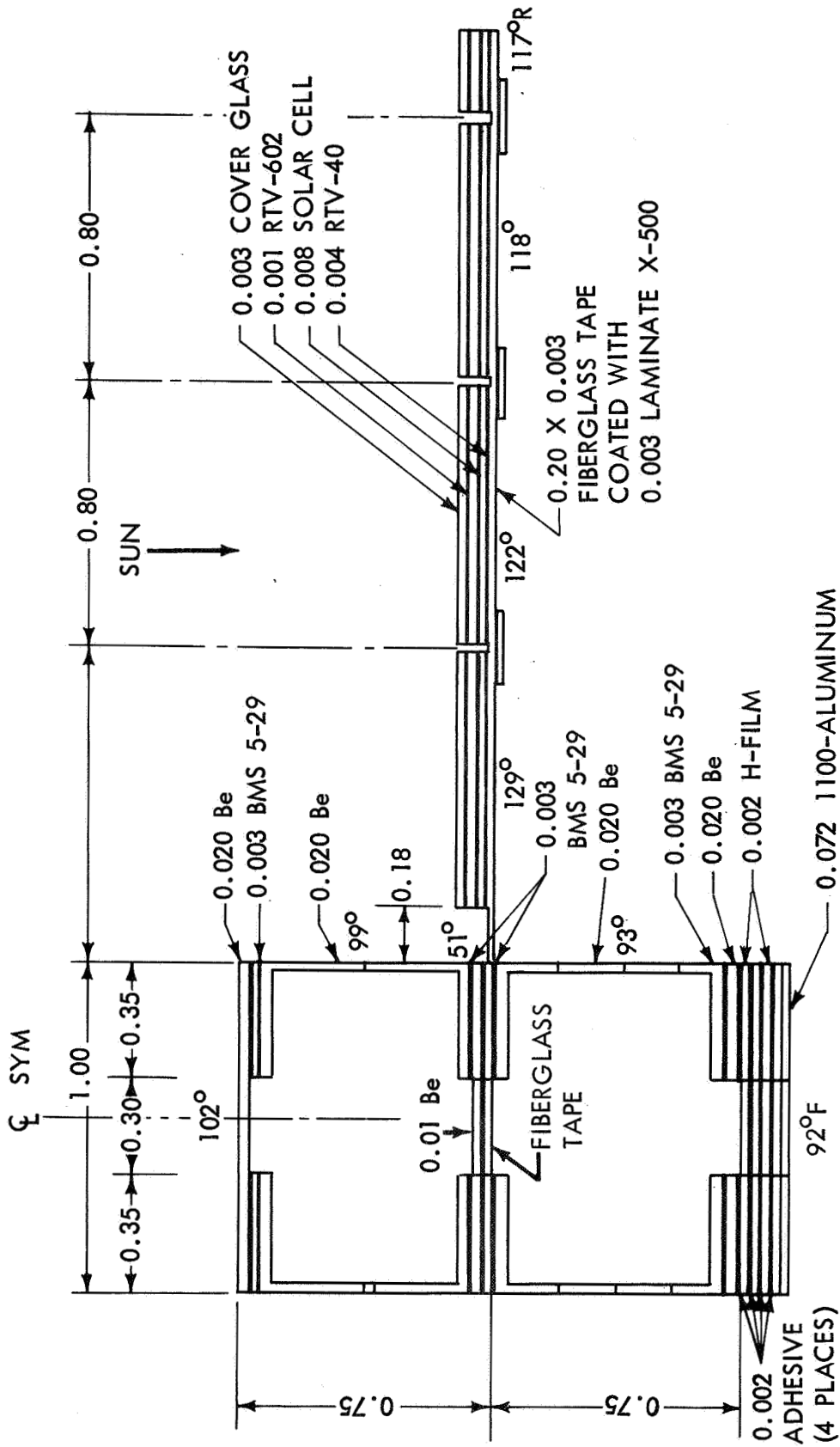
Figure 2-43: CENTER SPAR TEMPERATURE DISTRIBUTION--- DEPLOYED CONFIGURATION - LASA BASELINE

3.0 RELEASE AND DEPLOYMENT IN SPACE

This section describes the solar-array deployment system. The time-history of a solar-panel assembly deploying in space is discussed, and the loads imposed on the structure and mechanisms by the predicted space-deployment motions are analyzed.

3.1 DESCRIPTION OF SOLAR-ARRAY TIEDOWN-RELEASE
AND DEPLOYMENT SYSTEM

Deployment of the solar-array configuration is powered by redundant motors that release subpanels for deployment through sequentially operated mechanical devices.

The solar-array configuration release and deployment mechanisms must, upon command and in proper sequence, extend and lock the array into its deployed position. The release and deployment mechanisms designed to satisfy this requirement have three separate functions: release of the tiedown system, deployment of the main subpanels, and deployment of the auxiliary subpanels.

The release of the tiedown for the four solar-panel assemblies is accomplished simultaneously by the firing of an ordnance pin-release device located at solar panel Station 123.7. This device releases all tiedowns except the one on the center spar at Station 123.7.

Figure 3-1 shows the release mechanisms at Stations 123.7 and 169.86. The release of the tiedown structural system is activated by four primary ordnance pin-release devices that release a mechanical train at each of the four corners.

Five of the six center-spar tie cables are released mechanically by the circumferential cable, as shown in Figure 3-2. The individual cables are pre-tensioned prior before the solar panel is fitted to the space-craft on the pad. A clamping device keeps the cables taut until it is released by the circumferential cables.

The sixth center spar tie, also shown in Figure 3-2 and located at Station 123.7, is pre-tensioned before panel installation. This tie is released by firing an ordnance-actuated cable cutter simultaneously with actuation of the deployment motor after all other ties have been released and circumferential cables have been ejected. The sixth tie prevents inadvertent partial deployment of the solar subpanel stack during the coast period and acts as a clamp during boost. The firing of the cable cutter ordnance and actuation of the deployment motor initiates deployment.

STA 123.70

STA 169.86
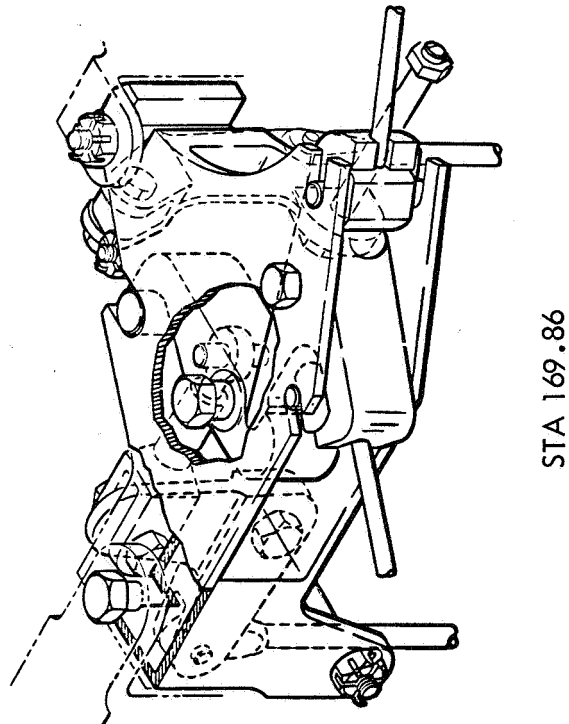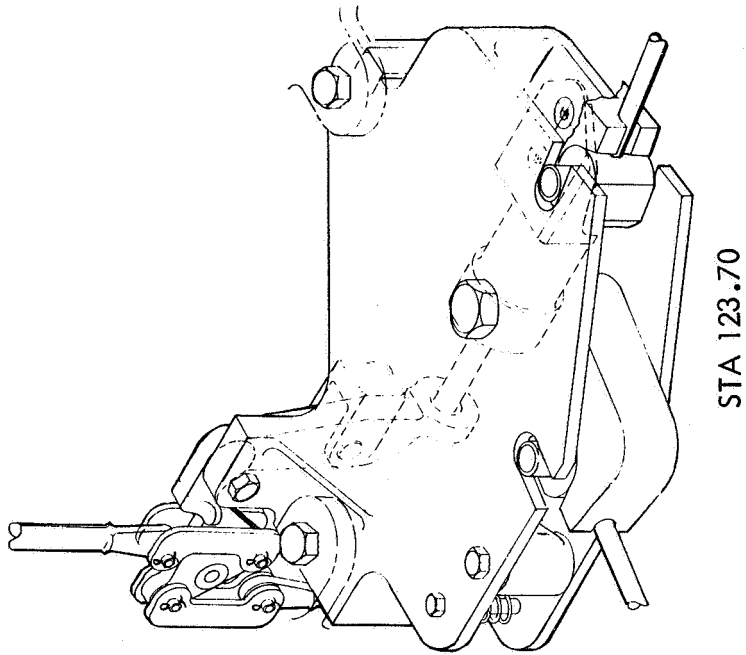
Figure 3-1: MAIN BOOST TIEDOWN

STA 123.7

Circumferential
Cable
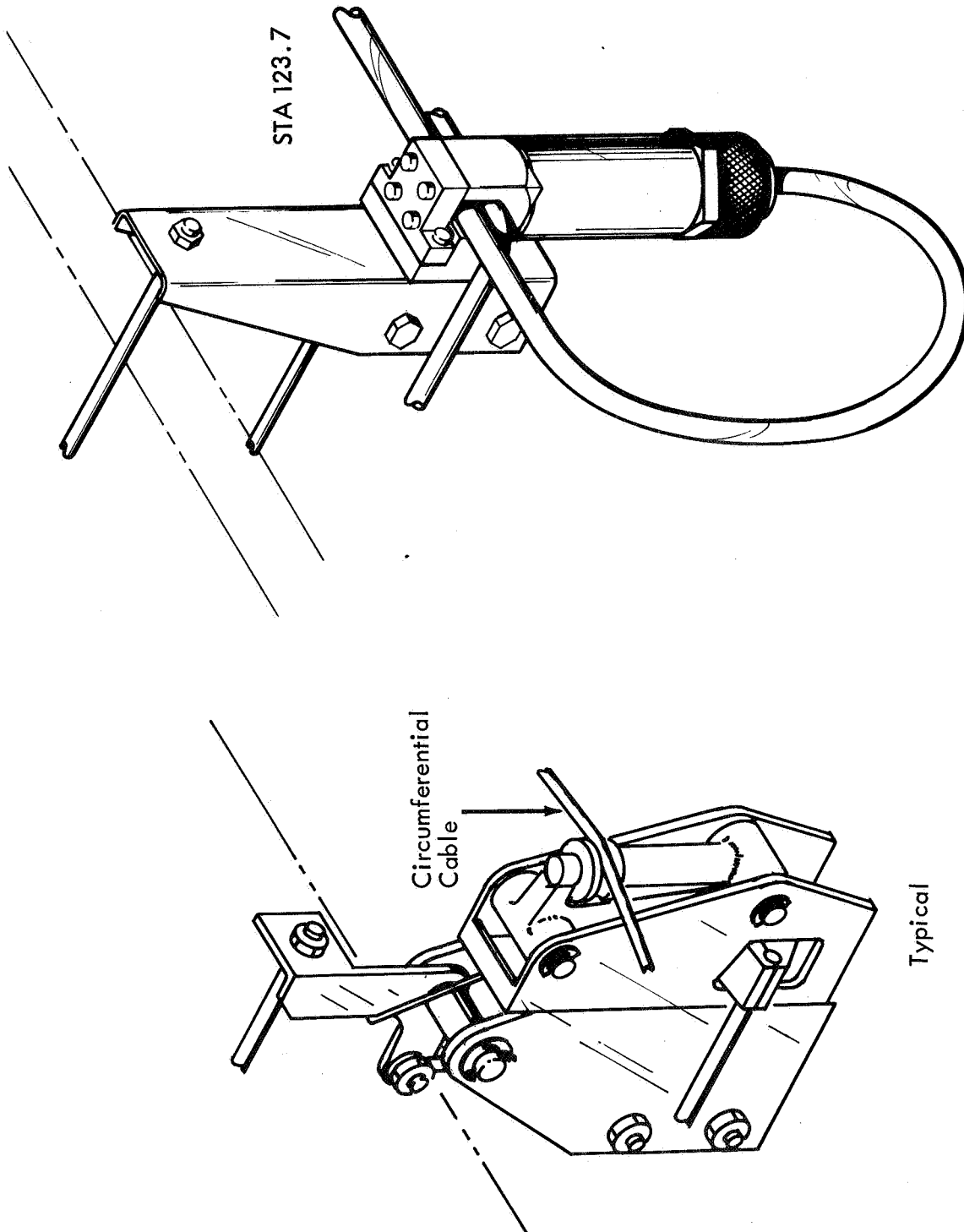
Typical

Figure 3-2:   TYPICAL CENTER SPAR TIEDOWN AND RELEASE

The main subpanel deployment system consists of four deployment motors located within the spacecraft envelope, as shown in Figure 3-3. The deployment cables are rigged so that diametrically opposite panels are driven by two motors operating in parallel. Each motor operates as the primary drive for the panel assembly mounted adjacent to the motor and, in addition, each motor serves as the backup drive for the panel assembly mounted opposite.

The deployment motor (Figure 3-4) includes a globe-type SS subminiature dc motor, rotating at 7,850 rpm as a prime mover. The winch drum must rotate at 0.265 rpm to produce the required cable rate of 2 inches per minute. The required overall transmission ratio is 7,850:0.265 = 29,622:1. This ratio is obtained in two stages:

1)   185:1 (approximate)---hermetically sealed harmonic drive and plane-
     tary first stage;

2)   160:1---harmonic-drive second stage.

The motor drives the input to the first stage, which is a ball planetary-type wave generator. The output is the circular spline, and the bell-cup shaped, hermetically sealed flexspline is held rotationally stationary.

As subsequent main subpanels are deployed, the previous auxiliary sub-panels hinged on the side of the main subpanels are sequentially unlatched and deployed by torsion springs. The rate of deployment near the latch-ing position is controlled by a small rotary damper. When the auxiliary subpanel reaches the deployed position, an overcenter latch snaps into place, locking the panels in a flat plane.

The direction of deployment of all 13 subpanels is indicated in Figure 3-5.

3.1.1   STRUCTURAL ANALYSIS OF RELEASE MECHANISM

The release mechanism was improved by changing from a simple mechanism requiring many ordnance devices to a more sophisticated mechanical system requiring only a few ordnance devices.

The required number of tiedowns necessitated an increase in the number of ordnance devices for the earlier and mechanically simple mechanism. This increase, in turn, decreased operational reliability.

A more sophisticated mechanical system for release was devised that would require only a few ordnance devices: a chain of mechanical (linkage) events was considered to be more reliable than a similar chain of ordnance events.
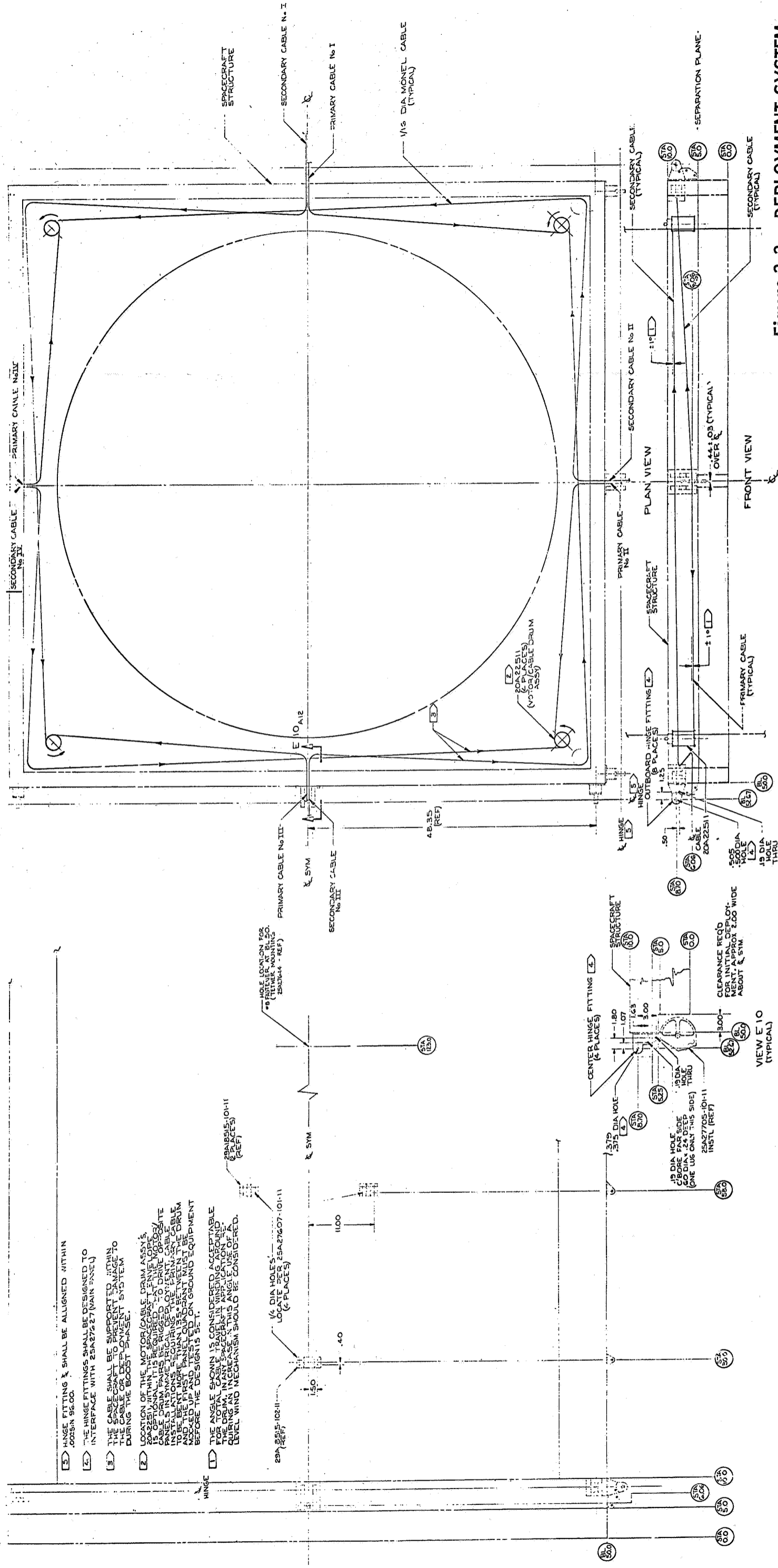
Figure 3-3: DEPLOYMENT SYSTEM

Motor

Thermistor Location

Ball Planetary
Wave Generator

Circular Spline
Second Stage

Hermetically Sealed
Flexspline

Second Stage Wave Generator
First Stage Circular Spline
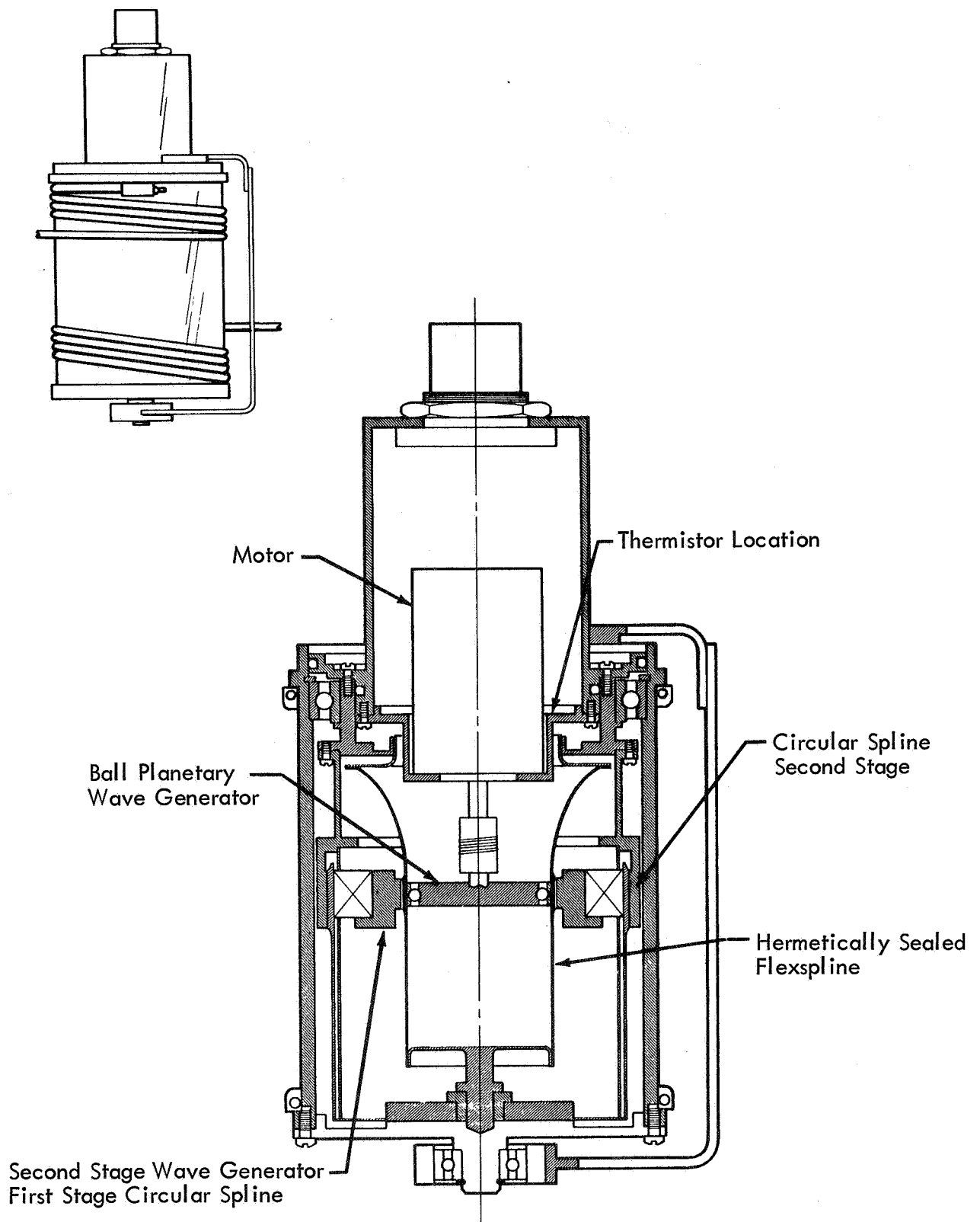
Figure 3-4:   ARRAY DEPLOYMENT DRIVE
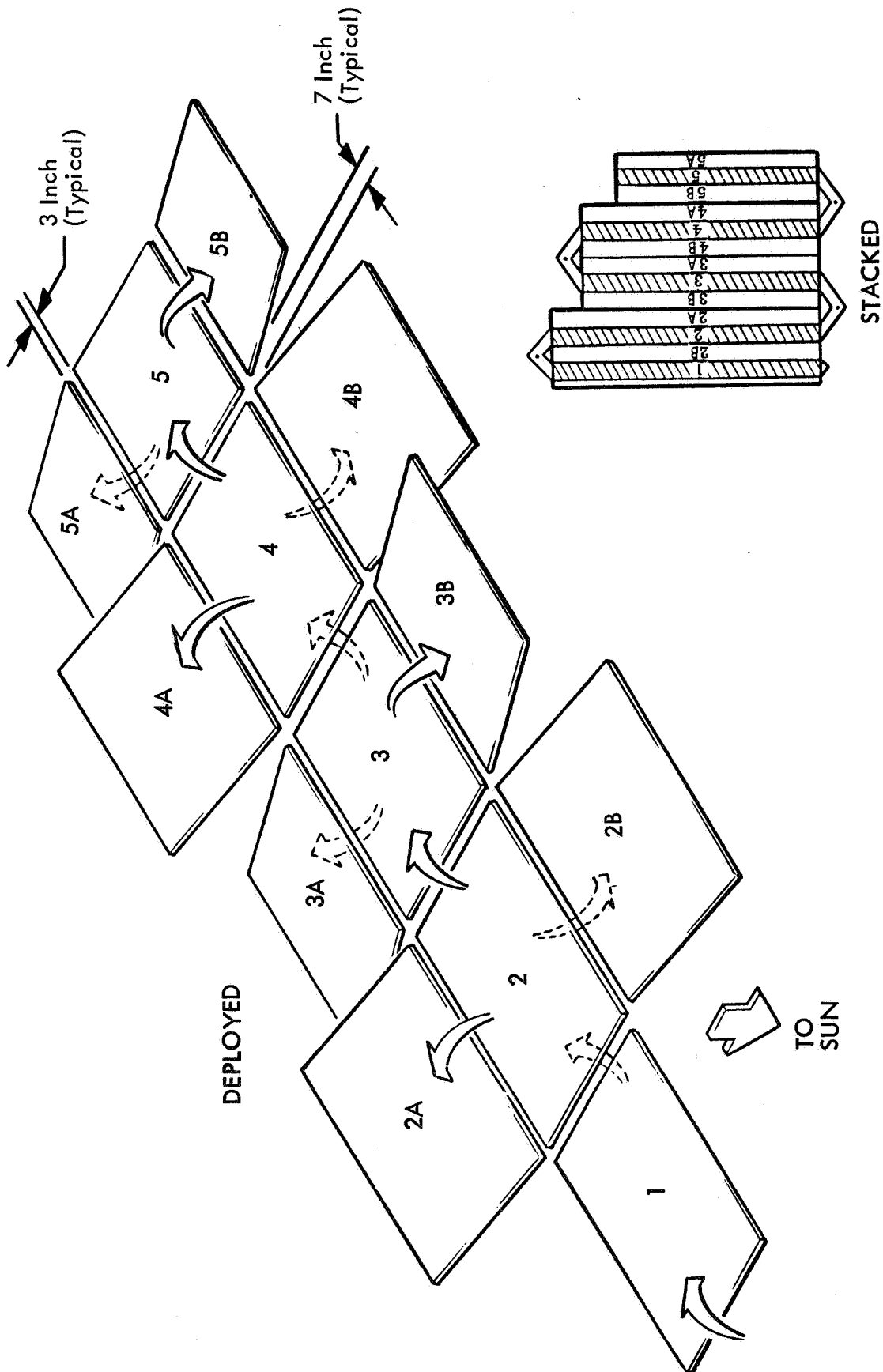
Figure 3-5: SUBPANEL DEPLOYMENT DIRECTION PICTURE

There are problems associated with bearing, galling, and sequence of
releases. A stress analysis shows that bearing stresses are rather high
for alodyn coating (that is, more than 20,000 psi). It is possible that
such stresses could cause damage to the coatings and thereby lead to
galling and high friction. These stresses occur during boost, with a
1.5-g dynamic reversing input while the pivots are not rotating. During
the deployment after boost, the pivots must freely rotate. Allowables
for this application are not presently available; however, it is
believed that a conservative estimate of these allowables will result in
an acceptable design.

3.2 TIME-HISTORY

The Large Area Solar Array panel assembly deploys in sequential motions
of the main subpanels and of the auxiliary subpanels with character-
istic motions for each. For the main subpanels these motions are a
transient time-history resulting from the cable flexibility and array
inertia and a transient caused by the locking forces. For the auxiliary
panels, the initial time-history results from an opening spring force,
followed by a locking transient.

The objectives of the deployment analysis are to select the combination
of parameters that will allow controlled deployment with minimized forces
and moments. In a broad sense, this includes the deployment motor speed,
deployment cable stiffness, restraining and opening spring stiffnesses,
and viscous damper values. Detail design of the hinges and locking
mechanisms depend on the selected combinations of opening velocity,
cable stiffness, retarding and deploying springs, and dampers.

3.2.1 TIME-HISTORY MOTIONS

*A means of retarding panel assembly motion is required to prevent
uncontrolled deployment.*

The time-history motion of each group of panel units rotating about its
hinge is controlled through the major arc of travel by a moment resulting
from tension in the deployment cable. At termination of rotation about
each hinge, a transient oscillation occurs, superposed on an initial
velocity. There are initial conditions to the time-history of motion
of the next sequence of deployment. When the effects of cable flexi-
bility, restraining spring forces, and dampers are examined, these
initial conditions are neglected.

The time-motion history for three characteristic deployments is shown
by Figure 3-6. In A, the inertia of the panel assembly causes more
tension in the cable than required for steady deployment and the panel
velocity increases and overruns the cable velocity to run free until
the sequence terminates, at which time it initiates deployment of the
next sequence. The free-run velocity is twice that for a rigid cable,
consequently, an uncontrolled deployment could result.

$\Theta/t = \Theta'$
Slope
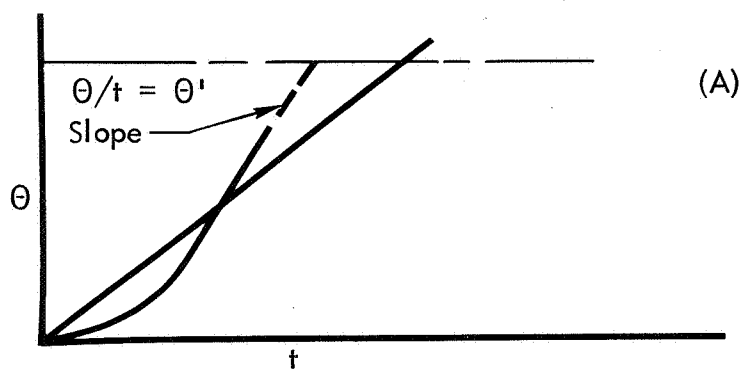
(A)
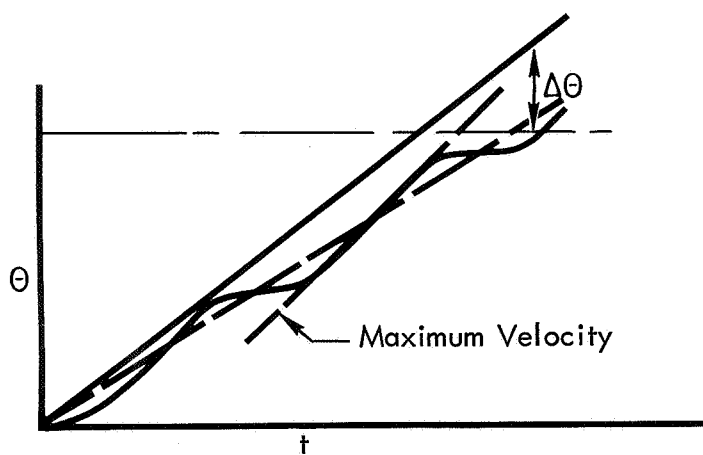
(B)
Restraining Spring

Maximum Velocity
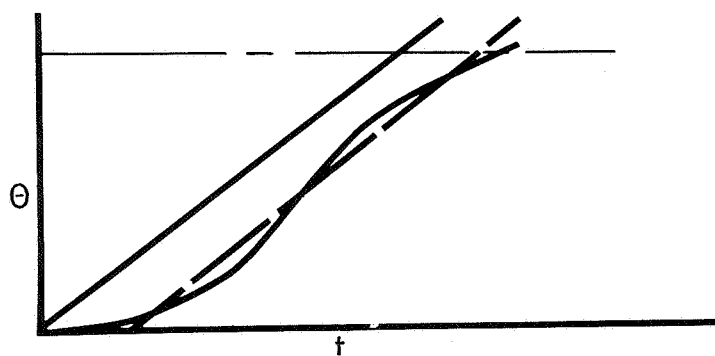
(C)
Viscous Damping

Figure 3-6: CHARACTERISTIC DEPLOYMENT TIME HISTORIES

Controlling the motion is shown in B and C. A characteristic deployment with a retarding spring is shown in B. A torsional stiffness between one eighth and one quarter of the cable spring torsion stiffness is required to prevent overrunning. The velocity at closing can approach twice the nominal opening speed (shown by the slope of the deployment curves), and the cable tension and moment can be large. Use of a damper instead of a retarding spring results in the deployment history shown at C. Here the velocity at closing can be close to the nominal velocity, and the moment at closing is known. A "biased" retarding spring, having an initial opening torque followed by a restraining torque, was also examined. The overshoot tendencies during the first oscillation were exaggerated, and the approach was discarded.

3.2.2 ANALYSIS OF TIME-HISTORY

Time-history studies have established the proper combinations of parameters required for successful deployment.

The characteristic time-history shapes are shown in Figures 3-7, 3-8 and 3-9. During the initial motion, the cable stretches and imparts a velocity to the panel set that is equal to nearly twice the nominal deployment velocity. The cable is then slack for a longer period, during which the retarding spring slows and reverses the motion until the cable is again stretched. The cycle then repeats until the full rotation of the sequence is reached. The maximum velocity always occurs at the end of the final cable-tension period. The retarding-spring force is selected so that the sequence stops shortly after the maximum velocity is attained. Then possible effects such as friction will tend to reduce the final velocity, and the cable will be slack at normal termination. For all sequences, however, the transient loads for design will be determined by maximum velocity.

Figure 3-7 shows time-history curves at the end of the third quarter for maximum and minimum expected cable stiffness (117.5 and 40 pounds per inch) with a retarding spring torque of 4 pounds per inch. The major difference is in the shorter time periods, during which the stiff cable accelerates the inertia. As a result, the maximum velocity attained before closing (0.032 radians per second is reached in a shorter time and at a smaller angle. The final velocity is then less than that for the softer cable spring. The effect is similar when the retarding spring torque is reduced.

Figure 3-8 shows the effect of the increased deployment angle with the same stiffnesses. Also shown is the effect of an initial velocity of 0.016 radians per second on the more flexible cable time history. Figure 3-9 shows the complete time-history curves for Sequence 3 for the stiffest expected cable with two values of the retarding spring. For the interval just before closing, similar curves for the most flexible cable have been added. The inset shows an enlargement of this period.

FIRST SEQUENCE: I = 7720

	K	k	$\dot{\theta}$ MAX	$\dot{\theta}$FINAL
———	117.5	4.0	0.032	0.0228
– – –	40.0	4.0	0.0307	0.0243
··········	40.0	3.2	0.031	0.0286
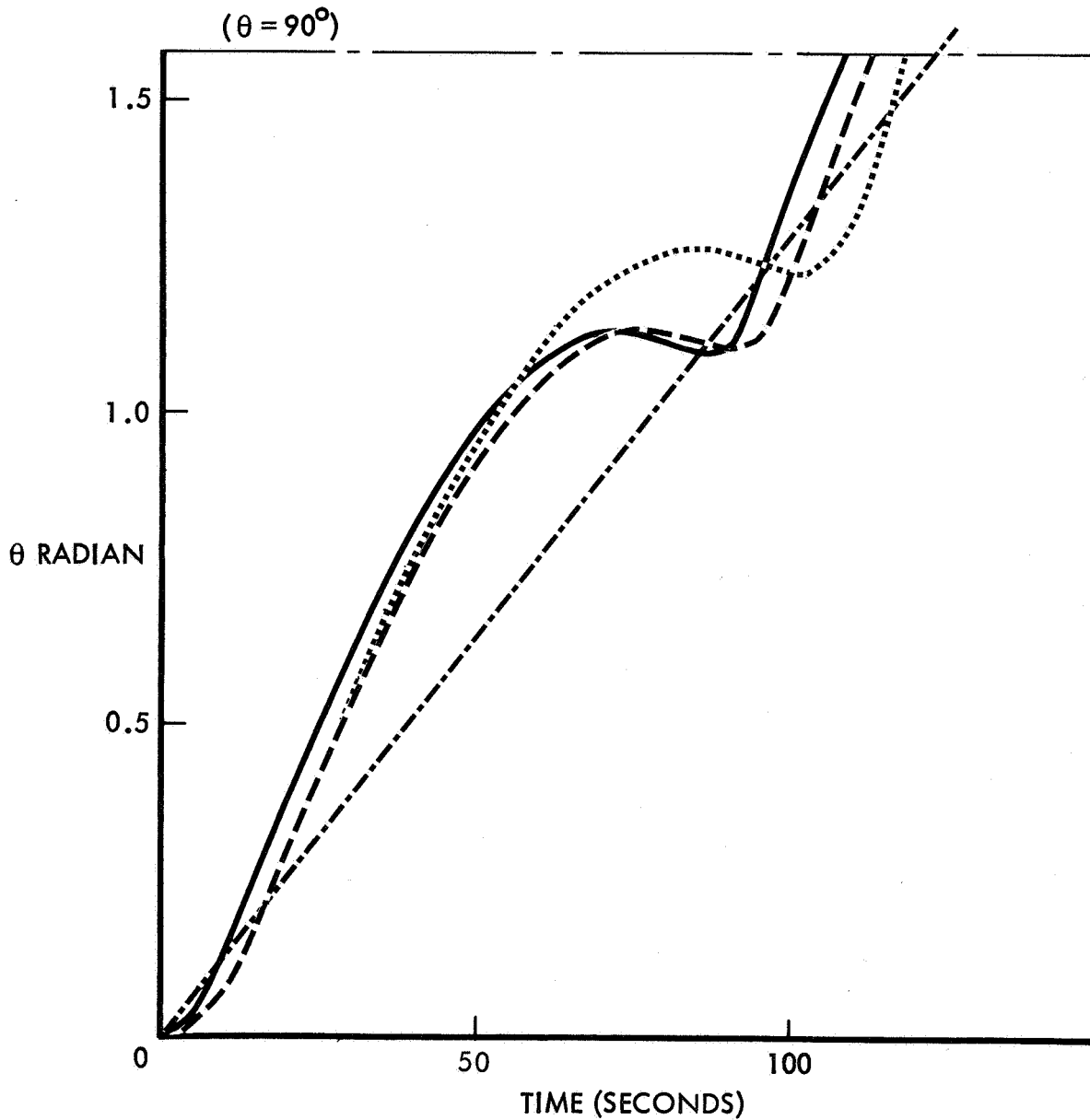
Figure 3-7: SPACE-TIME HISTORY — FIRST SEQUENCE

SECOND SEQUENCE: I = 10.750

	K	k	$\dot\theta$ MAX	$\dot\theta$FINAL	$\dot\theta$INITIAL
‒ ‒ ‒ ‒	40.0	4	0.0293	0.0293	0
··········	117.5	4	0.0314	0.0313	0
———	40.0	4	0.022	0.0186	0.016
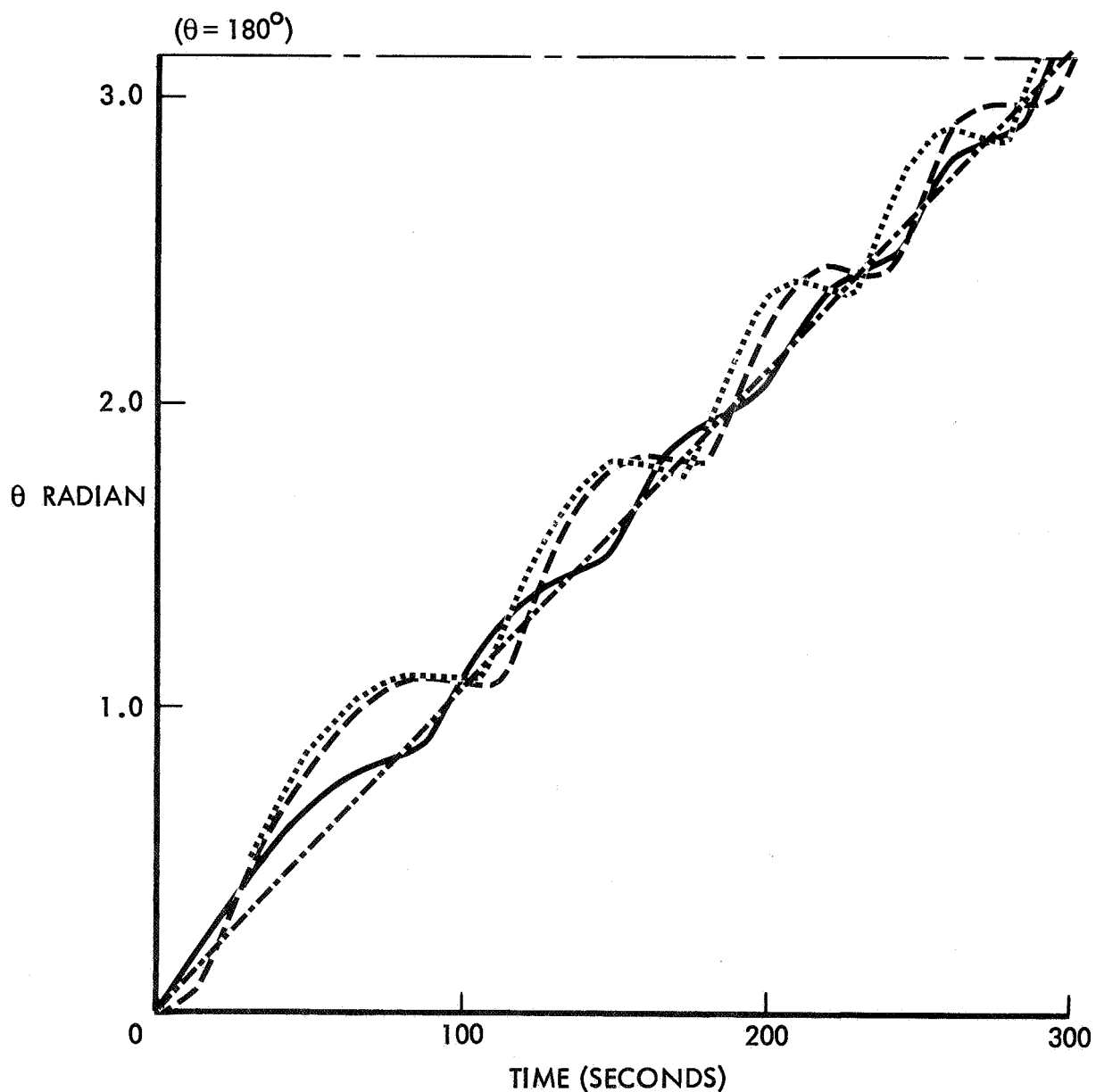
Figure 3-8:   SPACE-TIME HISTORY — SECOND SEQUENCE

THIRD SEQUENCE: I = 4500

	K	k	$\dot\theta_{MAX}$	$\dot\theta_{FINAL}$
———————	70.4	2	0.0321	0.0321
·················	70.4	4	0.0322	0.0322
—·—··—··—	40.0	2	0.0306	0.0023
— — — — —	40.0	4	0.0305	0.0112

(θ = 180°)
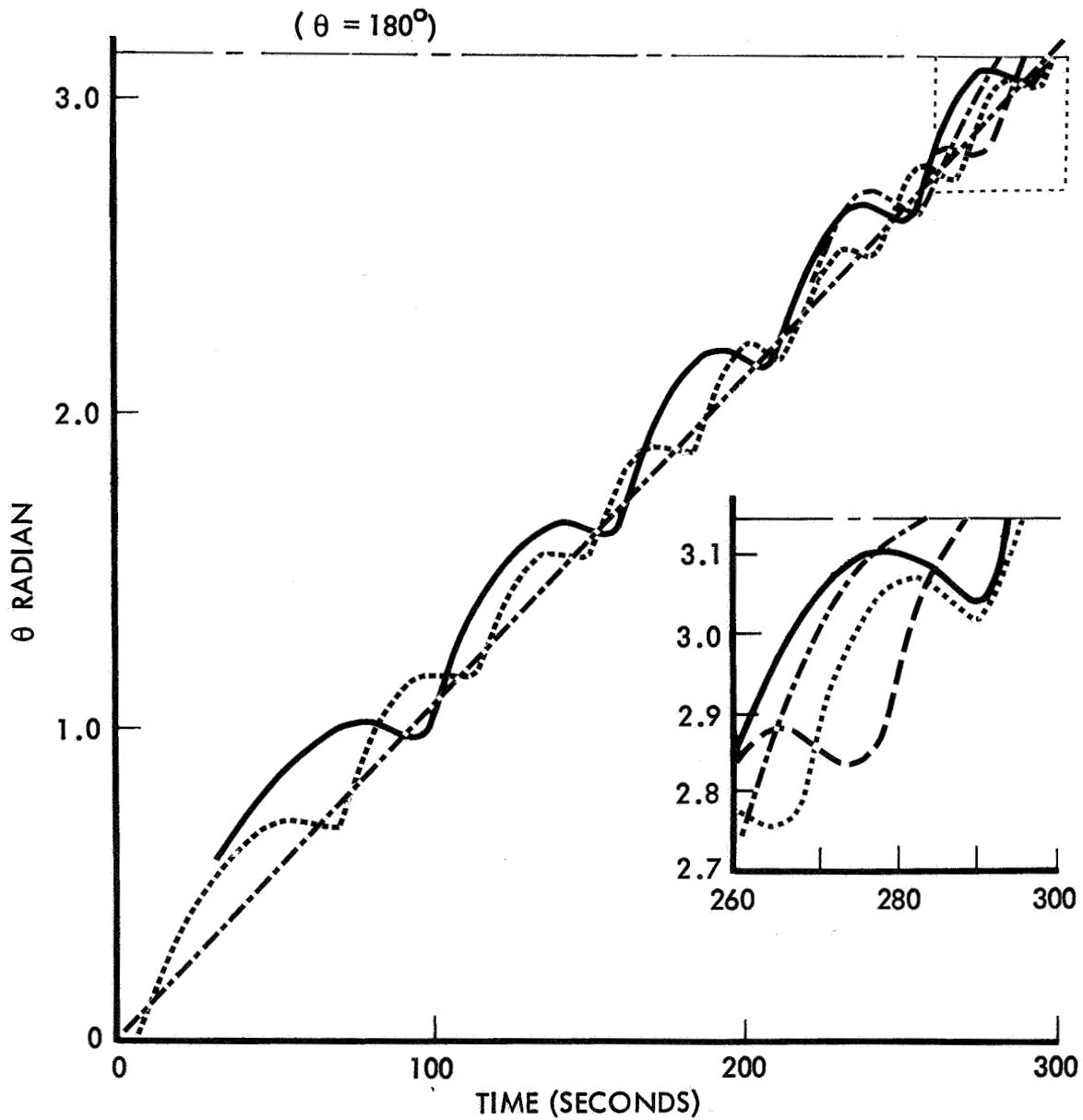
Figure 3-9:   SPACE-TIME HISTORY — THIRD SEQUENCE

The parameters determing the final velocity for the auxiliary panels are: deployed array torsion mode, auxiliary panel opening spring, auxiliary panel inertia, and damper characteristics. For the selected damper, a revised opening spring, and the auxiliary panel inertia resulting from an increased gap between main and auxiliary panels, a final velocity of less than 0.15 radians per second is obtained.

The time-history motions for the main panels are calculated with the assumption that there is no coupling with the transient oscillation motion. The folded panel sets are considered rigid. The cable stiffness is given an assumed maximum and minimum value, which relates to a high cable-quadrant friction and to zero cable-quadrant friction.

The differential equation used for solution, developed in Boeing Document D2-113355-1, has been expanded to include a viscous damping term, a velocity squared damping term, an initial cable tension term, and a constant force. The general form is:

$$I\ddot{\theta} + D\dot{\theta} + (Kr^2 + k)\ \theta = KrVt + K\theta_o + Z - CD\dot{\theta}^2$$

where:

I = Mass moment of inertia about hinge $\left(\dfrac{\text{lb-in.}^2}{g}\right)$

D = Viscous damping term (in.-lb/rad/sec)

K = Cable spring stiffness (lb-in.)

k = Retarding spring torque (in.-lb/rad)

r = Quadrant radius (inch)

V = Linear cable velocity (in./sec)

t = Time (seconds)

θ_o = Initial angle (rad)

Z = Constant applied torque (in.-lb)

CD = Air-damping term (in.-lb/(rad/sec)^2)

A required reduction in the quadrant radii caused an increase of 8.6% in the nominal opening rate of the panel and a consequent increase in the closing velocity. For design purposes, a closing velocity of 0.035 radians per second was used for calculation of transient loads.

The time-history motions for the auxiliary panels assume 2 degrees of freedom. The first is the first torsion mode of the partially deployed array; the second is rigid rotation of the auxiliary panel about its hinge. The solutions show only small motions of the array, indicating that a good approximation could be obtained with a 1-degree-of-freedom system.

3.3   IMPACT OF TRANSIENT LOADS

As a consequence of locking at the end of each sequence, transient oscillations are superposed on the initial rotational velocity of the following sequence. For all combinations of units except the fifth (last subpanel) the motion is described in 3 degrees of freedom, and the differential equations are solved by digital computer. For the last opening sequence, the transient oscillation is described in 2 degrees of freedom, and the equations are solved by Laplace transforms.

The transient forces and oscillations are caused by the requirement that the rotational velocity of the continuing units must be reversed by a force through the hinge connecting to the (stopped) inboard panels. Had the rotation reversed instantaneously, the force would be infinite. The magnitude is measured by the time interval during which it builds to peak value; the shorter the interval, the more severe the peak. Because the stiffness of the resisting structure is greatest for short spans, maximum forces can be expected from the initial sequences. The magnitude of the force is also directly by proportion to the velocity that must be stopped; for these analyses it is assumed to be equal to twice the nominal (rigid cable) velocity. This is the maximum if the panels are allowed to run free.

3.3.1   ANALYSIS OF TRANSIENT LOADS IN MAIN SUBPANELS

Transient-load analysis was required to determine loads and moments for mechanism components.

Initial analyses for transient loads used baseline weight and stiffness values. First iteration structural stiffness and the appropriate weight data were then incorporated. In addition, improved idealization of the physical problem was included and additional panel sequences analyzed. These had not been previously analyzed because they were expected to be less critical. The effect of stiffness changes between the first structural iteration and the final structural iteration was then examined.

Resonant frequencies of all modes used in the transient loads analyses were calculated using the final structural iteration data. When compared with frequencies used in the first iteration, insignificant changes were found. Of greater importance was the increase in closing velocities.

Design limit loads based on 0 to 0.032 radians per second, and the final design limit load values based on 0.035 radians per second, are shown in Figure 3-10. The final loads incorporate the effect of increased velocity. As expected, the added analysis for Panels 3 and 4 shows loadings less critical than for Panels 1 and 2. Values for Sequence 5 are not shown because the initial analysis, which showed it was not critical, is verified by the analysis trend of Panels 1, 2, 3, and 4.

The solutions for transient loads assume that values will reach maximum in the first seconds. Equations derived originally for large angle motions have been linearized for solution. Because the system geometry is changing continuously during the 180-degree rotation that precedes the next transient, a midsequence evaluation is made as described in Section 3.3.2. Other assumptions used in the idealization are: (1) the spacecraft attachment of the diagonal strut and main panel hinges is rigid; (2) panels inboard of the locking hinge bend as beams; (3) the panel immediately outboard of the locking hinge rotates as a rigid bar against the locking hinge stiffness; and (4) the following panel set rotates as a rigid bar about its inboard hinge.

The assumed degrees of freedom vary with the sequence, as described below:

Sequence 1---Three normal bending modes of Panel 1 as a beam pinned at the spacecraft hinge and at the diagonal strut, rigid rotation of Panel 1 about the spacecraft hinge against the diagonal strut stiffness, and rigid rotation of the following panel set about the Panel 1-2 hinge.

Sequence 2---One normal bending mode of Panel 1 pinned at the spacecraft and the diagonal strut, rigid rotation of Panel 1 about the spacecraft hinge against the diagonal strut stiffness, rigid rotation of Panel 2 against the locked hinge between Panels 1 and 2, and rigid rotation of the following panel set around its inboard hinges.

Sequence 3---Three normal bending modes of Panels 1 and 2 as a beam pinned at the spacecraft hinge and deflecting the diagonal strut, rigid rotation of Panel 3 against the locked hinge between Panels 2 and 3, rigid rotation of the following panel set around its inboard hinges.

Sequence 4---Three normal bending modes of Panels 1, 2, and 3 as a beam pinned at the spacecraft hinge and deflecting the diagonal strut, rigid rotation of Panel 4 against the locked hinge between Panels 3 and 4, and rigid rotation of the following panel set (5, 5A, 5B) around its inboard hinge.

3.3.2 ESTIMATE OF LOADS AT MIDSEQUENCE POINTS

A conservative analysis of midsequence loads indicate that they are not critical to design.

SEQUENCE	SHEAR FORCE		DIAGONAL STRUT LOAD F_S	HINGE MOMENT	
	Locking Hinge F_1 (lb)	Rotating Hinge F_2 (lb)		Locking Hinge (in.-lb)	Panel 1 – 2 Hinge (in.-lb)
1 a	–	10.2	177	–	–
1 b		11.2	193		
2 a	16.4	9.2	96	1680	1680
2 b	17.9	10.1	105	1840	1840
3 a	5.7	4.6	81	585	1710
3 b	6.2	5.1	88.5	640	1870
4 a	3.37	3.3	22.8	715	1240
4 b	3.68	3.61	24.9	782	1360

a. Based on $\dot{\theta}_i = 0.032$ rad/sec (D2-113355-3)

b. Based on $\dot{\theta}_i = 0.035$ rad/sec (Final design limit load)

Sketch is For Sequence 3
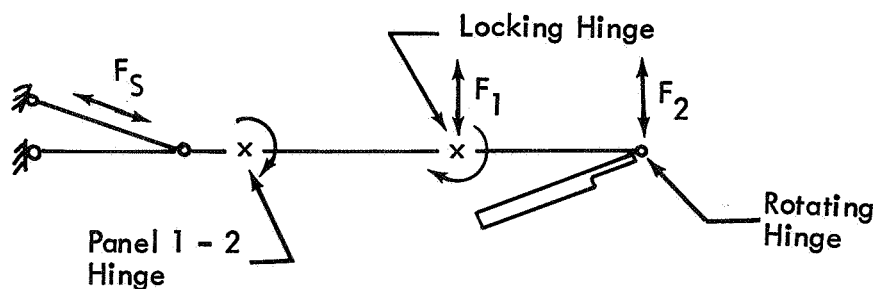
Figure 3-10: SPACE DEPLOYMENT LOADS

Evaluation of the loads that occur at midsequence assumes that all of the kinetic energy in the preceding rotating panel set at the instant of locking is absorbed by each of three bending modes. The modal frequencies and generalized inertias are determined for beams pinned at their inboard end and bending against the diagonal strut stiffness, with a concentrated mass attached at the outboard end.

The loads were originally determined for a closing velocity of $\dot{\theta} = 0.025$ radians per second for comparison, with transient load results calculated on the same basis. For the final closing velocity of 0.035 radians per second, the values of both the transient and midsequence loads increase by a factor of 1.40. In all cases, the midsequence loads remain less than those for the initial transient.

The assumption that the total energy is absorbed by *each* bending mode is conservative. Only a part of the energy causes oscillations of the following panel set and bending of the beam. The remainder causes a uniform rotary velocity of the panel set. Structural damping reduces the oscillation energy. Finally, the energy in oscillation that remains is shared by the bending modes, rather than being absorbed into each separate mode.

3.3.3 AUXILIARY PANEL DEPLOYMENT

Auxiliary subpanel deployment is accomplished with a simple drive and latch.

The auxiliary subpanels are deployed by an opening spring with an initial torque of 2.5 inch-pounds and a torque at closing of 1.25 inch-pounds. A rotary viscous damper is used to control the closing velocity. An overcenter four-bar linkage locks the panel in the extended position. The solution for motions is obtained by solution of the differential equations of a two-degree-of-freedom system by a computer program.

Each auxiliary subpanel is restrained during boost by use of the shear teeth shown in Figure 3-11. The panels are prevented from premature deployment by light-duty shear pins located on the outboard athwartship spar member. The single shear pin per auxiliary panel is withdrawn by the closing action of the main hinge latches (or the Panel 5 geneva in the case of 5A and 5B) located immediately outboard of the effected panels. This action guarantees proper sequencing of the auxiliary panels.

The spring deployment and latching mechanism is shown in Figure 3-11. Each of the two deployment springs has an initial torque of 1.25 inch-pounds for a total torque of 2.50 inch-pounds to deploy each auxiliary subpanel. During deployment, the latching spring is loaded and supplies some of the terminal hinge torque as well as the latching force (see Figures 3-12 and 3-13).

Hard Anodize Or Alodize

BMS 3-8 Solid Film Lubricant

63

Hard Anodize Or Alodize

BMS 3-8 Solid Film Lubricant

Typical Bolted or Pinned Pivot

Main Panel
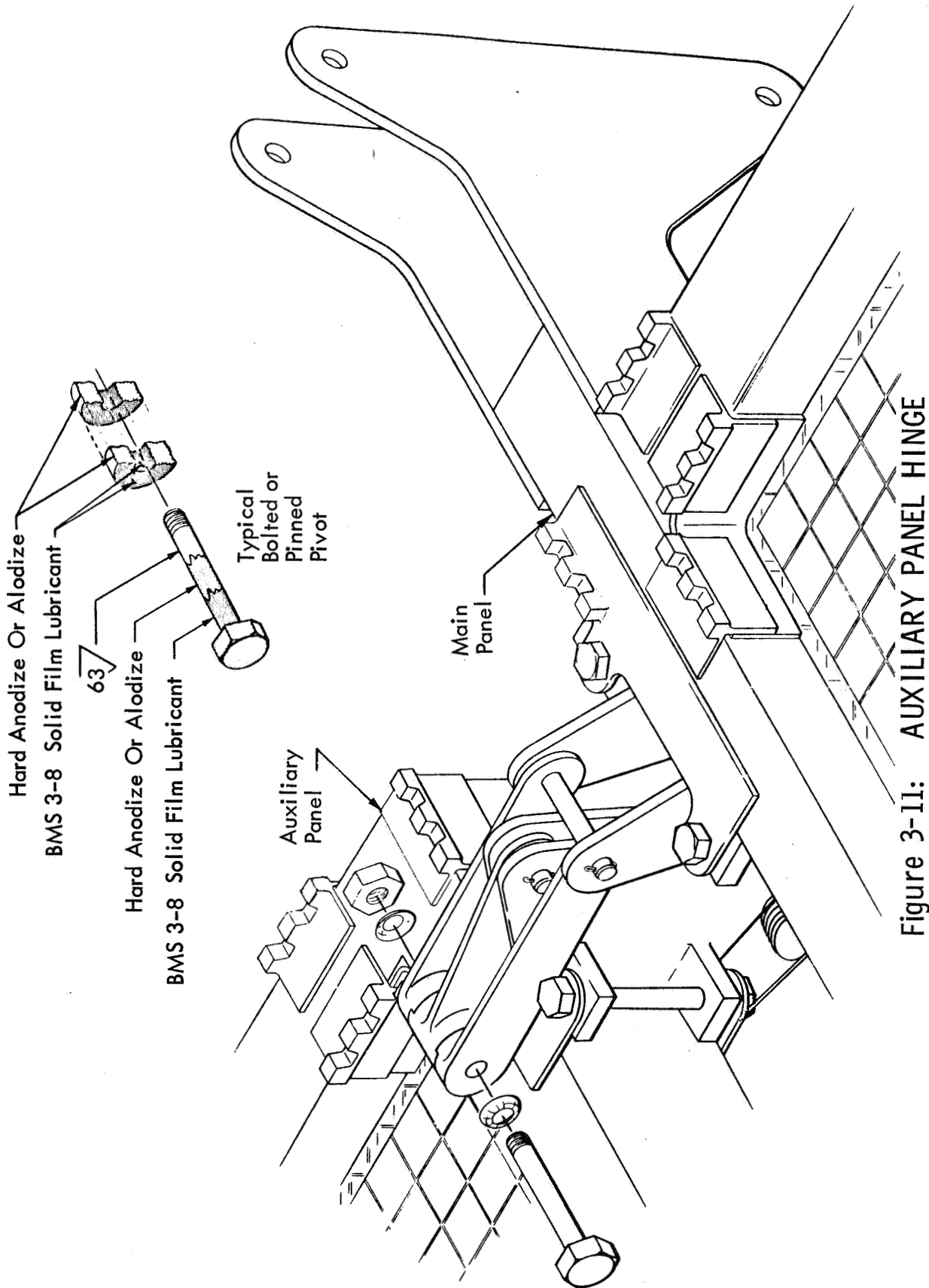
Auxiliary Panel

Figure 3-11: AUXILIARY PANEL HINGE

DEPLOYMENT
SPRING T_1

D= .475
d= .0475
f= 130,000 PSI
Kc= .92
θ_{MAX}= 304°
T_{MAX}= 1.25 IN #
N= 10 5/8 COILS

b

c

a

d

LATCH SPRING T_2

D= .375
d= .025
f= 130,000 PSI
Kc= .945
θ_{MAX}= 208°
T_{MAX}= .177 IN #
N= 6 COILS

SEE FIG
FOR COMPLETE
MOMENT CURVE

e

b: 2.15 LG

θ_3

T_4

T_1

θ_1

T_3

a= 2.00 LG.

c= 2.25 LG

90°−θ_2

θ_2

F_1

F_d

T_2

d= 2.75 LG

MOMENT DIAGRAM

$$F_1 = \frac{T_2}{d} = F_c \sin \theta_2$$

$$F_c = \frac{T_2}{d \sin \theta_2}$$

$$T_3 = F_c \cdot e \quad \& \quad e = b \sin \theta_3$$

$$T_3 = \frac{T_2 \, b \sin \theta_3}{d \sin \theta_2}$$

$$T_4 = T_1 - T_3$$

NET HINGE MOMENT

TRAVEL−DEG.

T_4
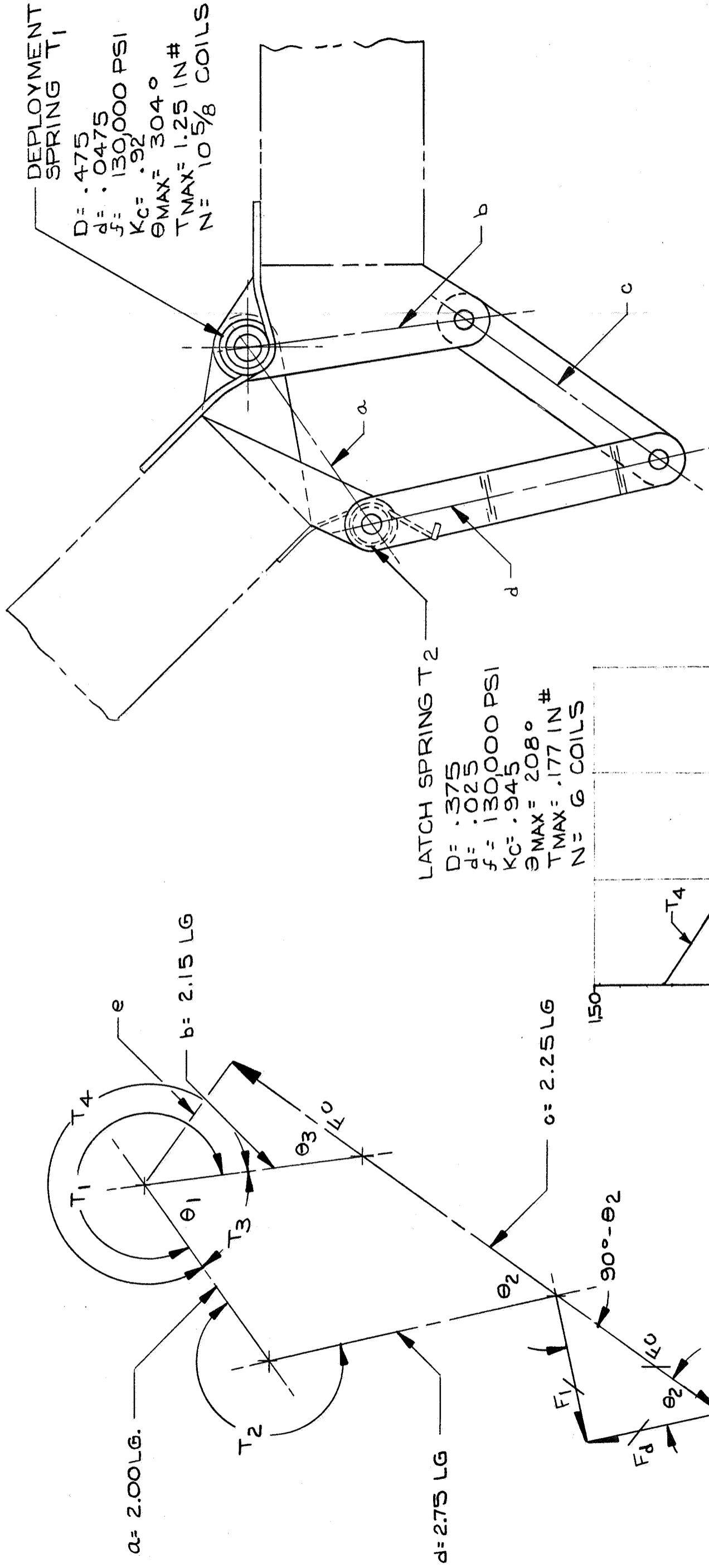
Figure 3-12: AUXILIARY HINGE
MOMENT
CALCULATIONS

3-21
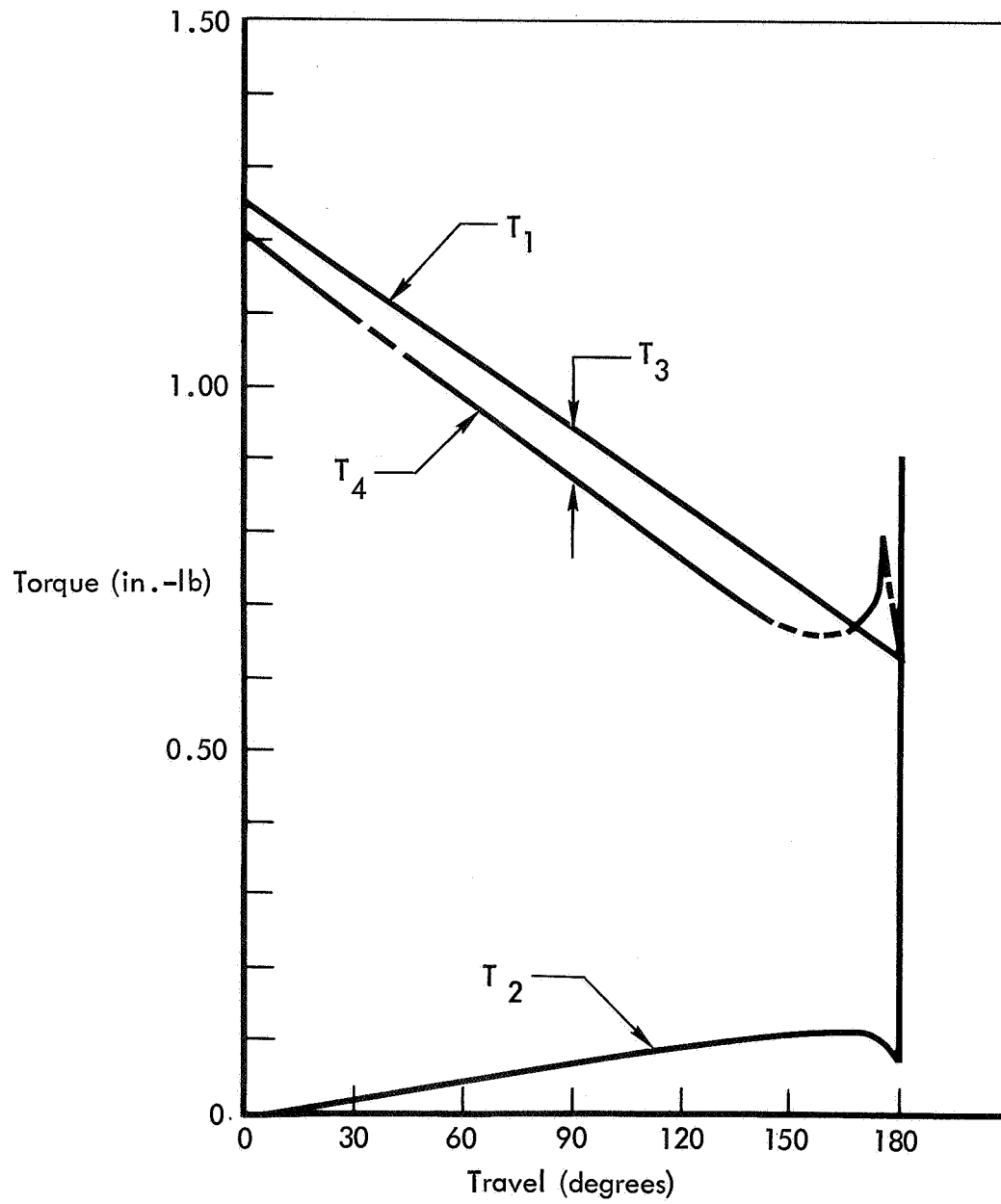
Figure 3-13: HINGE MOMENT AUXILIARY PANEL DEPLOYMENT

Initial analysis for both the auxiliary panel and main panel deployment
transients used a minimum number of degrees of freedom selected to derive
a conservative solution. The loads shown in Table 3-1 were determined
by the first five modes of the deployed array at the appropriate state
of deployment. The auxiliary panels were assumed to deploy simultaneously
for each subpanel unit. The latching was assumed to take place
instantaneously, transforming the closing rotary momentum of the auxiliary
panels into oscillations of five-array natural modes.

Table 3-1: AUXILIARY-PANEL DEPLOYMENT SOLUTION OF TRANSIENTS

$(\dot{\theta}_o = 0.15$ radians per second)

Panel	Bending Moment (inch-pounds)	Shear
2A	500	
3A	400	
4A	320	Not critical
5A	200	

NOTE: Total moment at two auxiliary panel hinges; use this value
for design load on one hinge.

Design Moment = 500 inch-pounds
Design Shear: Not critical

The closing velocity was selected as 0.15 radians per second, which
corresponds to those values obtained using one rotary damper with a
capacity of 6.0 to 6.5 inch-pounds per radian per second. This is
close to the high-temperature capability of an uncompensated rotary
damper of the type specified. Because the damper is velocity-sensitive,
it can never prevent deployment. Measurement and adjustment of damper
units will be used to pair units for each subpanel set and to match them
to auxiliary panel requirements. The force and deflection values were
taken as the sum of the maximum response values of each mode.

It has been assumed that seizure failure modes are both more likely and
more critical than the inadequate damping failure modes. Seizure could
prevent auxiliary panel deployment and shade both the auxiliary and the
associated main panel, thus causing significant power loss. While
inadequate damping could cause structural damage, it would also be
possible for the array to survive some damage and continue to function.
It has therefore been recommended that dual dampers not be used.

The damping characteristics used in panel design are based on the high-
temperature performance of the damper per Figure 3-14. The dampers are
physically located so that the solar heat will warm units exposed to low-
temperature extremes during the coast period. Cold and sluggish dampers
cannot permanently prevent deployment, and temperature control coatings
will be used to limit the high-temperature environment. In the space-
pressure environment, O-ring seals prevent loss of damping fluid.

NOTES:

Used on OV3-2 launched October 29, 1966.

Ratings: Operating Temperature Range -65° to 165°F. Damping Range 0.25 to 12.5 in-lb/Rad/Sec

Minimum Shaft Rotation: 180°

Backlash of Shaft: ±1/2° Maximum.

Acceptance Test: Following a dimensional check, each unit shall be functionally tested as follows:

1. Rotation - The shaft of each unit shall be rotated to determine the angular travel characteristics. Travel less than 180° and/or backlash in excess of 1/2° shall be cause for rejection.

2. Damping Rate - Damping rate of the unit shall be checked with the metering valve in the full open and full closed position. The damping rates shall be as follows: Fully open; .25 in-lb/Rad/Sec. Max. Fully closed; 12.5 in-lb/Rad/Sec. Min. at 75°F.

3. Following the above tests, there shall be no evidence of external leakage.

Temperature Affects at Various Valve Settings

Performance at Various Valve Settings at 70°F

Materials and Finish:

	ITEM	MATERIAL	FINISH
1	Cover	Magnesium Alloy Type AZ31B per QQ-M-31	Dichromate Pickle
2	Retaining Ring	Steel Type 1065.1090 per FED-STD-66	Cadmium Plate
3	Diaphragm	Silicone Rubber LS-53	
4	Seal Screw	Stainless Steel per A.P.H. Corp Spec. 5-6-32 x 1/4"	Passivate
5	Roll Pin	Stainless Steel Type 420	None
6	Value	Stainless Steel Type 416 per QQ-S-763	None
7	Bearings	52100 Steel	None
8	Abutment	Magnesium Alloy Type AZ31B per QQ-M-31	Dichromate Pickle
9	Vane Shaft	Stainless Steel Type 416 per QQ-S-763	None
10	Cap Screw	Stainless Steel Type 302, 303, 304 or 305 per FED-STD-66	None
11	O-Rings	Silicone Rubber LS-53 60 Durometer	
12	Case	Magnesium Alloy Type AZ31B per QQ-M-31	Dichromate Pickle
	Damping Fluid	DC-510, 500 CSTK	

Figure 3-14: ROTARY DAMPER

3-25

FOLDOUT FRAME 2

FOLDOUT FRAME 1

D2-113355-6

3.3.4 STRUCTURAL ANALYSIS OF DEPLOYMENT HINGES, QUADRANTS, AND LATCHES

Structural analysis of the deployment hinges, quadrants, and latches has been revised to reflect changes in design, load analyses, and material improvements.

The important changes and revisions are:

1) The deployment cable material was changed from dacron to monel;

2) Hinge moments were increased because of increased deployment velocities;

3) The hinge fittings has to be integrated with the revised shear tie fittings;

4) The deployment quadrant radius was changed rom 3.125 to 2.85 inches.

The dimensions of quadrants, hinges, and latches were dictated by the transient loads for the deployment of the main and auxiliary panels. The limit-loads applicable to the main and auxiliary panel hinges are given in Figure 4-2 and Table 3-1. The hinge links were examined for column capability, bolt-bearing and shear, and lug-tension failure. The hinge plates have been examined for load path to spar members and for adequate bond strength. The diagonal strut is critical for column loading at deployment. Analysis during the fourth quarter indicated that the initial strut configuration had to be improved. This was accomplished by spreading the legs farther apart and with some minor revisions to the fittings. Margins of safety are given in Table 3-2.

3.3.5 ANALYSIS OF THE DEPLOYED ARRAY

The structural strength and dynamic response of the deployed panel assembly are satisfactory.

The array was analyzed in the deployed condition to show compliance with the minimum frequency requirement, for response to a continuing square wave pitch excitation, and for response to steady g loading.

The bending frequency showed an adequate margin over the required 0.04 Hz with hinge stiffnesses between one third to one fourth of their actual values. The torsion frequency, at 0.192 Hz, was obviously adequate without a hinge stiffness evaluation. The control system rectangular wave excitation was not critical for either bending or torsion excitation, and the basic structure and critical hinge will withstand steady g loads several orders of magnitude greater than those required.

Table 3-2: MINIMUM MARGINS OF SAFETY HINGES, LATCHES,
AND DIAGONAL STRUT

Component	Margins of Safety	Critical Item	Predicted Failure Mode	Remarks
Main hinge (Panel 1-2)	0.17	Latch link	Compression buckling	
Main hinge (Panels 2, 3, & 4)	0.17	Latch link	Compression buckling	Same links are used on all main hinges; loads are reduced on outboard hinges as noted in Figure 4-2.
Auxiliary hinge (Panel 2)	0.33	Latch link	Compression buckling	
Auxiliary hinge (Panels 3, 4, & 5)	0.33	Latch link	Compression buckling	Same hinges are used on all panels; loads are reduced on outboard hinges as noted in Table 3-1.
Diagonal strut	0.08	Main strut member	Compression buckling	

All components are critical for deployment loads.

The bending and torsion fundamental frequencies with infinite hinge
stiffness were computed. A parallel investigation was made to determine
how finite hinge stiffness affects bending frequency (see Figure 3-15).
Five rigid rotation modes (one at each hinge) and a pinned-pinned bending
mode were used in this analysis. The solutions obtained were for three
sets of hinge stiffnesses for three assumed resonant frequencies of the
infinite hinge beam. For one configuration, two stiffness values for the
diagonal strut were used. The parameters used allowed evaluation near
the critical minimum frequency. Two levels of diagonal strut stiffness
(which bracket the actual stiffness) showed negligible effect on the
fundamental mode. The hinge stiffness levels used were between one
fourth and one third of the calculated hinge stiffness values, based
on deflections of the latching links alone. Additional hinge flexibility
will result from other members of the hinge, local distorsion of the
spars, and some free play.
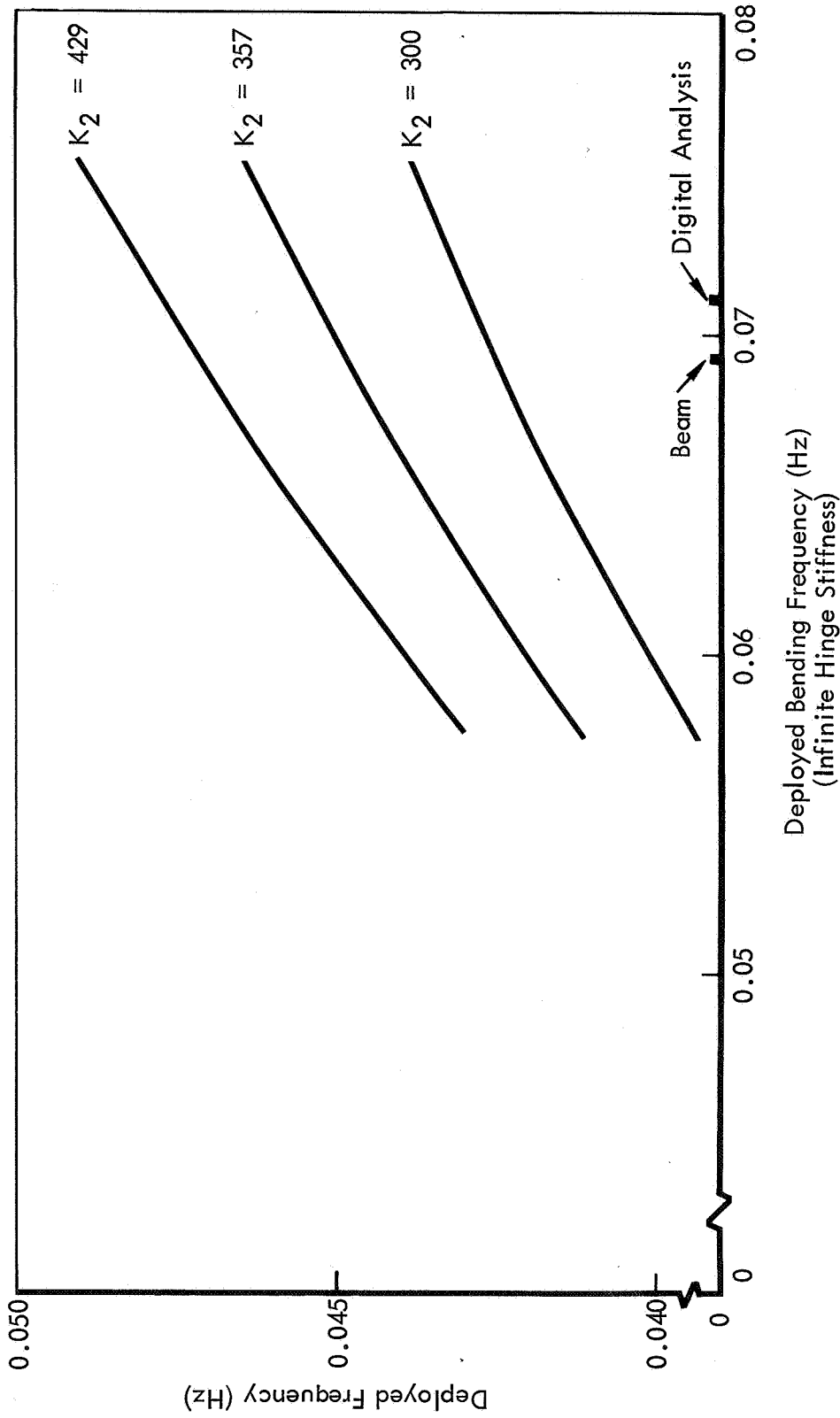
Figure 3-15:   EFFECT OF HINGE FLEXIBILITY ON DEPLOYED FREQUENCY

Evaluation for the frequency of the infinite-hinge bending mode was based on a uniform weight distribution from root to tip and a uniform stiffness.

The torsional frequency determined from the analysis of 0.192 Hz is sufficiently above the JPL Specification GMP-50505-FNC-B requirement of 0.04 Hz to justify ignoring the side panel hinge stiffness effect.

Response to the pitch acceleration of the deployed array was evaluated for a rectangular step function and for a rectangular wave function having equal positive and negative amplitudes. The duration of the rectangular wave was selected to match critically the resonant frequency of the bending array, and the maximum response was determined for a resonant magnification (Q) of 30. Solution of the problem with the step function was obtained with Laplace transforms. The square wave function was solved as a resonant system excited by the fundamental Fourier component of the square wave (see Figure 3-16).

The analysis required the inertia coupling term between the rigid rotation about the vehicle center line and the array bending mode. This was obtained by numerical integration of the product of lumped masses times the appropriate node shape products. A similar evaluation was required in determination of the torsional response to pitch excitation. For this case, the torsional frequency was sufficiently higher than the excitation to allow neglect of a "resonant excitation" analysis, and the coupling term was calculated in the same digital program from which the torsional frequency was obtained.
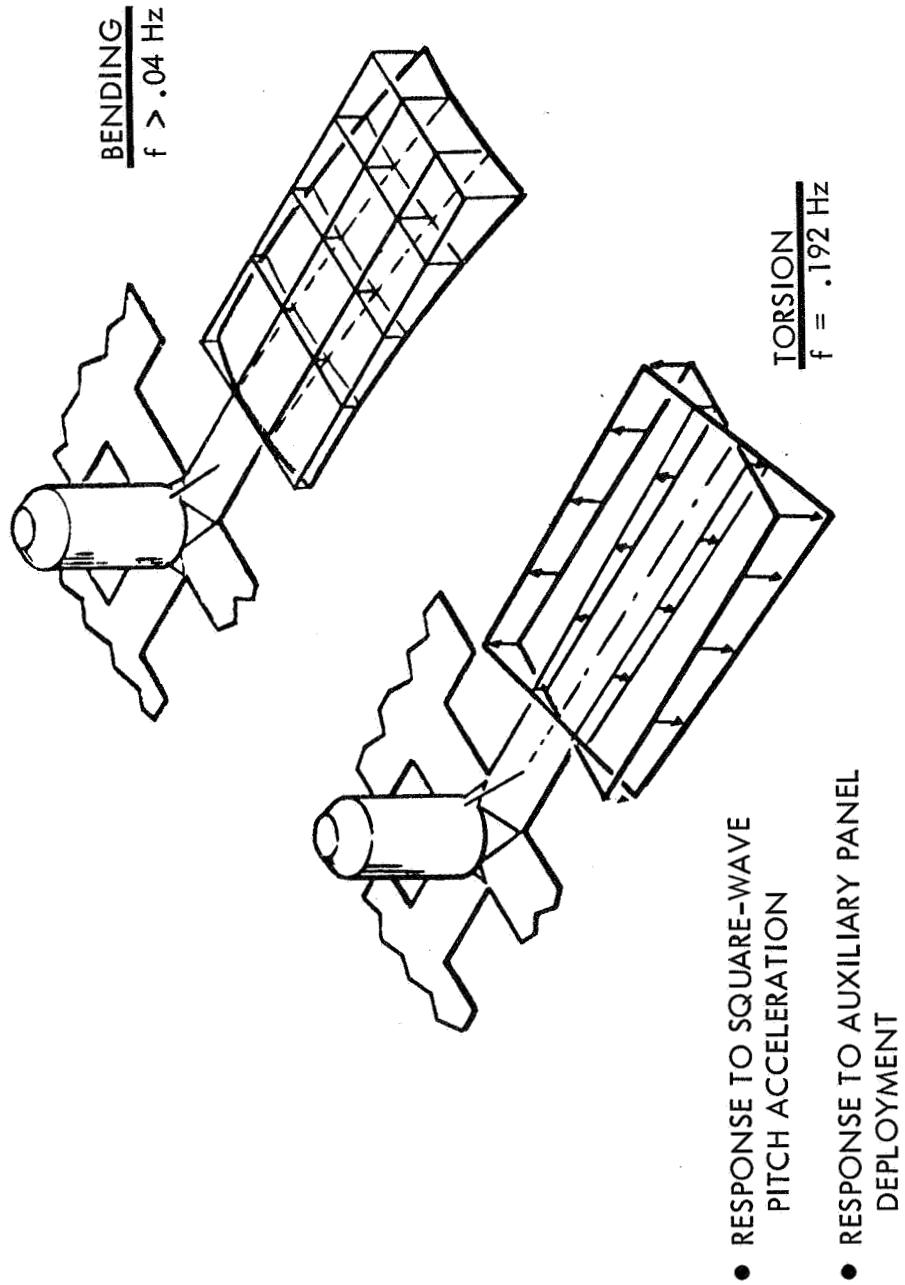
Figure 3-16: DEPLOYED ARRAY

BENDING
f > .04 Hz

TORSION
f = .192 Hz

● RESPONSE TO SQUARE-WAVE
  PITCH ACCELERATION

● RESPONSE TO AUXILIARY PANEL
  DEPLOYMENT

4.0 GROUND RELEASE AND DEPLOYMENT

The panel assembly will be deployed on the ground to obtain experimental test data to substantiate the ground-deployment analysis, and, by analogy, the analysis of the panel-assembly deployment in space. The following sections describe the effect of ground support equipment (GSE) inertias on the deployment test data and the approach to test-data analysis.

4.1 EFFECTS OF GROUND-DEPLOYMENT INERTIAS
ON TIME-HISTORY DATA

Ground-deployment inertias modify deployment time-history however, they have an insignificant effect on the closing velocities selected for determining transient loads.

The effect of the initial estimates of GSE weight and inertia on the shape and final velocities of time histories has been analyzed in the same manner as for space deployment.

The additional inertia changes the initial motion negligibly. During the slack-cable portion of the motion, the added kinetic energy causes a reversal in direction to occur at a later time and larger angle (Figure 4-1). The retarding spring must be adjusted to accommodate the range of possible cable stiffness values and the inertia change.

Friction and air-damping also produce an effect. The design of the deployment fixture has minimized friction forces. The digital program issued to calculate time histories for two types of system friction. The first program allowed a friction moment proportional to the cable tension. The second program provided for static friction until the cable tension exceeded a specified level, followed by a "running" friction proportional to the cable tension. When the panel velocity was reduced to zero, the static friction was again effective. The maximum velocity never exceeds twice the nominal for the range of friction parameters investigated.

Air-damping is estimated by using the drag coefficient of a flat plate normal to the flow. For the motion of the deploying panels (rotation about one end), this should result in an overassessment of the air moments. The effect of Reynolds number for this configuration is not known. The actual drag effect will be evaluated in the MTA-3 test during Phase II. The effect of the assumed air-damping is shown in Figure 4-1 for comparison to the zero-damped deployment test and space-deployment analysis.

The shapes of the ground deployment curves will change in varying degrees, depending on the parameters discussed above. The maximum velocity, which is selected as the closing velocity for determining the transient loads, varies only slightly from the selected value.

FIRST SEQUENCE: I = 9556

	K	k	$\dot\theta_{MAX}$	$\dot\theta_{FINAL}$	
————	117.5	3.2	0.0322	0.0321	
— — — —	117.5	3.2	0.0292	0.026	Air Damping
—·—··—·—	117.5	4.0	0.0306	0.025	
·············	40.0	4.0	0.032	0.023	I = 7720
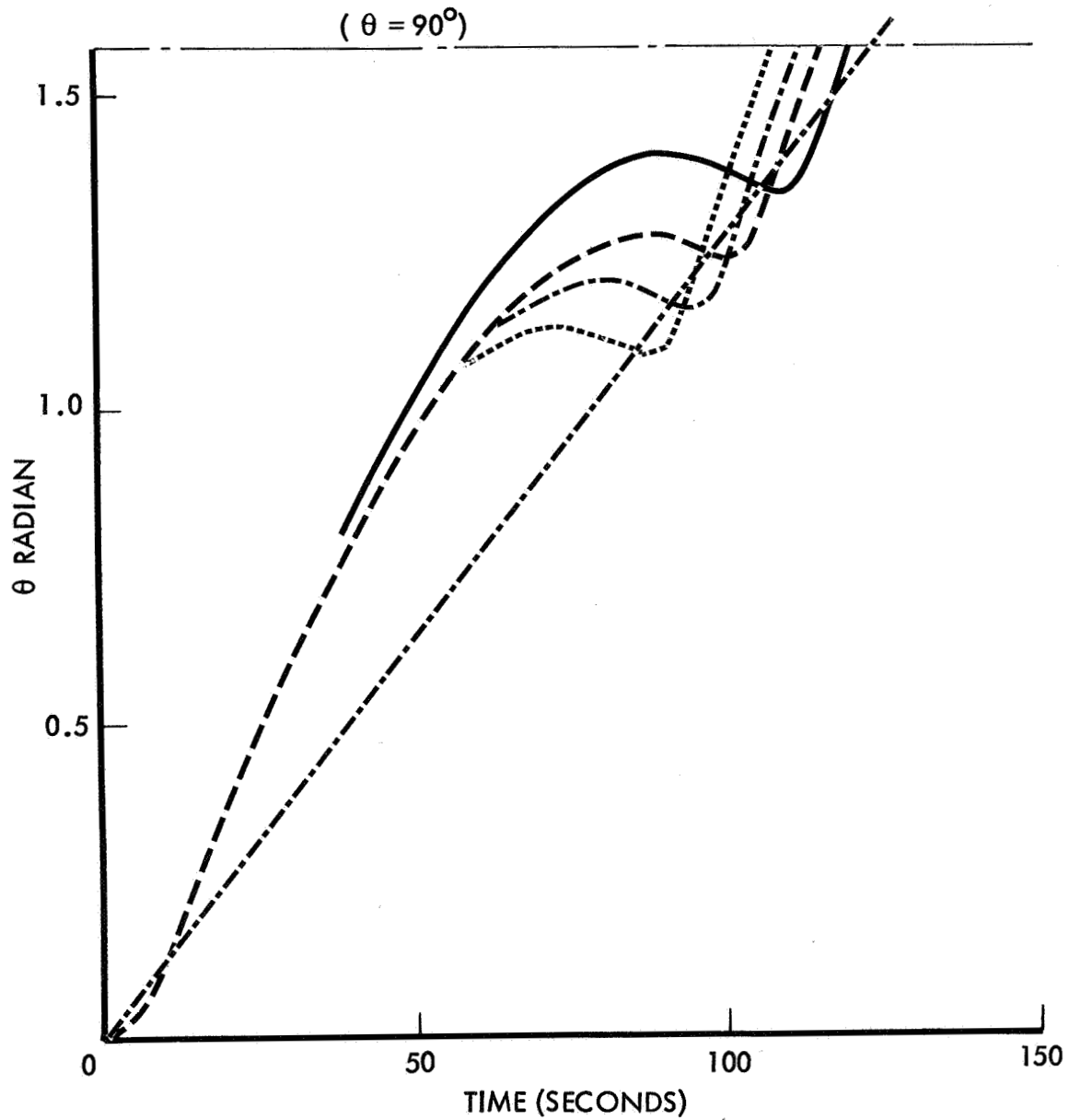
Figure 4-1:   VERIFICATION, TEST-TIME HISTORY — FIRST SEQUENCE

4.2 EFFECTS OF GROUND-DEPLOYMENT INERTIAS
ON TRANSIENT OSCILLATIONS

Ground-deployment inertias have an insignificant impact on the array design.

The effects of initial estimates of GSE-inertias have been obtained by using the same equations as used for space-deployment solutions. The initial velocity condition is considered the same as for space deploy-ment; therefore, the results reflect only the effect of the inertia increase.

In general, the added GSE weight increases the loads. The average increase is about 20%, with larger increases occurring on the smaller loads. Most critical is the moment on the hinges between Panels 1 and 2. It is higher by 22% and is the designing moment for the hinge. The tabulated values for moments, diagonal-strut load, and hinge shear forces are shown in Figure 4-2.

Refining the design of the GSE moving parts results in an appreciable reduction in the moment of inertia of each panel about its hinge line and hinge moments are reduced.

The increase in nominal deployment velocity from GSE inertia causes an increase in the final deployment velocity to 0.035 radians per second. The resulting, increased loads are tabulated in Figure 4-2 as the final design limit-loads.

Ground-deployment loads are not critical for the array structure. They dictate only the dimensions of the main panel hinges, whose weight contribution to the total weight is insignificant.

4.3 DEPLOYMENT TEST ANALYSIS

Data obtained from deployment tests will be used for the MTA-3 and -4 ground-deployment analysis. Once test data have been compared with those predicted by the deployment analysis, the validity of analytical parameters will be verified. In Phase III, this technique will be used to confirm the MTA-4 ground-deployment analysis and, by analogy, the analysis of panel-assembly deployment in space.

The MTA-3 main-panel deployment test differs from the Phase III MTA-4 test in several important respects. During the environmental test program, MTA-4 will experience thermal-vacuum, acoustic, and vibration conditions that could affect its deployment. The aluminum MTA-3 does not duplicate the stiffness or dynamic characteristics of MTA-4. In addition, the overhead support lines for MTA-3 are attached to fixed points rather than to overhead airbearings as in Phase III. Consequently, transient oscillations of MTA-3 after latching are not representative of MTA-4, and test data relate only to the time-history motion.

SEQUENCE		SHEAR FORCE		DIAGONAL STRUT LOAD (F_s) (lb)	HINGE MOMENT	
		Locking Hinge F_1 (lb)	Rotating Hinge F_2 (lb)		Locking Hinge (in.-lb)	Panel 1-2 Hinge (in.-lb)
1	a	–	41	170	–	–
	b		44.8	185		
2	a	18.0	13.1	107.5	2040	2040
	b	19.7	14.3	117.5	2230	2230
3	a	6.3	6.2	99.0	638	1740
	b	6.9	6.7	180.5	700	1900
4	a	4.1	5.8	27.2	790	1610
	b	4.5	6.3	29.6	856	1760

a. Based on $\dot{\theta}_i$ = 0.032 rad/sec (D2-113355-3)

b. Based on $\dot{\theta}_i$ = 0.035 rad/sec (Final design limit loads)

Sketch is for Sequence 3
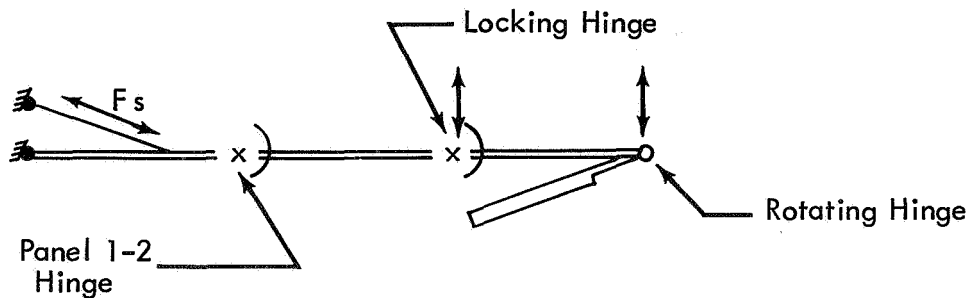
Figure 4-2:   VERIFICATION-TEST LOADS

MTA-3 inertial properties have been adjusted to match MTA-4, and proto-type mechanisms are used. With this similarity, the MTA-4 ground-deployment time-history will be essentially the same as that of MTA-3 with plastic membranes installed. Moreover, MTA-4 space deployment time-history will be essentially the same as that of MTA-3 with bare frames.

The adequacy of the measured test data to satisfy the analytical requirements is shown by: (1) describing the analytical equation used to conduct the analysis, (2) defining the parameter information required, and (3) relating the MTA-3 tests to the required information.

4.3.1 ANALYTICAL MODEL

Control of deployment motions and loads depends on an adequate analytical model.

The magnitudes of the array shear, bending moments, and diagonal-strut loads depend on the closing velocities of each deployment sequence. Control of the motion to limit the final velocity at latching is possible if the analytical model is adequate and parameter values are known. The analytical model consists of a differential equation that describes the time-history motion of the deployment. The differential equation used is the same as that presented in the Phase I final report, except that an additional friction force has been added:

$$I \ \ddot{\theta} + D \ \dot{\theta} + (Kr^2 + k) \ \theta = KrVt + H - DV(\dot{\theta})^2 - FRP$$

where:

I = Mass moment of inertia;

D = Viscous damping term;

K = Cable spring linear stiffness;

k = Retarding spring torsional stiffness;

r = Quadrant radius;

V = Linear cable velocity;

t = Time;

H = Constantly applied torque, initial cable tension, or slack;

DV = Air-resistance term;

FRP = Static-friction torque, followed by sliding-friction torque.

The equation (and the digital programs used for its numerical solution) allows for initial conditions (angular velocity and cable tension or slack) and for the dynamic motions caused by the cable spring and the retarding spring acting on the rotary inertia of the panel sets. Provision is also made for the damping effects of the panel rotating in air, for various friction forces, and for viscous damping. The effects of possible coupling with transient oscillation and the levelness or smoothness of the tracks are small and are not considered in the equation.

4.3.2 ANALYTICAL PARAMETERS

Prediction of the deployment time-history for MTA-4 depends on adequate knowledge of the important parameters of analysis.

The primary means of proving deployment capability in space is to show a good comparison of the predicted and actual response of ground deployments. This requires that the values of the parameters of analysis be known.

Figure 4-3 illustrates a typical first-sequence deployment. The nominal deployment time-history, which would apply if the deployment cable were rigid, is shown by the sloping straight line. The slope is determined by the motor velocity and quadrant radius.

Dynamic oscillations occur about the nominal line because of the stiffness characteristics of the deployment cable and retarding spring, in conjunction with the rotary inertia of the panel sets. The effective cable stiffness will be large if the friction between the cable and the quadrant locks it to the moving quadrant. It will be smaller if the friction is small and the cable stretches over its full length. The initial crossing from tension to slack cable depends on the effective cable stiffness. The crossing from slack cable to tension depends on the retarding spring stiffness.

An increase in the rotary moment of inertia increases the angle at which the first crossing occurs and the angle at which the retarding springs reverse the motion.

At closing, the transfer of momentum causes the following panel set to have an initial velocity equal to 50% to 90% of the final velocity. The weight, center of gravity, and rotary moment of inertia of the following panel set determines the exact value.

Values for the above parameters are required for space deployment without friction.

$$I\ddot{\theta} + D\dot{\theta} + (KR^2 + k)\theta = KRVT + H - DV(\dot{\theta})^2 - FRP$$
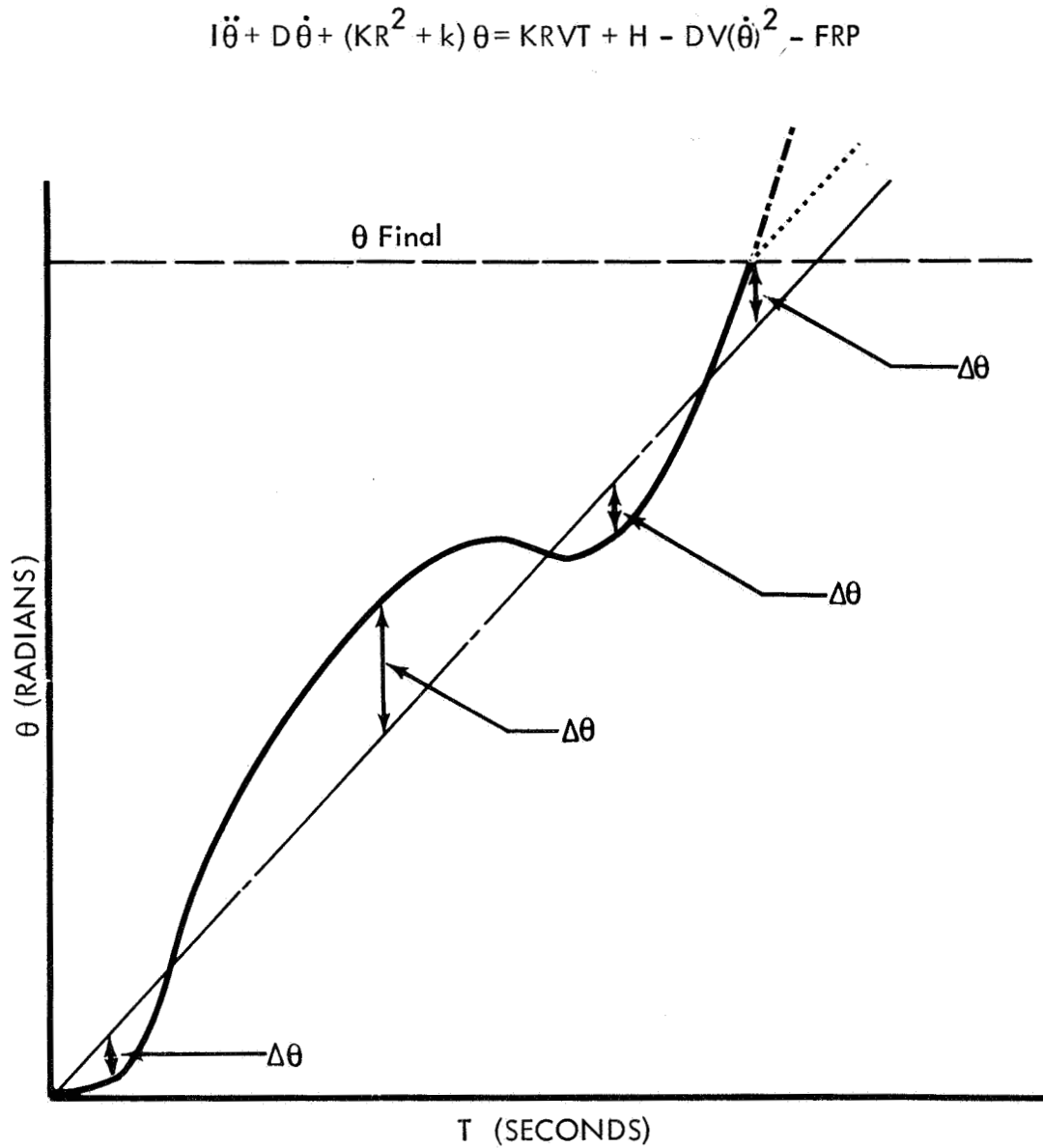
Figure 4-3:   DEPLOYMENT TIME-HISTORY ANALYTICAL EQUATION

Figure 4-4 illustrates the effect of an arbitrary, constant friction torque of 3 inch-pounds and 6 inch-pounds on the shape of the time-history curve. The energy absorbed by friction reduces the angle during which the cable is slack, and increases the number of crossings.

Friction torques in space can be caused by cable tension loads on the hinge pins and hinge-pin bending due to misalignments. Additional friction torques can result from GSE-induced hinge loads during ground deployment.

Figure 4-5 illustrates a time history, with initial conditions of velocity and slack cable resulting from the previous sequence.

4.3.3 MTA-3 TEST REQUIREMENTS

Useful tests for verification or modification of basic parameters have been defined.

The information needed to perform the MTA-4 time-history analysis is available from vendor data and the data resulting from manufacturing functional checkout, engineering equipment calibration, and MTA-3 mechanism and aerodynamic tests. The parameters for which data are required and the tests by which they are obtained are tabulated in Figure 4-6.

The first category of measured data, the no-load motor speed and the retarding spring torques, are design parameters. Reduction in the motor speed will result in a proportionate reduction in all main-panel deployment loads and an increase in deployment time. The retarding-spring torque controls the characteristic time-history shape. Vendor qualification and calibration measurements will show if design values are met. No-load motor speed will also be determined during an engineering calibration test.

A secondary category of measured data will verify expected parameter values. The motor-load speed, determined from measured values of motor angle versus time, is expected to vary little from the no-load motor speed. Track levelness and smoothness have been verified by test. Before each deployment test, levelness is measured and adjusted, if necessary. The combined effects of track levelness and smoothness and structural friction due to manufacturing misalignments are indicated during a manufacturing test, which allows each panel set to coast freely through its full deployment angle. An analytical prediction of initial (constant) velocity will be determined from an engineering test to calibrate the closing velocity resulting from suspension-line vertical angles, and the mechanism tests.
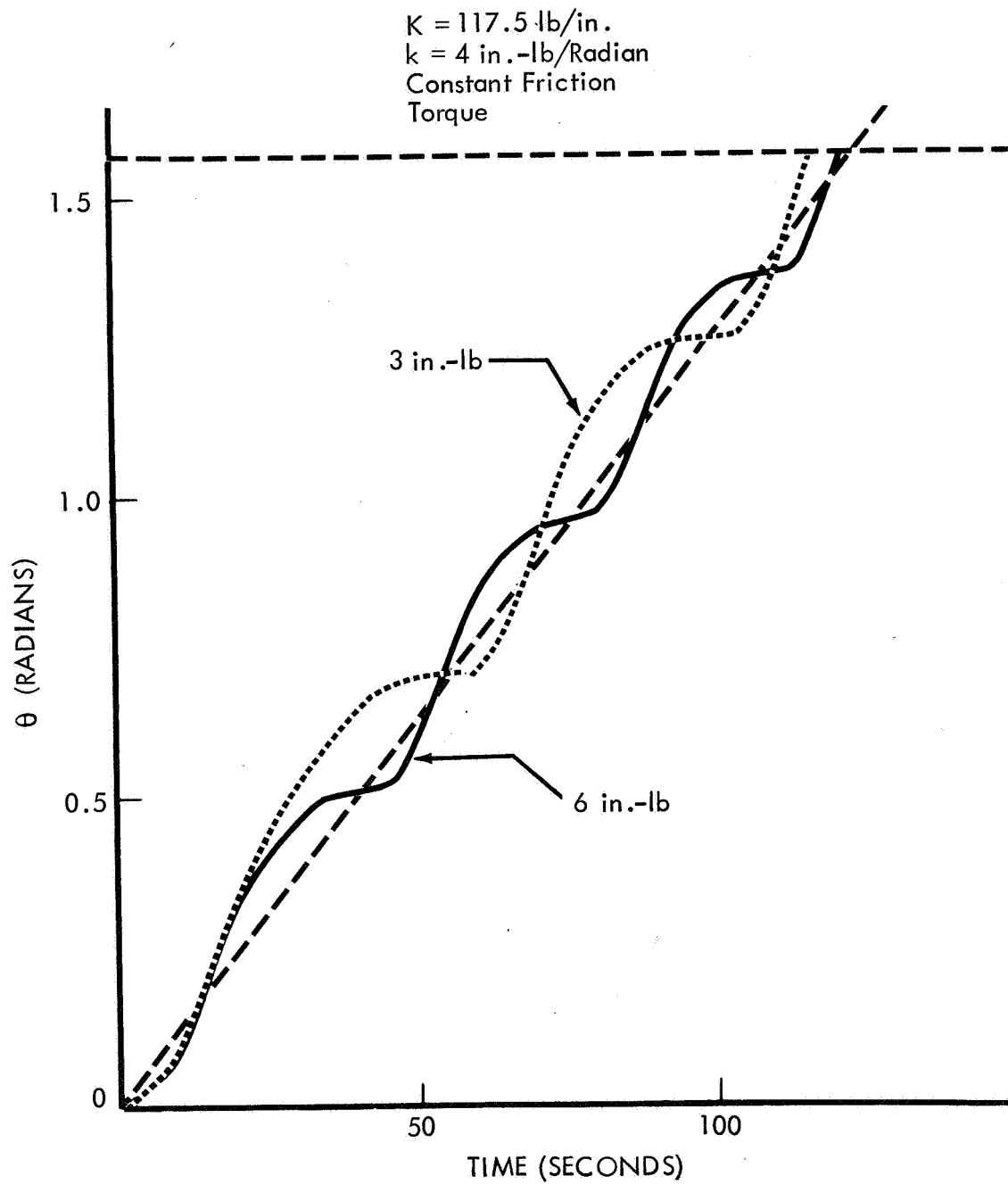
Figure 4-4: DEPLOYMENT TIME HISTORY
(First Sequence)

K = 40 lb/in.
k = 2.0 in.-lb/Radian
Initial Velocity =
  0.013 rad/sec
Initial Cable Tension =
  0.099 Radian (slack)
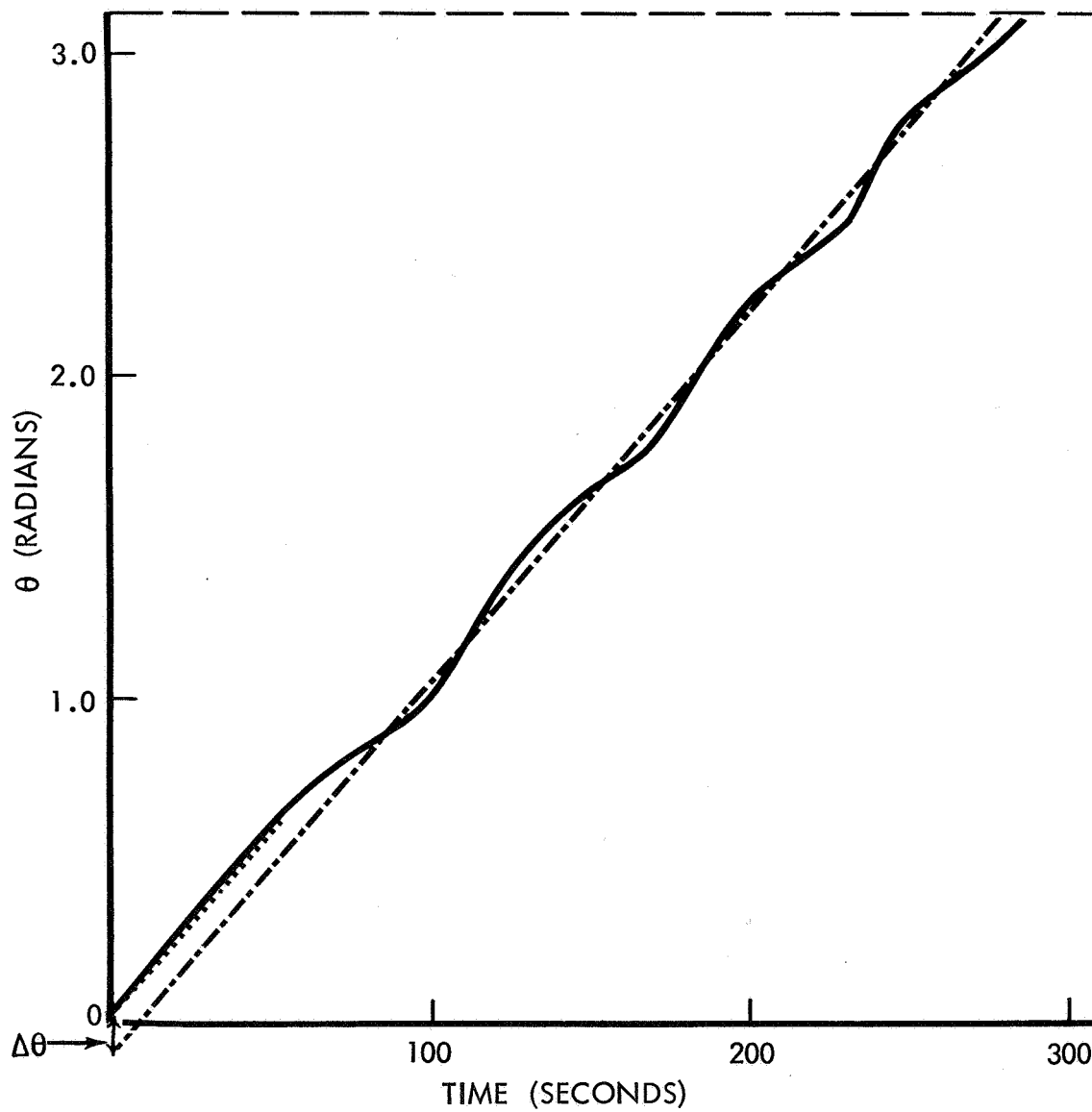
Figure 4-5: DEPLOYMENT TIME HISTORY
(Second Sequence)

Information Required	Test
● Design Variables	
Motor Speed (No Load)	Vendor Data, Engineering Equipment Calibration
Retarding Springs	Manufacturing Functional Checkout
● Verification	
Motor Speed (Loaded)	MTA-3 Mechanism Tests, Engineering Equipment Calibration
Track Levelness	Development Tests, Manufacturing Functional Checkout, Engineering Equipment Calibration
Friction	Manufacturing Functional Checkout
Initial Velocity	MTA-3 Mechanism Tests, Engineering Equipment Calibration
● Experimental Determination	
Cable Slip	SCM-I, MTA-3 Mechanism Tests, Engineering Equipment Calibration
Cable Stiffness	SCM-I
Deployment Angle	MTA-3 Mechanism Tests, Engineering Equipment Calibration
Cable Tension	MTA-3 Mechanism Tests, Engineering Equipment Calibration
Aerodynamic Drag	MTA-3 Mechanism, Aerodynamics Tests

Figure 4-6:   DATA CATEGORIES

A third category of data is experimentally determined. During small-component mechanism test SCM-1, static-friction force as it affects cable-tension and quadrant wrap angle will be measured. During the MTA-3 mechanism test and engineering checkout of the complete deployment procedure, measurements of motor speed, deployment angle, and cable tension will be taken to define actual deployment slip characteristics. The basic EA properties of the cable will also be determined during the SCM-1 tests. Aerodynamic drag is determined by comparison of MTA-3 time-history curves obtained during the mechanism and aerodynamic tests.

The GSE deployment equipment has been designed to minimize GSE-caused friction forces during deployment and perturbations caused by track levelness and smoothness. The panel and mechanism manufacturing tolerances have been specified to minimize construction misalignments that cause friction.

Tests will verify whether design values were met, or will define actual values where a range of values was assumed in the analysis. If measurements fall outside expected values, the measurements and analysis will define the problem area.

The deployment tests provide data to determine whether the 0.035 radian per second velocity will be exceeded at any point on the time-history curve, including at latching. Possible array-mechanism changes that would be made to adjust the closing velocity are:

1) Deploying motor-speed reduction;

2) Deploying cable stiffening;

3) Retarding spring rate change;

4) Incorporating an energy-absorbing damper;

5) Providing a ratchet on the hinges to prevent reverse motion;

6) Strengthening the hinge and latch members.

5.0 POWER-SOURCE ANALYSIS

The power-generation system consists of 192, 28-volt modules, and 584, 100-volt modules contained in four panels. The layout of the cells within a module was chosen to minimize electromagnetic fields.

With a cell area of 4.31 x 10^{-3} ft^2, and cell spacing of 0.010 by 0.020 inch, 1 square foot will contain 223 N/P front-connected cells. The total module area for the array is 4,590 square feet, giving an array generated power of 45.9 kw, based on 10 watts per square foot.

5.1 ELECTRICAL-POWER-SOURCE DESIGN

5.1.1 DEVELOPMENT OF SOLAR-CELL INTERCONNECTOR DESIGN

One interconnector design can be used to replace three parts with substantial tool cost savings.

The primary function of the solar cell interconnectors is to provide electrical continuity between cells within a module. They also provide the electrical connection between the module outputs and the power bus system. The configuration of the solar cell interconnectors is shown in Figure 5-1.

Four types of solar-cell interconnectors are required for the series-parallel wiring of the module:

1)   Positive termination (Detail III);

2)   Group-to-group connection (Detail I);

3)   Group-to-group connection at the end of a submodule or string (Detail IV);

4)   Negative termination (Detail II).

Because the first three types, 1, 2, and 3, are similar, an attempt was made to integrate their design to eliminate a specific tool for each part. Therefore, a method was developed to enable these three types of interconnectors to be made from one basic part, with substantial tool cost savings. The manufacturing procedure is described below.

The -1 part shown in Figure 5-1 is shear-cut and zee-formed in one combination die. This part is flattened, and the end tab is folded to make the positive termination. The -2 part for the group-to-group connection was made from the -1 part by cutting off the excess tab. The -3 part is made from the -1 part by flattening and cutting off the tab. The -4 part, flat and regular in shape, can be made with a straight shear operation. Close tolerances are required for all parts because of the close cell spacing.

DETAIL - III

-1
(JOINS STRING TO
POSITIVE TERMINAL)

DETAIL - I

-2
(JOINS GROUP TO GROUP)

-4
(JOINS STRING TO
NEGATIVE TERMINAL)

DETAIL - II

-4
(JOINS STRING TO
STRING)

-3
(JOINS STRING TO
STRING)

DETAIL - IV

Figure 5-1: CELL INTERCONNECTORS

FOLDOUT FRAME 2   5-3

-1

-2

-3

-4

FOLD LINE

FOLD LINE

DETAIL - IV

DETAIL - III

DETAIL - I

DETAIL - II

(-)(+)
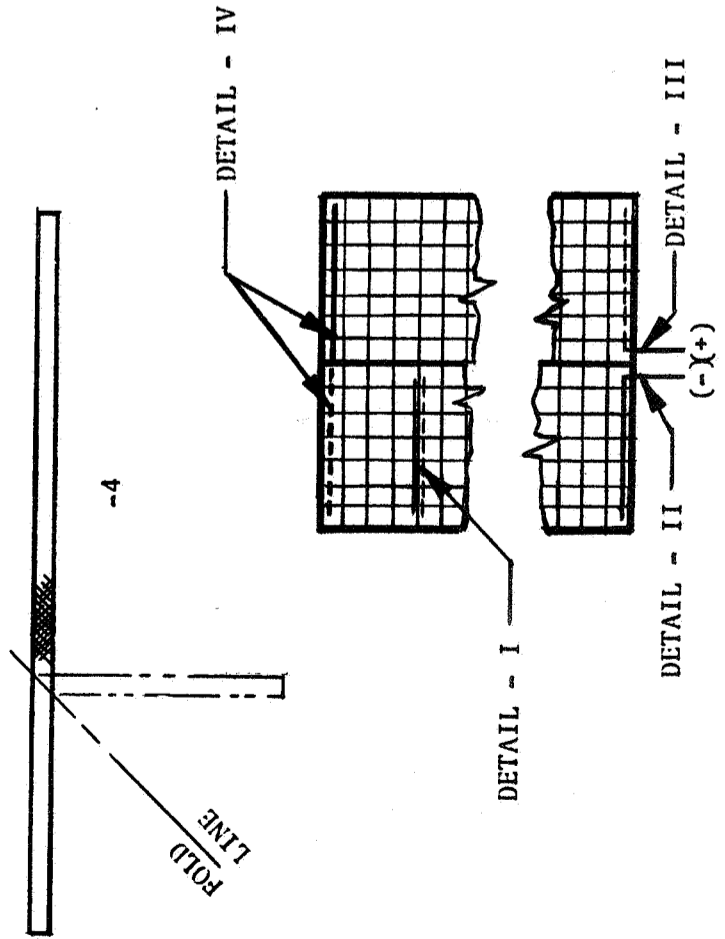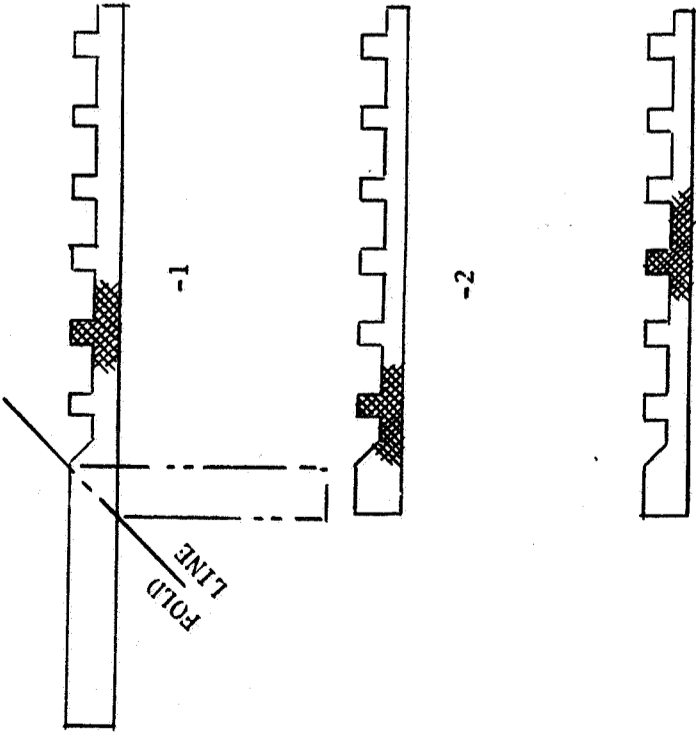
MODULE INTERCONNECTION
(TYPICAL)

FOLDOUT FRAME 1   5-2

The use of a simple cutting and forming die for three parts requires the use of a little more material; however, the tool can be constructed with a removable insert to make the -2 (short) parts without material waste. A cost estimate will determine the feasibility of the removable insert.

5.1.2 DEVELOPMENT OF SOLDERING PROCESS FOR SOLAR-CELL INTERCONNECTOR JOINTS

A pulse soldering process has been developed for use on solar-cell interconnector joints.

A pulse-soldering process using a Raytheon Weldpower Heat Programmer and weighted soldering electrode has been developed for use on solar-cell interconnector joints.

Five concepts were employed that contributed to the development of the soldering process by improving the soldering characteristics (flow and filleting) and/or peel strength of the interconnector joint. These were: (1) using paired solder spots for each joint, (2) flattening the solder areas on the interconnector to promote solder spot contact, (3) trimming the interconnector at exact node points to provide uniform heat transfer to the underlying solder spot for each solder operation, (4) using a weighted soldering electrode, and (5) soldering a single joint to compensate for surface irregularities.

The optimum pulse-heat setting for use in soldering was selected from a group of five diverse but workable settings on the basis of general filleting characteristics and a statistical evaluation of peel values of specimens. The optimum pulse-heat setting for the silver-mesh material with the equipment used was determined to be a pulse heat cycle comprised of a "weld" heat of 61% and a low heat of 20% at 5-kva output. For the tinned copper material, the equivalent settings were 57 and 80%, respectively, at the same output. The pulse soldering cycle is shown in Figure 5-2.
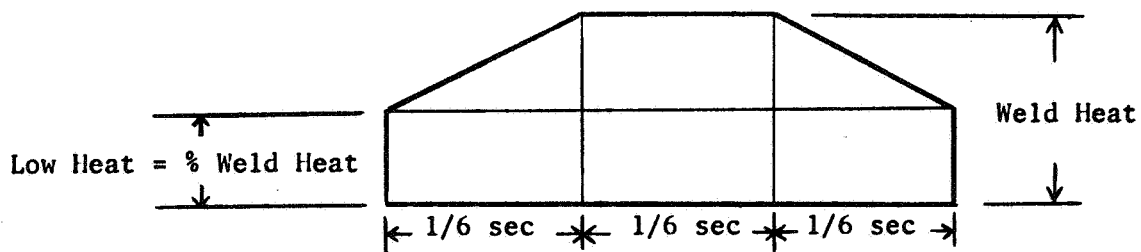
Figure 5-2: PULSE SOLDERING CYCLE

The best flux removal method was a dual solvent treatment using methyl-ethyl ketone and then ethanol.

The solder material used was Alpha No. 890-226 solder cream. The optimum composition was determined to be approximately 28% activated rosin flux plus volatiles and 72% 62Sn-36Pb-2Ag solder powder. The consistency of the solder cream during periods of extended usage can be measured using a Precision Scientific Company Penetrometer. Loss of volatiles in the solder cream can be detected, allowing compensation to be made.

The amount of solder residual on a solar cell after soldering and flux cleaning was small. For a cell with a full width connector attached, the weight of the solder was found to be about 1.6 milligrams.

5.1.3 DESIGN OF ELECTRICAL TERMINAL BRACKETS WITH SATISFACTORY ELECTRICAL AND MECHANICAL PROPERTIES

The electrical terminal-bracket design provides adequate mechanical support and allows for panel disassembly.

Terminal brackets are required at all crossover bus terminals. These brackets have several important functions. First, they provide mechanical support for the electrical junction between the flat bus termination and the crossover busses, which electrically connect adjacent subpanels. Second, they provide for easily detachable electrical terminals, which allows for panel disassembly. Third, they locate the crossover busses close to the subpanel hinge line to provide the shortest possible crossover bus length and minimum twist or bend during deployment.

The design of the terminal bracket must satisfy the following critical requirements.

1) It must be a good electrical insulator to ensure electrical isolation from structure.

2) It must have good mechanical strength to support the electrical terminal and crossover bus component during vibration and loading.

3) It must make a strong physical bond with the beryllium frame.

4) The electrical terminals must be detachable.

5) Materials must be space compatible and nonmagnetic. Surface finishes must be compatible to prevent electrogalvanic reactions while in a terrestrial atmosphere.

6) Electrical contact should be made directly between the surfaces involved. The nut and bolt should not be required to provide a conduction path.

The configuration of the terminal bracket and crossover bus terminal is shown in Figure 5-3. The selection of fiberglass for the bracket material is consistent with design requirements. Besides being light in weight, fiberglass is a good electrical insulator, mechanically strong, has good bondability, and is compatible with environment and other materials. The shape of the bracket is simple, an L-shaped angle. This makes manufacture easy and provides a large surface for bonding to structure. The mechanical strength of the bracket is easily controlled by specifying the number of glass-cloth layups to be used. Bolting the crossover bus terminals to the bracket provides firm attachment and easy disassembly. The terminal connection can be disassembled with two ordinary box or socket wrenches.

One disadvantage of fiberglass is that it does not have the malleability of some metals, and may tend to crack under the high-compressive loading of the nut and bolt. However, this condition can easily be overcome by the inclusion of a metal insert around the attaching bolt in the bracket where compression could be damaging.

5.1.4 ADVANTAGES OF DIODES FOR POWER-OUTPUT TESTS

Diodes provide the best method of circuit isolation for power-output tests.

The decision to use diodes is based on the requirement of circuit isolation of individual modules for power output measurements. Since the solar simulators do not have uniform outputs over areas as large as a subpanel, circuit isolation is required. If nonilluminated and partially illuminated modules are not isolated from the particular module being tested, they will act as an external load and meaningful data cannot be obtained.

An alternate to diodes for circuit isolation would be to leave all modules unwired from the main bus system. However, all modules would have to be wired for actual sunlight tests, where the composite module output is desired. For some test sequences, complete wiring and unwiring of modules might occur several times. This would be extremely time consuming and costly. Diodes, however, provide module isolation for solar-simulator testing, and also allow composite module output to be measured during sunlight testing.

The decision to use diodes on flight hardware would be made at some later date, when mission requirements are more precisely defined.

The diode installation configuration is shown in Figure 5-4. The diode case is bonded directly to structure to provide a conduction path for the heat generated in the diode. The diode leads are terminated at the bus tab and the module interconnector. A test jack is provided for power-output measurements.
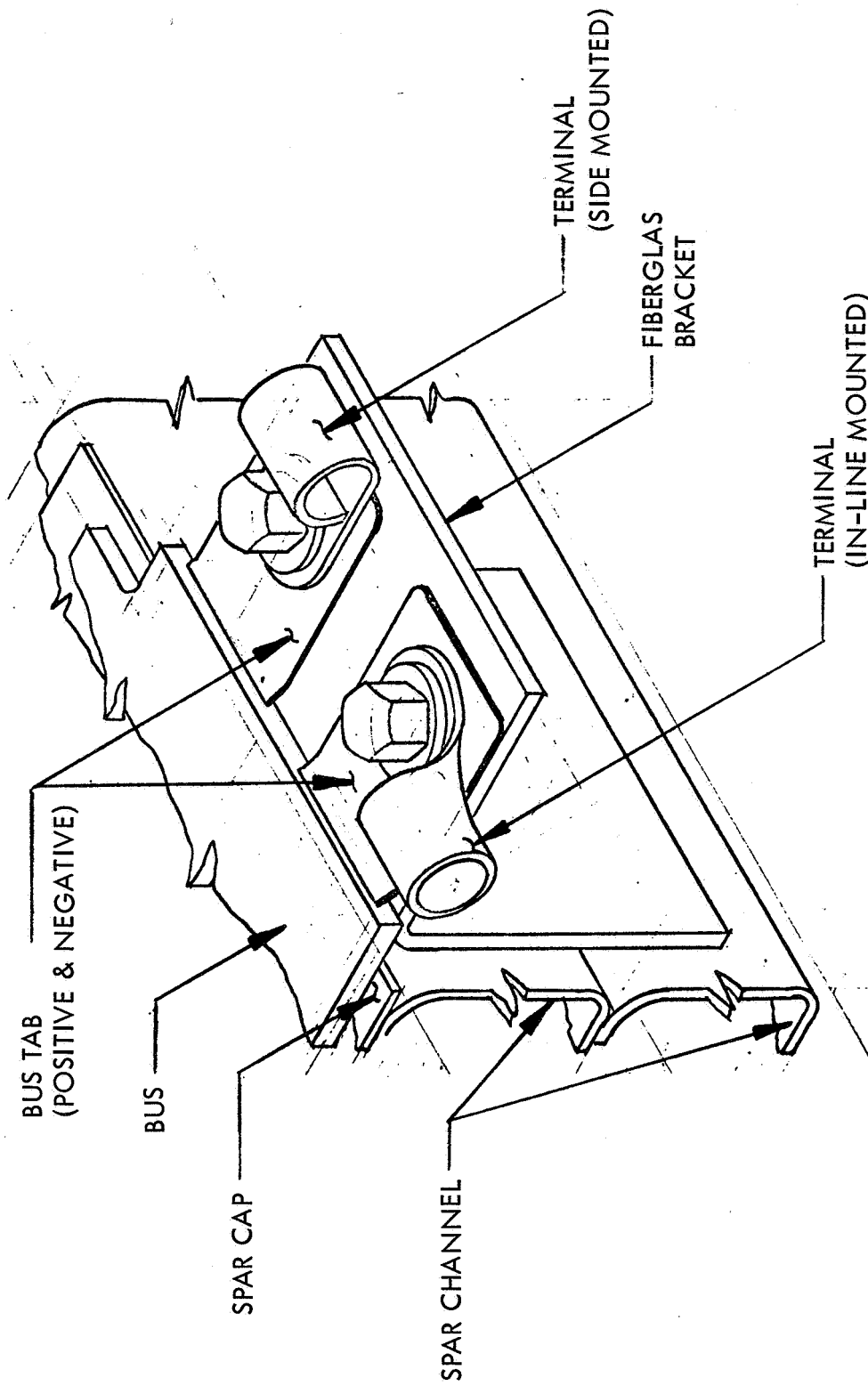
Figure 5-3: TERMINAL BRACKET
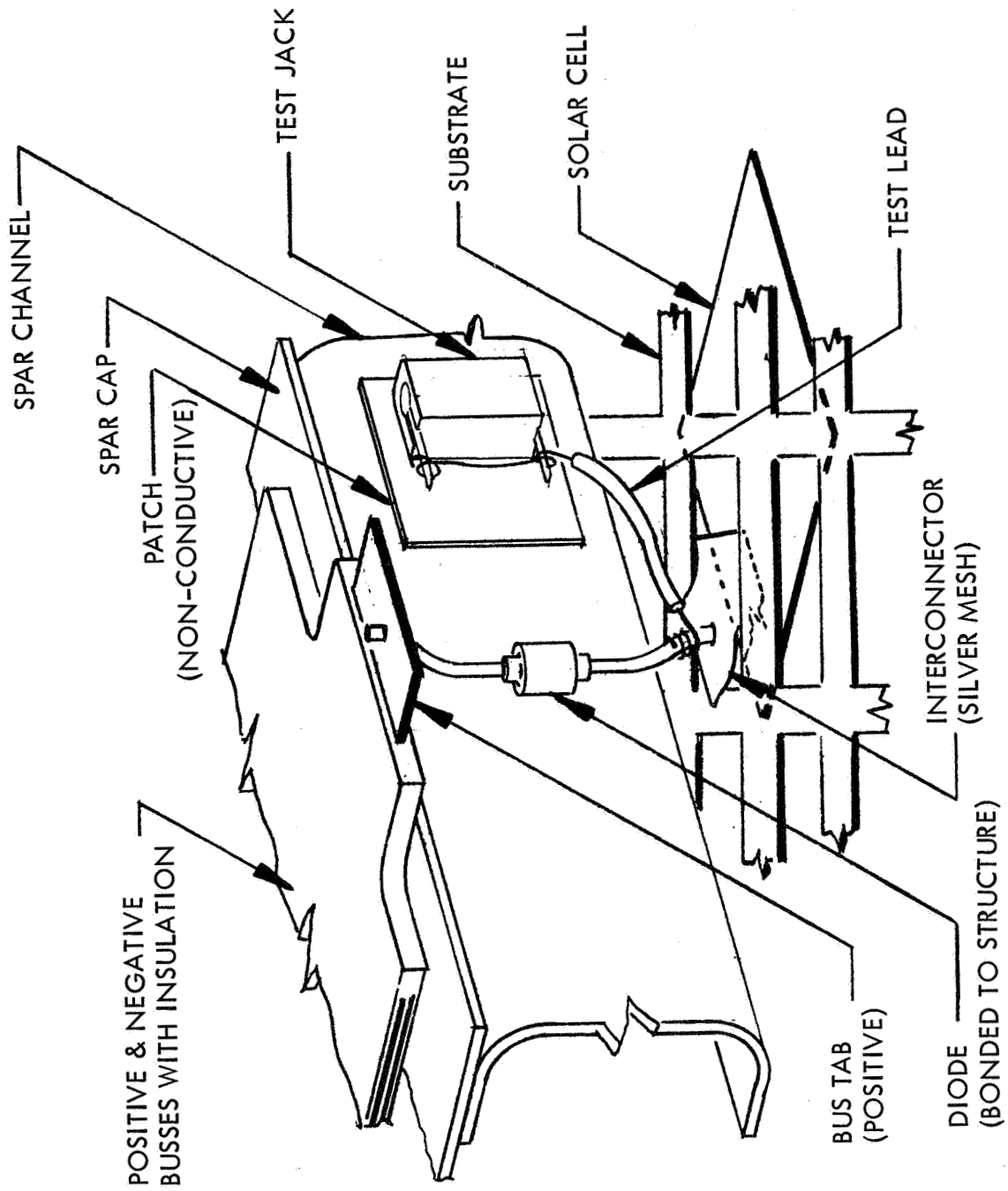
Figure 5-4: DIODE INSTALLATION

5.1.5 SUMMARY OF ELECTRIC-POWER DESIGN STUDIES

The electric-power system selected provides a lightweight system with low power loss.

To find a better power bus design, a trade study of busses and electric wiring was performed. Results of this study produced a concept for flat busses attached directly to structure. The original design, which used airplane-type wire, was found to be heavier, more difficult to terminate, and more vulnerable to physical damage than flat busses. High-purity aluminum (1100-H14) was selected for the high-current applications, and electrical-grade copper was selected for low-current use. The largest aluminum bus is 0.063-inch thick, and copper busses are 0.007-inch thick. A material search produced a silicone adhesive, RTV-630, for attaching the busses together and to the structure (Figure 5-5).

The original crossover busses were preformed beryllium-copper heat treated to acquire spring-like qualities. The spring resistance presented variable forces during deployment, and a new design was considered desirable. Results of the trade study produced a simple crossover that consists of straight-lay copper wire terminated in airplane-type lugs and insulated with self-adhesive, glass-fiber tape. Except for the insulation, the crossover bus is similar to welder's cable. These parts have no spring characteristics and are the same weight as the original crossovers. Crossover bus sizes vary from AWG Wire Size 14 to approximately 4. A typical bus is shown in Figure 5-6.

The type of material for the solar-cell interconnector was given a great deal of consideration. Plated molybdenum, Invar, and copper have all been used in spacecraft solar-cell systems, but none have the flexibility that is required for the semirigid construction employed by LASA. Plated materials were considered inferior to unplated, due to the variables encountered in the plating process. A comparison of plated copper versus pure silver showed small differences in cost and weight, and silver was selected. The high coefficient of thermal expansion for silver is offset by the inherent ductility of silver and by the mesh design. The silver foil is expanded to approximately twice its normal area by the mesh cutting and expanding operation. Foil of 0.002-inch thickness was considered to be adequate for both mechanical and electrical requirements. Plated molybdenum mesh was a possible choice until procurement was initiated. No vendor was interested in producing the small amounts required for Phase I testing. Silver mesh has proven satisfactory. Details of the silver mesh are shown in Figure 5-7.

Many configurations for the solar-cell interconnector were studied. Some of the considerations that affected the design were:

1) Accessibility of the rear contact for removal or repair;

2) Adequate cross section for the conduction of electric current;

4-Wire Copper Bus
Aluminum Bus
Structure
A-A

Sta. 118

Round Cable

Structure

A

A

To Spacecraft
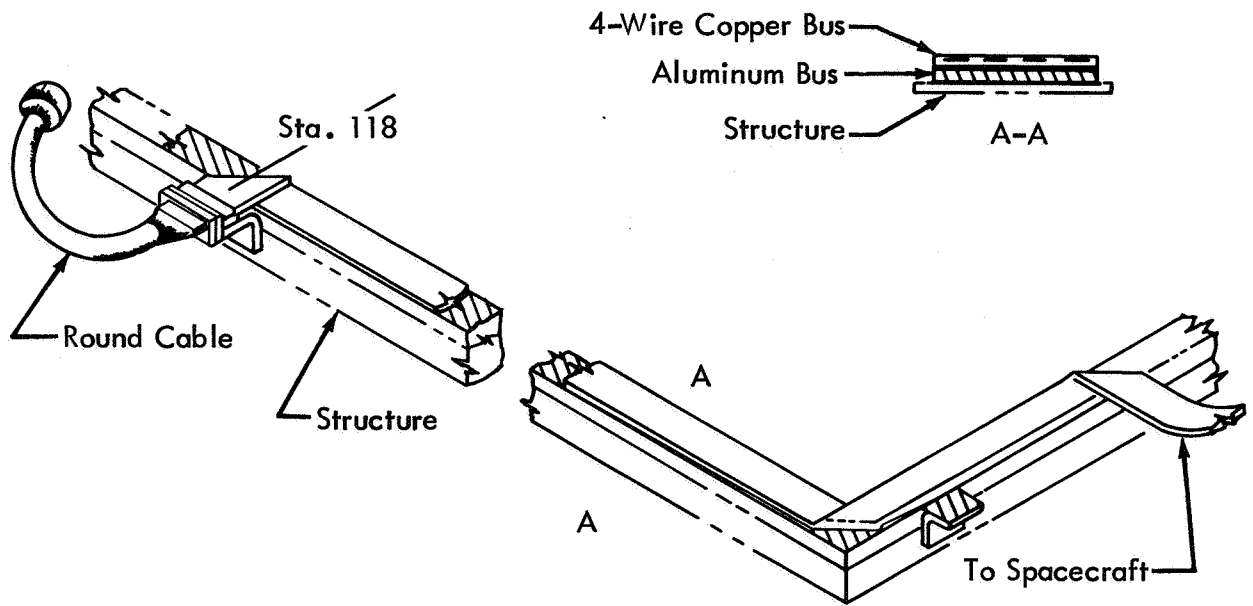
Figure 5-5:   BUS & BOOST TIE DOWN RELEASE WIRING

Structure

Straight
Terminal
Lug

Wrapped Cable

Glass Fiber
Bracket

Flag
Terminal
Lug

Bus Tabs

7.0
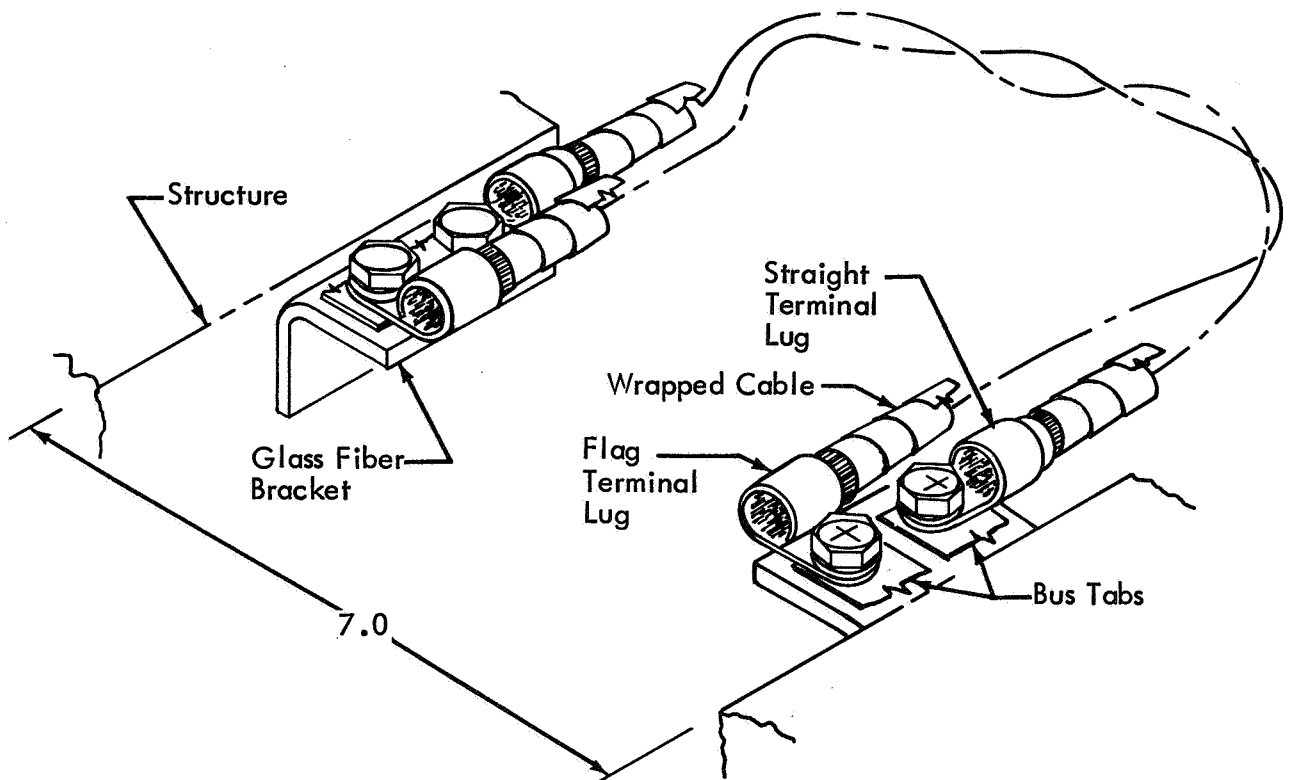
Figure 5-6:   MAIN CROSSOVER BUS
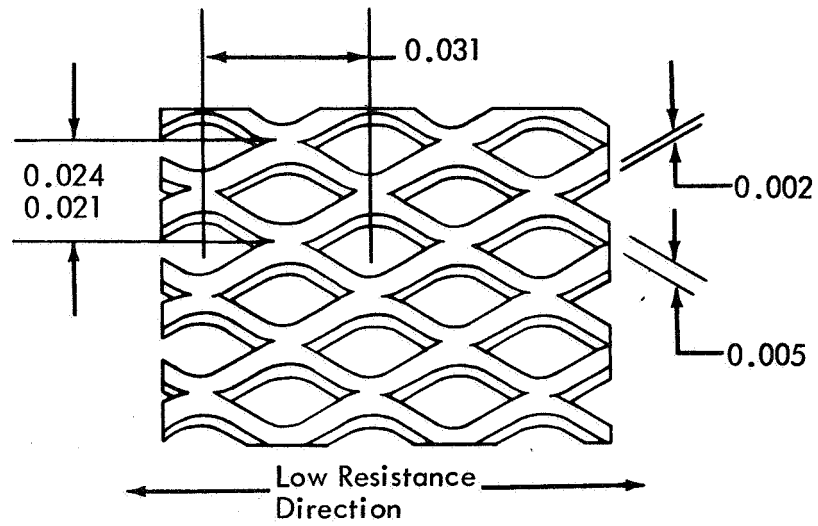
Figure 5-7:   DETAILS OF SILVER MESH MATERIAL
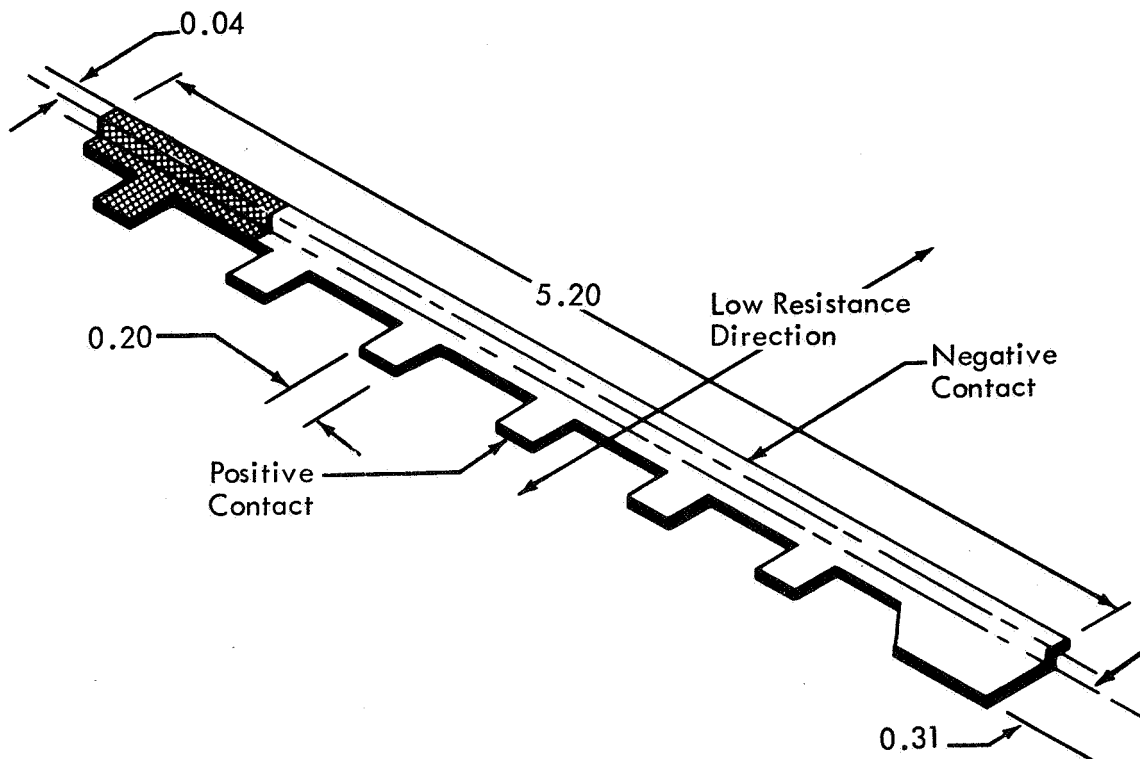
Figure 5-8:   SOLAR CELL INTERCONNECTOR

3)   Multiple use of one part to reduce tooling costs;

4)   Maximum physical strength because the part is inherently fragile.

The interconnector design shown in Figure 5-8, with the solder dot pattern shown in Figure 5-9, substantially meets all requirements.

The dimensions for the subpanel structure, as shown in studies previous to this contract, were not optimum for solar-cell layout. After many iterations of solar-cell layouts, the structure was redimensioned to achieve the following design goals:

1)   Eliminate the half modules on two subpanels;

2)   Each subpanel contains the maximum usable cell space;

3)   Module design has one standard size and shape;

4)   Cell layout minimizes electromagnetic fields.

These design goals were achieved and incorporated in MTA-1.

Cell spacing studies were made to determine the effect of cell spacing on array weight. Small changes in cell spacing have a considerable affect on weight; however, other factors, mainly structural, limited cell spacing choices. First, maximum structural envelope dimensions are defined; second, solar cells that are directly over the intercostal must be wholly over the intercostal because of possible cell breakage on launch. When these requirements were satisfied, the choice of cell spacing was limited. A power-generation summary is shown in Table 5-1.

5.2   ANALYSIS OF ELECTRICAL-POWER-SOURCE PERFORMANCE

5.2.1   POWER REDUCTION FROM RADIATION DEGRADATION

The baseline solar-cell stack assembly consisting of a 3-mil coverglass and an 8-mil cell will have acceptable radiation degradation characteristics for the 350-day reference trajectory.

For missions that do not include Earth orbits, essentially all radiation damage to cells is from protons emanating from the Sun. Various solar-cell coverglass shields have been used, such as quartz, sapphire, and special glasses. The coverglass selected for LASA is Corning Microsheet Code 0211, 3 mils thick. Because the coverglass does not completely protect the solar cell from damage, it is necessary to calculate the expected power decrease from radiation and to add a suitable area of cells to the array to compensate for the loss.

0.084
0.250
0.023

Solder Pair
(5 Places – Dark Side)
0.200

Sun

Sym

Solder
Pair
(4 Places–
Sun Side)

0.730
0.630
0.530

0.033 Dia (Typ)
0.043 (Typ)

Solder Pair
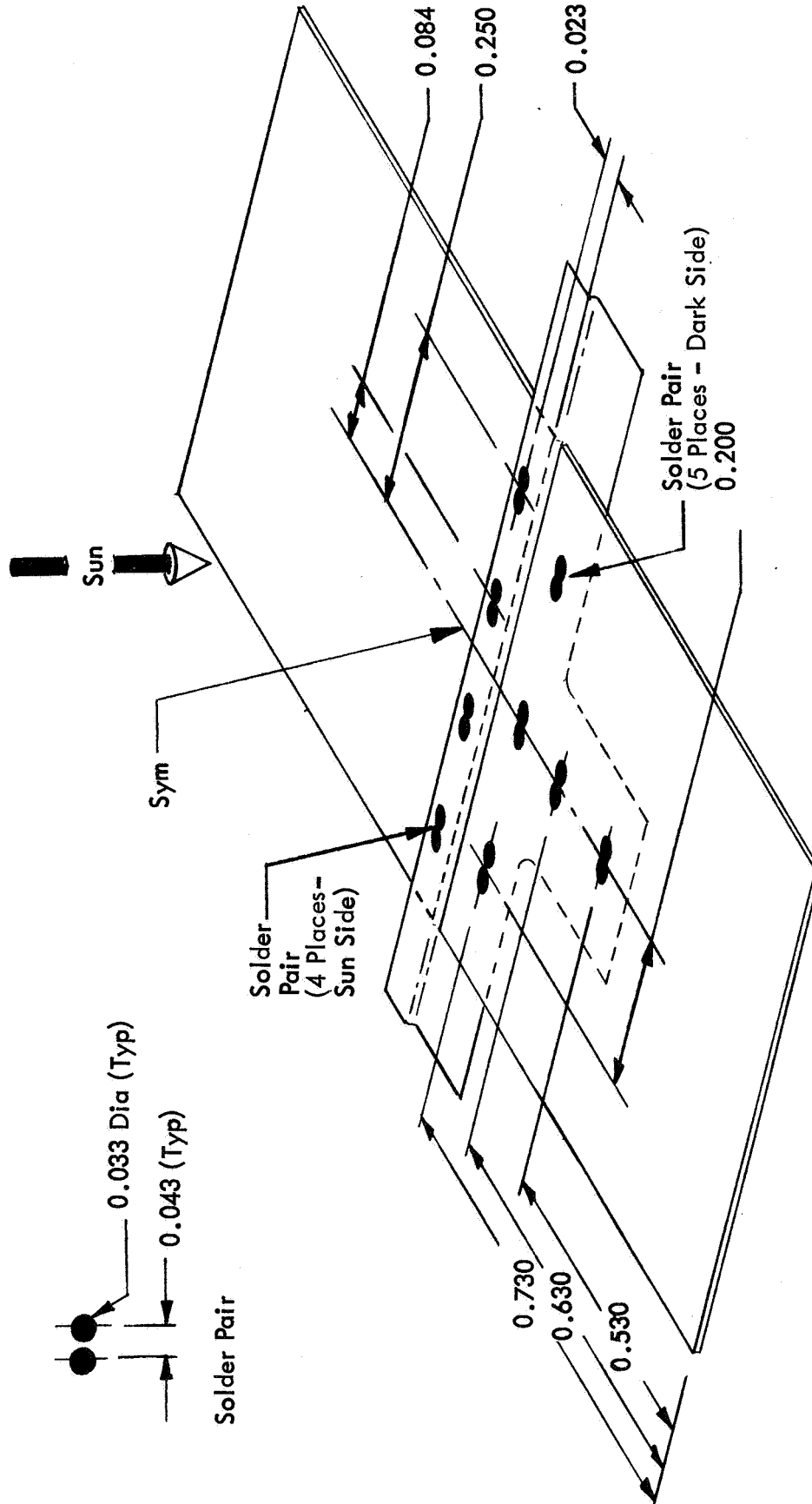
Figure 5-9:   SOLDER DOT PATTERN

Table 5-1: POWER-GENERATION SUMMARY

	Per Cell	Per Module		Per Main Subpanel					Per Panel	Per Array	Remarks
		28v	100v	1	2	3	4	5			
Number of Cells	–	406	1624	22,736	22,736	19,488	19,488	16,240	256,592	1,026,368	
Number of 28-volt Modules	–	–	–	48	0	0	0	0	48	192	
Number of 100-volt Modules	–	–	–	2	14	12	12	10	146	584	
Voltage @ 1.0 AU & 55°C	0.43v	25v	99v	–	–	–	–	–	–	–	
Voltage @ 1.67 AU & 55°C	0.55v	32v	127v	–	–	–	–	–	–	–	
Power & 1.0 AU & 55°C	0.44w	17.6w	71.5w	1.08kw	1.08kw	853w	853w	715w	11.3kw	45kw	Bus Loss Not Considered
Power @ 1.67 AU & 55°C	0.176w	6.85w	28.4w	402w	402w	343w	343w	284w	4.9kw	19.6kw	Bus Loss Not Considered
Gross Deployed Area	–	–	–	–	–	–	–	–	–	4924 ft^2	
Net Module Area	–	–	–	–	–	–	–	–	–	4590 ft^2	

A procedure presently accepted for analyzing the effects of radiation on the efficiency of the solar cells is to convert all radiation to equivalent 1-mev electrons, and to use the following assumptions:

1) Protons are the only significant damaging particle in an Earth-to-Mars trajectory;

2) The fluence of protons emanating from the Sun is inversely proportional to the distance squared.

The degradation constants used in the calculations were obtained from referenced documents (see Section 11.0). Details of the analysis are not repeated here.

Proton fluence depends on sunspot number. The maximum expected is 170; however, for the coming cycle, sunspot number will probably not exceed 112. Minimum that occurs is approximately 10. Damage has been calculated for each of these conditions.

Protons (2.8 mev) have a penetration range of 3 mils in quartz. The coverglasses of interest are Corning Microsheet Code 0211, which has a greater density than quartz. Results using the 2.8-mev value should be conservative.

From W.R. Doherty's work, the following values are obtained for the equivalent 1-mev fluence at 1 AU:

Sunspot number = 10

$$\phi_{eq} = 2.10 \times 10^{11} \ cm^{-2} year^{-1}$$

Sunspot number = 112

$$\phi_{eq} = 3.6 \times 10^{14} \ cm^{-2} year^{-1}$$

Sunspot number = 170

$$\phi_{eq} = 1.32 \times 10^{15} \ cm^{-2} year^{-1}.$$

These values do not assume a sharp cutoff of proton penetration at 2.8 mev as is often assumed for thicker coverglasses. Doherty has provided the above values as the result of a computer analysis made subsequent to the issuance of the referenced memorandum (see Reference 12, Section 11.0).

Figure 5-10 shows the flight time versus distance from the Sun for the Earth-Mars trajectory. With this information and the predicted fluence at 1 AU, the curves of Figure 5-11 may be obtained. Figure 5-11 provides the integrated fluence of equivalent electrons versus flight time, assuming an inverse square relationship with distance from the Sun. The curves of Figure 5-12 have been obtained from laboratory investigations of the effects of electron radiation on solar-cell efficiency. The information shown in Figure 5-12, plus that of the equivalent electron
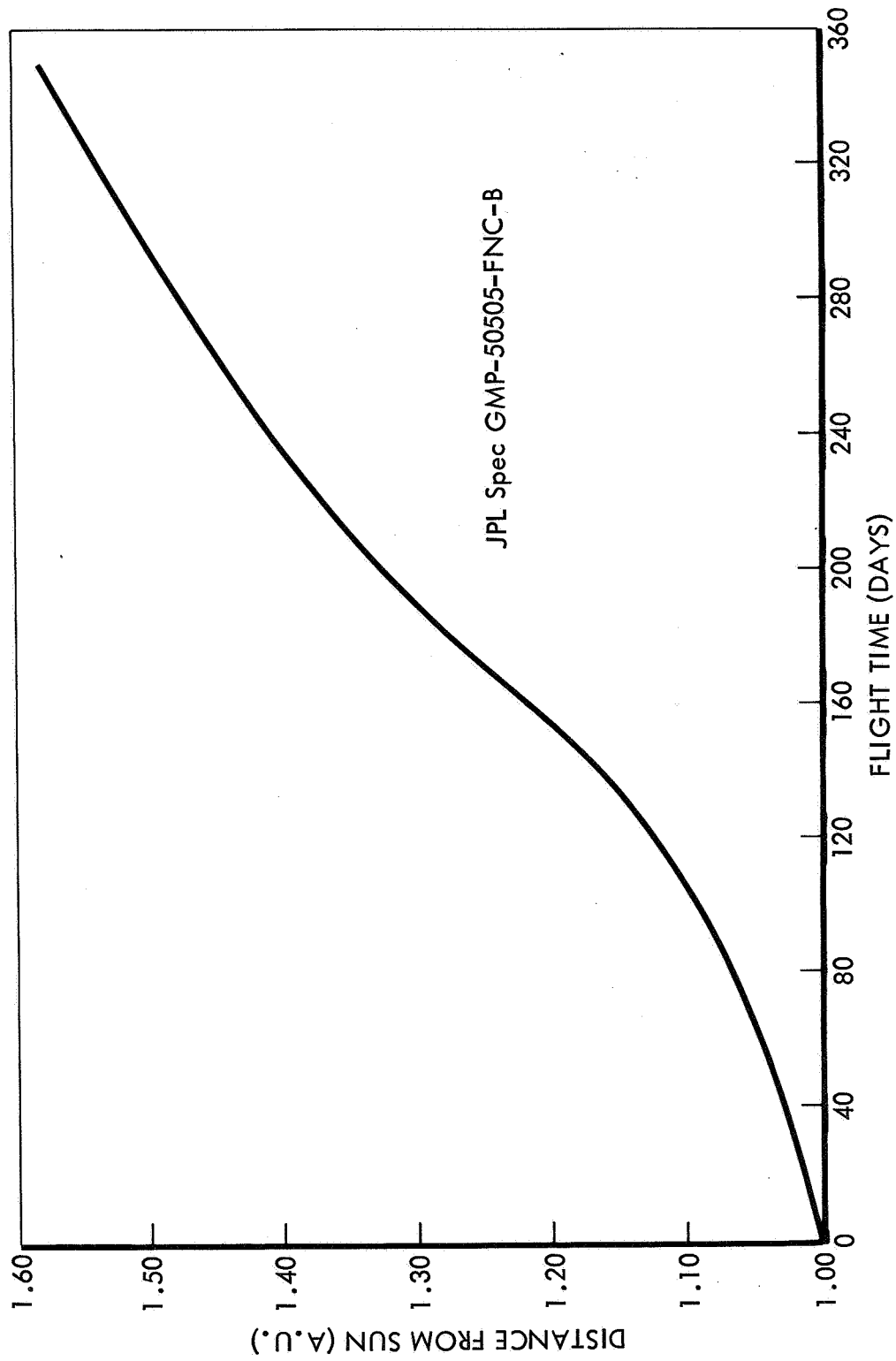
Figure 5-10: DISTANCE FROM SUN VERSUS TIME FOR EARTH-MARS —
Reference Trajectory Rendezvous
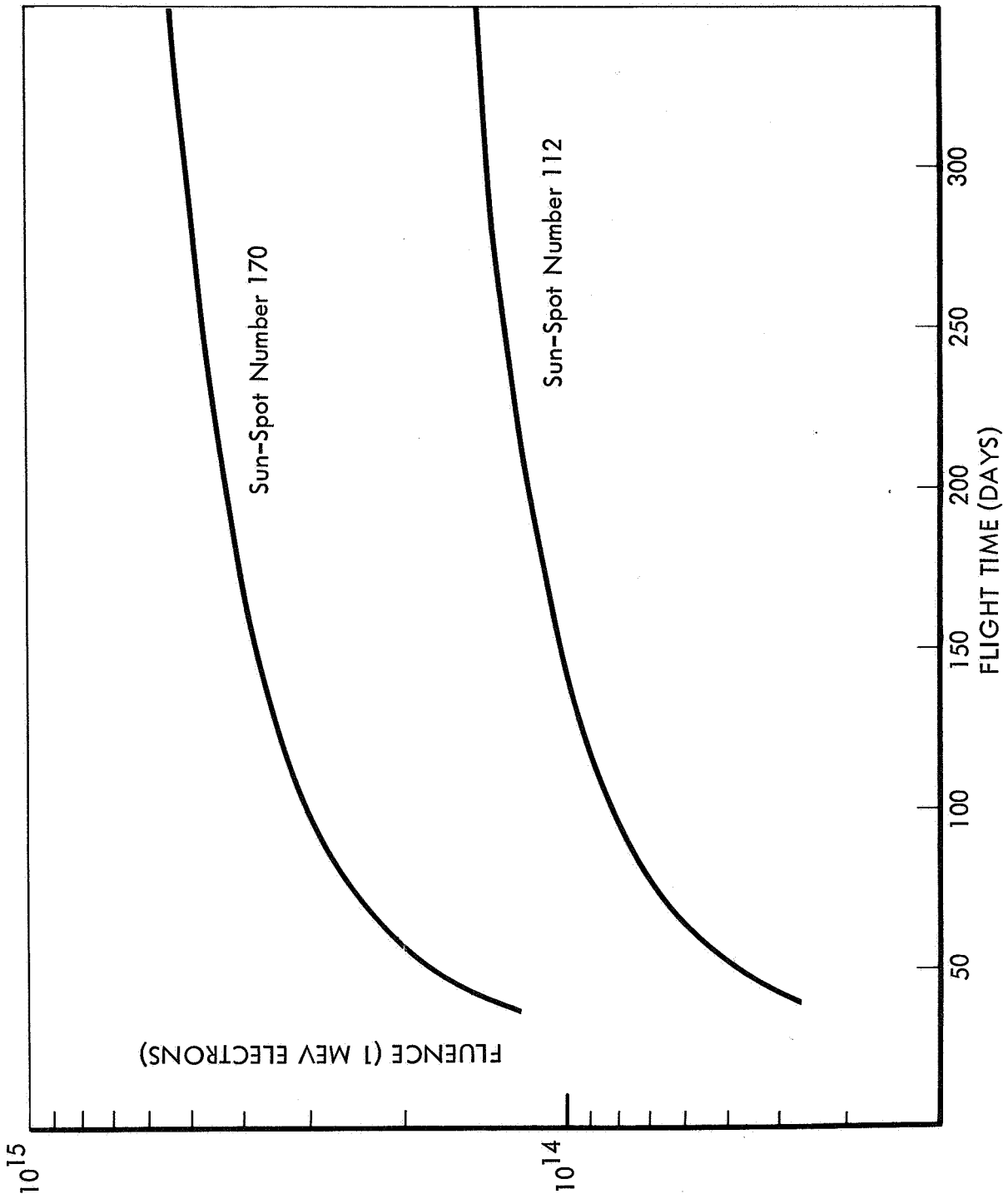
Figure 5-11:   FLUENCE VERSUS FLIGHT TIME AND SUN-SPOT NUMBER
FOR EARTH-MARS TRAJECTORY RENDEZVOUS
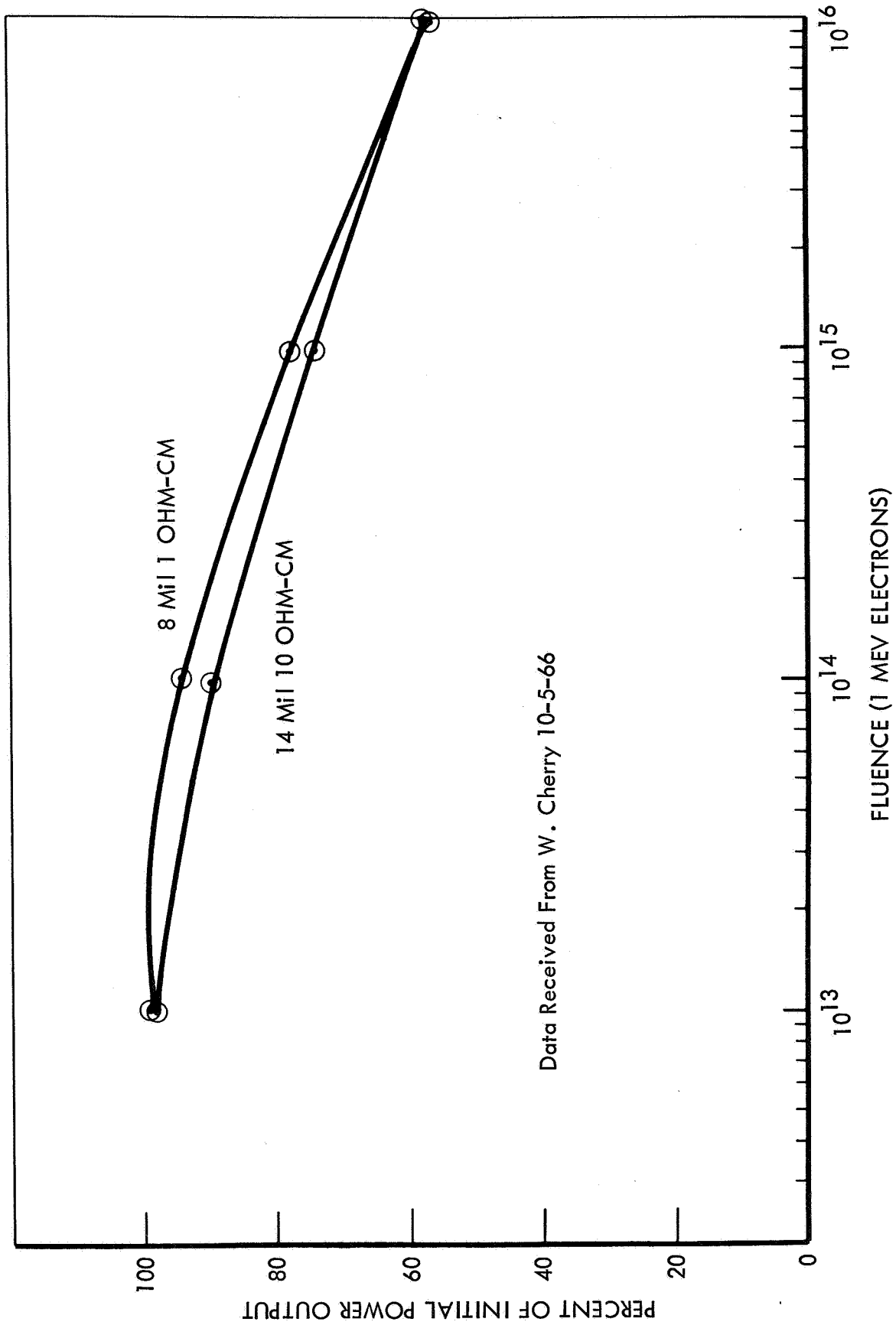
Figure 5-12:   RADIATION DEGRADATION CHARACTERISTICS OF
8-MIL / 14-MIL-THICK HELIOTEK SOLAR CELLS

fluence of Figure 5-11, can then be used to obtain the objective results of power versus flight time for Sunspot Numbers 112 and 170. Power-output versus flight time is shown in Figure 5-13 of this section.

Data on the radiation degradation characteristics of 8-mil-thick, 1-ohm-cm resistivity cells show less than 8% reduction in power due to radiation for the coming sunspot cycle with the reference trajectory.

5.2.2 SOLAR-CELL INTERCONNECTOR CONFIGURATION AND RESISTANCE

Mechanical stress on the cell-to-interconnector cell joints and the electrical resistance of the interconnectors will not adversely affect array performance.

Two areas of stress in the interconnector can be reasonably well defined: thermal stresses and loading stresses. The coefficient of thermal expansion of the substrate is 4.8×10^{-6} in./in./°F. The distance between cells is nominally 0.020 inch. With a 400°F change, the dimensional change is 38.4×10^{-6} inch. This change would have negligible effect on stresses. The maximum load expected on a substrate tape is 20 pounds. The modulus of elasticity of the tape is 8.4×10^{6} psi. With a 0.003-by 0.14-inch tape, the elongation between cells is 0.11×10^{-8} inch. The tape installation tolerances are considerably larger than 0.1 mil; therefore, the mechanical loading on the tape does not constrain the connector design. With 0.020 inch between the ends of cells, the distance between N and P connections is 0.0224 inch. Figure 5-14 shows the interconnector design. With this design, the distance between series groups may change by 18% without stressing the interconnector-to-cell solder joint.

A critical parameter in the evaluation of the interconnector was the determination of interconnector resistance. Specifications require that the resistance of the interconnector, plus solder, do not exceed 2% of the cell-series resistance.

Resistance of the interconnector and solder joint was measured, and results are shown in Table 5-2. The average resistance was 0.0014 ohm for the interconnector and joint. This is 0.7% of the average cell resistance shown in Table 5-3. The effect of power-output series resistance is shown in Figure 5-15. The resistance from the interconnector and joint will not significantly affect performance of the array.
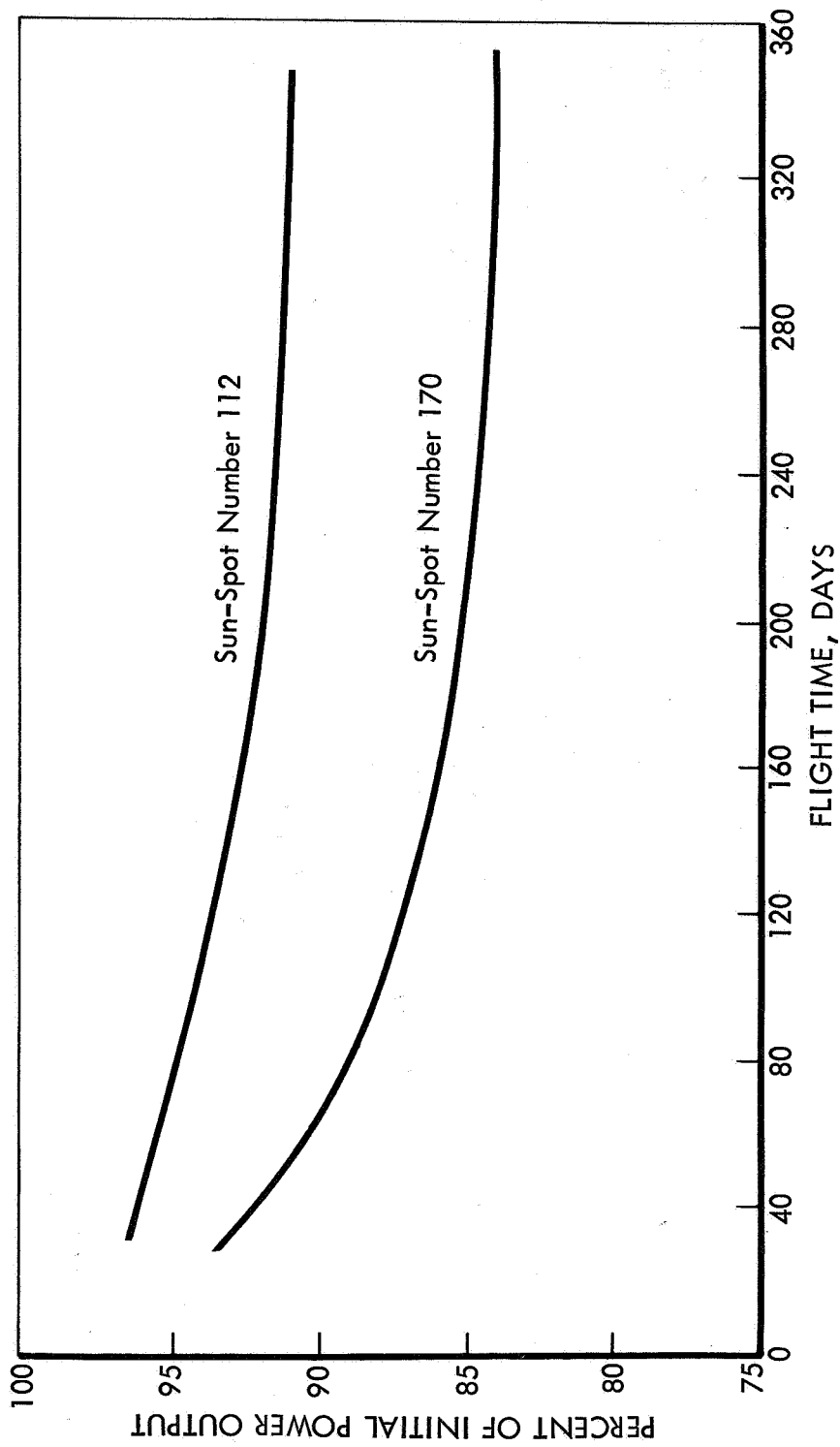
Figure 5-13: RADIATION DEGRADATION CHARACTERISTICS
VERSUS FLIGHT TIME FOR EARTH-MARS TRAJECTORY RENDEZVOUS
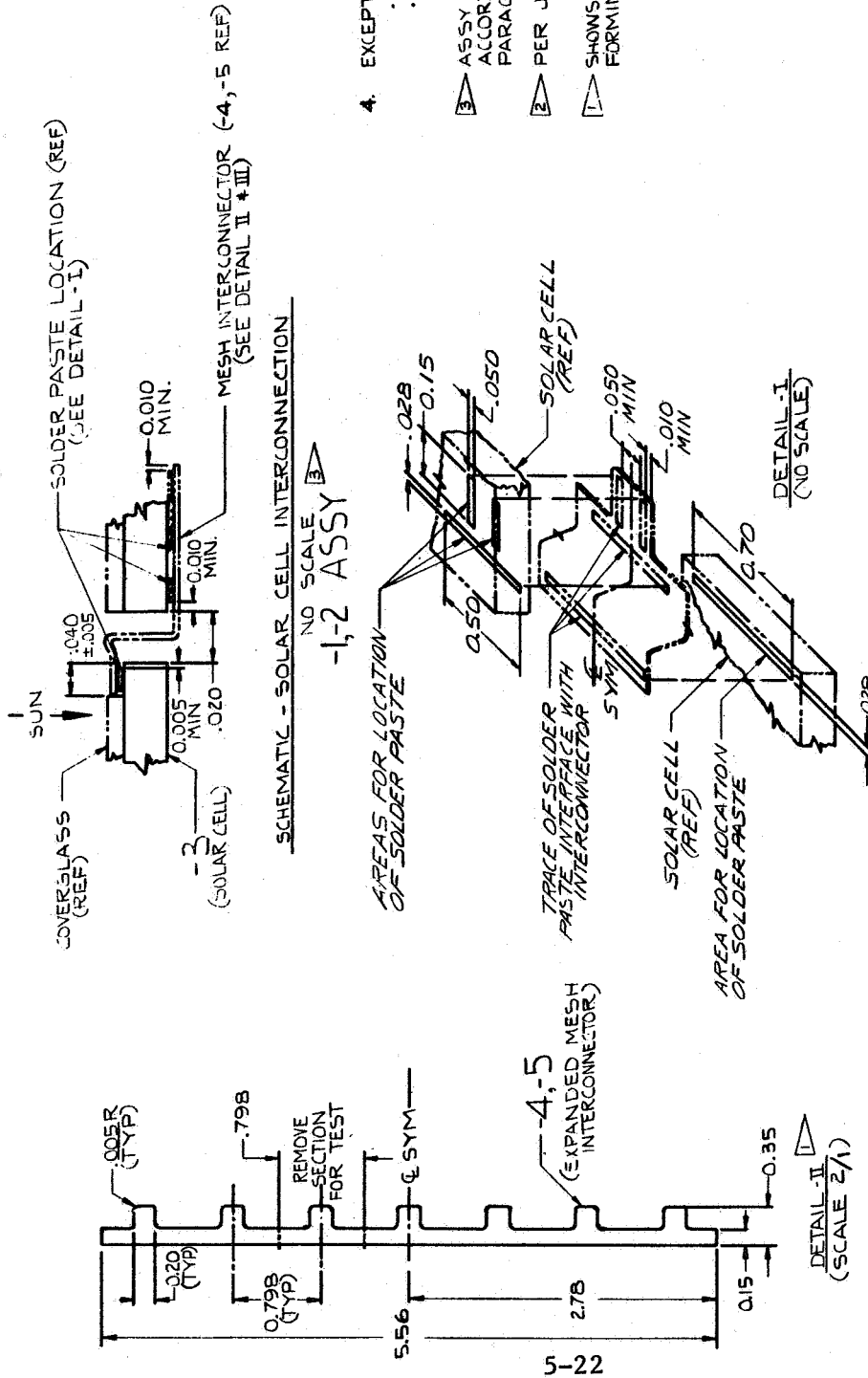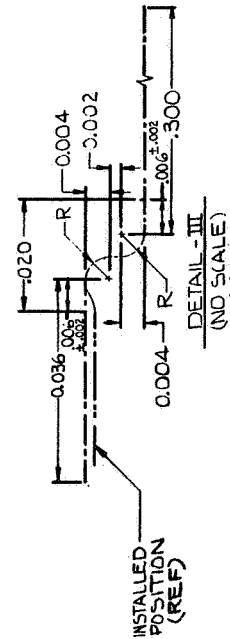
Figure 5-14:   SCC-3 TEST — ARTICLE SOLAR-CELL INTERCONNECTOR
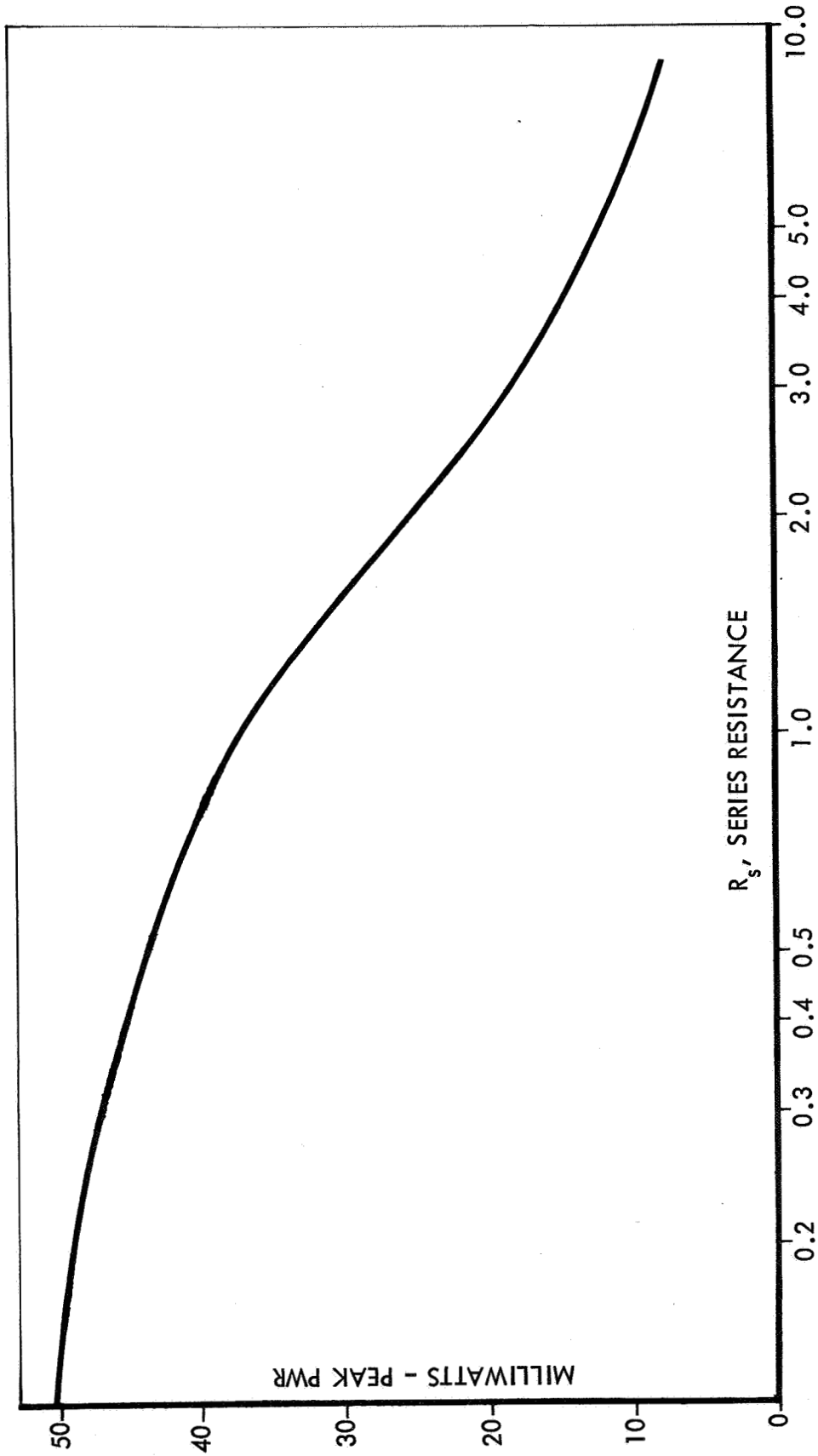
Figure 5-15: VARIATION OF SOLAR-CELL POWER WITH SERIES RESISTANCE

Table 5-2:   INTERCONNECTOR AND SOLDER-JOINT RESISTANCE

Cell	Joint	Uncorrected Resistance (ohm)	Corrected Resistance* (ohm)
118	N	0.001372	0.001320
360	N	0.001636	0.001584
361	P	0.001877	0.001825
362	P	0.001998	0.001946
363	N	0.001353	0.001301
369	P	0.001563	0.001511
375	N	0.001627	0.001575
918	P	0.001903	0.001851
919	N	0.001585	0.001533
920	P	0.002561	0.002509

*Corrected for lead resistance of 0.000052 ohm.

A specified requirement was that the interconnector and joints exhibit stable physical and electrical characteristics in both space and terrestrial environments. Three tests were made to ensure that these requirements were met.

1)   Silver-mesh interconnectors were soldered to the cell in preparation for evaluation. Subsequent to the soldering operation, each test article was thermal-cycled between +75 and -100°C for 100 cycles. Parameters measured before and after processing were open-circuit voltage, short-circuit current, current at the maximum power voltage, and the series resistance.

2)   Cells were illuminated for the short-circuit current, open-circuit voltage, and current at 0.47 volt, with the Xenon light source at an intensity of 100 milliwatts per square centimeter, as determined by the Heliotek Standard Cell 130. The test cell mounting block was maintained at 28 ±1°C.

3)   The cells series resistances were obtained by forward-biasing the cell, without illumination and at a temperature of 28 ±1°C. The voltage was read at current values in the ranges of 185 to 190 and 210 to 215 milliamperes. The series resistance of the cells was calculated from the ratio of the difference of the voltages to the difference of the currents.

Data obtained from tests made before and after processing of cells are tabulated in Table 5-3. "Before" indicates data obtained on the test article prior to soldering of interconnector to the cell. "After" indicates data obtained on the test article after the interconnector has been soldered to the cell and thermal cycled. Under the heading "Joint," N indicates the interconnector was soldered to the N electrode, and P indicates a solder joint to the cell P electrode.

Table 5-3: SOLAR-CELL CHARACTERISTICS BEFORE AND AFTER SOLDER OF INTERCONNECTORS AND THERMAL CYCLING

Cell	Joint	Short-Circuit Current (ma)			Open-Circuit Voltage (volts)			Current at 0.47v (ma)			Series Resistance (ohms)		
		B Before	A After	A-B	B Before	A After	A-B	B Before	A After	A-B	B Before	A After	B-A
17	N	96.0	98.2	2.2	0.560	0.560	0				0.211	0.208	0.003
129	P	94.0	94.2	0.2	0.566	0.560	0.006	88.0	91.5	3.5	--	0.212	--
130	P	98.5	99.2	0.7	0.565	0.560	0.005	91.0	89.5	-1.5	--	0.208	--
390	N	99.5	100.6	0.8	0.566	0.567	0.001	89.3	91.8	2.5	0.188	0.232	0.044
391	P	100.5	100.2	0.3	0.566	0.567	0.001	89.6	89.3	-0.3	0.225	0.232	0.007
393	P	99.5	97.1	-2.4	0.565	0.565	0	89.5	88.2	-1.3	0.212	0.232	0.020
394	P	95.0	95.8	0.8	0.562	0.559	-0.003	86.3	87.0	0.7	0.196	0.196	0
395	N	100.2	100.8	0.6	0.567	0.574	0.007	90.6	92.0	1.4	0.248	0.232	-0.016
396	N	96.8	99.3	1.5	0.573	0.565	-0.008	87.2	90.3	3.1	0.196	0.196	0
956	P	101.7	98.0	-3.7	0.570	0.561	-0.009	92.4	90.0	2.4	0.224	0.236	0.012
963	N	99.5	101.0	1.5	0.570	0.558	-0.012	90.0	91.9	1.9	0.224	0.200	-0.024
965	P	100.5	99.9	-0.6	0.575	0.563	-0.008	91.8	91.6	-0.2	0.212	0.216	0.004
966	N	99.0	100.5	1.5	0.569	0.565	-0.004	90.3	90.3	0	0.212	0.230	0.008

The approach to data analysis was to use accepted statistical methods in determining whether a significant change had occurred in the data before and after processing. These statistical methods permitted assessment of the confidence level of the conclusions made. The F-test and the t-test were used for this purpose. The F-test is a method of determining whether a significant difference exists between the variances of two data groups.

$$F_o = \frac{s_1^2}{s_2^2}$$

where:

s_1^2 is the variance of Data Group 1; s_2^2 is the variance of Data Group 2. Variance is a measure of dispersion of a frequency distribution.

Calculation and use of variance and standard deviations will not be additionally defined because they were found in standard texts and the given references.

The t-test is used to test for the significance of the difference between two means. This test determines if the difference between the means may be due to chance, and that the process has not necessarily made a change in the characteristics of the cells; or it determines that the two process averages do differ with any desired degree of certainty.

F_o and t_o were the values calculated from the data. F and t values were obtained from R.A. Fisher's, *Statistical Methods for Research Workers*, and Snedecor's, *Statistical Methods*.

B = before processing   A = after processing

	Short-Circuit Current (ma)			Open-Circuit Voltage (volts)		
	B	A	A-B	B	A	A-B
Mean:	98.5	98.8	0.22	0.567	0.563	-0.0035
Std Deviation:	2.25	2.09	1.66	0.0039	0.0044	0.00522
F_o:		1.16			1.24	
F:		2.66			2.66	
t_o:		0.48			2.44	
t:		2.16			1.16	
A-B, Limit of Mean, 90% Confidence:					0.00106 to 0.0113	

	Current at 0.47 Volt (ma)			Series Resistance (ohms)		
	B	A	A-B	B	A	B-A
Mean:	89.6	90.3	0.62	0.21	0.22	0.0047
Std Deviation:	1.72	1.59	1.89	0.016	0.015	0.0179
F_o:		1.17			1.21	
F:		2.79			2.72	
t_o:		1.13			0.88	
t:		2.17			2.20	

F and t were determined at the 95% level.

As indicated by comparison of the F and t values, no statistically significant change in either the mean or the variance has occurred in the short-circuit current, current at maximum power (0.47 volt) and the series resistance. A statistically significant change has occurred in the open-circuit voltage. The mean change was a decrease of 0.62% between the before and after processing measurements. For a confidence level of 90%, the limits of the mean change are 0.11% and 1.13%. From this data and analysis, it is clear that a small change has occurred in the operating characteristics of the cells due to the soldering and thermal cycling. The open-circuit voltage is the most accurately measured of the several parameters; that is, the precision of measurement of open-circuit voltage is better than for the other measurement parameters. For this reason, the small change has statistical significance. Small changes may have also occurred in the maximum power, short-circuit current, and series resistance. The conclusion is that a small degradation has occurred in the solder joint due to the thermal cycling.

Test data showed that no significant change had occurred in the operating characteristics of the cells due to the soldering process. The conclusion is that the small change is caused by thermal cycling reducing the effectiveness of the solder joint.

The small degradation was observed after 100 thermal cycles between -100 and +75°C. In operation on a Mars mission, thermal cycling would be much less, or nonexistent. Although the change was observed in the open-circuit voltage, a small change may have occurred in the short-circuit current or the current at the maximum power point. However, this change would be extremely small, as indicated by the t and F tests.

5.2.3 MAGNETIC INTENSITY PRODUCED BY SOLAR-CELL CURRENTS

Magnetic intensity caused by currents in the solar cells and intercon-nectors can be reduced from 200 gamma to less than 1 gamma by using counterflow of current.

The baseline configuration of modules utilized a conveniently uniform arrangement that would have a magnetic intensity exceeding 200 gamma.

The element of first interest in the analysis is the module. A module is comprised of four strings in series. Each string has 58 groups in series, and each group has seven cells in parallel. Nominal rating of each cell is 0.423 volt, 0.10 ampere. Nominal output of a module is 100 volts and 0.7 ampere.

Magnetic effects to be considered are due to currents in the solar cells and currents in the string-to-string interconnector at the ends of the module that conduct current between series strings (see Figure 5-16).
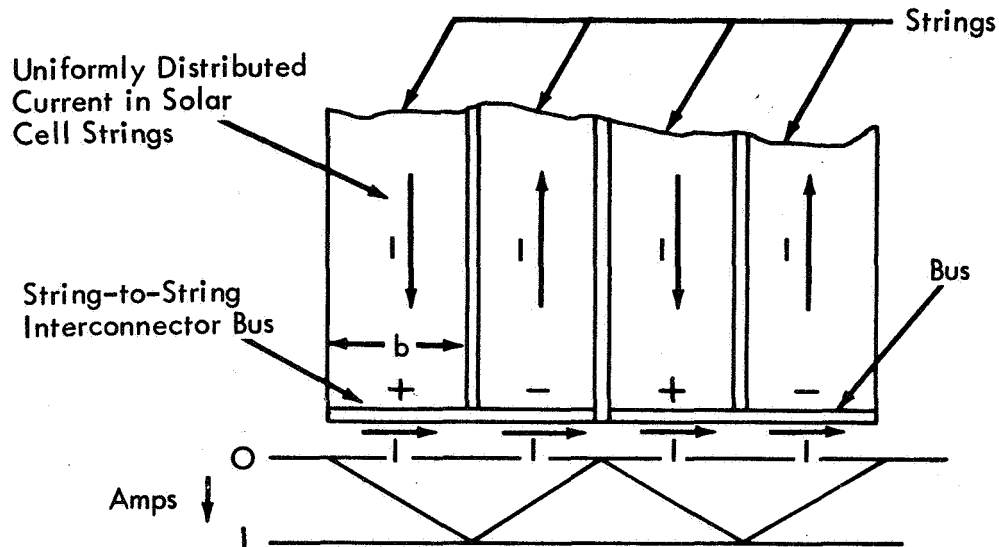
Figure 5-16: CURRENT DISTRIBUTION IN STRING INTERCONNECTORS

As shown in Figure 5-16, the current in the string-to-string interconnectors is not uniform, but varies along the width of the string.

Solar cells are considered to be in the Y-Z plane, with current flowing in the Z-direction in the strings and Y-direction in the bus at the end of the string.

$\overline{B}$ = Magnetic flux density;

N_R = Relative permeability = 1;

I = Current in string = 0.7 ampere;

S = Distance from P to plane of current = 1 meter;

b = Width of a string = 7 x 0.8 x 0.0254 = 0.142 meter;

W = Thickness of cell conductor;

L = Length of string = 59 x 0.8 x 0.0254 = 1.23 meters.

Field at edge of a string:

$$B_x = \int \frac{2 \times 10^{-7} N_R I y}{b (s^2 + y^2)^{1/2}} \, dy = \frac{N_R I 10^{-7}}{b} \ln \frac{s^2 + b^2}{s^2}$$

$$B_y = \int \frac{2 \times 10^{-7} N_R I s}{b (s^2 + y^2)^{1/2}} \, dy = \frac{2 \times 10^{-7} N_R I}{b} \tan^{-1} \frac{b}{s} \; .$$

Field at center of a module from current in cells:

$$B_x = \frac{N_R I \times 10^{-7}}{b} \left[4 \ln \frac{s^2 + b^2}{s^2} - 2 \ln \frac{s^2 + 4b^2}{s^2} \right]$$

$$B_x = 37.2 \text{ gamma}$$

$$B_y = 0.$$

Field at center of module from current in string-to-string interconnectors:

$$B_z = \frac{4 N_R I \times 10^{-7} bs}{R^2 (R^2 + 4b^2)^{1/2}}$$

$$B_x = 2N_R \, I \times 10^{-7} \left[\frac{1}{R^2 + 4b^2} \right]^{1/2} \left[\frac{1}{b} + \frac{3b}{R^2} \right]$$

$$- \left[\left(\frac{2}{b} + \frac{4b}{R^2} \right) \left(\frac{1}{R^2 + b^2} \right) \right]^{1/2} + \frac{1}{bR}$$

where:

$$R = \left(s^2 + \left(\frac{L}{2} \right)^2 \right)^{1/2}$$

$$B_z = 23.5 \text{ gamma}$$

$$B_x = 1.0 \text{ gamma}.$$

Total magnetic intensity from current in one module:

$$B_t = (37.2^2 + 23.5^2)^{1/2} = 43.9 \text{ gamma}.$$

Magnetic Intensity due to Currents in Subpanel---Several configurations are possible in arranging the subpanel modules. Figure 5-17 shows the current flow in the baseline arrangement. In this arrangement, all modules are placed uniformly to the negative and positive terminals of each module. The current in each section of string interconnector varies from zero to I along the width of each string. The current in all string connectors flows in the same direction. Adjacent connector currents sum to a magnitude of I.

The spacing between string interconnectors of adjacent modules is small compared to module length and width (0.005 meter compared to 1 meter). Accordingly, it is valid to assume that the spacing between adjacent interconnectors has a negligible effect on the magnetic field. For 60 modules with four string-to-string interconnections each:

$$B_z = -20 \times 10^{-7} \, N_R \, Isb \left[\frac{2}{[s^2 + (2L)^2 + (10b)^2]^{1/2} \, [s^2 + (2L)^2]^{1/2}} \right.$$

$$+ \frac{2}{[s^2 + L^2 + (10b)^2]^{1/2} \, [s^2 + L^2] + [s^2 + (10b)^2]^{1/2} \, s^2}$$

$$\left. + \frac{1}{[s^2 + (3L)^2 + (10b)^2]^{1/2}} \right]$$

$$B_z = 213 \text{ gamma}$$

$$B_x = \text{component is} < 1 \text{ gamma}.$$
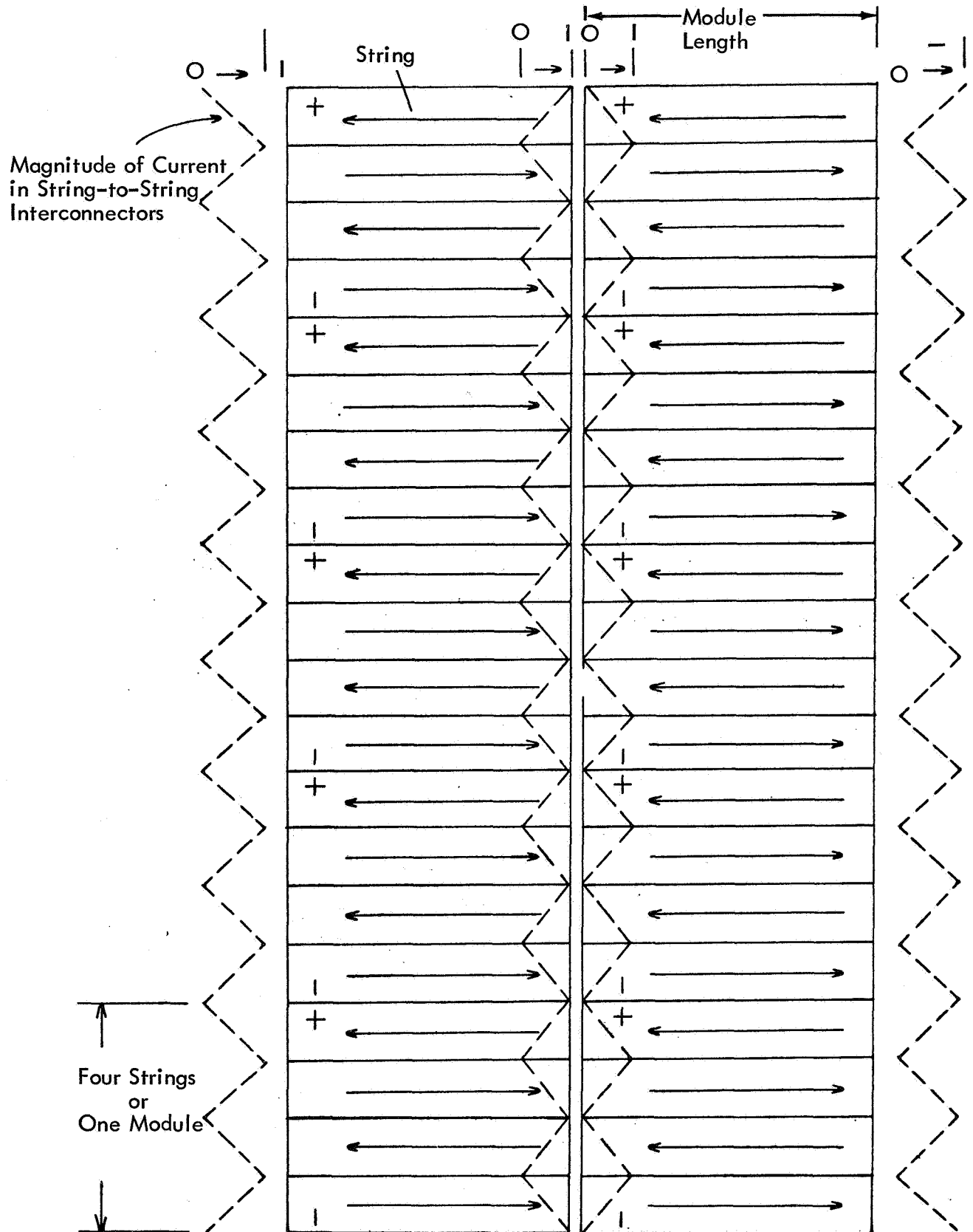
Figure 5-17: BASELINE MODULE ARRANGEMENT SHOWING VARIATION OF CURRENT IN STRING-TO-STRING INTERCONNECTORS

Magnetic Intensity due to Solar-Cell Current---For 10 strings on either side of the centerline:

$$B_x = \frac{2 \times 10^{-7} \, I \, N_R}{b}$$

$$\ln \frac{(b^2 + s^2)^2 (9b^2 + s^2)^2 (25b^2 + s^2)^2 (49b + s^2)^2 (81b^2 + s^2)^2}{s^2 (4b^2 + s^2)^2 (16b^2 + s^2)^2 (36b^2 + s)^2 (64b^2 + s^2)^2 (100b^2 + s^2)}$$

$$B_x = 50.7 \text{ gamma.}$$

Total intensity = 1 meter above centerline of Subpanel 4:

$$B_T = (50.7^2 + 213^2)^{1/2} = 219 \text{ gamma.}$$

This value is much greater than desired, and other arrangements of modules can be used that enable nearly zero field to be obtained.

Figure 5-18 shows the direction of current flow in the solar cells and string interconnections to produce a minimum field.

For a configuration with n-string widths (n/4 modules) on each side of centerline in one direction, and m-string lengths (module length) on each side of centerline in the other direction, the magnetic intensity from each string connector is:

$$B_{Z_{nm}} = N_R \times 10^{-7} \, SI \left[\frac{2}{b[s^2 + m^2 L^2 + (n-1)^2 b^2]^{1/2}} - \frac{2}{b[s^2 + m^2 L^2 + n^2 b^2]^{1/2}} \right.$$

$$+ \frac{(n-1)b}{(s^2 + m^2 L^2) \, [s^2 + m^2 L^2 + (n-1)^2 b^2]^{1/2}}$$

$$\left. + \frac{2}{(s^2 + m^2 L^2) \, [s^2 + m^2 L^2 + n^2 b^2)]^{1/2}} \right] (-1)^{n+m}$$

where:

s = Distance from panel to point of interest;

b = Width of a string;

L = Length of a string.

The magnetic intensity from the solar-cell current in each module is:

$$B = N_R \, 10^{-7} \frac{I}{b} \int_{y_1 z_1}^{y_2 z_2} \frac{(s^2 + y^2)^{1/2}}{(s^2 + y^2 + z^2)^{3/2}} \, dy dz.$$
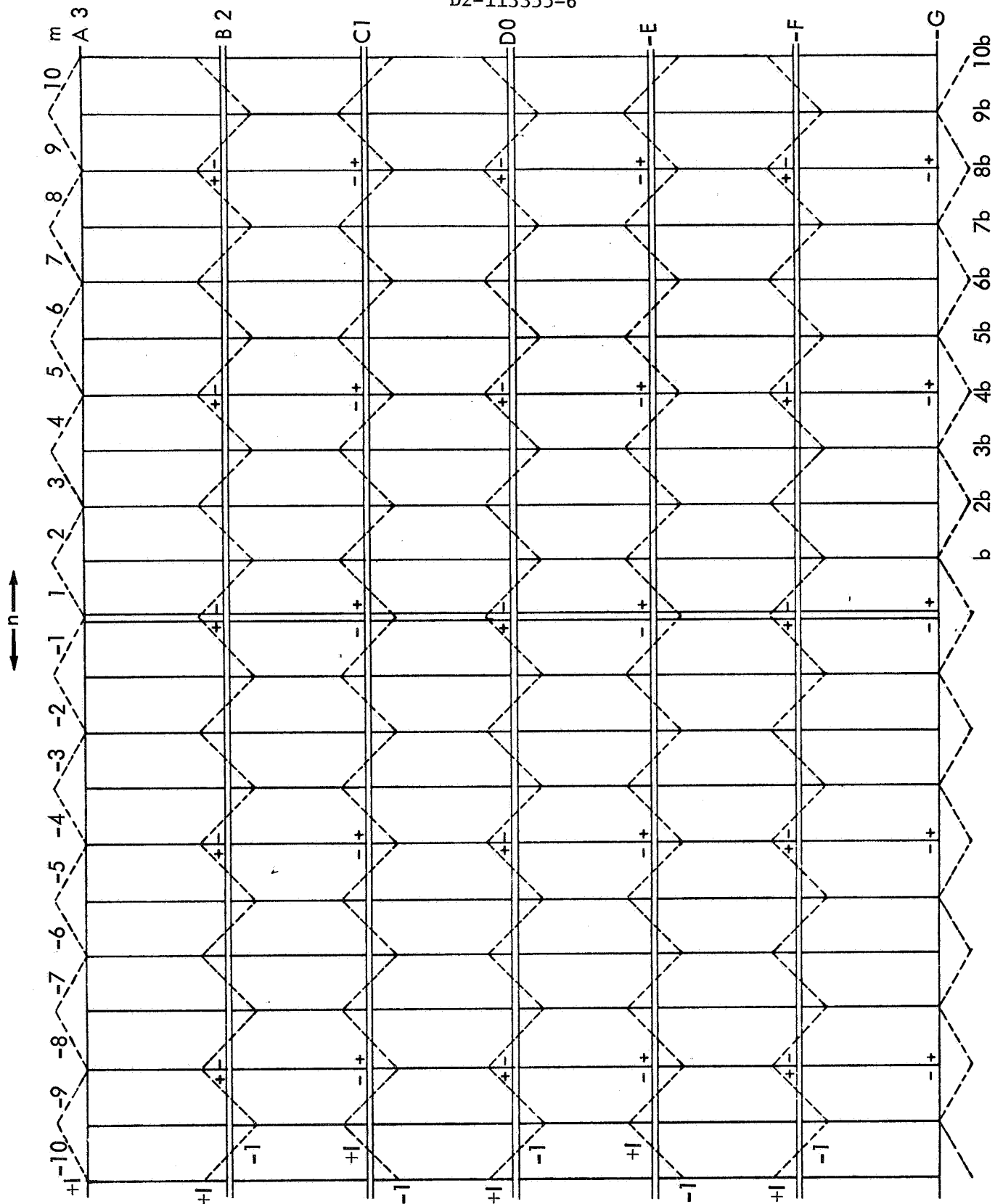
Figure 5-18: SUBPANEL SHOWING MAGNITUDE AND VARIATIONS OF
CURRENT IN STRING-TO-STRING INTERCONNECTORS
FOR A LOW MAGNETIC INTENSITY

For equal currents in all modules, the magnetic intensity is <1 gamma due to the string connector currents and the current through the solar cells. (See Figure 5-19 for alternate arrangement of cells and modules cancelling currents in string-to-string connectors.)

5.2.4 POWER LOSSES FROM CELL INTERCONNECTORS AND FABRICATION

Reduction in power output of the SCS-43 array from degradation of cells during fabrication, resistance of interconnectors, and busses was negligible.

Prediction of array performance was based on the measurements made on 56 cells at 28 ±1°C illuminated at 100 mw/cm^2 with the X-200 simulator. From these data, V-I curves were synthesized for the calibrated section of the array. These V-I curves are shown in Figures 5-20 and 5-21. Maximum power from the 56 cells was calculated to be 2.18 watts, and maximum power of the average cell was 0.0389 watt. Assuming a linear increase in power, the average cell has a maximum power output of 0.0545 at 140 mw/cm^2, 28°C. The maximum expected power output of the panel was 48.8 watts. The test panel would have less power because of coverglass reflection and losses in interconnectors, busses, and diodes. From the synthesized curves, the open-circuit voltage of the calibrated section was calculated at 4.54 volts for eight groups in series and the short-circuit current was 0.619 ampere. Using these results, the values for the complete panel at 28°C and 140 mw/cm^2 with no degradation would be: open-circuit voltage = 36.4 volts, short-circuit current 1.81 amperes, and maximum power 48.8 watts. To calculate characteristics of the array at other temperatures, the following temperature coefficients were used, as obtained, from J. Sandstrom, Jet Propulsion Laboratory.

1) Δ watts/Δ°C = -0.40%°C;

2) Δ open-circuit voltage/Δ°C = -2.5 mv/°C;

3) Δ short-circuit current/Δ°C = 0.0885 ma/°C.

At the maximum power point, the current in each module is approximately 0.85 ampere, and the diode voltage drop is nearly 0.75 volt for temperatures between 25 and 100°C. The power losses in the diodes were estimated to be 1.3 watts. Using Sandstrom's coefficient for power change with temperature, the power output at 55°C would be: 48.8 (1 - 27 x 0.004) = 43.5 watts. Power loss due to coverglasses was determined previously to be 2.9%, and the expected maximum power is then 43.5 x 0.971 = 42.3 watts. This value is further reduced by the series diode losses of 1.3 watts. The expected maximum power is 40.9 watts at 55°C (140 mw/cm^2).
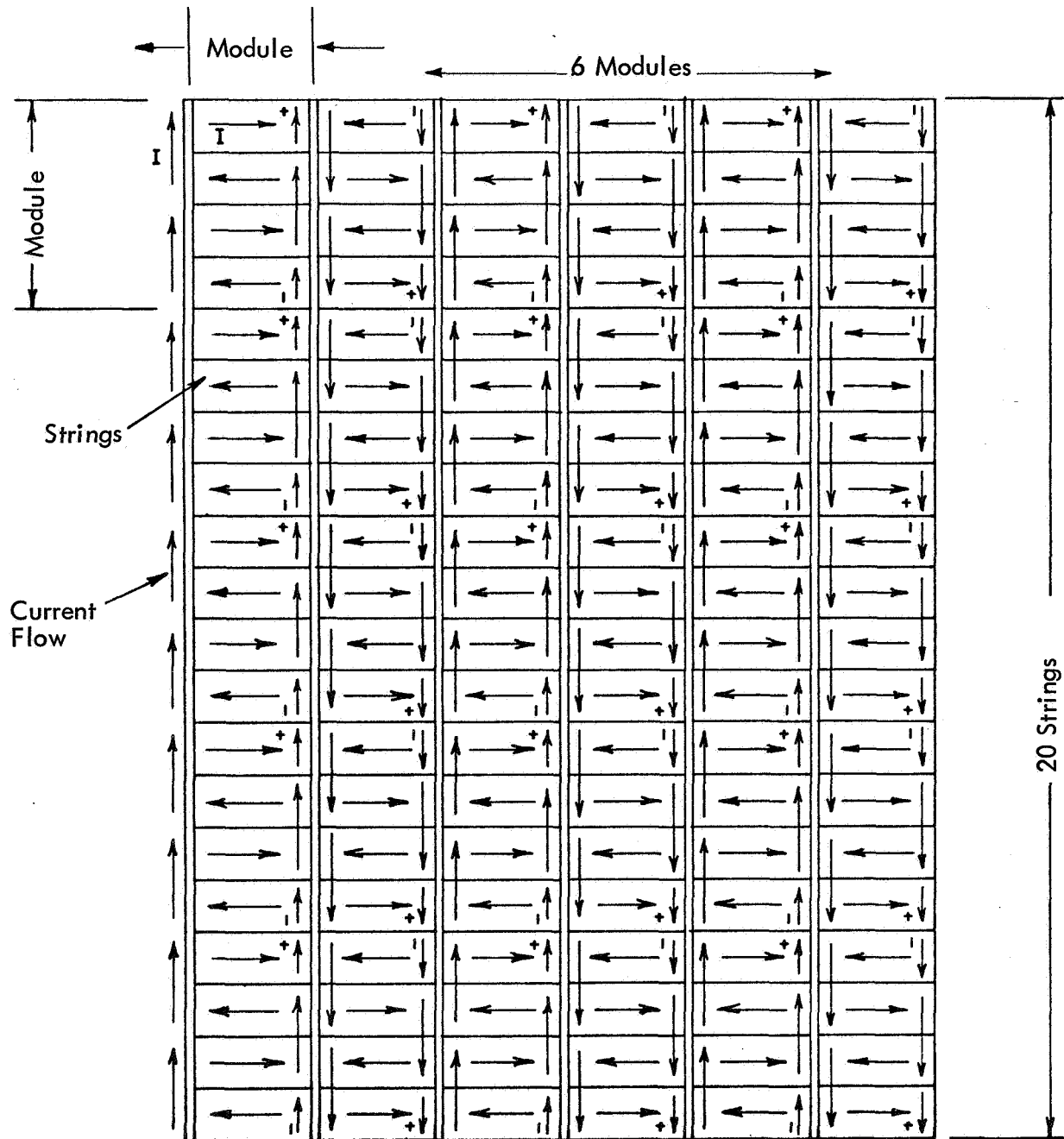
Figure 5-19: ALTERNATE ARRANGEMENT OF CELLS AND MODULES SHOWING CANCELLATION OF CURRENTS IN STRING-TO-STRING INTERCONNECTORS
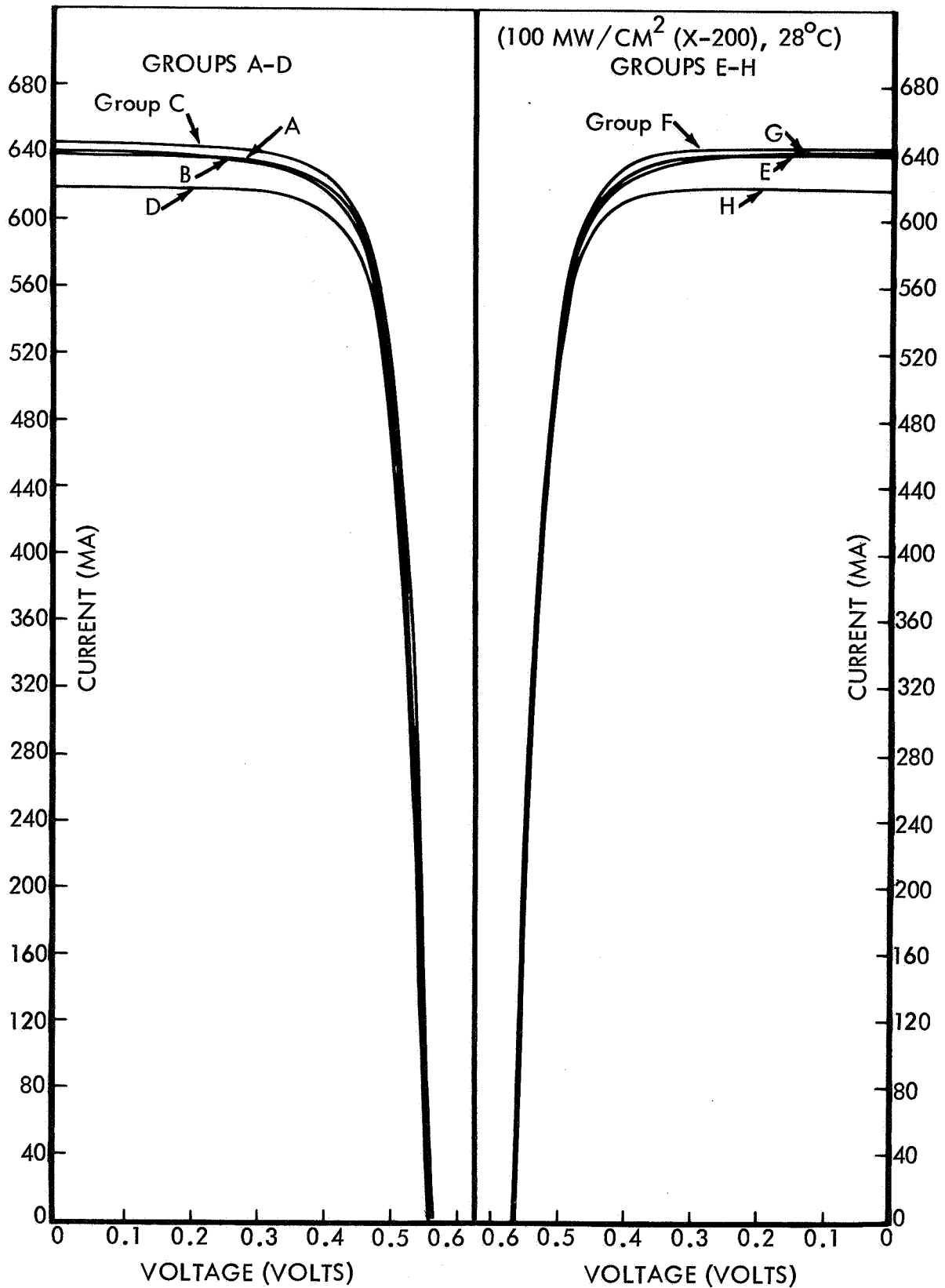
Figure 5-20:   SCS-43 SYNTHESIZED GROUP V-I CURVES
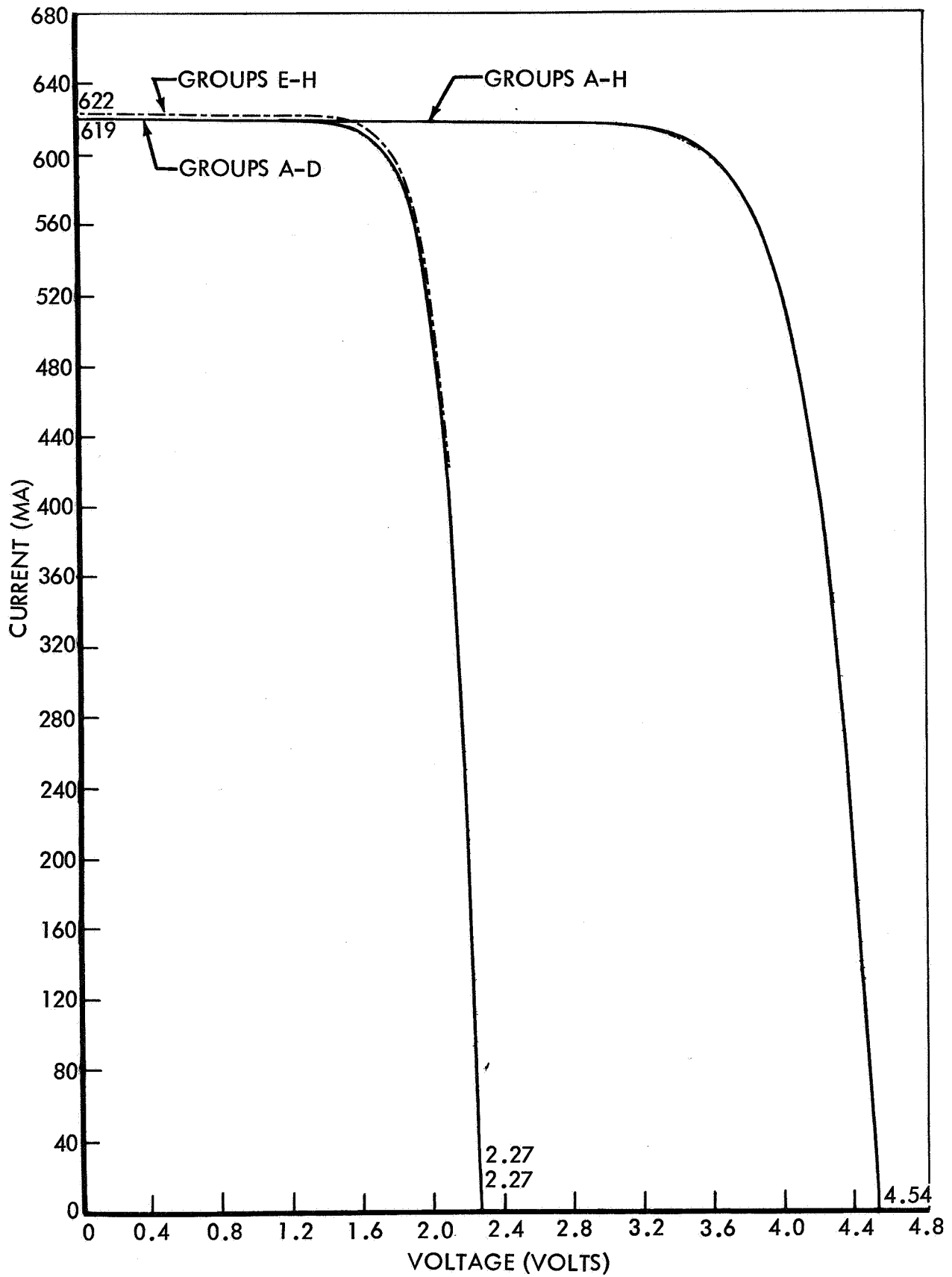
Figure 5-21: SCS-43 SYNTHESIZED MODULE V-I CURVES

The measured values on the 56-cell group at 140 mw/cm^2, and an average temperature of 69.2°C as measured by thermocouples were:

1)   Open-circuit voltage, 3.85 volts;

2)   Short-circuit current, 0.92 ampere;

3)   Maximum power, 2.59 watts.

Correction of the measured values to 55°C gives:

1)   Open-circuit voltage, 4.1 volts;

2)   Short-circuit current, 0.90 ampere;

3)   Maximum power, 2.74 watts.

The measured values at 100 mw/cm^2 and an average temperature of 58.3°C, as measured by thermocouples were:

1)   Open-circuit voltage, 4.0 volts;

2)   Short-circuit current, 0.67 ampere;

3)   Maximum power, 1.98 watts.

Correction of these measured values to 55°C gives:

1)   Open-circuit voltage, 4.1 volts;

2)   Short-circuit current, 0.67 ampere;

3)   Maximum power, 2.01 watts.

Values corresponding to the above, synthesized from individual cell measurements, were:

1)   Open-circuit voltage, 4.00 volts;

2)   Short-circuit current, 0.636 ampere;

3)   Maximum power, 1.94 watts.

Because of the relatively large temperature gradients in the array, the average temperature is better determined by open-circuit-voltage measurements than by thermocouple measurements. Using this method, an average temperature of the calibrated section is 55°C when illuminated at 100 mw/cm^2. Moreover, using the open-circuit-voltage method of obtaining

temperature gives a temperature for the calibrated section of 62.5°C when illuminated with 140 mw/°C. Correction of the data to 55°C gives:

1)   Open-circuit voltage, 4.00 volts;

2)   Short-circuit current, 0.92 ampere;

3)   Maximum power, 2.67 watts.

Summary of Results on Calibrated Cell Section---All data and calculated values below referred to 55°C. These results show that the output of the 56-cell section could be predicted within close limits and are useful in calculating the output of the entire panel.

Illumination (mw/cm^2)	Open-Circuit (volts)		Short-Circuit (ampere)		Maximum Power (watts)	
	Test	Calc	Test	Calc	Test	Calc
100	4.0	4.0	0.67	0.64	1.98	1.94
140	4.1	4.1	0.90	0.89	2.74	2.72

The actual power output of the array at the test temperature was 40 watts, maximum, as determined from V-I characteristics during three measurements with 30 minutes between the first and last measurement. The temperature across the panel varied from a minimum of 55°C to a maximum of 78.9°C, as measured by 11 thermocouples. The average temperature change of the panel during the 30-minute period was 0.33°C. The maximum temperature change occurred at minimum temperature---this change was a 1.7°C. With the large temperature gradient across the panel, the ability to calculate a meaningful average temperature from thermocouple values is doubltful. Another approach is to use the open-circuit voltage value as a measure of average temperature.

At 28°C, the calculated open-circuit voltage of the panel with no degradation was 36.4 volts. The measured voltage was 30.2 volts. Using the voltage difference between the 28°C calculated value and the measured voltage, and the voltage coefficient of -2.5 mv/°C, an average temperature of 66.7°C is obtained for the panel. The arithmetic mean of the temperatures measured by thermocouple was 70.0°C. Based on the open-circuit voltage temperature value, and a power coefficient of -0.4%/°C, the power output at 55°C, 140 mw/cm^2, is 41.9 watts. The power output of 41.9 watts compares favorably with the power output of 40.9 watts calculated for no degradation and with no allowances for power losses in the interconnectors. Thus, it is concluded that the power loss due to fabrication and interconnectors was insignificant.

Summary of Test Results (TASC 1)---

Temperature (°C)	Open-Circuit (volts)		Short-Circuit (amperes)		Maximum Power (watts)	
	Test	Calc	Test	Calc	Test	Calc
66.7	30.2		1.87		40.0	
55*	32.1	32.1	1.86	1.84	41.9	40.9

*Test values referred to 55°C, using JPL temperature coefficients.

5.2.5 POWER LOSSES FROM ENVIRONMENTAL TESTING

Environmental testing had a significant affect on the power output of the panel.

After conditioning the test panel in a thermal-vacuum environment and an acoustic test, the panel was illuminated with the X-200 Solar Simulator, and power-output tests were made as for TASC 1, and described in Section 5.2. An intensity and isosolar plot for the solar-simulator beam made immediately before the test are shown in Figures 5-22 and 5-23.

A typical V-I characteristic curve for this test is shown in Figure 5-24. At the maximum power point, the output was 38.3 watts. As measured by 11 thermocouples, the average temperature of the array was 65.3°C. The temperature from the lowest point on the panel to the highest varied from 52.2 to 72.8°C. Because of the large gradient, the open-circuit method of obtaining panel temperature was used. Using a calculated value of 36.4 volts (based on the analysis discussed in TASC 1), for the open-circuit voltage at 28°C, a measured value of 30.7 volts, and a temperature coefficient of -2.5 mv/°C, the panel temperature was calculated as 63.6°C. This compares favorably with the average thermocouple temperature of 65.3°C. Using either method of temperature-averaging gives essentially the same power output at 55°C. The power output of the panel at 55°C would be 39.7 watts. Before the thermal-vacuum and acoustic tests, the power output corrected to 55°C was 41.9 watts. The difference between the two power-output tests was a decrease of 5.3%. The predicted power output for the panel with no degradation was 40.9 watts. Thus, the power output after thermal-vacuum and acoustic conditioning was 2.9% less than the value predicted by analysis for no degradation. The short-circuit current at the test temperature was 1.78 amperes, and corrected to 55°C would be 1.77 amperes. The short-circuit current at 55°C for TASC 1 was 1.86 amperes. The reduction in short-circuit current between TASC 1 and 2 was 4.8%. This agrees closely with the change in maximum power computed from the V-I characteristic curves.
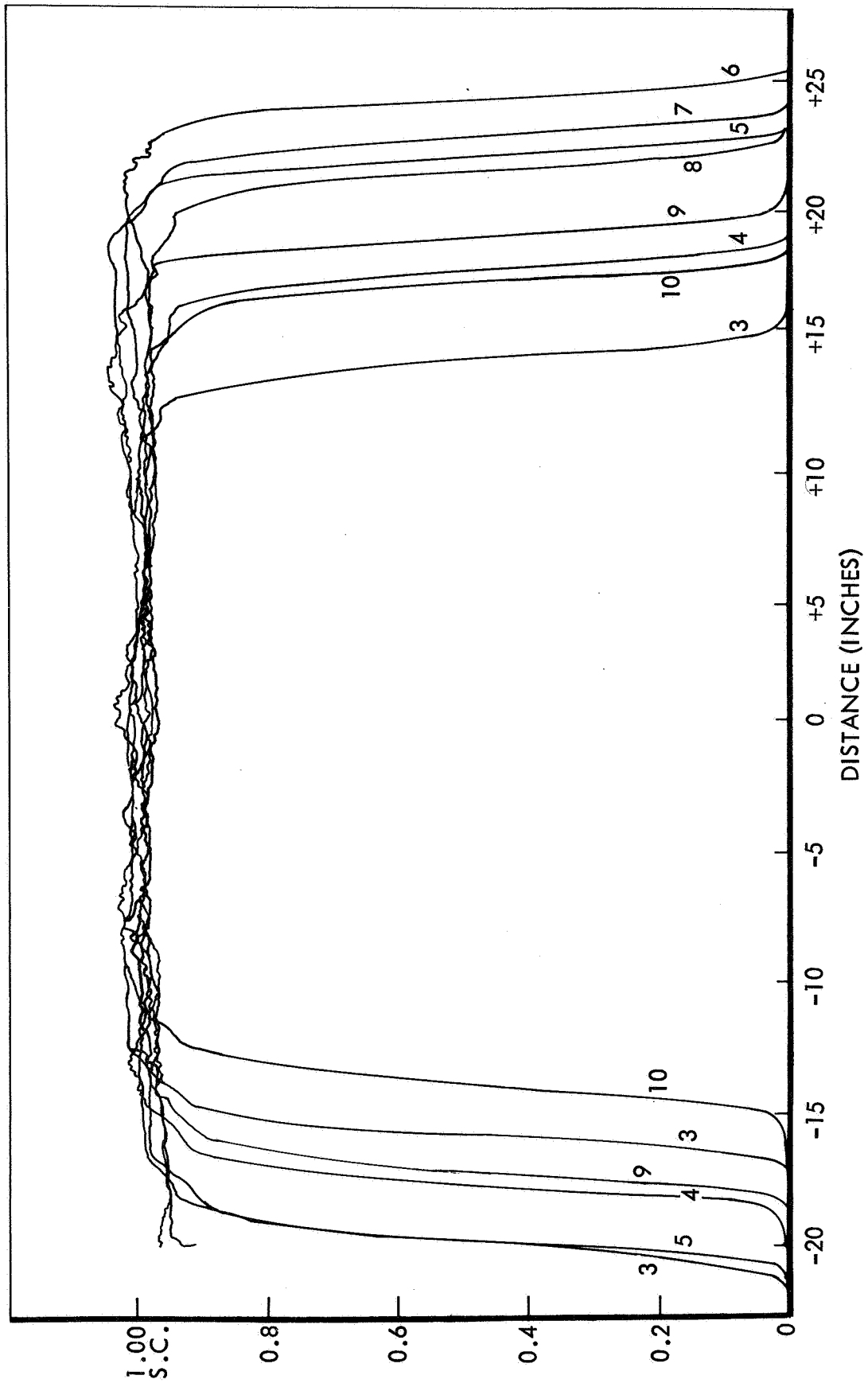
Figure 5-22: X-200 UNIFORMITY SCAN
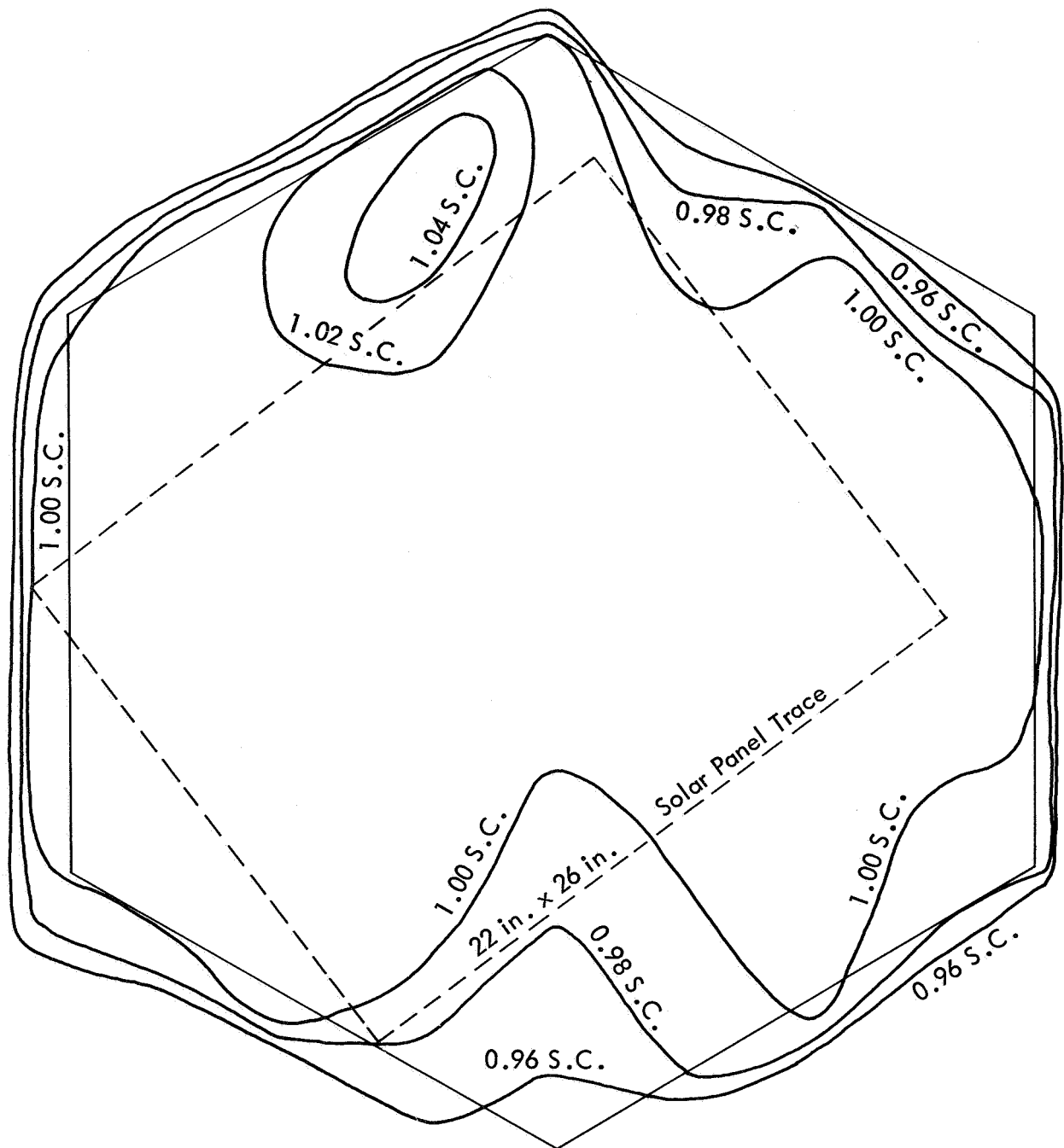
S.C. = SOLAR CONSTANT

Figure 5-23:   ISOSOLAR PLOT OF X-200 SOLAR SIMULATOR

Date: Sept. 18, 1967
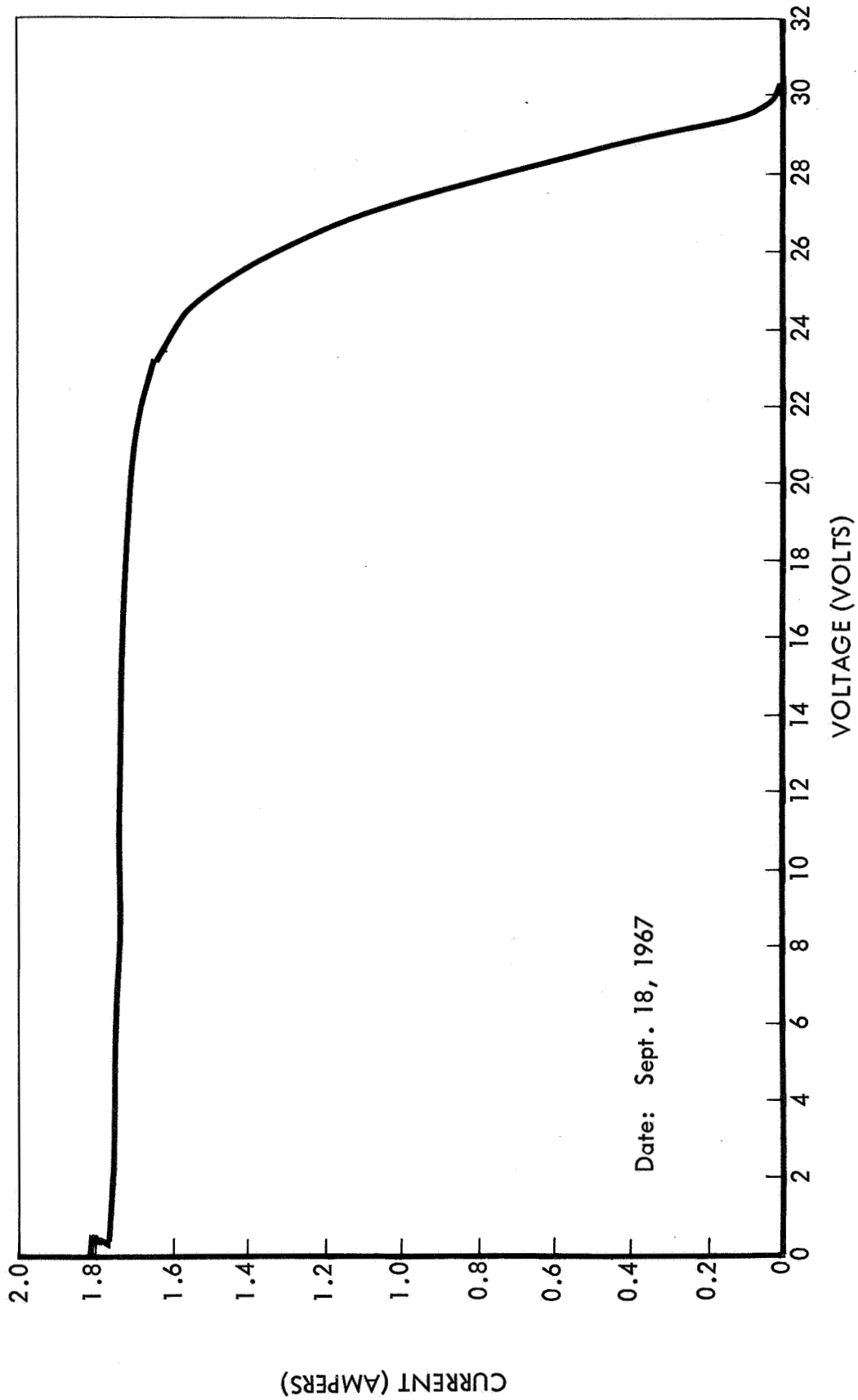
Figure 5-24: SCS-43; TEST 5

Temperature profiles for Status Checks 1 and 2 are shown in Figures 5-25 and 5-26. The panel was in the same vertical position for both tests, and was placed at the same location with respect to the solar simulator and within the test area. For TASC 1, with an illumination of 140 mw/cm^2, the temperature varied from 56.1°C at the lowest thermocouple on the panel to 78.9°C at the highest point. Examination of the temperature gradients indicated that this variation was due to convection. The temperature variation across the panel in TASC 2, with an illumination of 140 mw/cm^2, was from a low of 52.2°C to a high of 72.8°C. Good agreement existed between the thermocouple-measured temperatures and the values calculated from open-circuit voltage measurements. For TASC 2, the average temperature measured by thermocouple was within 1.7°C of the value calculated using open-circuit voltage. During the test, the average panel temperature measured by thermocouple changed by -1.4°C. Changes in individual thermocouple temperatures varied from -2.2 to +1.7°C. The open-circuit voltage did not change an observable amount during this period. A high-potential test at 400 volts d.c. was made with no breakdown.

The test panel was subjected to vibration test, and then retested to determine electrical characteristics. This test was made with the conditions as for the two previous TASC's. An intensity scan of the X-200 Solar Simulator is shown in Figure 5-27. The panel was illuminated with 140 mw/cm^2, as measured with the standard cell, Jet Propulsion Laboratory BFS 302. A small amount of dust particles were observed on the cells before the test. It appeared these would not appreciably affect power output, and the test was made without cleaning or conditioning the panel. The maximum power output determined from five V-I curves was 37.2 ±0.1 watts at the test temperature. A typical V-I characteristic curve is shown in Figure 5-28. Temperatures of the cells, as measured by thermocouple, ranged from 50.0 to 71.1°C. The average thermocouple temperature was 63.3°C. During the test period, the average thermocouple temperature varied from a minimum of 62.9°C to a maximum of 63.6°C. The open-circuit voltage did not change from 31 volts.

As measured by open-circuit voltage, the average temperature of the cells was 61.8°C. The difference between the two temperature-determination methods was only 1.5°C. A temperature profile of the array during TASC 3 is shown in Figure 5-29. Using the open-circuit-voltage temperature value, the power output of the panel (referred to 55°C) was 38.2 watts. The open-circuit voltage (referred to 55°C) was 32.1 volts; short-circuit current (referred to 55°C) was 1.68 amperes.

High-potential testing at 400-volts d.c. was made with no breakdown. Following the test to obtain the above data, particles on the solar cells were brushed from the panel with a soft brush. No observable difference was noted in power output. Electrical-test results are summarized in Table 5-4.

G18
174°F
151°F

G12
173°F
151°F

G17
169°F
145°F

G11
167°F
146°F

G16
147°F
129°F

G4
161°F
141°F

G8
163°F
145°F

G10
162°F
141°F

G9
151°F
133°F

G3
147°F
128°F

PANEL ILLUMINATED
AT 140 AND 100 MW/CM²

G2
133°F
119°F

X = 140 MW/CM²
X = 100 MW/CM²

Gx = Thermocouple
Location No.
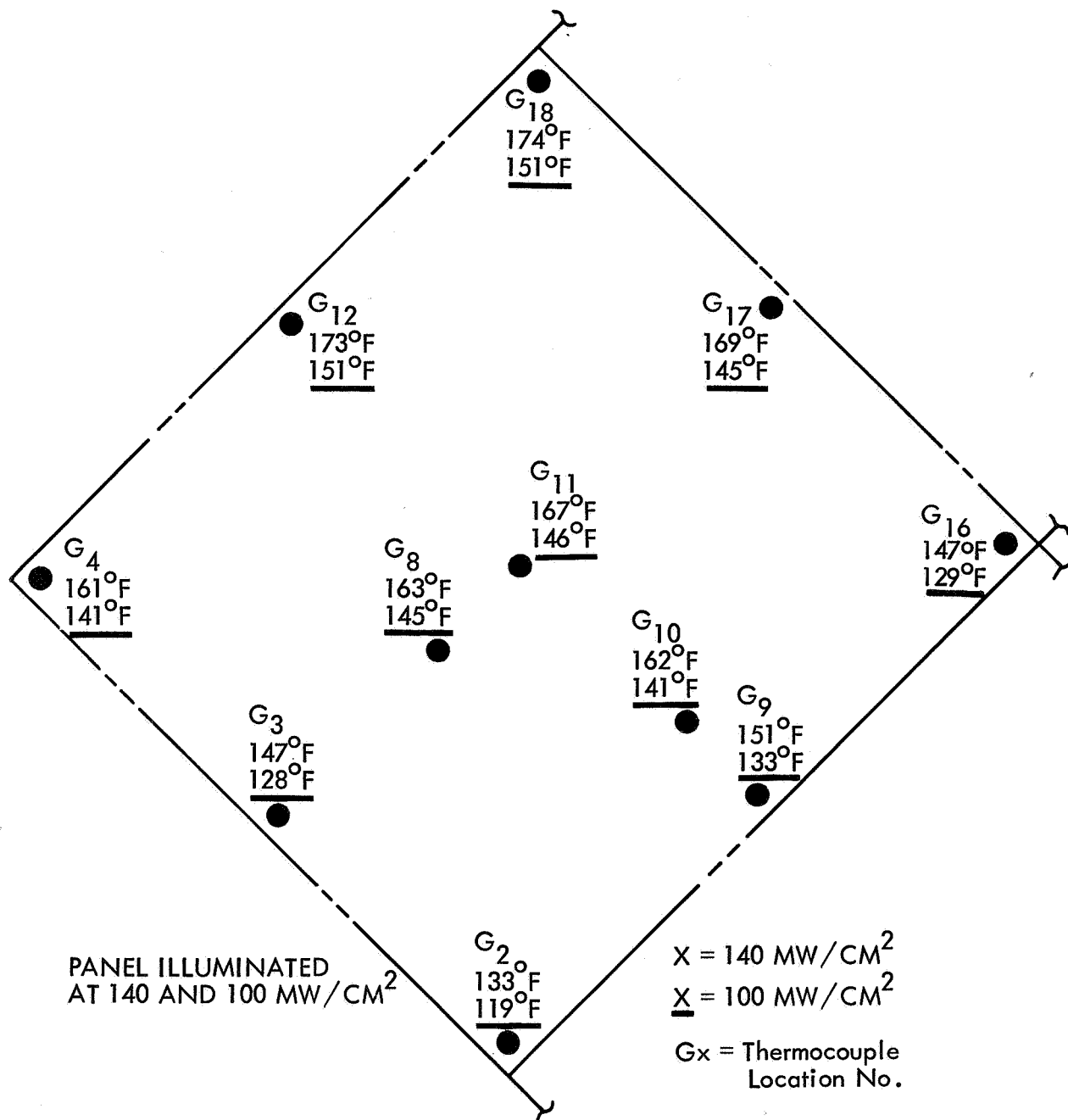
Figure 5-25: TEMPERATURE PROFILE OF SCS-43 TEST PANEL —
STATUS CHECK 1

G$_{18}$
163°F

G$_{17}$
156°F

G$_{12}$
160°F

G$_{11}$
156°F

G$_{16}$
160°F

G$_4$
144°F

G$_8$
156°F

G$_{10}$
159°F

G$_9$
143°F

G$_3$
159°F

PANEL ILLUMINATED
AT 140 MW/CM^2

G$_2$
126°F

Gx = Thermocouple
Location No.
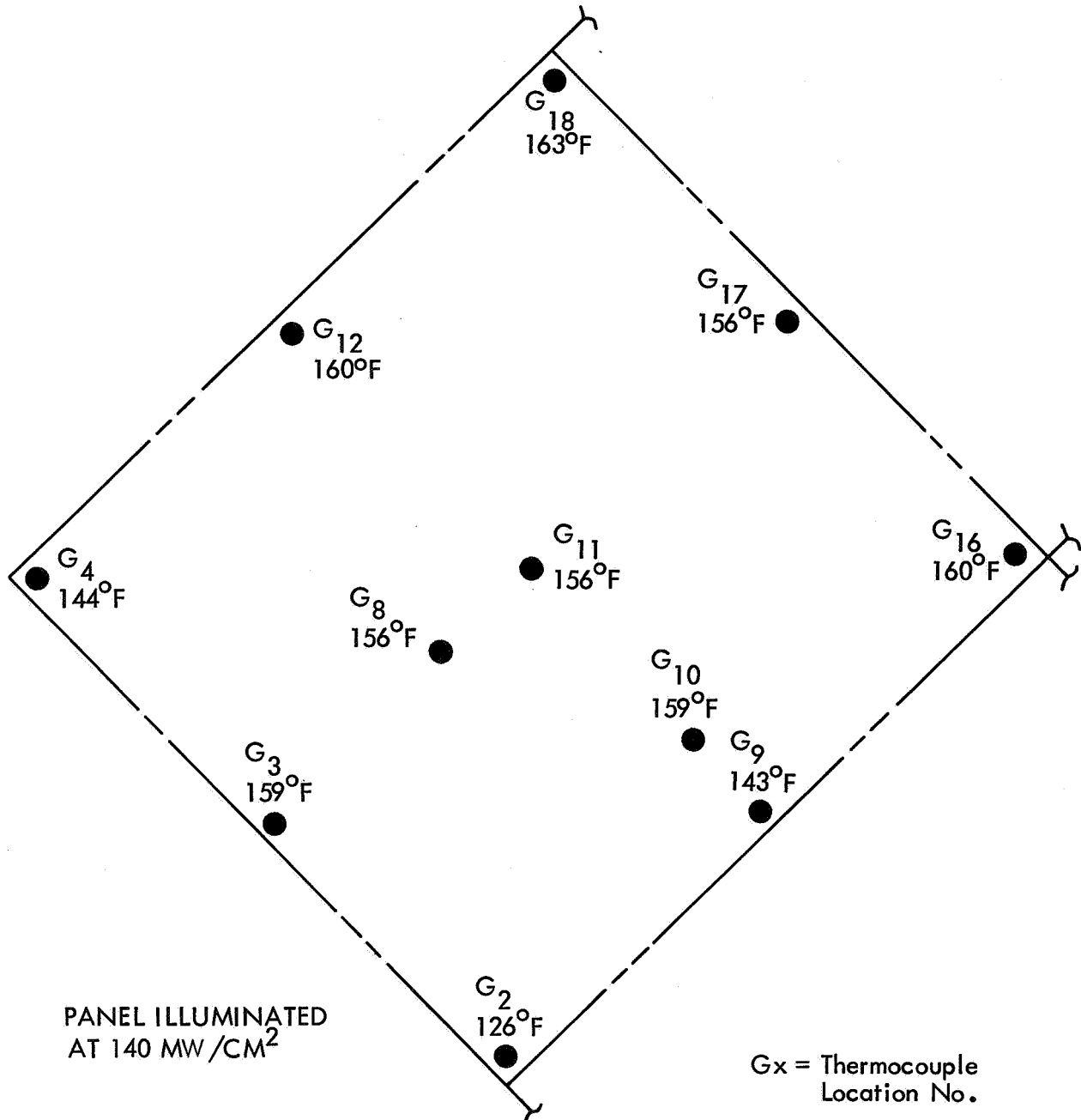
Figure 5-26: TEMPERATURE PROFILE OF SCS-43 TEST PANEL —
STATUS CHECK 2
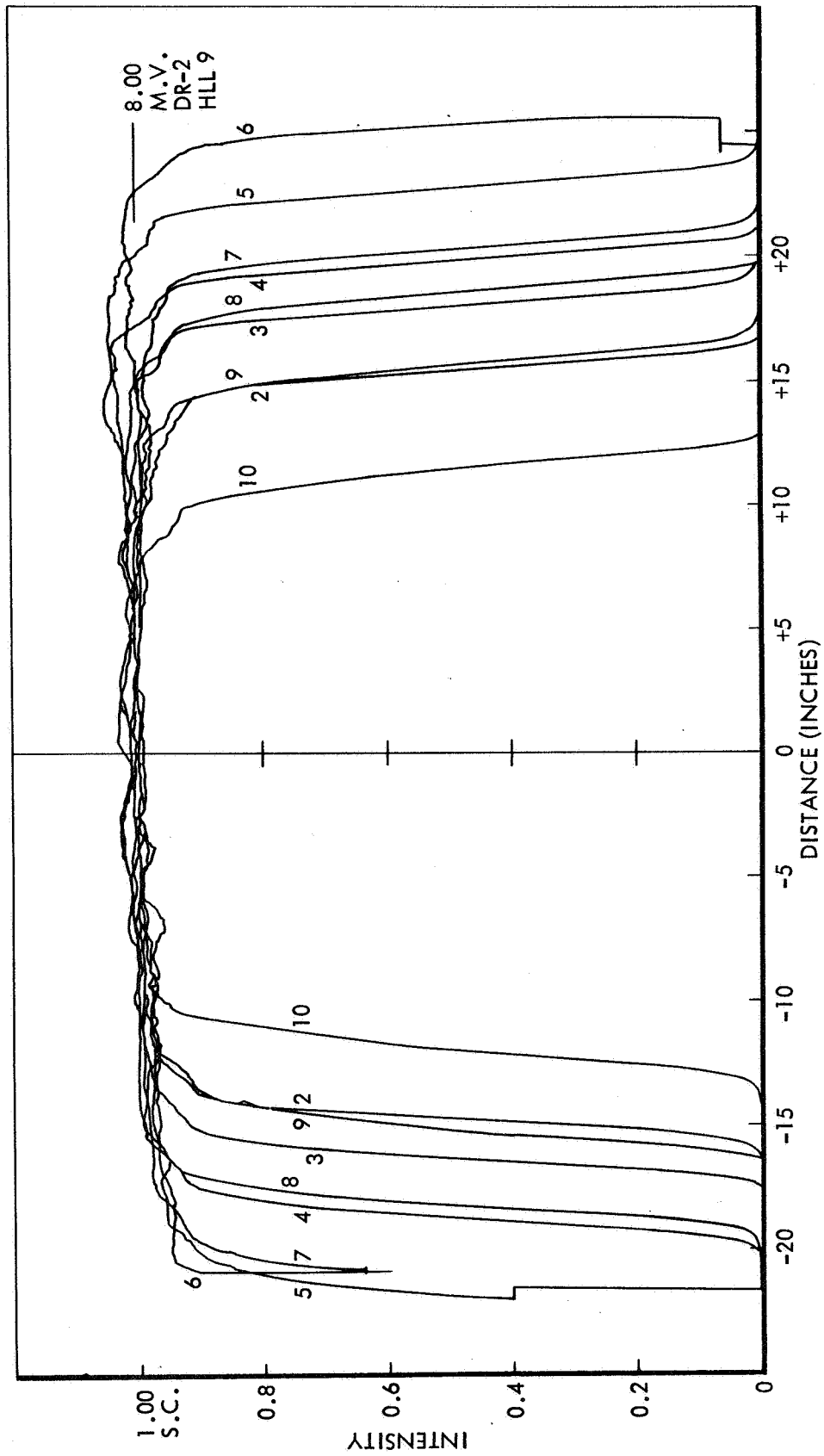
Figure 5-27: X-200 UNIFORMITY SCAN

Date: Sept. 21, 1967

VOLTAGE (VOLTS)
Figure 5-28:   SCS-43; TEST 2

CURRENT (AMPERS)

G_{18}
$160^{\circ}F$

G_{17}
$151^{\circ}F$

G_{12}
$157^{\circ}F$

G_{11}
$149^{\circ}F$

G_{16}
$157^{\circ}F$

G_4
$147^{\circ}F$

G_8
$149^{\circ}F$

G_{10}
$147^{\circ}F$

G_9
$135^{\circ}F$

G_3
$131^{\circ}F$

G_2
$122^{\circ}F$

PANEL ILLUMINATED
AT 140 MW/CM^2

Gx = Thermocouple
Location No.
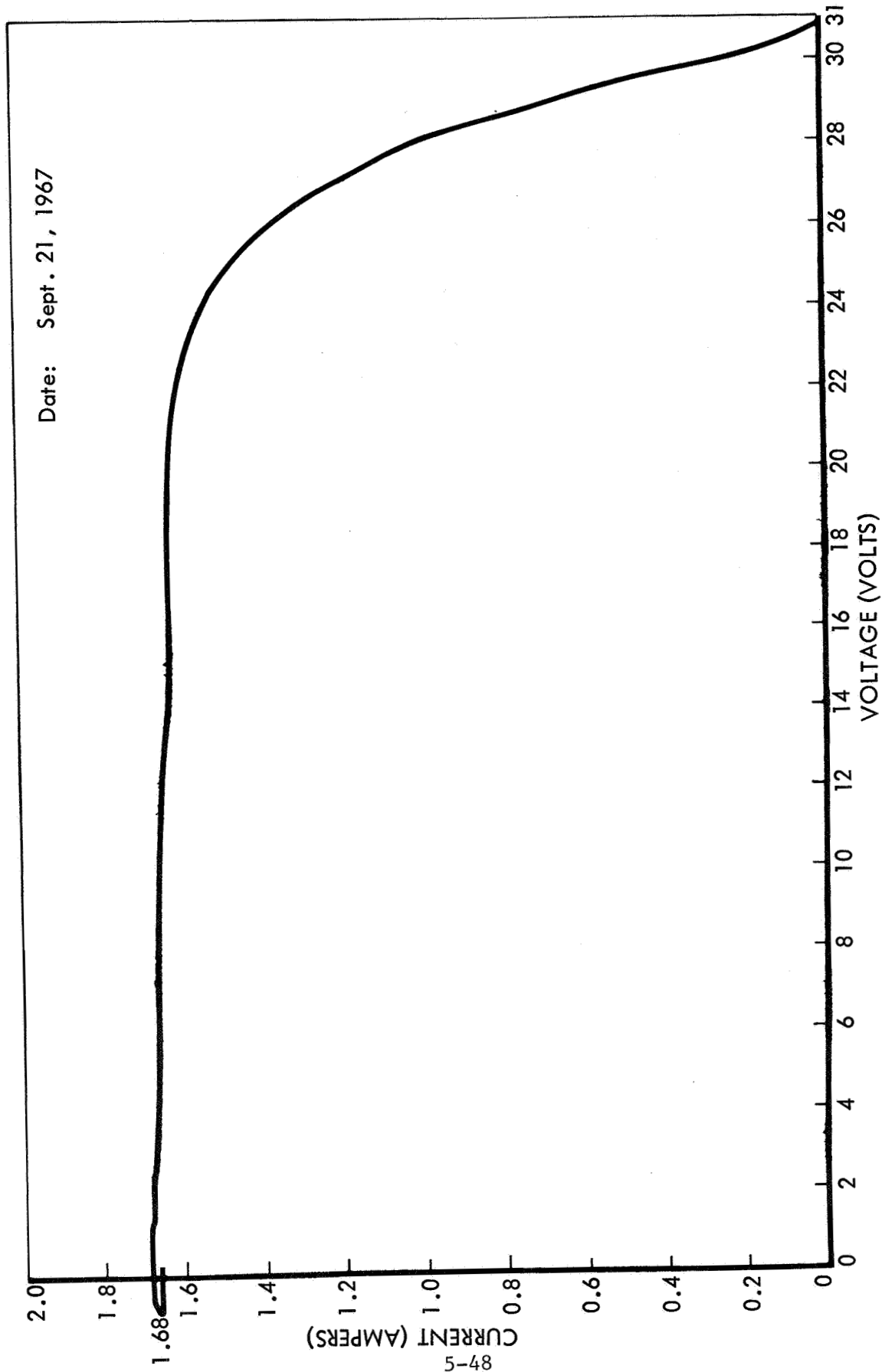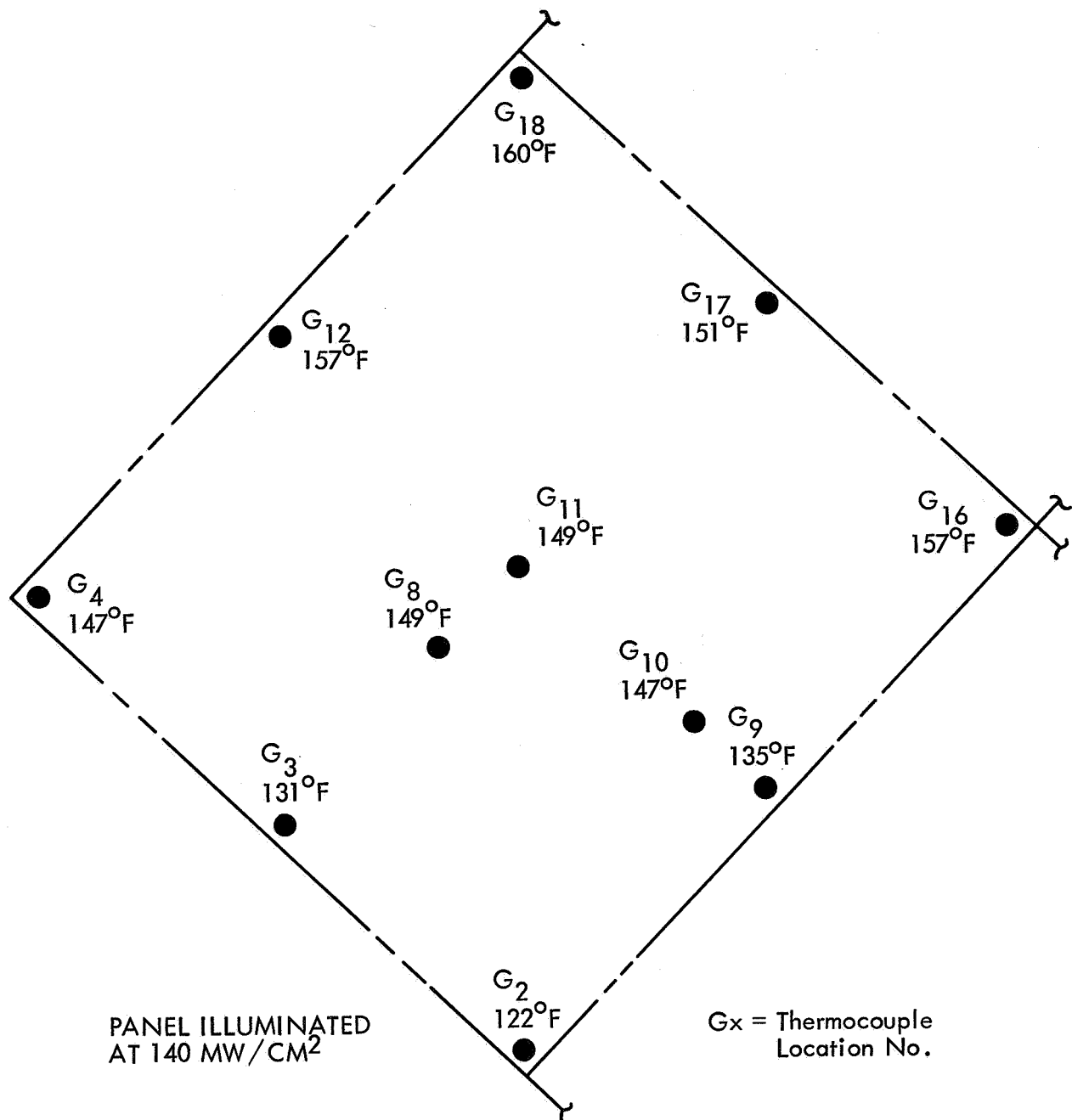
Figure 5-29: TEMPERATURE PROFILE OF SCS-43 TEST PANEL —
STATUS CHECK 3

Table 5-4:   SUMMARY OF ELECTRICAL SCS-43 TEST RESULTS
(140 mw/cm^2 Using X-200 Solar Simulator)

Status Check	Panel Temperature (°C)		Open-Circuit Voltage (volts)	
	Average Thermocouple	Open-Circuit Voltage Method	Test	55°C
1	70.6	66.7	30.2	32.1
2	65.3	63.6	30.7	32.1
3	63.3	61.8	31.0	32.1

Short-Circuit Current (amperes)		Maximum Power (watts)		Change in Power from TASC 1 (%)
Test	55°C	Test	55°C	
1.87	1.86	40.0	41.9	---
1.78	1.77	38.3	39.7	5.3
1.69	1.68	37.2	38.2	8.8

Test: Values from V-I characteristic curves at panel test temperature.

55°C: Test values (referred to 55°C) using JPL temperature coefficients.

Summary and Conclusions of TASC's---Power-output tests were made on the SCS-43 functional-test panel using the X-200 Solar Simulator to illuminate the panel. Tests were made:

1)   After completion of fabrication;

2)   After the thermal-vacuum and acoustic tests;

3)   After the vibration tests.

The complete panel contained 896 solar cells. A special group of 56 cells was measured before and after installation on the panel. From measurements made before installation, the power output of these cells after installation was predicted to within 0.02 watt, 0.7%, at 140 mw/cm^2. This information was used to predict the power output of the complete panel. The power output of the panel after fabrication was 2.4% greater than expected from measurements made on the 56 cells. However, power output after the thermal-vacuum and acoustic tests was 5.3% less than before these tests. Following the tests, the panel was subjected to vibration testing, and power output after vibration testing was 8.8% less than the initial value before thermal-vacuum testing. The panel withstood 400-volt, high-potential testing between cells and structure, with no indication of breakdown or low insulation resistance. During the electrical test, the average panel temperature stabilized within 5

minutes to less than 1°C change. Temperature variation across the panel was approximately 22°C, from minimum to maximum. This variation appeared to be due to convection heating associated with the vertical mounting of the panel during testing. Average temperature of the panel, as measured by thermocouples during the tests, was: TASC 1, 70.6°C; TASC 2, 65.3°C; TASC 3, 63.3°C. The precision with which the maximum power between successive measurements was determined for a TASC was approximately 0.25%. The amount of experience at this time with the X-200 does not justify an estimated, absolute accuracy of better than ±5%. However, the precision of the measurements indicates that the accuracy may be as close as ±2%. Therefore, it is concluded that the power-output decrease of the array was caused by the effects produced by the environmental-conditioning, thermal-vacuum, acoustic, and vibration tests.

6.0 MATERIAL PROPERTIES AND PROCESSES

This section presents the process specifications and structural design allowables established for the LASA program. Because of the brittleness of the material, special emphasis was placed on the investigation of beryllium fracture mechanics and the effects of flaws.

6.1 PROCESSES DEVELOPMENT

New combinations of materials and components required development and modification of process specifications for fabrication and assembly of LASA.

Processes and compatible material combinations for bonding of fiberglass tape, titanium, beryllium, and aluminum to meet LASA requirements were not available. The process, handling, and fabrication requirements for the fiberglass tape are new and unique. The rigid coverglass bond-line thickness required new processing techniques. The particular type of interconnector had never been soldered to solar cells and bus bars. Cleaning processes for bonding beryllium also had to be developed.

Processes were needed for:

1)   Coverglass bonding;

2)   Interconnector fabrication;

3)   Interconnector-to-solar-cell soldering;

4)   Fabrication of fiberglass tape substrate;

5)   Beryllium machining;

6)   Beryllium forming;

7)   Structural bonding;

8)   Solar cell bonding;

9)   Bus bar and diode bonding;

10) Thermal control coating

11) Bus interconnections;

12) Solar cell and interconnector repairs.

Some of these processes were derived from the LASA small components test program, whereas others were developed from existing Boeing material specifications. The specifications for these processes are presented in

Boeing Document D2-113354-1, *Process Specification, Large Area Solar Array*. In general, the document describes fabrication and assembly processes in the order needed.

<div align="center">6.2   STRUCTURAL DESIGN ALLOWABLES</div>

Allowables had to be established for glass tape, beryllium tensile strength, and certain adhesives.

Many, but not all, allowables are available in Boeing Design Document DM-5000, which contains material allowables. Some allowables in DM-5000 were modified and used for LASA. The small component test programs furnished the data for establishing design values for the allowables for fiberglass tape, beryllium tensile strength, and certain adhesives. Figures 6-1 through 6-6 represent allowables derived from the small component test programs of LASA. Figures 6-7 through 6-9 were furnished by Boeing Corporate Technical Staff for materials allowables. (See Figure 6-13 for beryllium tensile allowables selected for LASA.)

<div align="center">6.3   FRACTURE MECHANICS DEVELOPMENTS</div>

Design tensile strength and flaw size limits were established by fracture tests (SCS-5) for LASA.

The allowable tensile stress for beryllium depends on four factors: (1) the plane-strain fracture toughness coefficient K_{IC} of the material, (2) the largest flaw present in the material, (3) the rate of flaw growth, and (4) the required life of the part measured in load cycles. The first and third items are properties of the material and must be determined by test; the second is a function of the inspection to which the final parts are subjected; the fourth is determined by the environment. In turn, the fracture coefficient K_{IC} is a function of the temperature and the rate at which the material is being strained (see Reference 5, Section 11.3).

Structures fabricated of beryllium alloy (and even the raw material itself) contain flaws of various kinds and sizes. The lives of these structures are controlled by the flaw sizes required to cause fracture at the operating stress levels, the initial flaw sizes, and the sub-critical flaw growth characteristics of the alloy.

Accurate information on the values of K_{IC} and its relation to temperature and strain was not available; the SCS-5 tests were performed to obtain this information. These tests have been reported and analyzed in Boeing Document D2-113565-1.

<div align="center"></div>
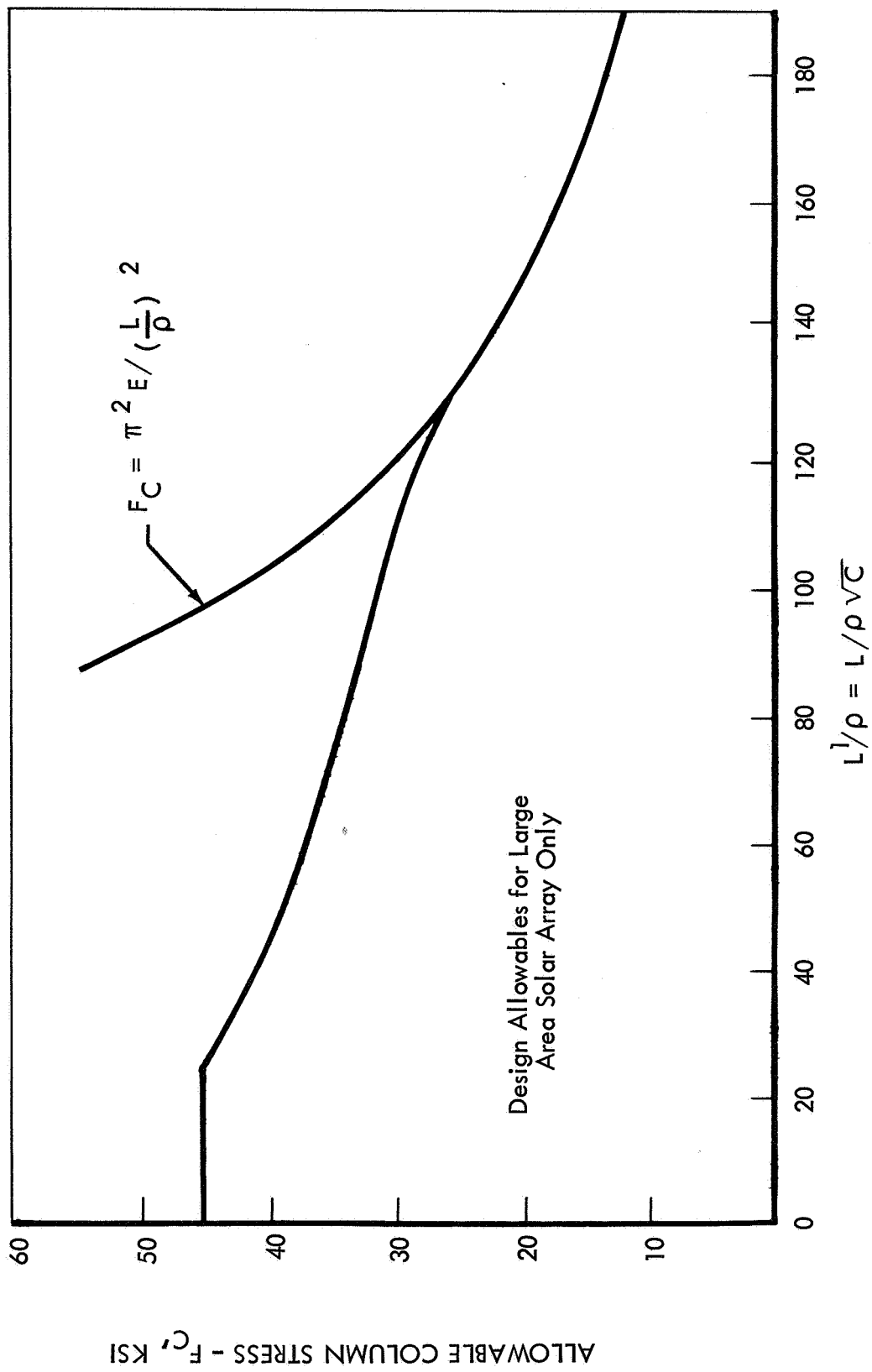
Figure 6-1: ALLOWABLE COLUMN STRESSES
AMS 7902 Beryllium (Stable Section 70°F)

$$F_C = \pi^2 E / \left(\frac{L}{\rho}\right)^2$$

$L'/\rho = L/\rho\sqrt{C}$

Design Allowables for Large
Area Solar Array Only

ALLOWABLE COLUMN STRESS - F_c, KSI

Solar Cells Bonded to Fiberglass Tape
(XP-251S) With RTV-40 Adhesive

Maximum Bondline Thickness: 2 mils
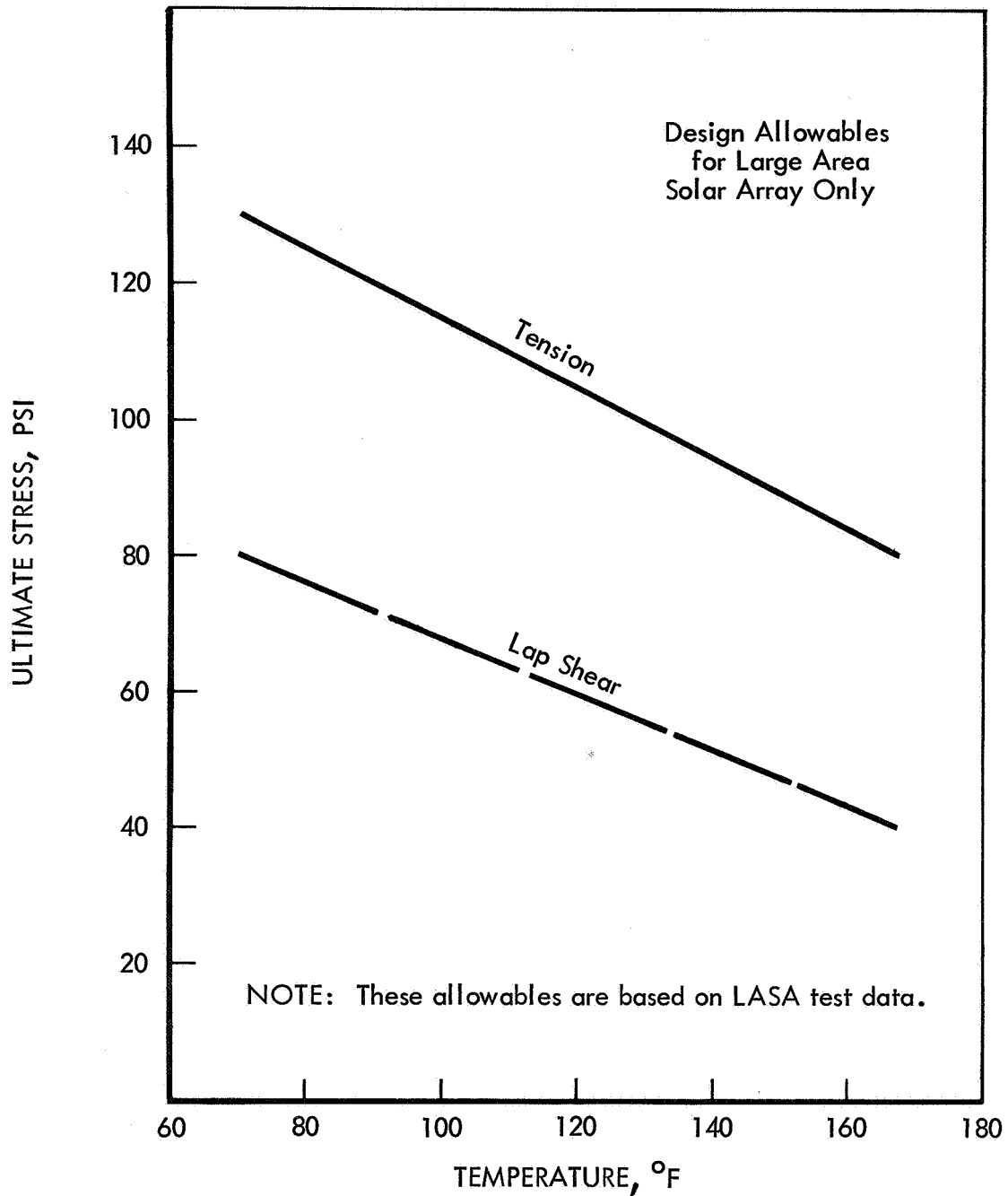
Figure 6-2: TENSION AND LAP SHEAR STRENGTH
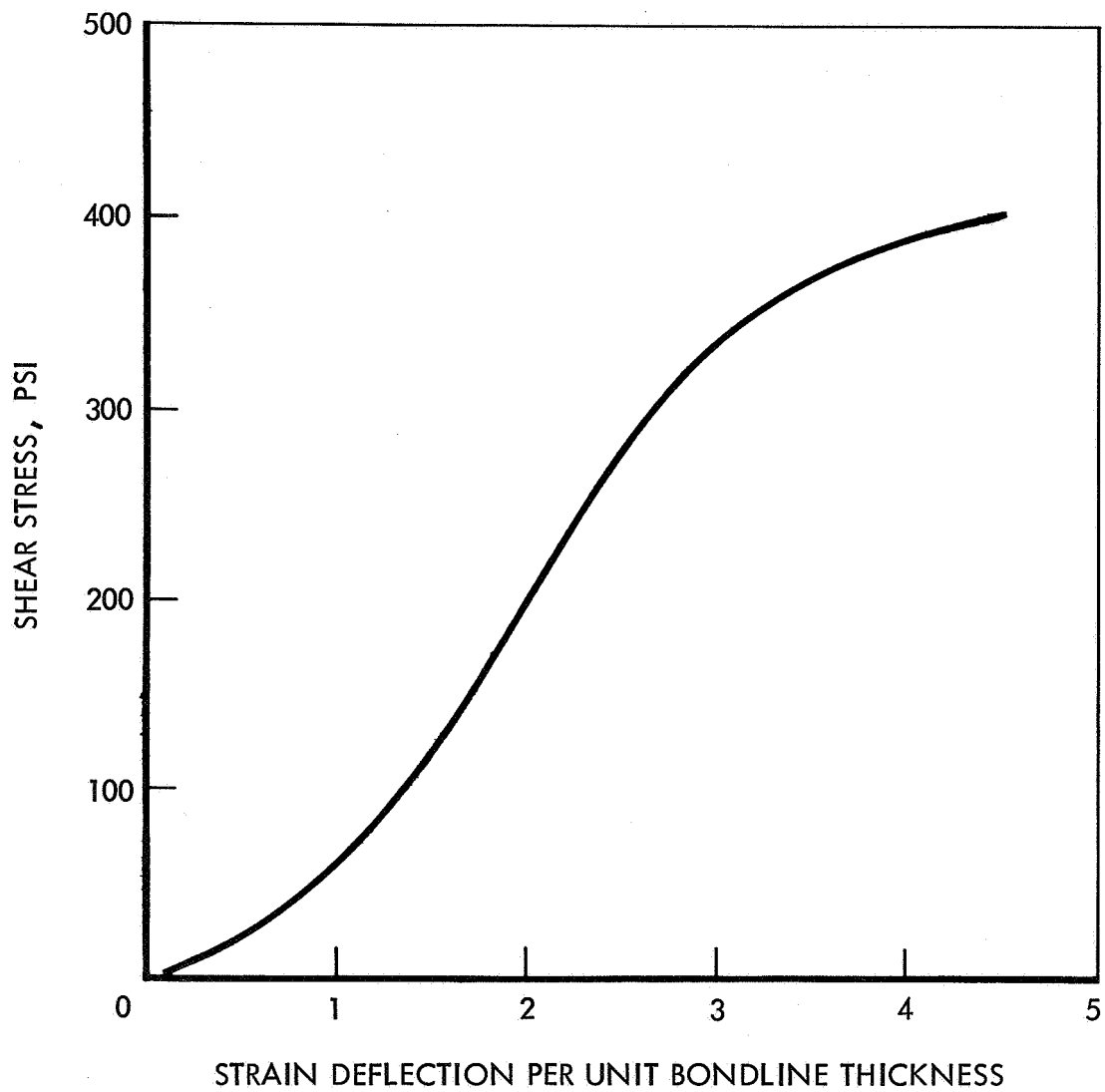
Figure 6-3: LAP SHEAR STRESS VERSUS STRAIN FOR RTV 630A
(Based on LASA Test Data)
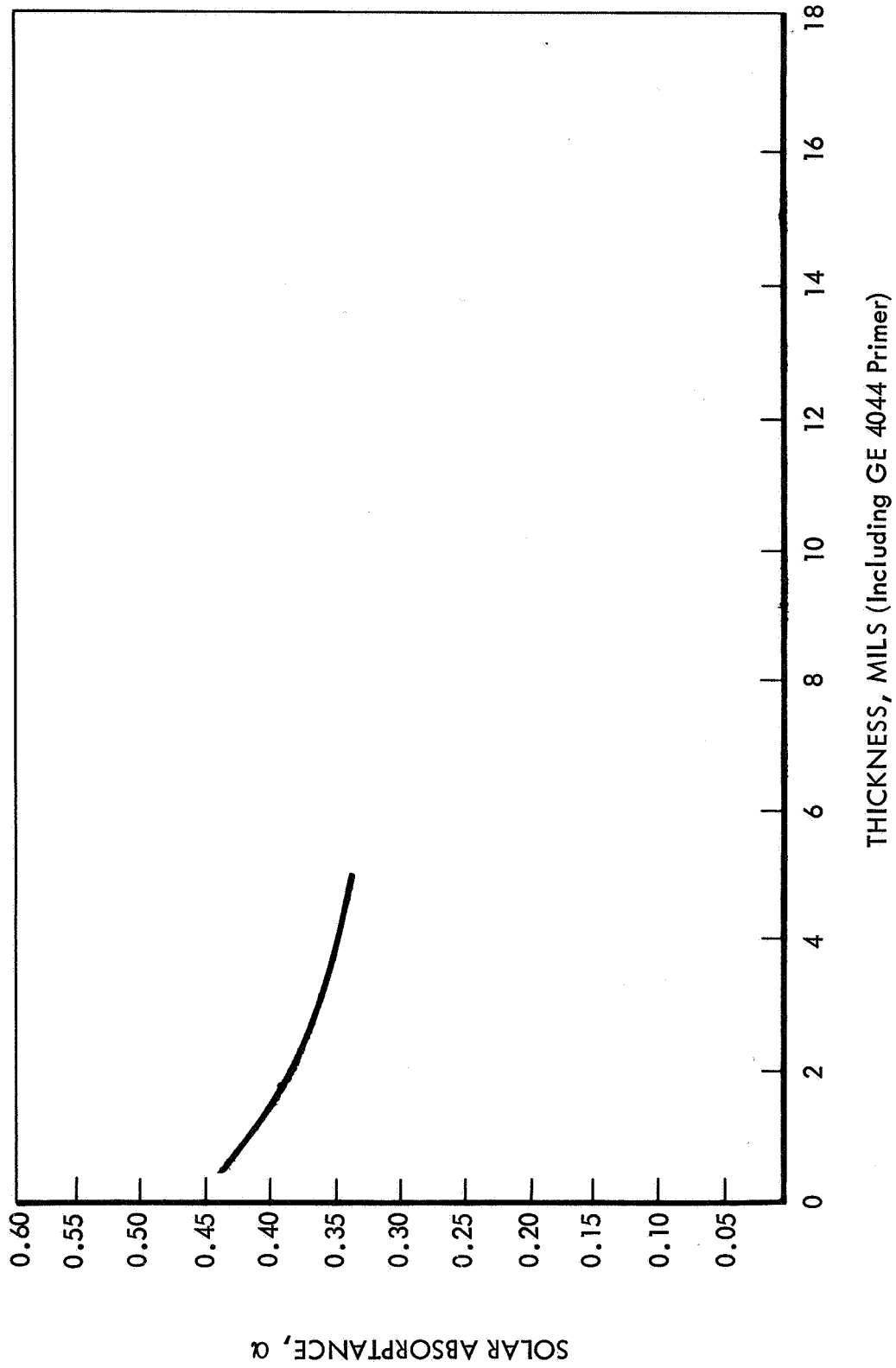
THICKNESS, MILS (Including GE 4044 Primer)

Figure 6-4: ABSORPTANCE VERSUS THICKNESS FOR RTV-40 PAINT

(From LASA Test Data)

SOLAR ABSORPTANCE, α

Note: Δα Due to ultraviolet
Exposure in a vacuum is 0.01

THICKNESS, MILS (Including GE 4044 Primer)

SOLAR ABSORPTANCE, α
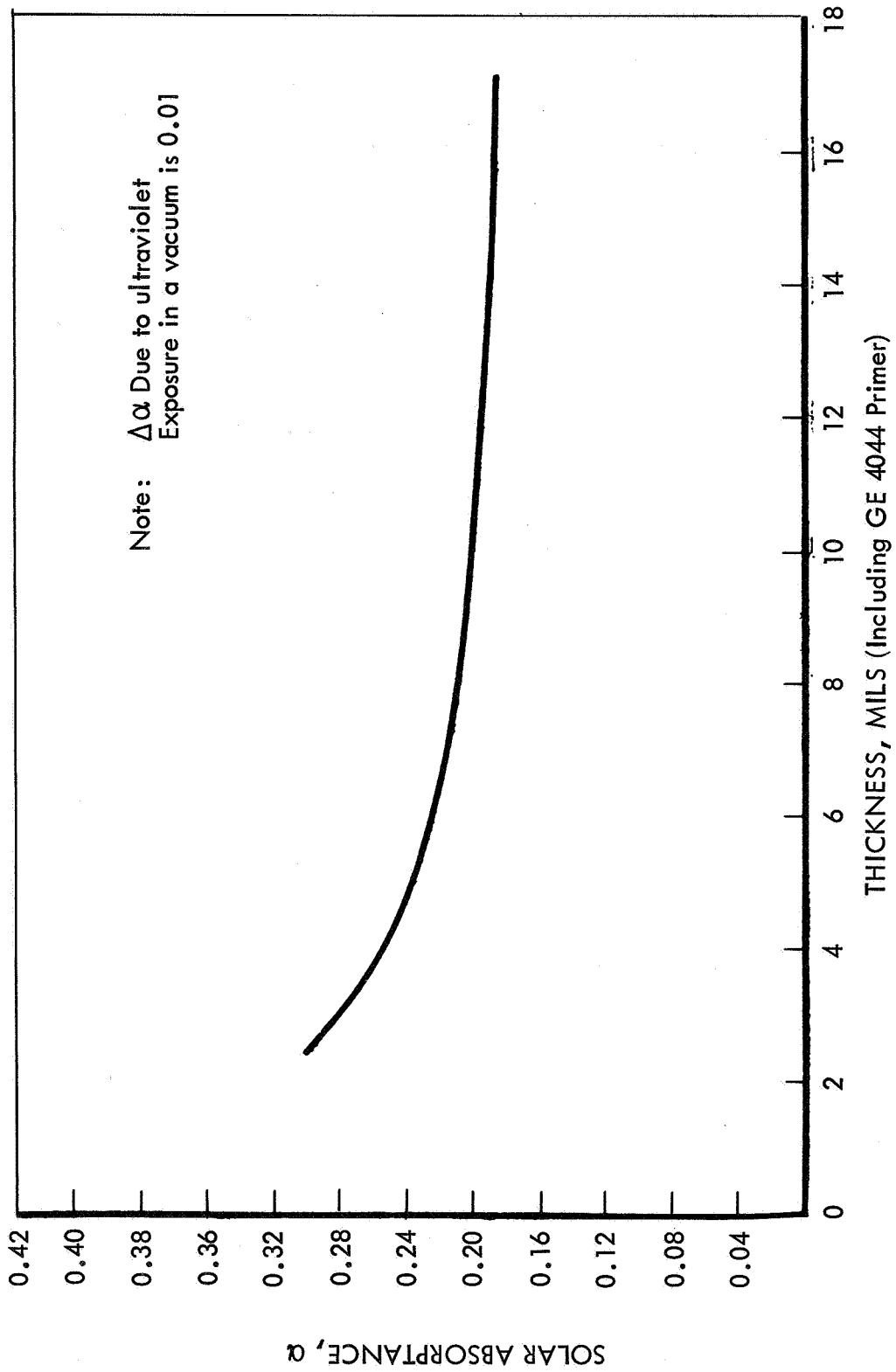
Figure 6-5:   ABSORPTANCE VERSUS THICKNESS FOR B-1060A PAINT
(For LASA Test Data)

USE FOR B-1060A ALSO
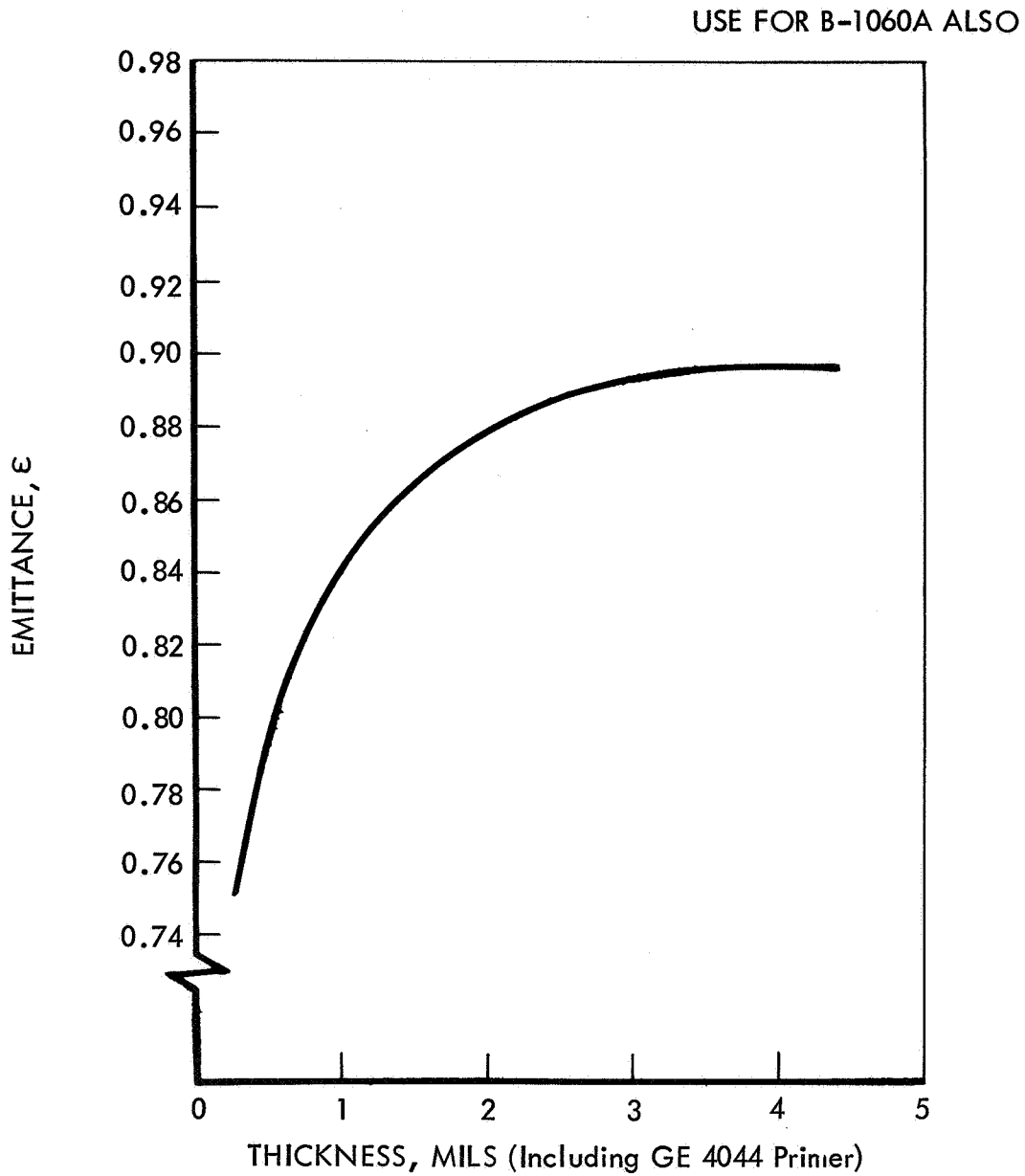
Figure 6-6: EMITTANCE VERSUS THICKNESS FOR RTV-40 PAINT
(From LASA Test Data)

TEST CONDITION: 0.5 HOUR AT TEMPERATURE
STRAIN RATE: 0.003 - 0.007 IN./IN./MIN

Be-2%BeO (XBMS 7-183)

$$F_{cc} = \frac{\Sigma b_n\, t_n\, F_{cc_n}}{\Sigma b_n\, t_n}$$
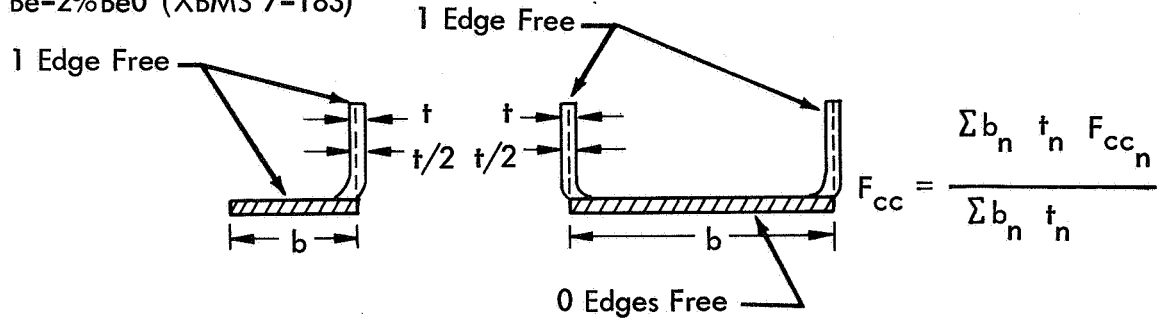
Number of Free Edges	g_f	B_{10}	m
1	1.0	0.039	0.80
0	2.7		

$70°$ (F_{cy} = 45,500 psi, E = 43.5 x 10^6 psi)

$300°$ (F_{cy} = 41,500 psi, E = 42.8 x 10^6 psi)

Design Allowables
for Large Area
Solar Array Only

F_{cc}, Ksi

$\frac{b}{g_f t}$
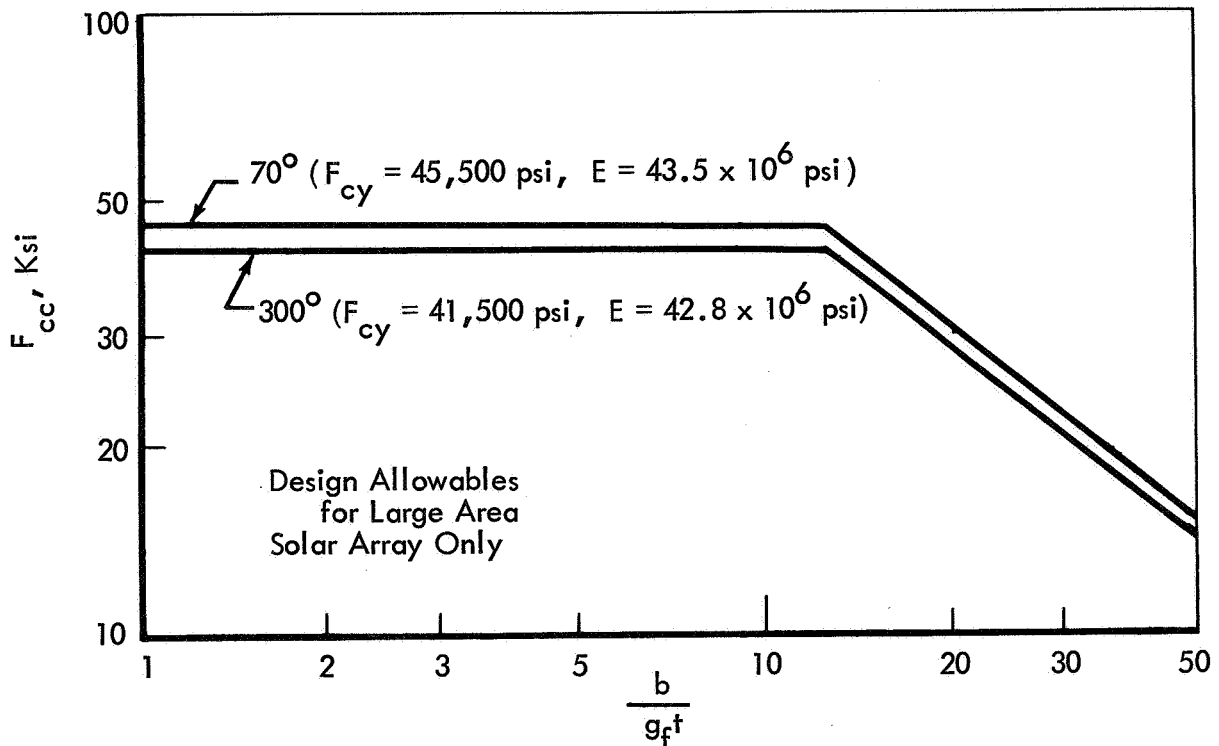
Figure 6-7: COMPRESSIVE CRIPPLING OF FORMED SECTIONS
Powdered Sheet (0.015 - 0.100)
Hot Rolled

Figure 6-8: STATIC MECHANICAL PROPERTIES OF "SCOTCHPLY" XP-251S PREPREG TAPE

BMS 5-51 type 1 primer (AE126 w/EC2320 primer)
with type 2, grade 5 film bonded per BAC 5514-551

ALUMINUM-TO-ALUMINUM

(Beryllium-to-Beryllium Equal or Better for LASA)
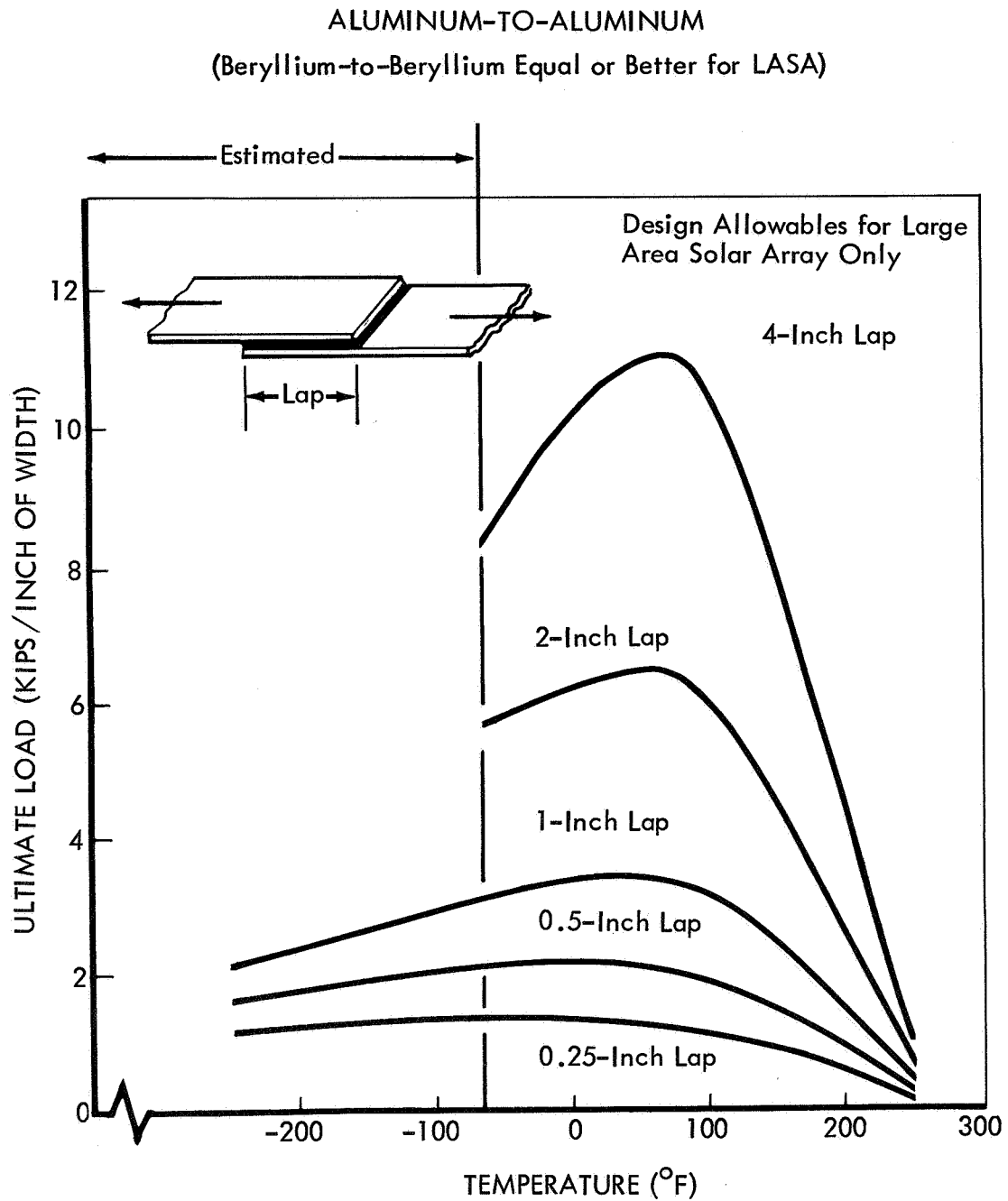
Figure 6-9: LAP SHEAR STRENGTH OF BMS 5-51 ADHESIVE

These tests were conducted on specimens having the initial flaw made by an electric discharge machine, as shown in Figure 6-11. A crack was started from this initial flaw by low stress intensity cycling. The value of K_{IC} is then computed thus:

$$K_{IC} = \sqrt{\pi}\ \sigma\sqrt{A_{cr}/Q_{cr}}$$

The technique used for predicting the subcritical cyclic or sustained-stress flaw growth involves fracture specimen testing and the stress intensity concept. The time or cycles to failure at a given maximum gross stress level depends on the magnitude of the initial stress intensity of the flaw tip, K_{Ii}, compared to the critical stress intensity, K_{IC}. The ratio of the initial-to-critical flaw size is related to the stress intensity ratio as follows:

$$\left(\frac{K_{Ii}}{K_{IC}}\right)^2 = \frac{A_i/Q_i}{A_{cr}/Q_{cr}}$$

The minimum strain rate that beryllium will experience in the LASA is about 0.2 sec^{-1}. For the low structural temperature extreme of -60°F, this results in the parameter P = 8 x 10^3. From seven tests at -60°F with high stress rates and one at -200°F with a low stress rate, a minimum K_{IC} of 11 ksi $\sqrt{\text{inch}}$ was found (Figure 6-12). This value is relatively insensitive to further reductions in temperature and/or increases in strain rate (to 0.9 x 10^5 sec^{-1}). At lower strain rates or higher temperatures, higher values of K_{IC} could be considered. A plot of test values of stress intensity ratio, K_{Ii}:K_{IC}, obtained for a cyclic stress---zero-max-zero (tension), 30 Hz, and -60°F---is shown in Figure 6-13. These data indicate that there will be an insignificant reduction in cyclic life at the 1,800 cycles predicted for LASA.

A revised curve of applied stress versus critical flaw size based on K_{IC} = 11 ksi $\sqrt{\text{inch}}$ is shown in Figure 6-14. It is apparent that this K_{IC} will permit the use of a higher design tensile strength than the previously used K_{IC} of 7.5 and will permit a larger flaw size. A design tensile strength of 45,000 psi was selected because the loads are reversible; therefore, no weight reductions can be made by using a design tensile strength greater than the design compression yield strength of the material.

Although a flaw size of 0.015 inch may be tolerated at this stress level, it is still advisable to inspect for as small a flaw as possible to ensure finding larger flaws. It is difficult to locate and measure the size of flaws in beryllium. Dye penetrant was used to locate surface flaws, and eddy currents to determine sizes; eddy currents can also be used to locate and measure the subsurface flaws. Flaws as small as 5 mils can be detected.
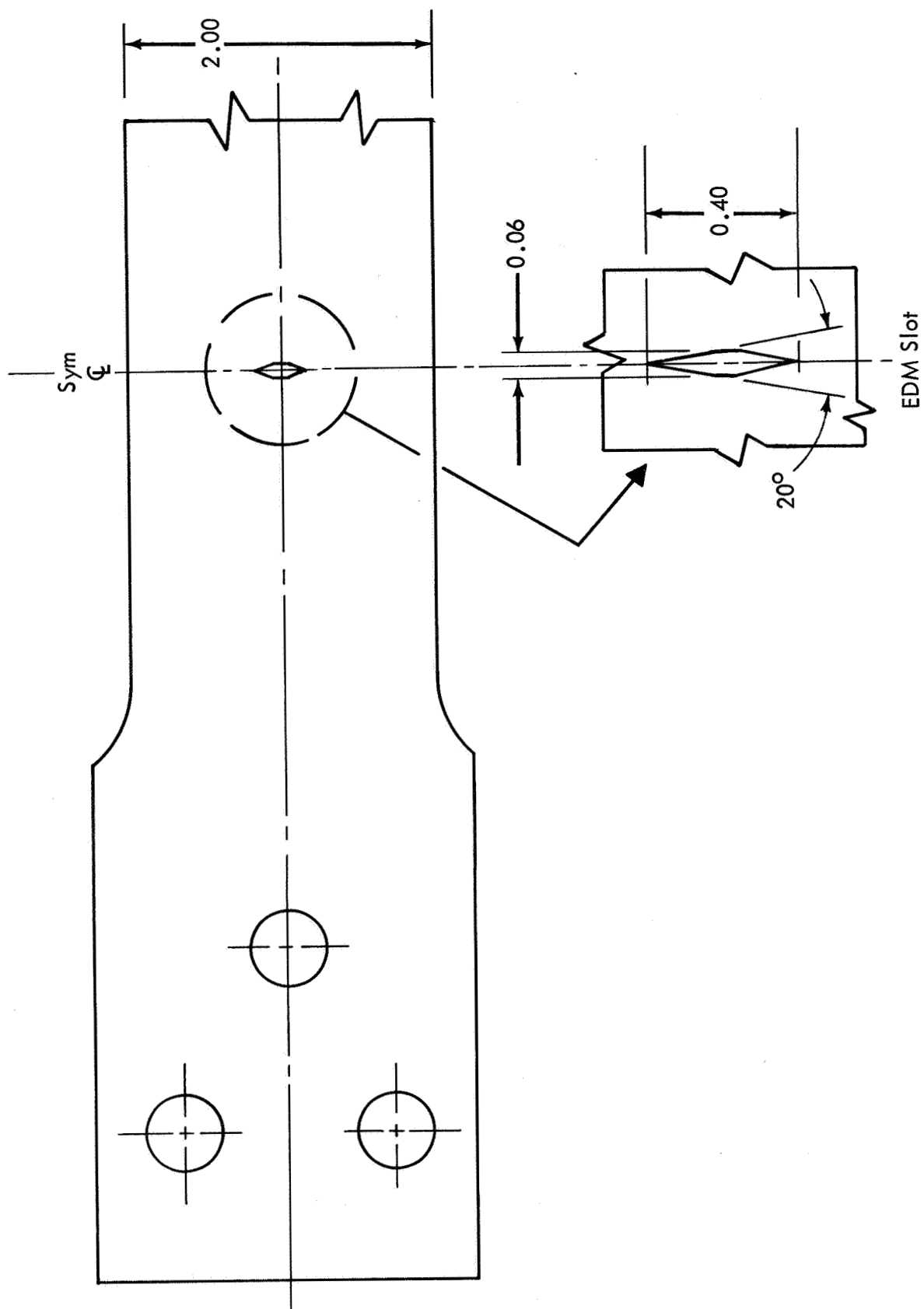
Figure 6-10: CENTER CRACKED SPECIMEN OF BERYLLIUM ALLOY

CENTER CRACK SPECIMENS
SCS – 5 TESTS

T – Temperature, ^{o}R
$\dot{\epsilon}_y$ – Strain Rate, in./in. sec
A – Frequency Factor, 10^{8} cycles/sec

$P = T \ln \dfrac{A}{\dot{\epsilon}_y}$ IN 1000'S
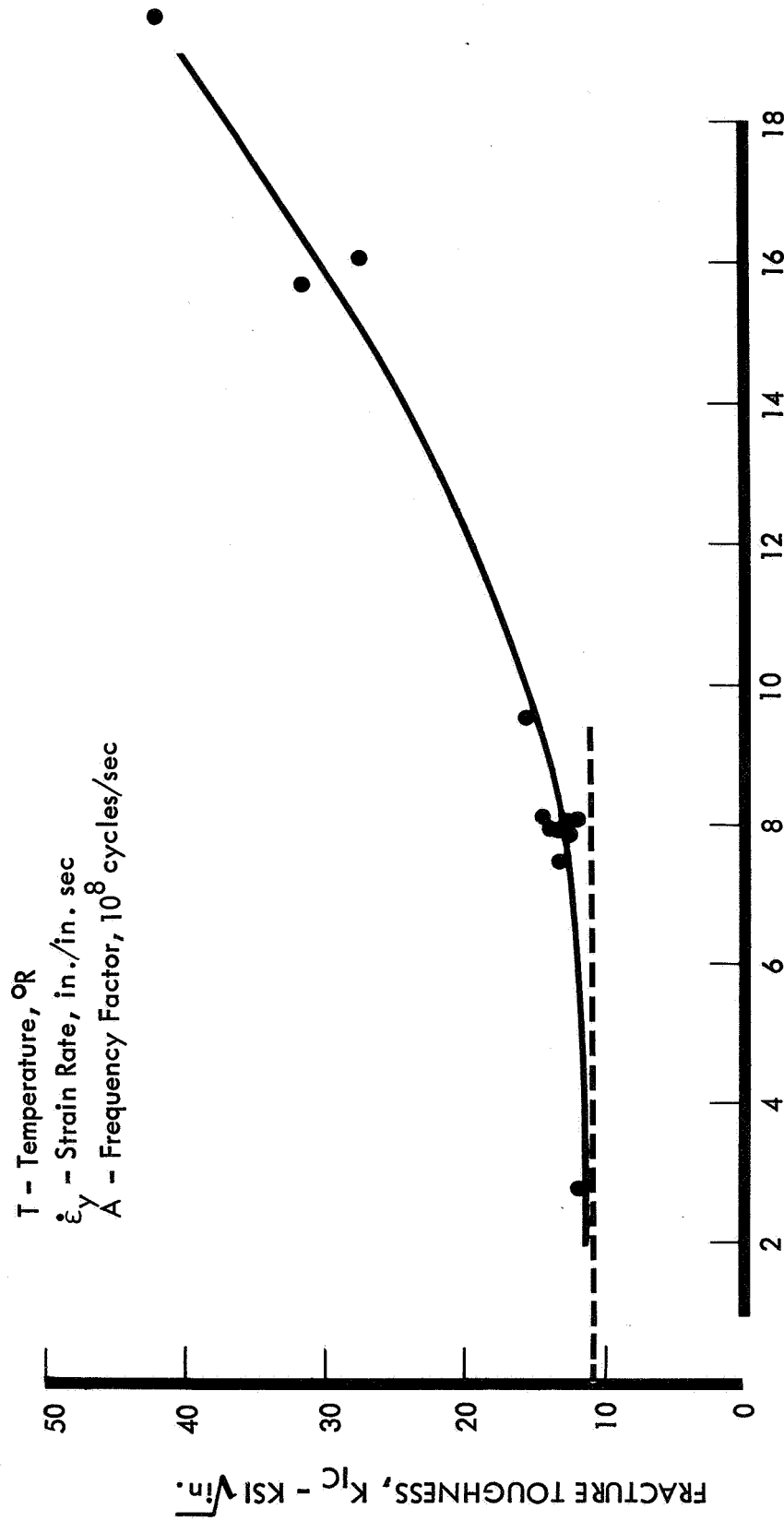
FRACTURE TOUGHNESS, K_{IC} – KSI $\sqrt{in.}$

Figure 6-11:   FRACTURE TOUGHNESS OF AMS 7902 BERYLLIUM AS FUNCTION OF TEMPERATURE & STRAIN RATE
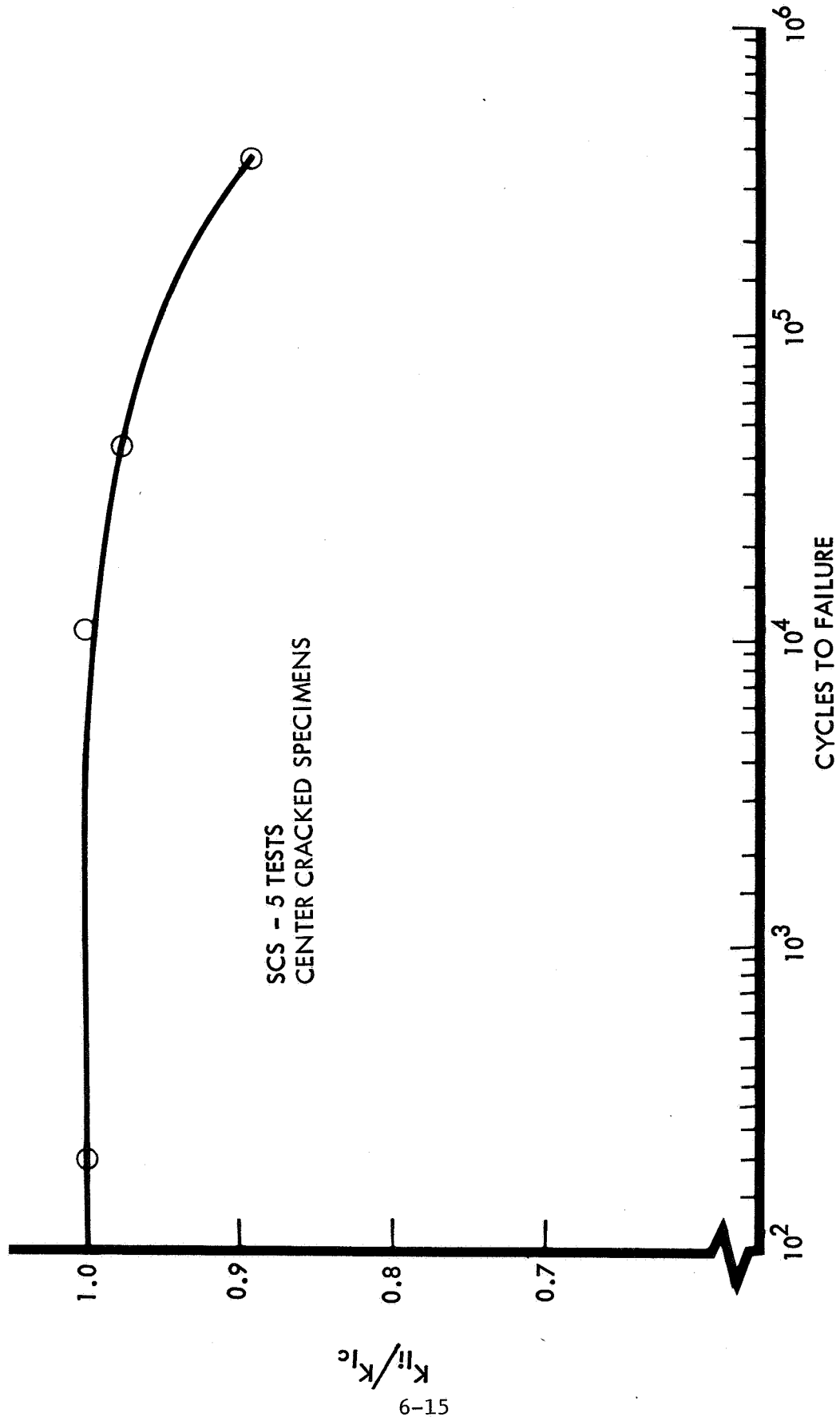
Figure 6-12:   CYCLIC GROWTH OF AMS 7902 BERYLLIUM (-60°F)

$$K_I = 1.95 \, \sigma \sqrt{^{a_{CR}}/Q_{CR}}$$

$$K_{IC} = 11. \; KSI \sqrt{in.}$$

$$0.2 \; SEC^{-1} < \dot{\varepsilon}_y < (0.9) \, 10^5 \; SEC^{-1}$$

IF $\dot{\varepsilon}_y < 0.2 \; SEC^{-1}$, $K_{IC} > 11 \; KSI \sqrt{in.}$

SURFACE FLAW

SUBSURFACE FLAW

where $2C \gg a$, $Q_{CR} = 1$

CRITICAL FLAW SIZE, $^{a_{CR}}/Q_{CR}$ - INCHES

DESIGN ALLOWABLES
FOR LASA ONLY

APPLIED STRESS, σ - KSI
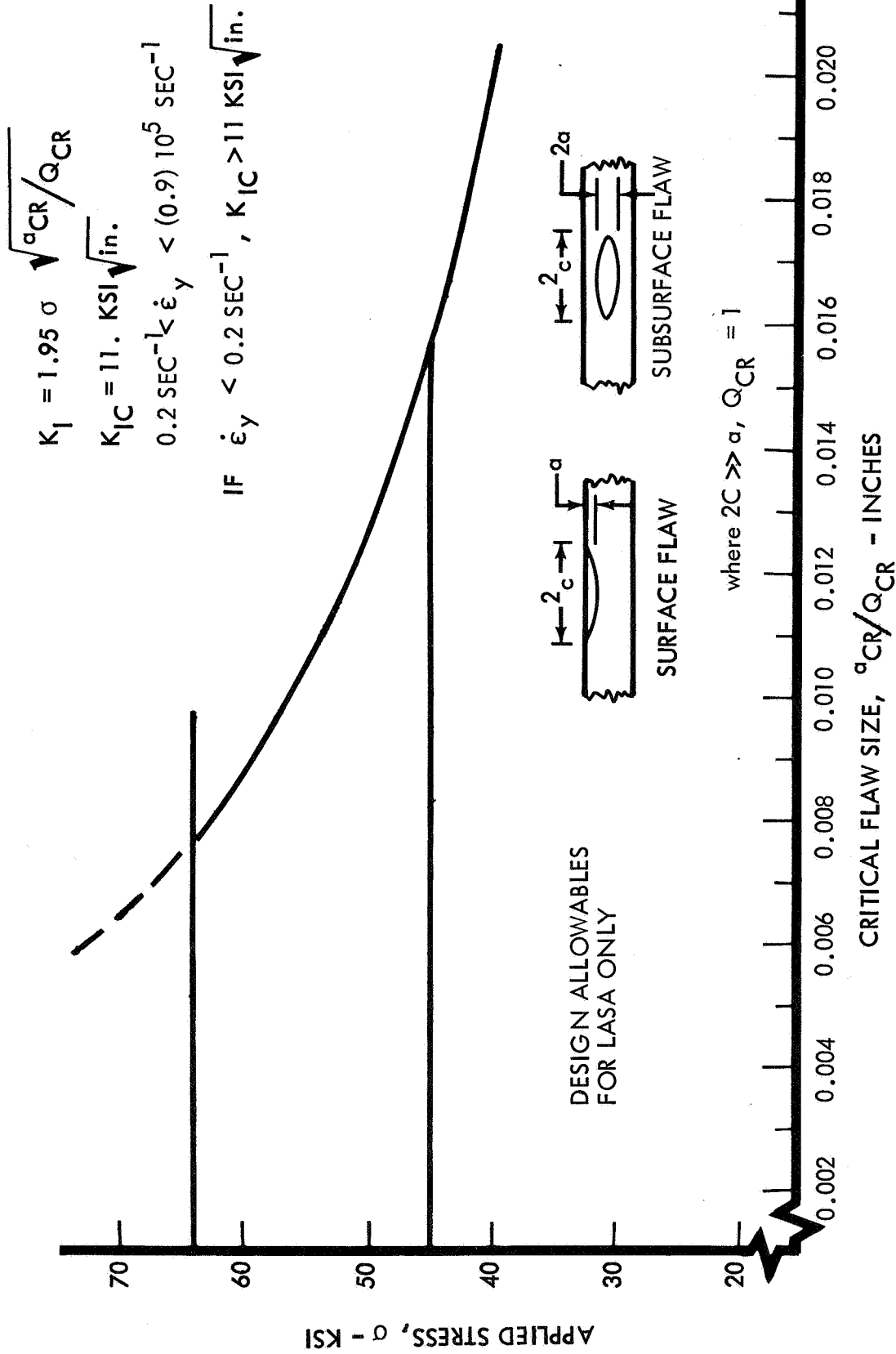
Figure 6-13:   APPLIED STRESS VERSUS CRITICAL FLAW SIZE

7.0 QUALITY ASSURANCE

7.1 EFFECTIVENESS OF TECHNIQUES FOR DETECTING DEFECTS

Investigation, refinement, and use of specific inspection techniques expedited the quality assurance program.

The design allowables established for this program required that Quality Control perfect a method to inspect beryllium for internal and external cracks as small as 5 mils in depth. Therefore, at the start of Phase I, investigations were started on nondestructive test (NDT) techniques used by Boeing on other beryllium programs and on methods used by other companies.

Radiographic techniques were first thought to be the most promising, and a study program was instituted. Special X-ray techniques are required for beryllium. Tests included use of a special vault darkroom, bare film, and inert gas atmospheres. These brief studies indicated that a comprehensive research program would be required before an operational technique could be developed, and that continued development work would cost much more than budgets allowed.

Ultrasonic techniques were considered, but all methods applicable to beryllium required the use of a liquid couplant. Liquid couplants are not compatible with LASA part configurations because of the difficulty of drying internal part surfaces.

Penetrant inspection techniques were also studied, and in mid-December 1966 a specific penetrant and inspection procedure were adopted to detect hairline surface cracks. Quality relied on the penetrant method after mid-December for inspection of defects after the chemical-milling operation. Although many defects might have been seen without the aid of the penetrant, there were times when defects would have gone undetected or the full extent of the defect would not have been known without penetrant inspection. On details where the penetrant inspection indicated a crack, particularly if it were on or in close proximity of a bend, the detail was routed to the quality assurance laboratory for a more thorough inspection with eddy current techniques. This afforded more detail (including accurate dimensions) on the crack, aided engineering in determining part dispositions, and permitted further development of eddy-current techniques for use in later program phases.

Eddy-current techniques are useful for detecting subsurface defects. Eddy current has distinguished between a 0.007-inch-deep crack in thin-gage beryllium and the surrounding surface roughness. The use of through-transmission (phase-detection) permits detection and measurement of 5-mil cracks.

Program parts subjected to eddy-current inspection included SCS-50 channels. One surface crack (originally detected by penetrant inspection) was measured and found to be less than 0.005 inch in its major dimension. Several minor laminar flaws were also detected, but the channels were accepted for use. Eddy-current inspection of SCS-43 and -50 had to be performed on individual parts before bonding operations. (After assemblies are bonded, adhesive covered areas and shear webs reduce the total area accessible to inspection.)

Inspection of the solar cell/coverglass assembly required the measurement of the bondline thickness. A light-section microscope was successfully employed for this purpose.

7.2 CONFIGURATION CONTROL

Initiation, processing, and use of hardware records are systematic and efficient, and provide a principal part of the configuration control package.

The first configuration-data item is the engineering drawing. Control points were the drawing and part number; lists of materials, notes and references; revision data; approval signature; and design. The completeness of quality review of engineering drawings was commensurate with the category of equipment; either complete or partial surveillance was involved. Drawings for complete surveillance items were thoroughly reviewed by Quality Control. Inspection of designs and line inspection requirements were the primary criteria.

The engineering shop support request (ESSR) established the release of drawings, materials, parts, and man-hours for specific fabrication activities. Program Quality Assurance reviewed and approved all ESSR's requiring quality control.

The integrated record system used in LASA consists of two basic forms. The first is the planned event record, completed by Manufacturing Planning personnel provides detail and sequential instructions to the shop concerning the fabrication of LASA hardware. This record references and supplements engineering drawings and documentation. Planned event records were reviewed and approved by Quality Control on all complete surveillance items before release to the shops or laboratories. Shop-line inspection and quality control laboratory personnel verify acceptable completion of planned event instructions on complete surveillance equipment. Quality Control laboratory reports containing details and results of evaluation tests (e.g., beryllium analysis and adhesive properties) form a part of the planned events.

The second basis form is the unplanned event record (UER), which makes up the last part of the configuration control system. These UER's can be initiated by any personnel aware and informed on a particular nonconformance during fabrication and assembly. They describe the rework or design changes required to fabricate acceptable hardware.

Processing of the unplanned records entails three basic entries: (1) a
statement of the hardware problem; (2) an engineering "disposition"
directing that the part be used as is or reworked or scrapped; and
(3) a statement (not always necessary) by the particular shop or lab-
oratory to explain what is being done to avoid recurrence of the
unplanned event.

As of February 15, 1968, over 500 individual part plans had been
reviewed by Quality Control and over 100 unplanned records concerning
solar cells, beryllium, and titanium had been processed. A discussion
of hardware quality trends, summarized from data collected on unplanned
records, is presented in Section 7.4 below.

Line-inspection personnel verified UER nonconformance and corrective
action requested by engineering. Nonconformances can be corrected by
rework to drawings or engineering changes to drawings, etc., or by con-
vening a material review board (MRB). An MRB evaluation results in one
of three dispositions: use as is, rework, or scrap. The planned and
unplanned records accompany their corresponding part and serial-
numbered hardware throughout plant processing so that an up-to-date,
on-the-spot status of program equipment is available. When assemblies
have been completed, all such records are sent to retention files. In
addition, Quality Control compiles a solar array configuration summary
containing actual configuration listings, identifying part numbers,
nomenclature, serial numbers, drawing revision data, and quantity.
Also included are brief statements identifying and explaining non-
conformance deviations and corrective action to which each end-item
part number was subjected. These data packages will be retained for a
maximum of 18 months after completion of Phase III, as stated in the
detailed quality assurance plan.

7.3 DESIGN REVIEWS, LABORATORY CERTIFICATIONS, AND LINE INSPECTIONS

*Direct Quality Assurance participation in design reviews, supplier
control, and inplant operations supports program tasks.*

As of May 1, 1968, 13 design reviews, 5 specification reviews, 14
laboratory certifications, and 3 supplier surveys have been completed.
Line and receiving inspections are continuous.

Initial surveys have been conducted of companies that supply beryllium
surface conditioning, shear teeth, and motor/cable drums.

Boeing has been represented during processing of beryllium at the
surface conditioning supplier's plant in Phase II.

Boeing service laboratories have submitted reports on LASA material
certifications for substrate tape, adhesives, beryllium, silver mesh,
solder, and several other items. Also, facilities and equipment have
been tested and certified to meet program requirements for processing

environments and conditions. Examples of the latter include cleanliness conditions, chemical ingredients of clean tanks, and conditions of penetrant inspection operations.

7.4 IDENTIFICATION OF HARDWARE PROBLEMS

Quality-trend reporting has highlighted significant problems, enabling timely corrective action.

Following collection and analysis of data from the unplanned record, hardware quality trends were plotted and submitted for program management review on a periodic basis. Figure 7-1 and Table 7-1 depict solar-cell/coverglass and beryllium part defects during MTA-1 processing. Beryllium defects are identified with the particular processes involved, along with a breakdown of final dispositions in each case.

Solar-cell/coverglass bond voids and delaminations (see Figure 7-1) were caused by defective tooling and short bondline curing time. Tooling was corrected and curing times were increased to solve this problem. Broken cell assemblies were mainly the result of improper handling. New trainees were closely supervised to control this problem. The silver peel problem was attributed to defective silver coating on solar cells received at Boeing. Solar-cell operations were suspended for this reason. Figure 7-1 shows that some 5,400 solar-cell/coverglass assemblies had been inspected.

The fabrication of MTA-1 involved the forming, chem-milling, and trimming of 777 beryllium parts and the receipt of 361 pieces of raw beryllium from vendors.

Table 7-1 summarizes 231 beryllium parts that were rejected by line inspection. Unplanned records were processed for these parts, and material reviews conducted. Of the total, 79 parts were dispositioned "use-as-is", 46 parts were used after rework, 103 were returned to vendors, and 3 were scrapped. The three parts scrapped (actually removed from fabrication and put in isolated storage) consisted of two channels approximately 40 inches in length and one flat part of 1- by 0.5-inch area.

Early in Phase II, cracks, die marks, and straightness and dimension defects were caused by problems with forming dies. Manufacturing Development personnel investigaged and corrected alignment, pressure, and shimming conditions of forming tools to eliminate these defects. Surface pitting and part-straightness defects were observed after chemical-milling. Clean etching of parts and better shipping container packaging techniques decreased the number of defects.
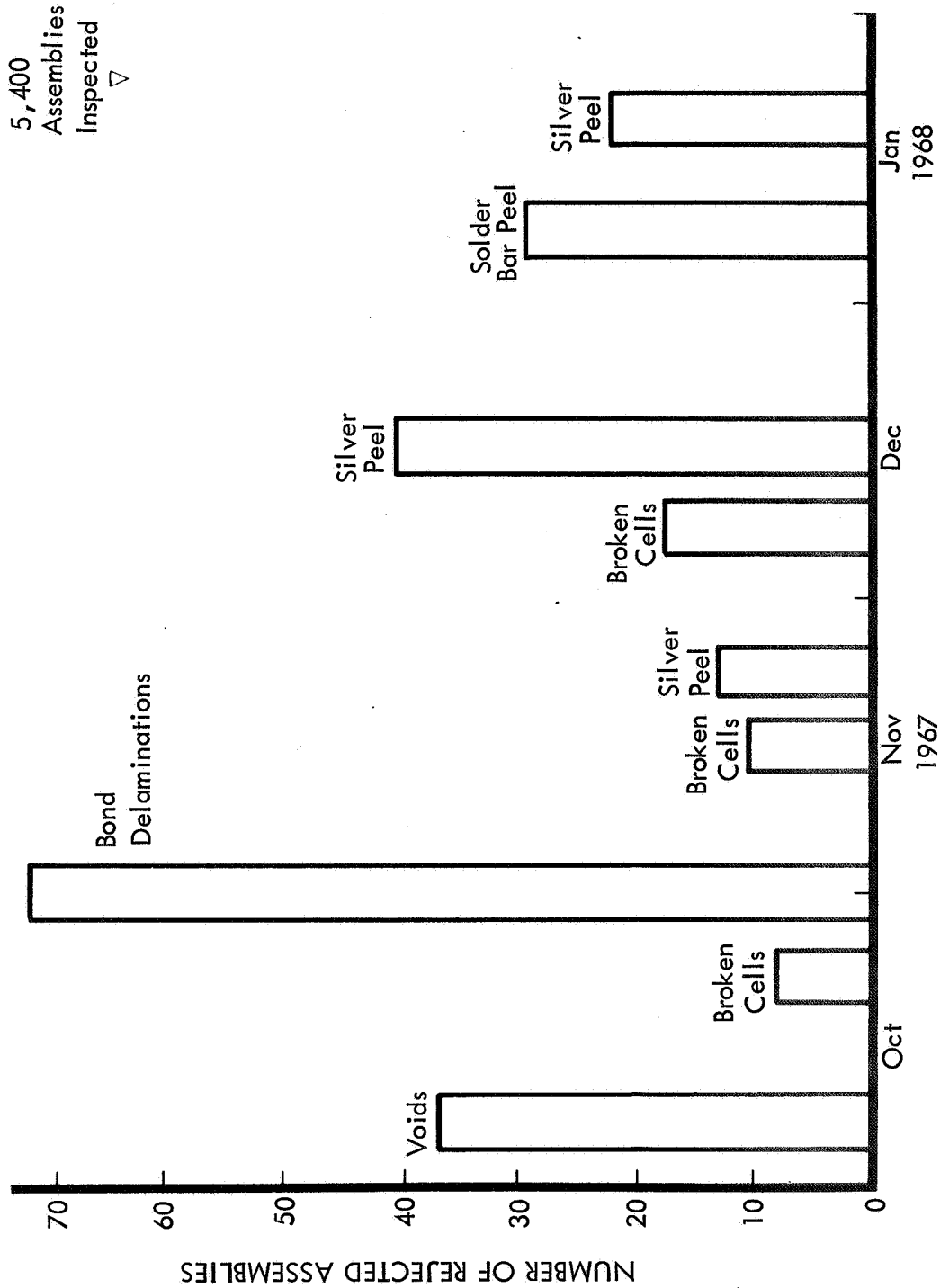
Figure 7-1: SOLAR-CELL/COVER-GLASS ASSEMBLY REJECTION VERSUS TIME

Table 7-1: BERYLLIUM PART REJECTIONS---DEFECT AND DISPOSITION BREAKDOWN

Process	Parts Rejected (Total Processed)	Parts Defects						Part Disposition			
		Cracks	Die Marks	Dimensions	Flatness	Pitting	Other Surface	Use As Is	Use As Is After Rework	Return To Vendor	Scrap
Beryllium channel forming and trimming	25 (436)	7	4	5	3	6	--	13	9	--	3
Chemical-milling	140 (341)	1	--	2	23	14	100	33	7	100	--
Receiving and inspection	66 (361)	--	--	31	2	--	33	33	30	3	--
Totals	231 (1,138)	8	4	38	28	20	133	79	46	103	3

8.0 PRODUCT ASSURANCE AND RELIABILITY

The following sections discuss failure mode and effects analysis (FMEA), reliability predictions, product safety, and maintainability, together with comments on significant program developments.

8.1 FAILURE MODE AND EFFECTS ANALYSIS (FMEA) OF ARRAY

The failure mode and effects analysis of the array is suitable as an initial baseline for future flight-article analyses.

The complete failure mode and effects analysis, including the collated FMEA data sheets, appropriate functional diagrams, and a more detailed description has been published separately as Boeing Document D2-114081-1, *Failure Mode and Effect Analysis, Large Area Solar Array*, in which electrical power, mechanisms, and structural subsystems are treated separately.

A special thermal effects summary has also been included in D2-114081-1. This summary deviates from the usual FMEA data sheet format because it attempts to tabulate the effects of thermal anomalies and to identify the responsible or cognizant personnel and organization and the relevant tests and control measures.

The results of the FMEA confirm the lack of critical failure modes with a serious risk on the electrical power subsystems. The buses and cross-overs are the obvious critical components both for open and short circuits; however, risk appears to be negligible.

The mechanism subsystems have many critical failure modes that could prevent 100% deployment. Jamming, interference, or excessive friction in the tiedown release or deployment sequence are possible. The FMEA on the boost tiedown release was not developed to a lower level of hardware, because the result would be repetitious. Single failure of any of the center-tie releases or of the corner releases at Stations 123.7 or 169.9 would be critical, as would failure of most of the cable release and linkage system. The deployment subsystem is also critical as to jamming or seizure failure modes. In summary, the FMEA of the mechanisms subsystems confirms the critical need for thorough review, test, quality control, and system checkout to ensure that all of the critical components of these subsystems are reliable.

8.2 FAILURE MODE AND EFFECTS ANALYSIS (FMEA) OF GSE

A documented analysis is advisable to identify possible risks of damage to test articles or of invalid test data.

Boeing Document D2-114081-2, *Failure Mode and Effects Analysis, Ground Support Equipment, Large Area Solar Array,* is an analysis of deployment equipment and other GSE to identify known potential causes of damage to test articles or of invalid test data. Because the LASA subpanels and panel assemblies are much larger in area than customary spacecraft components and are vulnerable to damage, it is important that the handling equipment not introduce preventable risk of damage.

Usage diagrams or flow charts that show the use of GSE and the inter-faces with test articles and operations are based on the test article flow. The FMEA data sheet format was modified for GSE. Known human error risks and externally caused conditions were noted. The objective was to identify these risk areas in addition to the customary hardware failure risks so that test personnel can take effective precautions.

A preliminary FMEA for the MTA-4 deployment and handling equipment has also been included in this phase.

Significant risks in deployment operations noted in the FMEA include:

1) Air gusts---It will be necessary to enforce strict supervision of entrances to the high-bay test area during deployment test operations;

2) Track defects;

3) Loosening of potentiometer attachments;

4) Tipping, collision, or improper support during loading of the test articles into the deployment fixture or during deployment;

5) Failure to follow air sled with tender;

6) Improper adapter installation to cause binding.

Human error and externally caused conditions have been found to consti-tute the major risk areas for handling equipment operations. Some of the risks are:

1) Interference of protruding parts of the protective covers with the subpanel during installation or removal of the covers;

2) Dropping, upset, or collision caused by error in transporting the handling frame or dolly;

3) Collision of other vehicles with the unprotected subpanels;

4) Defects in the GSE such as omission of support pads and out-of-tolerance conditions;

5) Failure to use clamps and other pieces of equipment properly.

8.3 RELIABILITY PREDICTION

Reliability prediction calculations indicate that an adequate design concept has been achieved.

The effects of solar cell random failures on array performance are covered in a separate book, Boeing Document D2-114070-1, *Effects of Random Solar Cell Failures on a Large Area Solar Array*. It has been shown that the maximum possible power loss to an array should be less than 1.5% with an estimated probability of 0.999968+. (Note: These data are obviously not applicable with ohmic contact deterioration as noted during Phase II. It has been assumed that this problem will be resolved.)

In this document, the statistics for single cell, group, module, and higher assemblies have been developed and combined with electrical data on the effects of single or multiple cell failures within a group. Precise mathematical models and calculation procedures developed in D2-114070-1 will permit future analyses and comparisons to be performed quickly and accurately.

Reliability predictions for the electrical power subsystems and the mechanism subsystems, including boost tiedown release and deployment, are defined in Boeing Document D2-114080-1, *Reliability Prediction Calculations, Large Area Solar Array*. The electrical subsystems have been shown to be relatively free of critical failure modes. The reliability of the 100-volt array subsystem is predicted as 0.99952. The reliability of the 28-volt array subsystem is 0.99984. In both cases, the predicted reliability was determined by the probability of failure of critical crossovers in the transmission system. Other failures, including open and short circuits within modules, were found to cause nothing more serious than a small power loss. In the absence of defined mission criteria, an arbitrary decision was made to classify as critical only those failures that caused more than a 5% power loss.

The overall mechanism subsystem reliability of 0.988942 includes a reliability of 0.99002 for the boost tiedown release, and 0.998912 for the deployment sequence. In contrast to the electrical power subsystem, the mechanisms subsystems are essentially single-thread systems. The failure of any of the 24 center-tie releases or the main corner latch releases at Stations 123.7 and 169.9 could result in release failure. Similarly, a sequence of events must be successfully completed on all four panel assemblies to ensure successful deployment of 100% of the array. Continued attention to details in the mechanism will be necessary during test and checkout activities.

The available data are inadequate to make quantitative predictions of structural subsystem reliability for LASA. Document D2-114080-1 includes a brief qualitative discussion of the structural subsystem. In general, the test data have been encouraging; however, there are not enough data yet available to attempt a proper statistical approach to strengthen allowables determination.

8.4 PRODUCT SAFETY

Adequate provisions have been made for product safety and range safety.

A review of the requirements of AFETRM 127-1 showed that any system including explosive devices would require a final interpretation and approval by range safety personnel. The review also confirmed that the LASA design should be capable of qualification per AFETRM 127-1 criteria. The pin-puller design has been qualified and used on Lunar Orbiter as a Category B device. Off-the-shelf cable cutters will be used and supplier qualifications checked out. The firing circuits have been designed by following accepted practices for aerospace systems.

In actual practice, product safety has been demonstrated by an absence of major damage to finished test articles that have been handled in several plant areas. There has been some damage to beryllium detail parts, and this has resulted in increased effort by shop management and personnel to improve shop attitudes and controls.

Handling frames and other ground support equipment are designed to prevent damage to completed panels. Deflection limits have been specified for such equipment, and padded contact surfaces and protective covers are used. These measures are the result of GSE design policy, including systematic design reviews and a documented failure mode and effect analysis.

8.5 MAINTAINABILITY/REPAIRABILITY

Limited repairability has been demonstrated by tests and by actual repairs required to SCS-43, SCS-35, SCS-37, and MTA-1.

Laboratory evaluation of repairability involving cell replacement and interconnector repairs was accomplished under the SCC-8 and SCC-10 tests.

In addition to the laboratory evaluation, practical repair experience has been gained. Necessary repairs to the SCS-35, SCS-37, SCS-43, and MTA-1 test articles were performed in working shops. Repairs have been accomplished outside of the engineering laboratory environment, and those on SCS-43 and MTA-1 were documented on formal integrated record system (IRS) paper.

It should be noted that repairs were successful: test articles showed no evidence of repair failure; however, this does not conclusively prove the adequacy of the repair techniques used. In particular, the ability of repair cleaning procedures to remove all possible surface contaminants to assure consistent bonding has not yet been proved.

8.6 SIGNIFICANT PROGRAM DEVELOPMENTS

Several design changes have been implemented that significantly affect product reliability.

The following items are considered significant to overall array reliability and performance:

EPON 934 Adhesive---The elimination of EPON 934 adhesive reduced the risk of bond failures associated with the peeling failure mode of this relatively brittle adhesive.

Flat Bus Bars---The use of flat bus bars bonded to the structure eliminated the risk of secondary or "nuisance" failure modes associated with the initial wire-bundle-and-clamp concept. The insulation and adhesive bonding combination used has also resulted in effective redundant insulation.

Twisted Wire Crossovers---The use of flexible wire crossovers appears to offer reduced risk of vibration-induced failures and also reduces the torque applied about the hinge centers by the crossovers, thus offering less interference with mechanisms during deployment.

Overcenter Latches---The use of overcenter latches avoided the risk of misalignment and failure to engage associated with the previous bayonet latch concept.

Substrate Bonded Intersections---The decision to retain bonded tape intersections reduces the risk of cell bond separation or cell damage that might result from localized relative motion at unbonded tape intersections.

Cell Dimensional Control and Separation Gaps---Because cell lengths and widths tended to the high side of specification tolerances, careful attention to dimensional control of separation gaps was necessary. It is recommended that any statistical treatment of cumulative tolerances be based on actual measurements taken from an adequate sample.

9.0 WEIGHT STATUS SUMMARY

Comparison of initial to final weight summaries shows a weight increase with design evolution.

The array weight based on the Phase I design of the feasibility model has increased 12.7% over the weight reported in the final report of the feasibility study. The number of mounted solar cells has increased in this period by 3.8%. Assuming that the array output power is directly proportional to the number of cells, the effective weight increase is 8.6% on a pounds-per-watt basis.

Cell module weights in Figure 9-1 include cells, coverglasses, interconnectors, and solder. Determination of actual weights of cells and cover glasses between the feasibility study final report and the first quarterly report resulted in a slight weight increase. Connector and solder weight was reduced in the third quarterly report, based on actual weights and test results.

Structure weights include substrate, frame members, joint details, and shear ties. There have been three major weight increases: The first was the addition of a diagonal brace. The second was caused by stress and dynamic analysis of basic members. The third increase reflects the change of shear clips and gussets from beryllium to titanium at all joints and also reflects the finalized shear tie design.

Mechanisms incurred a major weight increase due to the development of a satisfactory boost tiedown system design.

Bus weight decreased because of bus simplification and the use of lightweight diodes.

Adhesives and TCC weight includes coverglass and cell-to-substrate adhesives and thermal control coating weights. The major change has been a reduction in thermal control coating weight. This reduction was based on elimination of thermal control coating on the space side of the substrate on all panels except 5A and the use of RTV-40 as the primary thermal control coating material.

The weight status for the final report is summarized in Table 9-1.

Table 9-2 shows the weight status of the MTA-1 frame assembly, based on detailed parts weights and calculated weights. The weight difference between actual and the calculated is primarily in the weight of the titanium weldments.
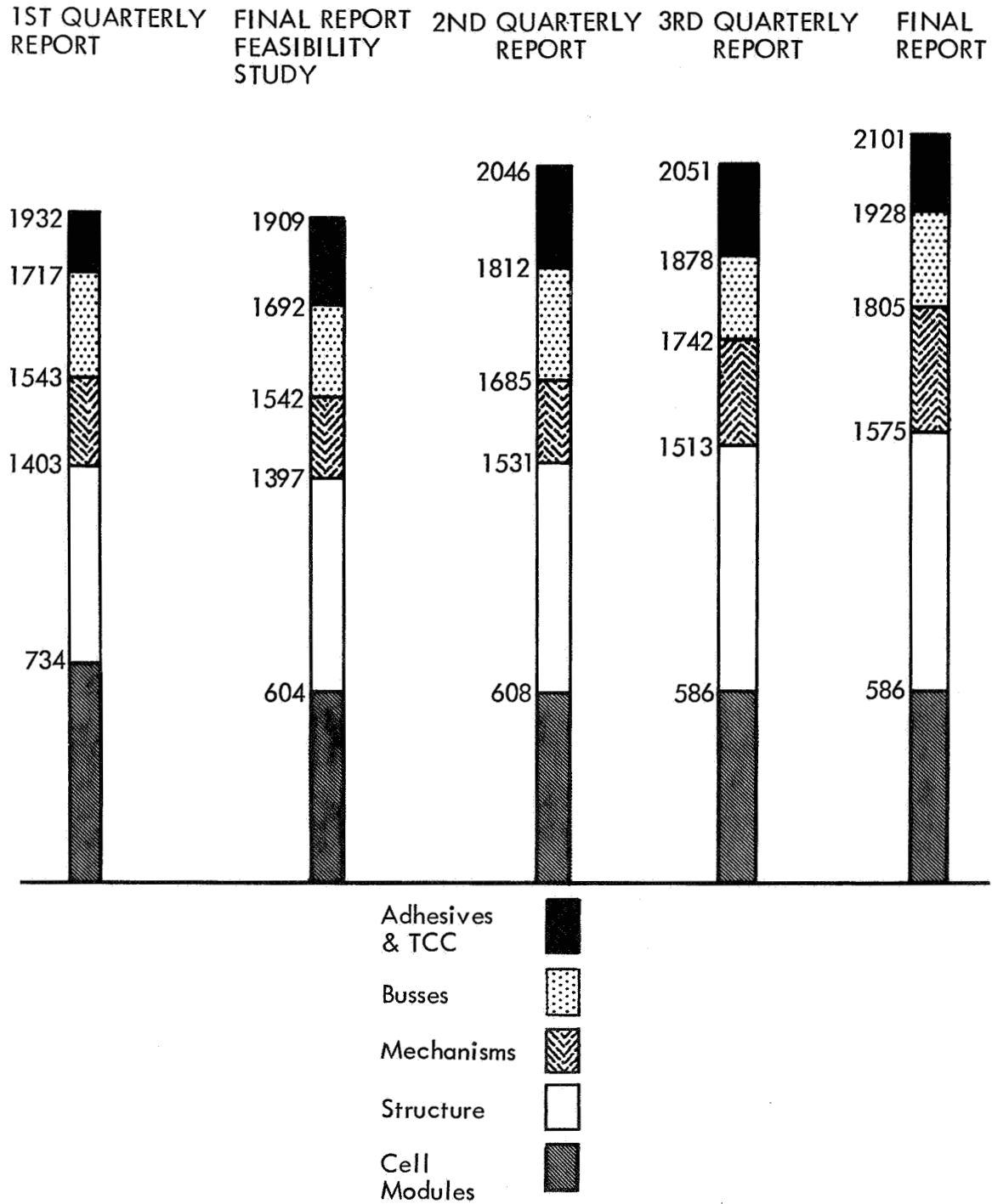
Figure 9-1:   WEIGHT STATUS SUMMARY

Table 9-1: WEIGHTS

Cell Stack, Substrate, and Thermal Coating	Weight (pounds) (838.50)	
Coverglasses	160.11	
Coverglass adhesive	18.44	
Cells	392.07	(362.1 spec max)
Connectors	56.36	
Solder	3.68	
Substrate adhesive	63.20	
Substrate	67.12	
Thermal coating	77.52	
Structure	**(949.24)**	
Panel 1 (without substrate)	214.50	
Panel 2B	80.26	
2M	74.97	
2A	66.58	
3B	59.00	
3M	63.28	
3A	59.32	
4B	59.08	
4M	59.80	
4A	60.30	
5B	46.48	
5M	48.72	
5A	56.95	
Mechanisms	**(242.0)**	
Main hinges and latches	22.9	
Auxiliary hinges, latches, and dampers	50.9	
Quadrants and sequencers	30.3	
Strut assemblies	14.5	
Solar curtains	13.2	
Boost tiedown system	71.0	
Cable, drive, and miscellaneous	39.1	
Electrical Connections	**(123.0)**	
Busses and diodes	81.6	
Pigtails and connectors	12.8	
Squib wiring	3.7	
Terminals and crossover busses	25.2	
	2,152	(2,122 based on maximum spec. weight for cells)

Table 9-2: MTA-1 ASSEMBLY WEIGHT STATUS

ITEM	WEIGHT		COMMENT
Cell module - including cells, coverglass, adhesive solder, and connector	1.50		Cell and coverglass weights are based on samplings of components obtained for use on MTA-1. Cell weight is based on distribution by grade. Connectors, solder and coverglass adhesive weights were verified on SCS-43.
Simulated cells	12.48		Based on specification nominal weight, which is based on actual cell stack weight.
Substrate adhesive and thermal coating	2.88		100% calculated: partially verified on SCS-43.
Busses	6.57		100% calculated
Frame assembly			
Substrate	1.48		Calculated weight based on actual weight of material samples.
Beryllium members	31.59		84% actual, 16% calculated; actuals are 0.9% greater than calculated weights.
Titanium fittings	17.32		100% actual: actual are 8.4% lighter than calculated.
Assembly & integration	6.35	(A)	6% actual, 94% calculated: adhesive weight based on actual weight of material samples.
TOTAL	80.17	(A)	56.2% actual
	78.54	(A)	74.0% actual and based on actual
			MTA-1 calculated weight

10.0 SUMMARY OF SPECIFIC PERFORMANCE

10.1 SUMMARY OF CRITICAL SAFETY MARGINS

The overall margin of safety is positive.

Critical margins of safety are summarized below:

Structural Category	Critical Areas	Margin of Safety	Critical Condition
Subpanel 1 members	Outboard spar	0.0	In-plane panel vibration
	Diagonal brace	0.0	Combined axial and bending stress
Subpanel 1 joints	Outboard spar to lower edge member (Sta 10.5)	0.5	In-plane panel vibration combined axial and bending stress (Note: Joint factor of safety of 1.15 is included)
	Outboard spar to lateral spar (Sta 123.7)	0.00	
Subpanels 2-5 members	Subpanel 2B outboard spar	0.003	Beryllium members critical for boost sinusoidal vibration environment; stresses due to combined bending and axial internal loads
	Subpanel 2M outboard spar	0.09	
	Subpanel 2B center spar	0.05	
	Subpanel 3B center spar	0.04	
	Subpanels 2-5 lateral spar	0.009 to 0.06	
	Subpanels 2B-3A bottom edge	0.003 to 0.09	
	Subpanel 5A bottom edge	0.06	
	Subpanel 2B upper edge	0.04	
Boost tie-down and release system	Tiedown cable assembly at Sta 123.7	0.15	Preload and boost vibration
Deployment hinges	Latch link (Compression)	0.17	Transient loads during latching
Diagonal strut	Column compression	0.01	Transient loads during latching

10.2 POWER-TO-WEIGHT RATIO

The power-to-weight ratio is 21.4 watts per pound at AMO.

The total array weight has been increased from 1,932 to 2,152 pounds.
Based on JPL specifications, power output calculations are based on an
output of 10 watts per square foot at AMO and 55°C. The total active
area of the array is 4,590 square feet. Accordingly, the total power
output is 45,900 watts, and the power-to-weight ratio is 45,900/
2,152 = 21.4 watts per pound.

11.0 BIBLIOGRAPHY AND DEFINITIONS

Individuals or organizations desiring documented information are
advised to contact JPL.

11.1 MAJOR PROGRAM DOCUMENTS

Document Number	Title
D2-113349-1	*Large Area Solar Array Design Program Plan*
D2-113350-1	*Large Area Solar Array Design General Test Plan*
D2-113350-2	*Large Area Solar Array Design Test Procedures*
D2-113350-3	*Large Area Solar Array Design Test Reports*
D2-113351-1	*Large Area Solar Array Design Detailed Quality Assurance Plan*
D2-113353-1	*Large Area Solar Array Design Manufacturing Plan and Specifications*
D2-113354-1	*Large Area Solar Array Design Process Document*
D2-113355-1	*Large Area Solar Array Design First Quarterly Report*
D2-113355-2	*Large Area Solar Array Design Second Quarterly Report*
D2-113355-3	*Large Area Solar Array Design Third Quarterly Report*
D2-113355-4	*Large Area Solar Array Design Final Report*

11.2 ADDITIONAL PROGRAM DOCUMENTS

Document Number	Title
D2-113352-1	*Large Area Solar Array Design GSE Requirements (Volume I, General Requirements)*
D2-113352-2	*Large Area Solar Array Design GSE Requirements (Volume II, Detail Requirements)*
D2-113352-3	*Large Area Solar Array Design GSE Requirements (Volume III, Master Equipment List)*
D2-113352-4	*Large Area Solar Array Design GSE Requirements (Volume IV, Phase I GSE Preliminary Design)*
D2-114070-1	*Effects of Random Cell Failures on a Large Area Solar Array*

Document Number	Title
D2-114080-1	*Reliability Prediction Calculations on a Large Area Solar Array*
D2-114081-1	*Failure Mode and Effect Analysis, Large Area Solar Array*
D2-113565-1	*The Influence of Strain Rate and Temperature Upon the Fracture Toughness of AMS 7902 Beryllium*
D2-113445-1	*Large Area Solar Array Structural Design Criteria*

11.3 MISCELLANEOUS REFERENCES

1. GMP-50505-FNC-B, "Functional Specification, Solar Cell Array, 20-watt-per-Pound

2. Walter C. Hurty, "Dynamic Analysis of Structural Systems Using Component Modes," *AIAA Journal*, Vol 3, No. 4, April 1965

3. M. J. Turner, H. C. Martin, and R. C. Weikel, "Further Developments to The Direct Stiffness Method of Structural Analysis," paper presented to AGARD in Paris, France, 1962

4. L. B. Kiersky, *COSMOS, A Computer Program for Structural Analysis*, Boeing Document D2-4513

5. H. T. Corten, A. K. Shoemaker, "Fracture Toughness of Structural Steels as a Function of the Rate Parameter T $\ln A/\dot{\epsilon}$," paper 66-WA/Met-8

6. Steven J. Fenves, R. D. Logcher, S. P. Mauch, and K. F. Reinschmidt, *STRESS: A User's Manual*, MIT Press, Massachusetts Institute of Technology, September 1964

7. S. J. Fenves, R. D. Logcher, and S. P. Mauch, *STRESS: A Reference Manual*, MIT Press, Massachusetts Institute of Technology, January 1965

8. James C. Almond, *Thermal Analyses II, Section 1.0---Engineering Usage Guide*, Boeing Document AS-1917, May 23, 1966

9. *Air Force Eastern Test Range Manual* (AFETRM) 127-1

10. Cooley and Janda, *Handbook of Space-Radiation Effects on Solar Cell Power Systems*, NASA SP-3003

11. Boeing Documents D2-23942-1 thru -5, *Fabrication Feasibility Study of a 20-Watt-Per-Pound Solar Cell Array*

12. W. R. Doherty, memorandum dated December 8, 1966, "Solar Proton Hazard to a Solar Cell Array in an Earth-Mars Mission"

13. L. V. Di Domenico, SCS-43 and SCS-50, "Configuration Summary"

11.4 SYMBOLS, TERMS, AND DEFINITIONS

LASA	Large Area Solar Array
GSE	Ground Support Equipment
SPAT	Stowed Panel Assembly Transporter
PADM	Panel Assembly Deployment Model
SCS	Small Component Test Article---Structures
SCC	Small Component Test Article---Cells
SCE	Small Component Test Article---Electrical
SCM	Small Component Test Article---Mechanisms
MTA	Major Test Article
Electric Power	Spacecraft prime electrical power is provided by one or more two-wire, ungrounded systems. Power is supplied by solar cells and is available as unregulated direct current at specified voltages.
Load, Electrical	Any component or subsystem that uses electric power and is normally operated as a unit is considered to be a load.
Voltage Range	This expresses the upper and lower voltage limits that will permit normal operation of load equipment in a mission environment.
Limit Loads	Limit loads represent the maximum loads the structure is expected to experience under specified conditions of operation, use, or test. All loads and load factors used in this document are limit loads unless otherwise noted.
Limit Design Loads	A limit design load is a limit load multiplied by the appropriate hazard factor. For the test loads specified herein, the hazard factor is unity. The yield design load is identical to the limit design load.
Ultimate Design Load	The ultimate design load is the limit design load multiplied by 1.25.

Allowable Load	The allowable load for a structural element is that load at which failure is imminent for the yield or ultimate condition, as appropriate.
Bus Voltage	The bus voltage is measured at the main electrical bus terminals. The measured value will vary with the load but will always be within the specific voltage range.
Transients, Electrical	An electrical transient is the changing condition of a characteristic that goes beyond the steady-state limits and returns to the steady-state limits within 10 milliseconds.
Electrical Load Profile	A chart or graph showing power demands (watts) at the main electrical bus as a function of time.
Source (Generation) Impedance	The source impedance is a variable that depends on solar intensity, temperature of the solar cells, and the amount of electrical load.
Reverse Current	A condition where current flow reverses direction due to a higher generated voltage from the electrical load. Reverse current is defined as having a duration of 10 milliseconds or more and is therefore not considered a transient occurrence.
Inrush Current	Inrush current is current greater than normal operating current that may be caused by various conditions, but it is always associated with switching on an electrical load.
Fault Current	Fault current is the increment of current that appears at the generator terminals and is caused by a physical short-circuit of the power leads.
Ripple	Ripple is the a.c. variation of voltage about a fixed d.c. voltage during steady-state d.c. electrical system operation.
Solar Array Configuration Solar Panel (Assembly)	Four Solar Panels---A complete assembly for one vehicle. The largest element of the solar array that attaches to the spacecraft.
Subpanel	A subpanel is the largest element of a solar panel.
Subpanel Unit	A subpanel unit is a main subpanel and two auxiliary subpanels.

Solar Cell Module	A solar cell module is the minimum group of solar cells that will independently produce the electrical subsystem voltage at the output terminals of the cell group. Modules will assume various physical outlines as required by the configuration of the structural support. Electrical power output will vary with the number of solar cells used in the module.
Solar Cell	A solar cell is the smallest electrical producing element of the module. Single crystal silicon elements are utilized.
Substrate	Substrate is the fiberglass tape matrix that supports the solar cells.
Electrical Bus	Electrical buses are metallic conductors that provide electrical continuity between solar cell modules and between each solar panel assembly and the spacecraft.
Bus Crossovers	Bus crossovers are flexible or hinged buses that provide electrical continuity across solar panel, subpanel, or solar array hinge points.